



# Updates to the ASCE-41-13 nonlinear modelling provisions for performance-based seismic assessment of new and existing steel moment resisting frames

Alexander Riley Hartloper

DEPARTMENT OF CIVIL ENGINEERING AND APPLIED  
MECHANICS

MCGILL UNIVERSITY, MONTREAL

December 6, 2016

A thesis submitted to McGill University in partial fulfilment of the requirements of the  
degree of Master of Engineering.

© Alexander R. Hartloper, 2016

# Abstract

## English

In the context of performance-based earthquake engineering, the ASCE-41-13 nonlinear modelling guidelines have historically been used by practising engineers for the performance-based seismic evaluation of new and existing steel frame buildings. The component models provided in ASCE-41-13 for steel moment-resisting frames (MRFs) are primarily based on available experimental data that was fairly limited until recently. Furthermore, a number of key limitations are present in the ASCE-41-13 guidelines with respect to the nonlinear modelling of steel beams, columns, column splice connections, and column base connections. Additionally, the effects of the composite slab on the steel beams and panel zones has been overlooked in the current ASCE-41-13 guidelines. Each of these limitations leads to a reduction in the reliability of nonlinear buildings models for steel MRFs. As such, the goal of this thesis is to improve the state of knowledge of the nonlinear component modelling of steel MRFs for performance-based earthquake engineering.

This goal is to be completed through the development of a comprehensive set of nonlinear component modelling recommendations for performance-based seismic evaluations of new and existing steel MRFs. State-of-the-art component models are developed through multiple-regression analysis procedures carried out on developed datasets from available experimental data. The resulting component models are validated via statistical tests, and through comparisons with test data. Finally, the effects of implementing the proposed modelling

recommendations are evaluated through system level case studies. Nonlinear static and dynamic analysis procedures are carried out on archetype steel frame buildings designed in highly seismic regions in North America.

The proposed nonlinear modelling recommendations provide an update to the ASCE-41-13 guidelines for steel MRFs. The recommendations provided in this thesis will be incorporated in future updates to the ASCE-41 provisions for steel MRFs.

# Français

Dans le cadre de la conception parasismique axée sur les modèles de la performance, les génies ont utilisé les consignes du ASCE-41-13 pour les modèles non linéaires pour l'évaluation sismique basée sur la performance des bâtiments neufs et existants construits en acier. Les modèles de composants fournis dans l'ASCE-41-13 pour les cadres rigides («moment-resisting frames (MRF)») en acier sont principalement basés sur les données expérimentales qui étaient plus ou moins limitées jusqu'à récemment. Il y a beaucoup de limitations clés qui sont contenues dans les consignes du ASCE-41-13 par rapport aux modèles non linéaires de poutrelles en acier, de piliers, de raccordements boulonnés de colonnes et des raccordements de base de colonnes. De plus, les effets de la dalle composite sur des poutrelles en acier et sur des zones de panneau étaient négligés dans les consignes actuelles du ASCE-41-13. Ces limitations mènent à une réduction de la fiabilité des modèles de bâtiments non linéaires de MRF en acier. Le but de cette thèse est d'améliorer l'état des connaissances de modèles de composants non linéaires de MRF en acier.

Ce but sera réalisé par le développement d'un ensemble exhaustif de conseils pour les modèles non linéaires de l'évaluation sismique basée sur la performance des bâtiments neufs et existants construits de MRF en acier. Des modèles de composants avancés sont développés par l'analyse de régressions multiples qui étaient réalisées par les bases de données qui ont de données expérimentales déjà existantes. Le résultat est que les modèles de composants sont validés par des tests statistiques avec des comparaisons avec les données des tests. Finalement, l'effet de l'implémentation des recommandations des modèles proposés sont évalués par des études de cas. Des analyses non-linéaires et dynamiques sont effectuées sur des archétypes de bâtiments avec de MRF qui ont été conçus pour les régions très sismiques en Amérique du Nord.

Les conseils pour les modèles non linéaires proposés dans cette thèse mettent à jour les consignes du ASCE-41-13 pour les MRF en acier. Les conseils dans cette thèse seront incorporés dans les prochaines mises-à-jour des ASCE-41 provisions pour les MRF en acier.

# Acknowledgements

To my supervisor, Professor Dimitrios Lignos, thank you for the guidance, support, and patience during my time under your tutelage. It has been a privilege and true pleasure to work with you, during this period I have learned an immeasurable number of things. I would like to thank as well the rest of the Department of Civil Engineering and Applied Mechanics for the knowledge that I have gained over the past six years here at McGill, and I would like to extend a special thanks to Professor Shrivastava, from whom I have learned a great deal. A personal thanks to Professor Colin Rogers for his help with many matters over the past few years.

To my office mates, and fellow members of the Lignos research group: thank you for your friendship. Ahmed, Sarven, and Seong-Hoon: thanks for your help at various points over the past few years.

This thesis relies on results and financial support obtained under Task Order 38 of the NEHRP Consultants Joint Venture (a partnership of the Applied Technology Council and Consortium of Universities for Research in Earthquake Engineering), under Contract 1140-22-025, Earthquake Structural and Engineering Research, issued by the National Institute of Standards and Technology. This financial support is acknowledged. Financial support was also provided through a McGill University graduate scholarship. The views expressed are those of the authors do not necessarily represent those of the organizations identified above.

Finally, to Anna: for your love, patience, and support—thank you.

# Contents

<b>Abstract</b>	<b>i</b>
<b>Acknowledgements</b>	<b>iv</b>
<b>Table of Contents</b>	<b>v</b>
<b>List of Figures</b>	<b>ix</b>
<b>List of Tables</b>	<b>xix</b>
<b>1 Introduction</b>	<b>1</b>
1.1 Scope . . . . .	1
1.2 Objectives . . . . .	4
1.3 State of knowledge . . . . .	5
1.4 Research contributions . . . . .	8
1.5 Outline . . . . .	9
<b>2 Literature Review</b>	<b>15</b>
2.1 Introduction . . . . .	15
2.2 Performance including damage progression . . . . .	16
2.2.1 Beams as a part of fully-restrained beam-to-column connections . . . . .	16
2.2.2 Beams as a part of partially restrained beam-to-column connections with intermediate stiffness . . . . .	18

2.2.3	Steel columns . . . . .	19
2.2.4	Beam-to-column joint panel zones . . . . .	24
2.2.5	Steel column splices . . . . .	25
2.2.6	Column base connections . . . . .	27
2.3	Available nonlinear component models . . . . .	30
2.3.1	Steel beams . . . . .	30
2.3.2	Steel columns . . . . .	35
2.3.3	Beam-to-column joint panel zones . . . . .	38
2.3.4	Column splice connections . . . . .	40
2.3.5	Column base connections . . . . .	41
2.4	Summary . . . . .	44
<b>3</b>	<b>Development of Nonlinear Modelling Recommendations</b>	<b>69</b>
3.1	Introduction . . . . .	69
3.2	Methodology for the development of component models . . . . .	70
3.2.1	Data collection . . . . .	70
3.2.2	Regression analysis . . . . .	73
3.3	Hinge model for steel beams . . . . .	78
3.3.1	Monotonic backbone curve . . . . .	78
3.3.2	First-cycle envelope curve . . . . .	82
3.3.3	Composite steel beams . . . . .	88
3.3.4	Beams as a part of pre-Northridge WUF-B connections . . . . .	91
3.3.5	Non-conforming beams as a part of fully-restrained beam-to-column moment connections . . . . .	94
3.3.6	Comparison with existing modelling options and experimental data . . . . .	95
3.4	Column hinge model . . . . .	99
3.4.1	Steel wide-flange columns . . . . .	99
3.4.2	Hollow structural steel columns . . . . .	115

3.5	Beam-to-column joint panel zone . . . . .	123
3.5.1	Bare steel beam-to-column joint panel zones . . . . .	124
3.5.2	Composite beam-to-column joint panel zones . . . . .	126
3.6	Beams as a part of partially-restrained beam-to-column connections . . . . .	127
3.7	Column splice connections . . . . .	130
3.7.1	Pre-Northridge connections . . . . .	130
3.7.2	Post-Northridge connections . . . . .	131
3.8	Column base connection hinge model . . . . .	132
3.8.1	Exposed column base connections . . . . .	132
3.8.2	Embedded column based connections . . . . .	137
3.9	Summary . . . . .	143
<b>4</b>	<b>Case Studies</b>	<b>215</b>
4.1	Introduction . . . . .	215
4.2	Description of archetype buildings . . . . .	216
4.2.1	Ground motion selection . . . . .	217
4.2.2	Numerical modelling of the steel special moment frames . . . . .	217
4.2.3	Nonlinear static analysis . . . . .	221
4.2.4	Nonlinear response history analysis . . . . .	223
4.3	Results of the nonlinear static analysis . . . . .	223
4.4	Results of the nonlinear response history analysis . . . . .	227
4.5	Summary . . . . .	229
<b>5</b>	<b>Summary and Conclusions</b>	<b>245</b>
5.1	Summary . . . . .	245
5.2	Conclusions and Recommendations . . . . .	247
5.2.1	Limitations with the ASCE-41-13 nonlinear modelling provisions for steel moment-resisting frames . . . . .	247

5.2.2	Proposed component modelling recommendations . . . . .	248
5.2.3	Findings from case studies . . . . .	252
	<b>References</b>	<b>255</b>

# List of Figures

1.1	Generalized component model based on the ASCE-41-13 provisions (ASCE, 2014). . . . .	10
1.2	Diagram of physical steel moment-resisting frame and its structural components, from ATC-114 (ATC, 2016). . . . .	11
1.3	Effects of loading history on steel frame structure components, from ATC-114 (ATC, 2016). Test data from Suzuki and Lignos (2015) and Tremblay et al. (1997). . . . .	12
1.4	Effects of loading history on steel column behaviour, from Suzuki and Lignos (2015). . . . .	13
1.5	Influence of the web-slenderness ratio on the pre-peak plastic rotation for steel wide-flange columns. . . . .	14
2.1	Connection details and geometry of beams in RBS connections, from Uang and Fan (2001). . . . .	45
2.2	Deduced moment-rotation relation for bare beam with RBS, from FEMA (2000). . . . .	46
2.3	Typical damage progression for bare beam with RBS, from FEMA (2000) and Zhang and Ricles (2006). . . . .	47
2.4	Deduced moment-chord rotation and typical damage progression for composite beams with RBS. From Elkady and Lignos (2014), FEMA (2000), and Zhang and Ricles (2006). . . . .	48

2.5	Left: Typical connection detail for pre-Northridge beam-to-column connection (WUF-B). Right: deduced moment-rotation relation of a steel beam as part of a Pre-Northridge beam-to-column connection. From FEMA (1997a) and Lu et al. (2000). . . . .	49
2.6	Typical failure modes observed in steel beams as part of pre-Northridge welded-flange-bolted-web beam-to-column connections, from FEMA-289 (FEMA, 1997a).	49
2.7	Typical shear tab connection. From FEMA (2000). . . . .	49
2.8	Typical deduced beam moment-chord rotation relations of single plate shear-tab beam-to-column connections including damage progression, from Liu (2000) and Liu and Astaneh-Asl (2004). . . . .	50
2.9	Typical damage progression in deep slender wide flange steel columns under cyclic loading, from Elkady and Lignos (2016). . . . .	51
2.10	Typical deduced moment rotation relation of stocky wide flange columns including damage progression, from Newell and Uang (2006). . . . .	52
2.11	Deduced column end moment-chord rotation relation for deep and slender wide flange steel columns under constant compressive axial load ratios, from Elkady and Lignos (2016). . . . .	53
2.12	Failure modes associated with large deformations in steel wide flange steel columns; (a) loss of column axial load carrying capacity; (b) and (c) fracture due to high distortion in the k-area, from Suzuki and Lignos (2015). . . . .	54
2.13	Comparison of unidirectional loading with bidirectional loading. Left: W24X146 $P_g/P_{ye} = 0.2$ ; right: W24X84 $P_g/P_{ye} = 0.2$ . From Elkady and Lignos (2016).	55
2.14	Deduced column end moment-chord rotation relation for W14X61 wide-flange steel columns under constant compressive axial load ratio and varying axial load coupled with symmetric lateral loading protocols. Images from ATC (2016), data from Suzuki and Lignos (2015) and Lignos et al. (2016). . . . .	56

2.15	Typical deduced column end moment-chord rotation relation of HSS steel columns including damage progression Suzuki and Lignos (2015). . . . .	57
2.16	Elephant foot local buckling mechanism, from Suzuki and Lignos (2015). . .	58
2.17	Typical hysteretic response of beam-to-column joint panel zone, from Engelhardt et al. (2000) and Newell and Uang (2006). . . . .	58
2.18	Typical hysteretic response of beam-to-column joint panel zone. Image from ATC (2016), data from Engelhardt et al. (2000), and Krawinkler et al. (1971).	59
2.19	Typical column splice details. From Bruneau and Mahin (1990). . . . .	59
2.20	Typical moment curvature relation for complete joint penetration welded splice. From Bruneau and Mahin (1991). . . . .	60
2.21	Weld fracture in welded column splice. From Shaw (2013). . . . .	61
2.22	Typical detail, moment-curvature relation and damage progression for pre-Northridge column splice connections, from Bruneau and Mahin (1991). . . .	62
2.23	Typical exposed column base details. From Fisher and Kloiber (2006). . . .	63
2.24	Damage progression of exposed column base connections, from Gomez (2010).	64
2.25	Hysteretic response of exposed column base connections, from Gomez (2010).	65
2.26	Typical embedded column base details and force transfer mechanisms, from Grilli (2015). . . . .	65
2.27	Moment drift relations for embeded type column base connections, from Grilli (2015). . . . .	66
2.28	Typical failure modes observed in embedded column base connections, from Grilli (2015). . . . .	66
2.29	The general component model for the modelling of steel frame components based on ATC-114 (ASCE, 2014). . . . .	67
2.30	Methods used to develop the fist-cycle envelope, from ASCE (2014) data from FEMA (2000). . . . .	67

2.31	Comparison of panel zone modelling options. Image (a) from Gupta and Krawinkler (1999), (b) from Charney and Downs (2004) . . . . .	68
2.32	Idealized cyclic panel zone behaviour. From Kim and Engelhardt (2002). . .	68
3.1	General component model for the ATC-114 project, from ATC (2016). . . .	157
3.2	Deduced moment-rotation data, showing first-cycle envelope curve and fitted tri-linear curve, data from Yu et al. (2000). . . . .	158
3.3	Trends on the pre-peak plastic rotation for steel beams with other-than-RBS connections based on the first-cycle envelope curve. . . . .	159
3.4	Trends on post-peak plastic rotation for steel with other-than-RBS connections based on the first-cycle envelope curve. . . . .	160
3.5	Trends on pre-peak plastic rotation for steel beams with RBS connections based on the first-cycle envelope curve. . . . .	161
3.6	Trends on post-peak plastic rotation for steel beams with RBS connections based on the first-cycle envelope curve. . . . .	162
3.7	Diagnostics for the regression of $\theta_p^*$ of the first-cycle envelope component model for beams with non-RBS connections. (a) Residuals versus fitted values; (b) Fitted values versus test data; (c) QQ-plot; (d) Histogram of residuals. . . .	163
3.8	Diagnostics for the regression of $\theta_{pc}^*$ of the first-cycle envelope component model for beams with non-RBS connections. (a) Residuals versus fitted values; (b) Fitted values versus test data; (c) QQ-plot; (d) Histogram of residuals. .	164
3.9	Diagnostics for the regression of $\theta_p^*$ of the first-cycle envelope component model for beams with RBS connections. (a) Residuals versus fitted values; (b) Fitted values versus test data; (c) QQ-plot; (d) Histogram of residuals. . . . .	165
3.10	Plot of the residuals of the $\theta_p^*$ equation for the first-cycle envelope component model for beams with RBS connections. . . . .	166

3.11	Diagnostics for the regression of $\theta_{pc}^*$ of the first-cycle envelope component model for beams with RBS connections. (a) Residuals versus fitted values; (b) Fitted values versus test data; (c) QQ-plot; (d) Histogram of residuals. . . . .	167
3.12	Plot of the residuals of the $\theta_{pc}^*$ equation for the first-cycle envelope component model for beams with RBS connections. . . . .	168
3.13	Composite effects on the hysteretic behaviour of steel beams. Images from Elkady and Lignos (2013, 2014), experimental data from Ricles et al. (2004). . . . .	169
3.14	Trends on pre-peak plastic rotation for steel beams in pre-Northridge WUF-B connections. . . . .	170
3.15	Diagnostics for regression of $\theta_p$ for beams with pre-Northridge connections. (a) Residuals versus fitted values; (b) Fitted values versus test data; (c) QQ-plot; (d) Histogram of residuals. . . . .	171
3.16	Plot of residuals versus $d$ for the $\theta_p$ equation for beams with pre-Northridge connections. . . . .	172
3.17	Flexural strength of bare steel beams with respect to their unbraced length, from ATC-114 (ATC, 2016). . . . .	173
3.18	Comparison of deduced beam moment-rotation response with predicted response from ASCE-41-13 and proposed ATC-114 component models. Data from: (a,b) Tsai and Popov (1988); (c) Popov et al. (1997); (d) Chi and Uang (2002); (e) Engelhardt et al. (2000); (f) Ricles et al. (2002); . . . . .	174
3.19	Comparisons of proposed modelling recommendations with ASCE-41-13 for composite steel beams, data from Zhang and Ricles (2006). . . . .	175
3.20	Comparisons of proposed modelling recommendations with ASCE-41-13 for steel beams as part of pre-Northridge beam-to-column connections. Data from FEMA (1997a); Tsai and Popov (1988); Engelhardt and Sabol (1994). . . . .	176
3.21	Plot of the web versus flange width-to-depth ratios from the database of steel wide-flange columns. . . . .	177

3.22	Trends on pre-peak plastic rotation, $\theta_p$ , for steel wide-flange columns subjected to monotonic loading protocols. . . . .	178
3.23	Trends on post-peak plastic rotation, $\theta_p^*$ , for steel wide-flange columns subjected to symmetric cyclic loading protocols. . . . .	179
3.24	Trends on post-peak plastic rotation, $\theta_{pc}$ , for steel wide-flange columns subjected to monotonic loading protocols. . . . .	180
3.25	Trends on pre-peak plastic rotation, $\theta_{pc}^*$ , for steel wide-flange columns subjected to symmetric cyclic loading protocols. . . . .	181
3.26	Trends on hardening ratio, $a = M_{max}/M_y^*$ , for steel wide-flange columns subjected to monotonic loading protocols. . . . .	182
3.27	Trends on hardening ratio, $a^* = M_{max}^*/M_y^*$ , for steel wide-flange columns subjected to symmetric cyclic loading protocols. . . . .	183
3.28	Diagnostics for the regression of $\theta_p$ for the monotonic backbone component model for wide-flange columns. (a) Residuals versus fitted values; (b) Fitted values versus test data; (c) QQ-plot; (d) Histogram of residuals. . . . .	184
3.29	Plot of residuals versus $P_g/P_{ye}$ for $\theta_p$ for the monotonic backbone component model for wide-flange columns. . . . .	185
3.30	Diagnostics for the regression of $\theta_{pc}$ for the monotonic backbone component model for wide-flange columns. (a) Residuals versus fitted values; (b) Fitted values versus test data; (c) QQ-plot; (d) Histogram of residuals. . . . .	186
3.31	Plot of residuals versus $P_g/P_{ye}$ for $\theta_{pc}$ for the monotonic backbone component model for wide-flange columns. . . . .	187
3.32	Diagnostics for the regression of $a = M_{max}/M_y^*$ for the monotonic backbone component model for wide-flange columns. (a) Residuals versus fitted values; (b) Fitted values versus test data; (c) QQ-plot; (d) Histogram of residuals. . . . .	188
3.33	Plot of residuals versus $P_g/P_{ye}$ for $a = M_{max}/M_y^*$ for the monotonic backbone component model for wide-flange columns. . . . .	189

3.34	Diagnostics for the regression of $\theta_p^*$ for the first-cycle envelope component model for wide-flange columns. (a) Residuals versus fitted values; (b) Fitted values versus test data; (c) QQ-plot; (d) Histogram of residuals. . . . .	190
3.35	Plot of residuals versus predictors of $\theta_p^*$ for the first-cycle envelope component model for wide-flange columns. . . . .	191
3.36	Diagnostics for the regression of $\theta_{pc}^*$ for the first-cycle envelope component model for wide-flange columns. (a) Residuals versus fitted values; (b) Fitted values versus test data; (c) QQ-plot; (d) Histogram of residuals. . . . .	192
3.37	Diagnostics for the regression of $a^* = M_{max}^*/M_y^*$ for the first-cycle envelope component model for wide-flange columns. (a) Residuals versus fitted values; (b) Fitted values versus test data; (c) QQ-plot; (d) Histogram of residuals. . . . .	193
3.38	Plot of residuals versus predictors of $a^* = M_{max}^*/M_y^*$ for the first-cycle envelope component model for wide-flange columns. . . . .	194
3.39	Comparison between test data and proposed ATC-114-1 monotonic backbone component model for wide-flange beam columns. Data from Suzuki and Lignos (2015). . . . .	195
3.40	Comparison between test data and proposed ATC-114-1 component model based on the first cycle envelope for wide-flange beam columns. Data from Elkady and Lignos (2016), and Lignos et al. (2016). . . . .	196
3.41	Trends of pre- and post-peak plastic deformations with respect to the cross-section web local slenderness ratio for modelling the monotonic backbone curve of steel wide-flange columns, from ATC (2016). . . . .	197
3.42	Trends of pre- and post-peak plastic deformations with respect to the cross-section web local slenderness ratio for modelling the first-cycle envelope curve of steel wide-flange columns, from ATC (2016). . . . .	197
3.43	Comparison of unidirectional loading with bidirectional loading. Left: W24X146 $P_g/P_{ye} = 0.2$ ; right: W24X84 $P_g/P_{ye} = 0.2$ . From Elkady and Lignos (2016). . . . .	198

3.44	Comparisons of proposed modelling recommendations with ASCE 41-13 for end columns as part of steel MRF systems. Images from ATC (2016), data from Newell and Uang (2006) and Lignos et al. (2016). . . . .	199
3.45	Trends on modelling parameters for steel HSS columns subjected to symmetric cyclic loading protocols. . . . .	200
3.46	Trends on modelling parameters for steel HSS columns subjected to symmetric cyclic loading protocols. . . . .	201
3.47	Trends on modelling parameters for steel HSS columns subjected to symmetric cyclic loading protocols. . . . .	202
3.48	Diagnostics for the regression of $\theta_p^*$ of the first-cycle envelope component model for HSS columns. (a) Residuals versus fitted values; (b) Fitted values versus test data; (c) QQ-plot; (d) Histogram of residuals. . . . .	203
3.49	Plot of residuals of $\theta_p^*$ versus $P_g/P_{ye}$ for the first-cycle envelope component model for HSS columns. . . . .	204
3.50	Diagnostics for the regression of $\theta_{pc}^*$ of the first-cycle envelope component model for HSS columns. (a) Residuals versus fitted values; (b) Fitted values versus test data; (c) QQ-plot; (d) Histogram of residuals. . . . .	205
3.51	Diagnostics for the regression of $a^* = M_{max}^*/M_y^*$ of the first-cycle envelope component model for HSS columns. (a) Residuals versus fitted values; (b) Fitted values versus test data; (c) QQ-plot; (d) Histogram of residuals. . . .	206
3.52	Comparison of experimental data with proposed component modelling options for HSS columns, data from Suzuki and Lignos (2015). . . . .	207
3.53	Trends of pre- and post-peak plastic deformations with respect to the cross-section web local slenderness ratio for modelling the monotonic backbone curve of HSS columns, from ATC (2016). . . . .	207
3.54	Image (a) from Gupta and Krawinkler (1999) and (b) from Elkady and Lignos (2014), with data from Engelhardt et al. (2000). . . . .	208

3.55	Boundary forces acting on interior composite panel zone, image from Elkady and Lignos (2015b). . . . .	208
3.56	Idealized moment-rotation relation for hinge model for beams as part of partially-restrained connections with intermediate stiffness. Image from ATC (2016), adopted from Liu and Astaneh-Asl (2004). . . . .	209
3.57	Effective depth for calculation of moment capacity. Image from ATC (2016), adopted from Liu and Astaneh-Asl (2004). . . . .	209
3.58	(a) Modified envelope curve for composite shear tab connections including flexural strength stiffening as a result of beam binding; (b) illustration with experimental data. Image from Elkady and Lignos (2015b), test data from Liu and Astaneh-Asl (2004). . . . .	210
3.59	Stress distributions assumed in current U.S. design practice for (a) low; and (b) high-eccentricity conditions, from Kanvinde et al. (2012). . . . .	211
3.60	Assumed deformation mode and contribution of various components, from Kanvinde et al. (2012). . . . .	211
3.61	Comparison between test data and proposed ATC-114-1 first-cycle envelope component model for exposed column bases. Data taken from Gomez (2010). . . . .	212
3.62	Load resisting mechanisms for embedded column bases (a) horizontal bearing and panel zone accompanied by vertical bearing and skin friction, (b) critical condition for horizontal bearing failure; in the case shown $d_{effective} = d_{embed}$ . Images from Grilli (2015). . . . .	213
3.63	Comparison between test data and proposed ATC-114-1 first-cycle envelope component model for embedded column bases. Data taken from Grilli (2015). . . . .	214
4.1	Plan view of archetype buildings, from NIST (2010). . . . .	236
4.2	General component model for the ATC-114 project, from ATC (2016). . . . .	237
4.3	Visualization of the 4-story numerical model with explicit modelling of the beam-to-column joint panel zones. . . . .	238

4.4	Physical details and model representations of beam-to-column joint panel zones for RBS connections. . . . .	239
4.5	Global pushover curves based on single-mode nonlinear static procedure and various component-modelling options. . . . .	240
4.6	Prediction of the nonlinear static response of the first story interior beam-to-column panel zone joint of the 12-story steel SMF based on first-mode nonlinear static procedure. . . . .	241
4.7	(a) Compressive axial force column demands for 12-story archetype based on nonlinear static procedure, first-mode lateral load pattern. Representative moment-rotation relation of a W24X192 steel column with varying axial load ratios, $P_g/P_{ye}$ : (b) 50%, symmetric protocol (c) 75%, symmetric protocol and (d) 50%, collapse consistent protocol. . . . .	242
4.8	Predicted peak story drift ratios along the height of the 12-story archetype based on nonlinear static procedure, first-mode lateral load pattern. . . . .	243
4.9	NSP to NRHA comparison of predicted story-based engineering demand parameters, 12-story archetype; left DBE seismic intensity; right MCE seismic intensity. . . . .	244

# List of Tables

3.1	Summary of the results from the regression analysis of $\theta_p^*$ for beams in non-RBS fully-restrained beam-to-column connections. . . . .	148
3.2	Summary of the results from the regression analysis of $\theta_{pc}^*$ for beams in non-RBS fully-restrained beam-to-column connections. . . . .	148
3.3	Summary of the results from the regression analysis of $\theta_p^*$ for beams in RBS fully-restrained beam-to-column connections. . . . .	148
3.4	Summary of the results from the regression analysis of $\theta_{pc}^*$ for beams in RBS fully-restrained beam-to-column connections. . . . .	148
3.5	Modification factors for composite steel beams, values from Elkady and Lignos (2014). . . . .	149
3.6	Summary of the results from the regression analysis of $\theta_p^*$ for beams in pre-Northridge WUF-B connections. . . . .	149
3.7	Modelling parameters for first-cycle envelope of beams as a part of fully-restrained beam-to-column connections, with $L_b/r_y = 50$ and $L = 150$ in. †Outside range of predictive equations for RBS connections. ‡Outside range of predictive equations for non-RBS connections. . . . .	150
3.8	Summary of the results from the regression analysis of $\theta_p$ for wide-flange columns based on the monotonic backbone. . . . .	151
3.9	Summary of the results from the regression analysis of $\theta_{pc}$ for wide-flange columns based on the monotonic backbone. . . . .	151

3.10	Summary of the results from the regression analysis of $a = M_{max}/M_y^*$ for wide-flange columns based on the monotonic backbone. . . . .	151
3.11	Summary of the results from the regression analysis of $\theta_p^*$ for wide-flange columns based on the first-cycle envelope. . . . .	152
3.12	Summary of the results from the regression analysis of $\theta_{pc}^*$ for wide-flange columns based on the first-cycle envelope. . . . .	152
3.13	Summary of the results from the regression analysis of $a^* = M_{max}^*/M_y^*$ for wide-flange columns based on the first-cycle envelope. . . . .	152
3.14	Modelling parameters for monotonic back bone curve of wide-flange columns, with $L = 13$ feet $F_{ye} = 55$ ksi. †Outside of the range of the predictive equations.	153
3.15	Modelling parameters for first-cycle envelope of wide-flange columns, with $L = 13$ feet $F_{ye} = 55$ ksi. †Outside of the range of the predictive equations. .	153
3.16	Summary of the results from the regression analysis of $\theta_p^*$ of the first-cycle envelope component model for HSS columns. . . . .	154
3.17	Summary of the results from the regression analysis of $\theta_{pc}^*$ of the first-cycle envelope component model for HSS columns. . . . .	154
3.18	Summary of the results from the regression analysis of $a^* = M_{max}^*/M_y^*$ of the first-cycle envelope component model for HSS columns. . . . .	154
3.19	Modelling parameters for monotonic backbone of HSS columns, with $L = 13$ feet $F_{ye} = 70$ ksi. †Outside of the range of the predictive equations. . . . .	155
3.20	Modelling parameters for first-cycle envelope of HSS columns, with $L = 13$ feet $F_{ye} = 70$ ksi. †Outside of the range of the predictive equations. . . . .	156
4.1	Member sizes and elevations for each of the archetype frames. From NIST (2010). . . . .	232
4.2	Story nodal loads and masses for the archetype buildings. . . . .	233
4.3	Model periods and static overstrength for nonlinear static analysis. . . . .	234
4.4	Target roof displacement ratios per the ASCE-41-13 coefficient method. . . . .	235

# Chapter 1

## Introduction

### 1.1 Scope

Despite the advancements in building technology in the past few decades, seismic activity has led to the collapse of numerous buildings over this time period. Moreover, in the event that a building does not collapse during an earthquake, the costs incurred due to repairs may be significant, and in certain situations they may be demolished in any case. In an effort to reduce monetary losses and to prevent the loss of livelihood associated with earthquakes, engineers utilize a number of nonlinear analysis procedures to predict the state of structures during and following earthquakes.

Increasingly, practising engineers are utilizing the performance-based earthquake engineering framework to achieve building designs that minimize the losses associated with a targeted building performance level. Performance-based assessments make use of a robust decision making tool that takes into account the probabilistic nature of both the seismic hazard and the structural response, thereby allowing the designers to better manage the risks associated with earthquakes. One of the essential inputs into this decision making tool are the estimates of the building's engineering demand parameters (EDPs). The EDPs are representative of the building's response to seismic events, and can be predicted by the results of nonlinear

structural analysis. EDPs are reported in terms of deformations, forces, or any other relevant parameters of interest.

Numerical building models for performance-based seismic assessments require that a number of assumptions are made with regards to the behaviour of the individual structural components under seismic loading. It follows then, that in order for the nonlinear structural analysis to be reliable, the assumptions surrounding the modelling of the individual structural components must themselves be reliable. Since performance-based earthquake engineering is a probabilistic framework, we would like to minimize the uncertainties related to the structural analysis in order to achieve a reliable solution. Therefore, it is clearly seen that the confidence in the results of the performance-based seismic assessment are in part dependant on the reliability of the nonlinear component models.

For all structural systems and materials, practising engineers are developing numerical building models for seismic assessments based on the provisions provided in ASCE-41-13, *Seismic Evaluation and Retrofit of Existing Buildings* (ASCE, 2014). The component models in ASCE-41-13 are phenomenological, such that the complex behaviour of each structural components are represented through a force-deformation relation. With reference to Figure 1.1, the ASCE-41-13 component model describes the behaviour of the structural component in terms of the component strength,  $Q$ , that could be a stress, force or moment; and the deformation,  $\Delta$ , that could be a rotation, displacement, curvature, or elongation.

With reference to Figure 1.1 the elastic behaviour of the structural component is represented by the line AB, where the response is determined by the effective elastic stiffness of the component. The plastic behaviour of the component can be clearly divided into three regions, the first of these is the pre-peak plastic region, delineated by the line BC. In the pre-peak plastic region, the component strength increases with deformation due to hardening. At a certain point, deterioration in the component strength and stiffness will initiate due to local, global, and/or lateral-torsional instabilities. The region of deterioration is the post-peak plastic region, and is represented by the line CD. Finally the plateau region from DE is

representative of the residual strength of the component. The point E is associated with the loss of gravity carrying capacity of the respective component.

Typically the definition of the ASCE-41-13 component model shown in Figure 1.1 requires the calculation of the response parameters  $Q_y$ ,  $a$ ,  $b$ , and  $c$ . The equations for calculating these response parameters are based on empirical relations deduced from the statistical analysis of experimental data; or in many cases, they were estimated based on engineering judgement due to a lack of experimental data.

Looking specifically at steel moment-resisting frames (MRFs), there are several issues to be addressed with the ASCE-41-13 component models, some of these issues are summarized as follows:

- Current ASCE-41-13 recommendations do not provide guidelines on how to construct component models for nonlinear response history analyses
- The current component models were developed based on experimental data from almost 30 years ago
- The ASCE-41-13 component models may not consider all local, global, and lateral-torsional instability related deterioration mechanisms
- There is a lack of component modelling provisions for column splices, column base connections, and composite steel beams
- The component models in ASCE-41-13 do not consider the variability of input data

The need to provide updates to the ASCE-41-13 component models was seen by the Applied Technology Council (ATC), in their call for the project ATC-114, *Guidelines for Nonlinear Structural Analysis for Design of Buildings* (ATC, 2016). Each of the aforementioned issues are addressed in turn in this thesis through the development of a set of recommendations for the nonlinear modelling of structural components in steel frame buildings. These recommendations are based on state-of-the-art component modelling procedures in the context of performance-based earthquake engineering. It is shown that the reliability of nonlinear analyses for steel MRFs can be increased by utilizing the proposed set of recommendations developed in this

thesis. The proposed nonlinear modelling provisions are a part of the recommendations proposed in the ATC-114 project for steel MRFs. The ATC-114 project will be used to form the next generation of component models in future versions of ASCE-41.

## 1.2 Objectives

The goal of the research carried out in this thesis is to improve the reliability of nonlinear structural analysis for the performance-based seismic assessment of new and existing steel MRFs by improving the state of knowledge of nonlinear component modelling for steel frame buildings. There are three main objectives associated with this goal; the first is to assess the state of the current component modelling provisions for steel MRFs, and to identify the major limitations and research needs for the nonlinear modelling of structural components for performance-based earthquake engineering. This is done through a review and gathering of the existing literature on the modelling of steel MRF components, and available experimental data on structural steel components. An evaluation of the review is done to determine if each of the component models will provide a reliable estimate of the structural component behaviour, or if an update to the component model is required.

The second objective of this thesis is to provide a set of nonlinear component modelling recommendations for each of the structural components in steel MRFs. The proposed nonlinear component models can be utilized for either nonlinear static or response history analysis procedures, and are intended to be used for the performance-based seismic assessment of new and existing steel MRFs. For the component models where deficiencies are noted as a part of the literature review, new formulations are developed based on a multiple-regression analysis of experimental data. As a part of fulfilling this objective nonlinear modelling recommendations are provided for each of the structural components in steel MRFs.

As the last objective, the effects of implementing the proposed component modelling recommendations are evaluated. A series of case studies are conducted on archetype office

buildings with steel MRFs as their lateral load resisting system. Comparisons are drawn between the building models developed according to the current state of practice, and the proposed component modelling recommendations. Nonlinear static and response history analyses are conducted on building models of various complexities, then the engineering demand parameters are analysed in order to evaluate the benefits associated with the implementation of the proposed modelling provisions.

### 1.3 State of knowledge

There are seven categories of steel MRF systems identified in the ANSI/AISC 341-10 (AISC, 2010a) and ASCE/SEI 7-16 (ASCE, 2016) provisions, they are summarized as:

1. Ordinary Moment Frame (OMF)
2. Intermediate Moment Frame (IMF)
3. Special Moment Frame (SMF)
4. Special Truss Moment Frame (STMF)
5. Ordinary Cantilever Column System (OCCS)
6. Special Cantilever Column System (SCCS)
7. Moment frames designed without seismic detailing

Generally for each of these steel MRF systems we are interested in modelling the following structural components:

- Columns
- Beams as a part of fully-restrained beam-to-column connections
- Beams as a part of partially-restrained beam-to-column connections
- Beam-to-column joint panel zones
- Column base connections
- Column splice connections

A view of a typical steel MRF and each of the components under consideration is given in Figure 1.2.

For each structural component we can develop two force-deformation relations, one based off of the first-cycle envelope curve fitted to a deduced force-deformation relation of the respective structural component subjected to a reversed-cyclic loading history. The other is based on the monotonic backbone curve, where the strength and deformation parameters of the component model are calibrated based on experimental data deduced from components tested under monotonic loading protocols. Representations of both the first-cycle envelope curve and monotonic backbone curve are shown in Figure 1.3.

Therefore, the force-deformation relation based on the monotonic response is said to be characteristic of the component, as it is independent of the loading history. The advantage of basing the component model on the monotonic backbone curve is that it can be used in nonlinear response history analysis procedures that explicitly take into account the cyclic and in-cycle strength and stiffness degradation of the component. However, for the component based on the first-cycle envelope curve, the force-deformation relation is now dependant on the loading protocol used. The dependence of the component response on the loading protocol can be seen in Figure 1.3. In this figure, two nominally identical steel wide-flange columns are subjected to different cyclic loading protocols, resulting in two different deduced moment-rotation histories. The advantage of the component model based on the first-cycle envelope curve is that the cyclic and in-cycle variations in strength and stiffness are inherently included. This means that the component models based on the first-cycle envelope will also inherently include these effects, making them suitable for nonlinear analysis procedures that can not explicitly model cyclic and in-cycle degradation in strength and stiffness.

With regards to the ASCE-41-13 provisions for steel MRFs, the first issue to be addressed is that for most of the structural components, only the component models based on the first-cycle envelope curve are provided. Therefore, the component models provided in ASCE-41-13 are not suitable for nonlinear response history analyses. This is an important issue

because nonlinear static analysis may not provide as reliable of an estimate of key EDPs as a nonlinear response history analysis. Additionally it is not possible to capture certain EDPs, such as peak absolute floor accelerations, through nonlinear static analysis procedures. Recently Lignos and Krawinkler (2010, 2011) have developed component models for certain structural components in steel MRFs based on the monotonic backbone curve; however there are still many components where this is yet to be done.

The next issue to be addressed is that the component models in ASCE-41-13 do not consider all deterioration mechanisms that are observed from experimental data. For example, shown in Figure 1.5 is the relation between the web-slenderness ratio,  $h/t_w$ , and the pre-peak plastic rotation,  $\theta_p$ , of wide-flange steel columns from experimental data. The relation between  $h/t_w$  and  $\theta_p$  is not captured in the ASCE-41-13 provisions for columns, however we can see the clear influence that this parameter has on the component response. Therefore the component models may not inherently capture all relevant local, global, and lateral-torsional instability related deterioration mechanisms, limiting the applicability of the current generation of component models for the modelling of steel MRFs. One further consideration is that the component models developed in ASCE-41-13 are based on test data that is nearly 30 years old, new component models can take advantage of the wealth of data that has been published during this time period. For these reasons, an update to the existing component models should be provided in order to take advantage of both recent research and experimental data.

The third issue is that ASCE-41-13 does not provide a complete set of component modelling recommendations for steel MRFs. First, there are no provisions or component models for column base connections, or column splice connections. Second, Elkady and Lignos (2014) have shown that including the effects of the composite slab on both the response of the beam and panel zone components is important to the overall response of the structure; whereas the effects of the composite slab have been overlooked in the current ASCE-41-13 provisions. Furthermore, modelling recommendations specific to certain components such as non-conforming beams, columns subjected to varying axial loads, and columns under

bi-directional loading are not provided in ASCE-41-13. Another major drawback of the current provisions is that steel columns with an axial load exceeding 50% of their critical load,  $P_{cr}$ , are treated as force-controlled elements. Recent research has shown that the 50%  $P_{cr}$  limit is an overly conservative assumption, and should be re-examined.

The final major issue to be addressed is that the component models provided in ASCE-41-13 do not take into account the uncertainty of their predictions of the response parameters. Therefore statistical values, such as the coefficient of variation, should be provided with each of the response parameters in the component model to provide an estimation of the uncertainty in the numerical model.

## 1.4 Research contributions

It is clear based on the preceding section that the provisions provided in ASCE-41-13 should be updated in order to increase the reliability of performance-based seismic assessments for steel MRFs. To this end, this thesis addresses these issues by:

- Providing a systematic, rationale based method for determining the response parameters from cyclic test data.
- Developing a set of recommendations for the nonlinear modelling of steel MRF components based on a thorough statistical evaluation of experimental data.
- Carrying out a series of case studies to demonstrate the efficacy of the proposed component modelling recommendations, and showing an increase in the reliability of analyses carried out on the building models developed based on the proposed recommendations.

## 1.5 Outline

The literature review in Chapter 2 provides an overview of the structural components in steel MRFs, as well as the deterioration mechanisms of these components. The available mathematical component models based on both the first-cycle envelope curve and the monotonic backbone curve for each of these components are then provided, and the limitations of the current ASCE-41-13 provisions are noted.

Chapter 3 provides the proposed recommendations for the nonlinear modelling of steel MRF components. First the statistical procedures used in developing the component models are discussed. This is followed by a listing of the models for each of the structural components included in the recommendations. For each of the component models developed as a part of this thesis, the statistical methods are provided in detail, as well as illustrative examples showing a comparison with the existing component modelling provisions and experimental data.

Chapter 4 contains the case studies that are based on the nonlinear structural analysis of archetype steel frame buildings. Specifically, a series of low- and high-rise office buildings designed in a highly seismic region in North America with steel SMRFs as the seismic force resisting system are modelled according to both the current ASCE-41-13 provisions and the proposed recommendations provided in Chapter 3. From the building models, an estimate of the EDPs are provided through nonlinear static and response history analyses. Finally, the EDPs are analysed in order to highlight the limitations of the current ASCE-41-13 modelling provisions, and to determine the benefits of utilizing the proposed component models for the performance-based seismic assessment of steel MRFs.

In Chapter 5 the conclusions from Chapters 3 and 4 are summarized, and future directions for research are provided.

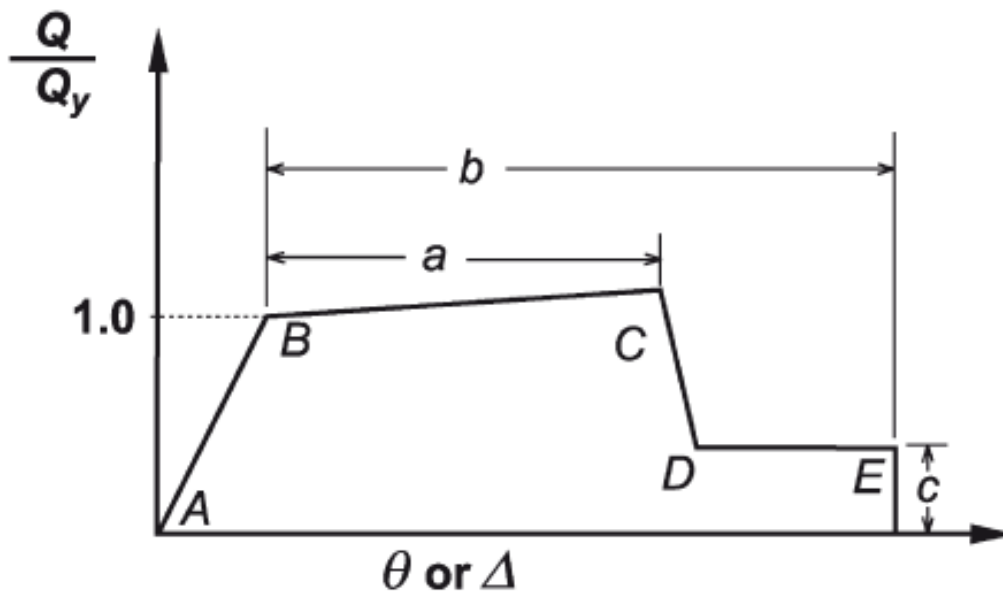


Figure 1.1: Generalized component model based on the ASCE-41-13 provisions (ASCE, 2014).

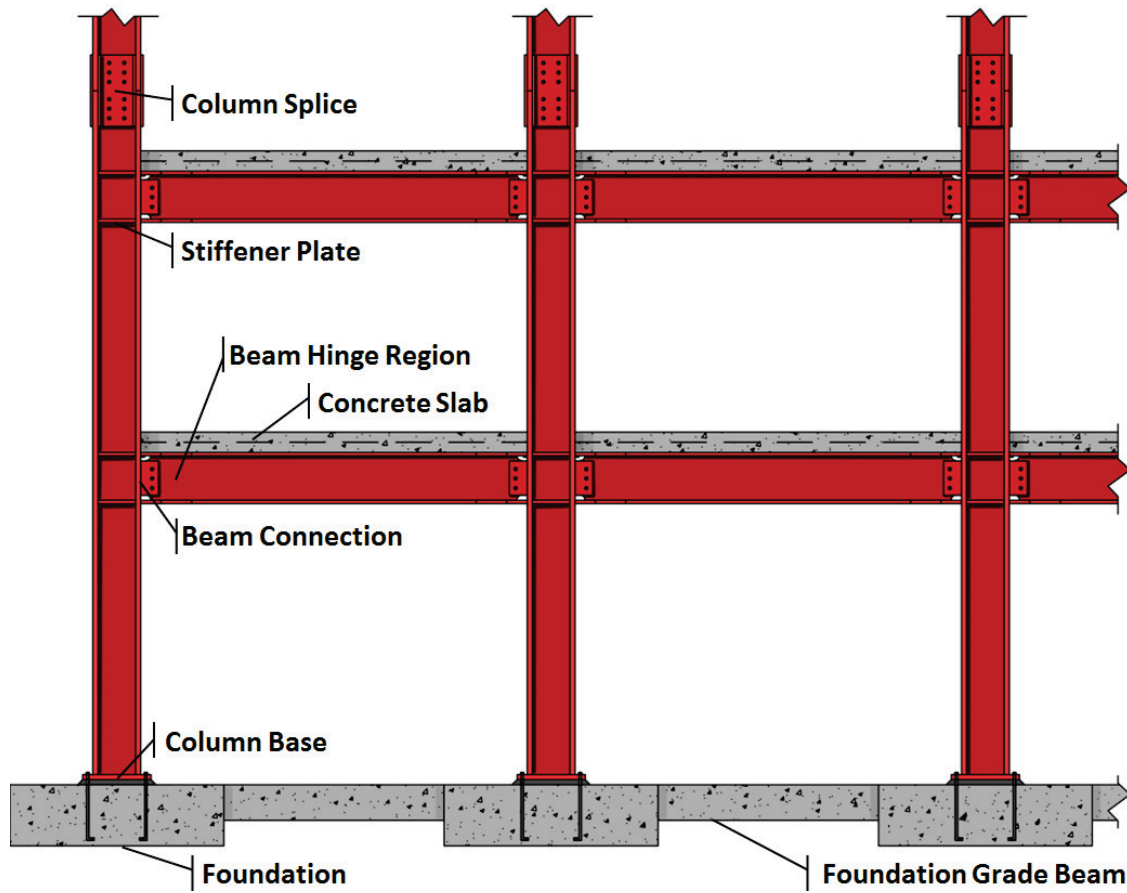
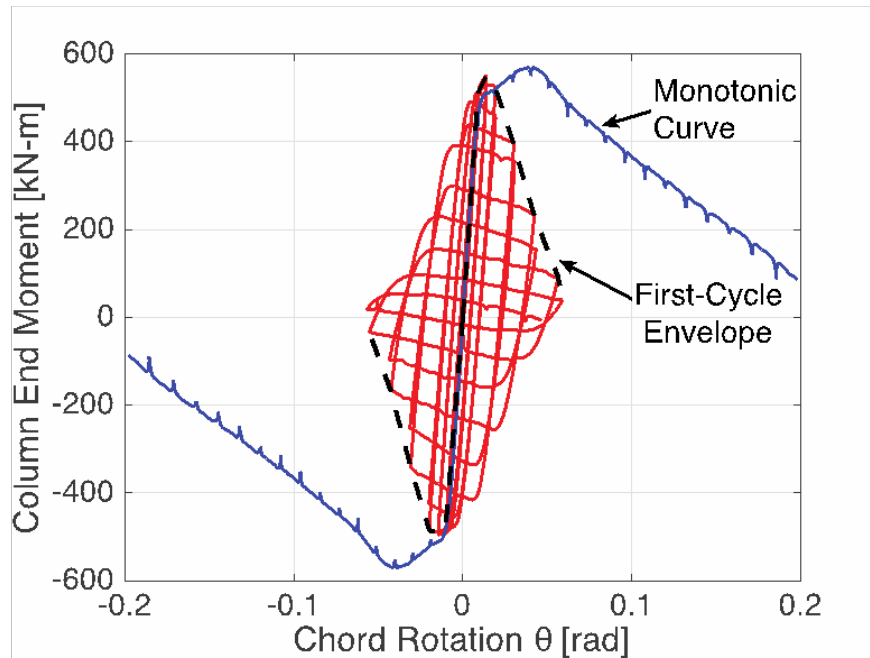
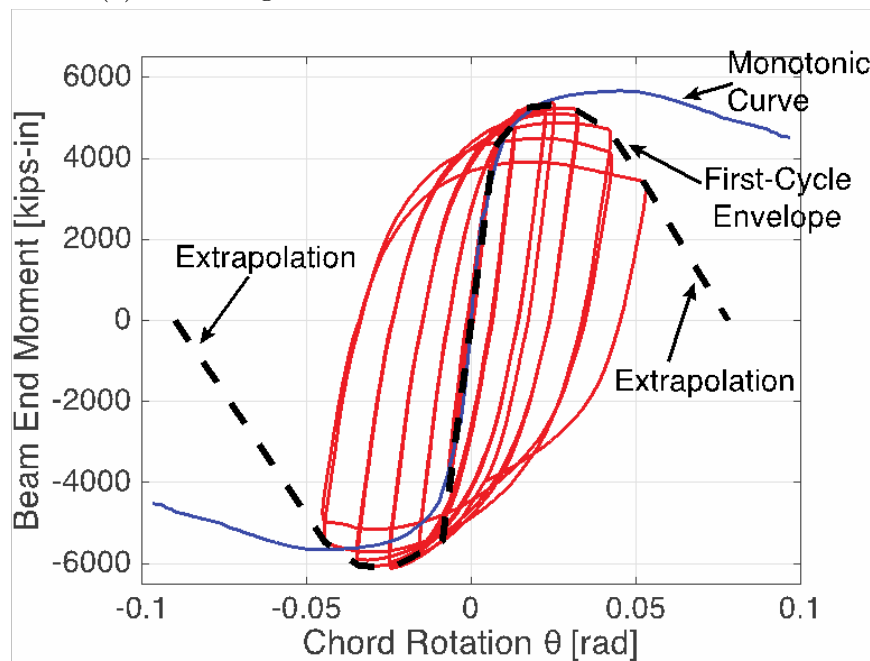


Figure 1.2: Diagram of physical steel moment-resisting frame and its structural components, from ATC-114 (ATC, 2016).



(a) wide-flange steel column under constant axial load



(b) steel beam with RBS as a part of fully-restrained beam-to-column connection

Figure 1.3: Effects of loading history on steel frame structure components, from ATC-114 (ATC, 2016). Test data from Suzuki and Lignos (2015) and Tremblay et al. (1997).

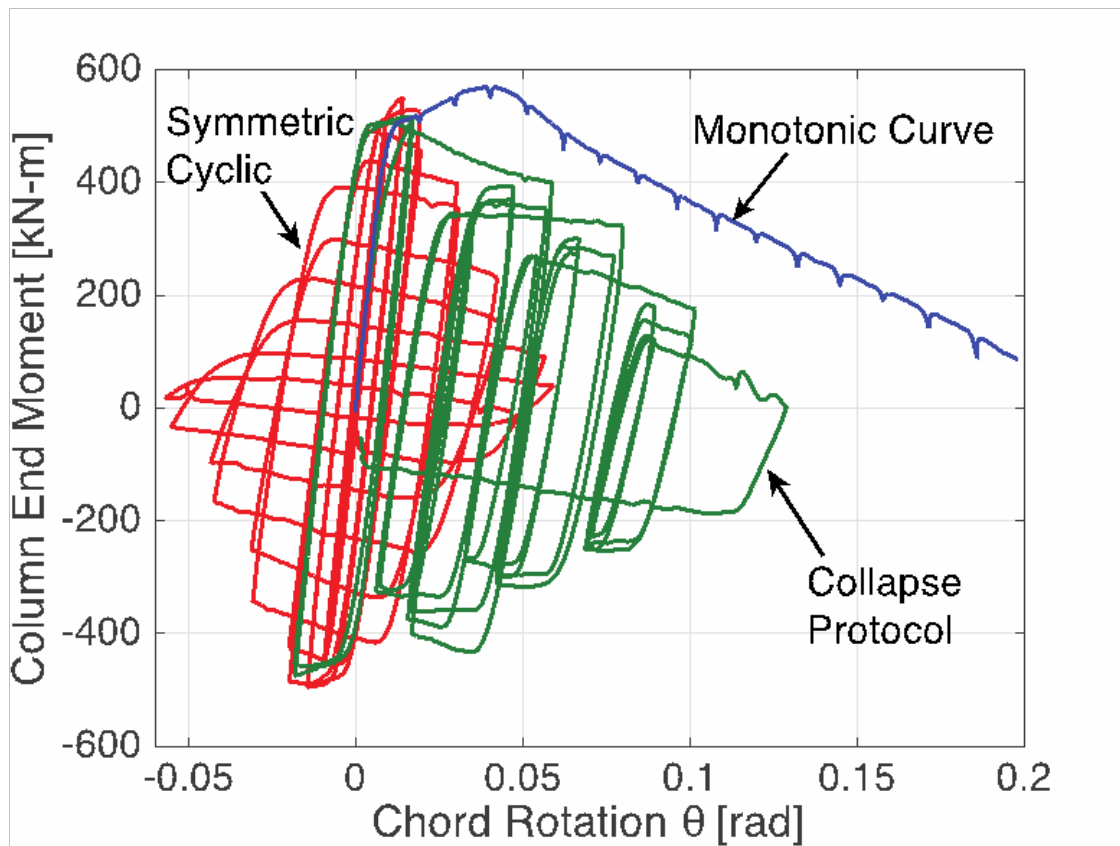


Figure 1.4: Effects of loading history on steel column behaviour, from Suzuki and Lignos (2015).

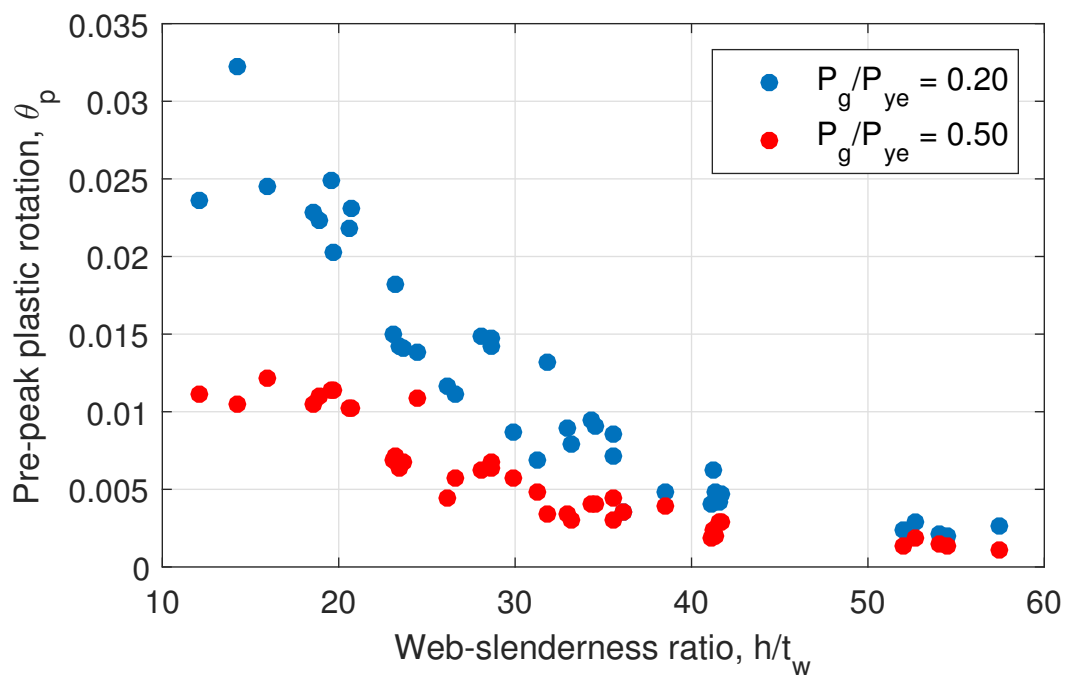


Figure 1.5: Influence of the web-slenderness ratio on the pre-peak plastic rotation for steel wide-flange columns.

# Chapter 2

## Literature Review

### 2.1 Introduction

The goal of this thesis is to advance the state of knowledge for the nonlinear modelling of structural components in the context of performance-based earthquake engineering. This is to be done through by updating the ASCE-41-13 (ASCE, 2014) guidelines for steel MRFs. With respect to this goal, the first objective is to evaluate of the current state of knowledge with regards to the nonlinear modelling provisions for structural components in steel MRFs. This objective is to be accomplished through a literature review.

In order to develop models for steel MRF structural components, we must first address the mechanisms by which the components deteriorate. This is a necessary step in order to ensure the phenomenological component model accurately describes the observed behaviour of the structural component under seismic loading conditions. Phenomenological component models can greatly reduce the complexity of analysis procedures, however extensive test data must be available in order to properly calibrate the deterioration model parameters.

With this in mind, the first part of the literature review will be to provide a summary of the damage progression for each structural components modelled in steel MRFs. Following the review of damage progression, a summary of the available nonlinear component models in

the context performance-based seismic assessments of steel frame buildings is provided. As a part of this process, the limitations of the ASCE-41-13 provisions for MRFs are highlighted in the context of the current state-of-the-art component modelling recommendations, and the deterioration mechanisms presented in this chapter. Upon completion of the literature review, the recommendations to address the limitations present in ASCE-41-13 will be provided in Chapter 3.

## **2.2 Performance including damage progression**

### **2.2.1 Beams as a part of fully-restrained beam-to-column connections**

A fully-restrained beam-to-column connection is specified such that the connection is able to develop moment resistance at the joint between the beam and column, and develop shear resistance at the beam-to-column joint panel zone. Due to the moment distribution across the beam, typically the regions near the column face will experience the highest moment demands, and therefore flexural yielding will initiate in these areas. For beams with a reduced beam section (RBS), as shown in Figure 2.1, the flexural yielding will initiate in the RBS region due to the reduced moment-carrying capacity of the beam in these locations. The effects of cyclic hardening may increase the expected yield moment by up to a factor of 1.4, as observed from test data (Lignos and Krawinkler, 2009, 2011). The initiation of yielding can be seen at point 1 in Figure 2.2.

The deterioration of steel beams with fully-restrained beam-to-column connections depends on the local, global, and lateral-torsional slenderness of the beam. Typically deterioration begins with local buckling of the flanges and webs of the beam, this can be identified by point 2 in Figure 2.2. In accordance with increased lateral drift demands on the beams, the local buckles will grow, leading to flexural strength deterioration, this can be seen in Figure 2.3a. After the onset of local buckling, depending on the level of lateral bracing provided to the

beam, out of plane deformations and lateral torsional buckling may be triggered, as shown in Figure 2.3b.

If the lateral torsional buckling is severe, the out-of-plane deformations will lead to deterioration in the flexural stiffness of the beam. As the local buckles grow severe, ductile tearing of the beam cross section may initiate, as seen in Figure 2.3c. It should be noted that the ductile tearing failure mode is a stable failure mode.

Consideration for the modelling of the composite slab effects should be made when modelling steel beams in MRF systems. Generally, composite steel beams exhibit an asymmetric hysteretic response under cyclic loading. The deduced moment-rotation hysteresis of a composite steel beam is shown in Figure 2.4a. The asymmetric behaviour of composite steel beams is a result of the slab providing little contribution to the flexural strength in tension (i.e., negative bending moment). Furthermore, the shift of the neutral axis towards the slab will increase the likelihood of lateral torsional buckling when the beam is subjected to negative bending moments. Local buckling of the steel deck contributes as well to the strength degradation of the composite beam component, which can be seen in Figure 2.4b. The effects of composite action are seen to be lost when the slab begins to crush against the column face, which has been observed at beam chord rotations of around 4% radians, as shown in Figure 2.4c. As discussed in Lignos et al. (2011b) the response of interior and exterior subassemblies are generally consistent in the presence of a composite slab, however when gaps are present between the column face and the slab edge, the composite slab effects are greatly reduced as shown by Tremblay et al. (1997).

Prior to the 1994 Northridge earthquake there were a number of issues with the fully-restrained beam-to-column connections in steel MRFs that often lead to brittle failure of the connection at rotations well below the expected ultimate rotation capacity. The details of a typical pre-Northridge WUF-B beam-to-column connection are shown in Figure 2.5. These issues were largely related to the welding procedures of the connection, connection geometry, plastic hinge location, and the flexibility of the beam-to-column joint panel zones (FEMA,

2000). Excessive panel zone yielding combined with poor weld performance often lead to fracture of the beam-to-column weld located at the bottom flange, such failure modes can be seen in Figure 2.6. Other failure modes included fracture or excessive plastic deformation in the column web or flange due to inadequate continuity plates (FEMA, 2000). In some cases, the fracture developed into a crack of the column flange material behind the complete joint penetration (CJP) weld and a portion of the column flange remained bonded to the beam flange, but pulled free from the remainder of the column, known as divot or nugget failure. Once such fractures have occurred the steel beam has experienced a significant loss of its flexural strength and stiffness as shown in Figure 2.5. The bolted web shear tab was also subject to failure including weld fractures of the shear plate to the column or fractures through the weak section of shear plate aligning with the bolt holes. In case that supplemental welds were used to the beam web, fracturing of these welds was also a common failure mode.

## **2.2.2 Beams as a part of partially restrained beam-to-column connections with intermediate stiffness**

Typically partially-restrained connections in buildings with steel MRFs as the lateral load resisting system are assumed to be modelled with pinned boundary conditions. However work by Liu and Astaneh-Asl (2004) has shown that beams in partially-restrained moment connections with intermediate stiffness can carry up to 45% of the beam's plastic flexural capacity in the presence of a composite slab. The following partially-restrained connections are considered: T-stub connections, double-flange angle connections, and conventional single plate shear-tab beam-to-column connections; however the following discussion is centred around single plate shear-tab connections due to their pre-eminence in North American steel frame construction. The typical details of the single plate shear-tab connection are shown in Figure 2.7.

Partially-restrained beam-to-column connections in steel MRFs tend to have a pinched, asymmetric moment-rotation relation, as shown in Figure 2.8a. The asymmetry can be

attributed to two factors: the initial gravity load present on the beam, and the effects of the steel beam bottom flange binding against the column face. Liu and Astaneh-Asl (2000, 2004) have identified a number of deterioration modes present in beams that are part of single plate shear-tab partially-restrained beam-to-column connections: yielding of the gross area of the shear tab or web of the beam, bearing failure of the bolt holes on either the shear tab or web of the beam, crushing of the concrete floor slab against the flange of the column, net section fracture of the shear tab or beam web, and fracture of the bolts or welds of the connections.

Crushing of the concrete slab was found to happen at around 4% radians, as shown in Figure 2.8c. After crushing of the slab has occurred, the composite action of the connection is lost, and the response of the beam as a part of the partially-restrained beam-to-column connection will be based on the bare cross section. At rotations near 6% radians, binding between the beam flanges and the column face can occur as shown in Figures 2.8a and 2.8b. The binding action leads to a large increase in flexural strength of the connection, these high moment demands can lead to bolt shear failure as well as block shear failure of the connection. As the plastic deformation with the beam increases, other failure modes may be observed, such as failure by shear yielding or plate buckling of the shear tab depending on the distance between the bolts and the column face (Hertz et al., 2015).

The moment-rotation behaviour of beams in partially-restrained beam-to-column connections will be heavily influenced by the presence of the composite floor slab, and the hysteresis will become highly nonlinear in both loading directions. The deduced beam moment versus chord-rotation of a beam in a single-plate shear-tab connection in the presence of a composite slab can be seen in Figure 2.8b. In Figure 2.8c the in-cycle deterioration of the beam flexural strength due to the crushing of the concrete slab can be seen as well.

### **2.2.3 Steel columns**

Wide flange steel columns are typically subjected to axial load coupled with lateral drift demands during an earthquake. The applied compressive axial load on interior steel columns

in moment-frame systems remains more-or-less constant during the building response history. Based on a number of analytical studies of the seismic behaviour of modern steel moment-resisting frames (NIST, 2010; Gupta and Krawinkler, 2000a,b; FEMA, 2000; Elkady and Lignos, 2014, 2015a) the expected applied compressive axial load ratio on these columns ranges from  $P_g/P_{ye} = 0.10$  (i.e., low rise steel moment-frame systems) to  $P_g/P_{ye} = 0.30$  (i.e., mid- and high-rise steel SMFs) depending on the number of stories. Where,  $P_g$  is the gravity load demand on the column;  $P_{ye}$  is the column axial yield strength based on expected material properties. However, end columns in steel frame buildings may experience large axial load variations due to dynamic overturning effects ranging from  $P_g/P_{ye} = -0.2$  in tension to about 0.50 in compression (Suzuki and Lignos, 2014, 2015). Note that steel columns in existing steel frame buildings in the West-Coast of the US often experience gravity loads in the range of  $P_g/P_{ye} = 0.6$  (Bech et al., 2015).

In North America, current practice mostly uses wide-flange steel columns in planar moment-resisting frame systems. An alternative but less common option may be the use of hollow square steel columns. In particular, the use of such members was common in late 1970s in the US (Bech et al., 2015). This section discusses the damage progression for both alternatives based on available results from recent full-scale experimentation.

### **Wide-flange columns**

Many researchers have studied the behaviour of wide-flange steel column subjected to combined axial loading and lateral drift demands (Popov et al., 1975; Nakashima et al., 1990; MacRae et al., 2009; Suzuki and Lignos, 2015; Uang et al., 2015; Elkady and Lignos, 2016; Elkady, 2016; Lignos et al., 2016). The inelastic behaviour of columns in steel frame buildings depends not only on the column cross section and lateral bracing; but also on both the axial load present in the column, the column boundary conditions, and the direction of lateral loading. Deterioration of wide-flange steel columns in MRFs typically begins at the base of the column where moment demands are highest. The deterioration begins with

local buckling in the column flanges (Figure 2.9a), followed by local buckling of the web and axial shortening, followed by out of plane deformations (Figure 2.9b and 2.9c). Due to the plastic hinge formation at the base of the column the inflection point will lower with respect to the height of the column. As a result of the shift in the inflection point in the column, the moment demands at the top of the column will increase. Therefore, it is possible for plastic hinge formation following a similar path as presented above to form at the top of the column as well.

Column cyclic strength deterioration is accelerated by both high axial load levels, and high local and global slenderness of the column. Therefore columns with thick webs and flanges have a more stable deterioration path versus deep slender columns within the limits of highly ductile members per ANSI/AISC 341-10 AISC (2010a). The decrease in the rate of flexural strength deterioration for stocky columns can be attributed to the lower global slenderness ratios, and increased warping and torsional constants that reduce the likelihood of global and lateral-torsional instabilities, even at large drift and axial force demands. The evidence of this is shown in Figure 2.10a, from the deduced moment-rotation history of a W14X176 column under reversed-cyclic loading we observe a stable response even at 10% lateral drift ratio. However, deep slender columns with width-to-thickness ratios near the limits of seismic compactness per ANSI/AISC 360-10 (AISC, 2010b), show a comparatively rapid rate of deterioration. For example, the relatively slender W24X146 columns shown in Figure 2.11a subjected to reversed cyclic loading at two constant axial load ratios deteriorate rapidly compared to the relatively stock W14X176 column shown in Figure 2.10a.

Depending on the member global slenderness as well as warping and torsional properties of the cross-section, local buckling may be coupled with global geometric instabilities. Global and lateral-torsional instabilities are associated with lateral torsional and/or global buckling as shown in Figures 2.9b and 2.9c, and may occur at relatively small chord rotations, in the range of 0.02 radians or less, depending on the applied compressive axial load ratio and member end boundary conditions. Lateral torsional and/or global buckling typically causes

flexural stiffness deterioration as shown in Figure 2.11. In slender wide-flange steel columns, flexural hinging at the column ends is normally coupled with member axial shortening due to web local buckling. This deterioration mode, which can be seen in Figure 2.12a, causes axial strength deterioration to the steel column and ultimately loss of its axial load carrying capacity. Depending on the local slenderness ratio, high axial shortening and large local buckling of the column web can also lead to fracture in the k-area of the wide-flange, as shown in Figure 2.12b.

### **Steel wide-flange columns under bidirectional loading**

The following is a discussion from ATC-114 (ATC, 2016). Experimental data on nominally identical steel columns subjected to unidirectional and bidirectional symmetric lateral loading suggests that the plastic deformation capacity of a column is practically not sensitive to the type of loading (Elkady and Lignos, 2016). This observation holds true regardless of the cross-sectional slenderness. Experimental data points to an increase in the rate of in-cycle deterioration in flexural strength under bidirectional loading of a column, this can be attributed to the additional flexural demands due to weak-axis bending of the column. The aforementioned observations can be seen in Figure 2.13 that shows the moment-rotation relation of a W24X146 and a W24X84 column subjected to unidirectional and bidirectional symmetric lateral loading protocols. In this figure, the column end moment has been normalized with respect to the plastic bending moment of the cross-section for comparison purposes. Similar observations hold true for the level of axial shortening with respect to the inelastic cumulative damage that a column experiences under unidirectional and bidirectional loading.

### **Steel wide-flange columns under varying axial loads**

The following is a discussion from ATC-114 (ATC, 2016). Due to the combination of the dynamic overturning effect and lateral drift demands seen in MRFs under earthquake loading,

the columns in the MRF will experience varying axial loads. This effect is especially prevalent in the end columns of steel MRFs. Through tests based on columns with nominally identical cross sections under similar assumptions (i.e., identical initial gravity offset and tributary area), a comparison is drawn between a column tested with a constant axial compressive load of 30%  $P_g/P_{ye}$  (Suzuki and Lignos, 2015) representing an interior column, and one with a varying axial load range of -15% to 75%  $P_g/P_{ye}$  (Lignos et al., 2016) representing an end column.

As shown in Figure 2.14a, the interior column loses its axial load carrying capacity during the second excursion to 4% lateral drift ratio due to severe axial shortening that triggered fracture at the k-area of the column near the base (see Figure 2.14b). For the end column, an asymmetric moment-rotation response is observed due to the varying axial load on the column. In particular, end columns maintain their flexural strength once the axial load is in tension. This is due to straightening of the flange and web local buckling when the axial load varies from compression to tension. The descending portion of the moment-rotation envelope curve of an end column becomes fairly steep when the axial load increases from the initial gravity load to a higher axial compressive load. However, the in-cycle flexural strength deterioration of an end column is fairly small compared to that of an interior column. Due to the application of the constant axial load ratio in the case of interior columns the axial shortening is much larger than that observed in end columns for the same lateral drift amplitude. These differences are more pronounced when non-symmetric lateral loading histories are employed (Suzuki and Lignos, 2015) or relatively stocky cross-sections are used in column member (Newell and Uang, 2006).

### **Hollow structural steel columns**

The behaviour of hollow structural steel (HSS) columns under axial load and lateral drift demands is similar to that of wide-flange sections, except that practically the deterioration mechanisms associated with lateral-torsional instabilities do not occur. The damage pro-

gression in HSS columns begins with local buckling located near the base of the column, followed by axial shortening. Figure 2.15a shows the deduced moment-rotation history of an HSS10X20X3/8 subjected to constant axial load under a reversed-symmetric loading protocol. Local buckling begins to occur in the neighbourhood of 0.015 radians chord rotation, and after this point in-cycle deterioration in strength is observed as the size of the local buckles increase with the increasing excursions at 3% and 4% radians chord rotation. Evident in Figures 2.15b and 2.15c are the effects of axial shortening.

Once the HSS column loses its axial load carrying capacity, it is often common to observe fracture near the corner part of the HSS member due to high distortion resulting from local buckling, as shown in Figure 2.15d. For HSS sections with low local slenderness ratios,  $D/t < 20$ , “elephant foot” local buckling failure models may be observed, as shown in Figure 2.16. However, there is no practical difference in the force-deformation response of components failing in this manner.

## 2.2.4 Beam-to-column joint panel zones

The panel zone force-deformation behaviour is composed from the contributions of both the panel zone volume in shear, and the column flanges in flexure. The panel zone volume consists of the column web, as well as any doubler plates that may be welded to the web in order to satisfy the panel zone design requirements. It is observed that the panel zone volume will first yield in shear followed by yielding in the column flanges (Krawinkler et al., 1971; Krawinkler, 1978). After yielding of the column flanges has occurred, the panel zone strength capacity will increase due to strain hardening. Shear yielding is assumed to be a stable failure mechanism, however in practice shear buckling in the panel zone may be observed, leading to a deterioration in panel zone shear strength. These two deterioration mechanisms can be seen in Figures 2.17a and 2.17b.

Bare steel panel zones are shown to follow a symmetric hysteretic response when subjected to reversed-symmetric loading, as seen in Figure 2.18. When considering the effects of the

concrete slab on the panel zone, there will be an increase in the effective depth of the panel zone when the slab is in compression, however when the slab is in tension, the effective depth of the composite panel zone will be very close to that of the bare steel (Kim and Engelhardt, 2002). Due to these differences in behaviour of the composite panel zone considering positive and negative flexure, exterior panel zones show asymmetric behaviour, as the slab is present on only one side of the panel zone. However, the interior panel zones will benefit from the slab on both sides, and therefore the behaviour is observed to be symmetric.

Design provisions allow for controlled yielding of the panel zones, as excessive panel zone yielding has been shown to lead to local kinks in the column flanges. These local kinks can in turn lead to premature fracture of the beam-to-column connection (Krawinkler et al., 1971). Excessive panel zone yielding was seen to be a contributing factor to early fracture in pre-Northridge beam-to-column connections (FEMA, 2000). However, data from full-scale experiments have shown that panel zone yielding could be an acceptable method of energy dissipation in steel MRFs without decreasing pre-qualified beam-to-column connection performance (Zhang and Ricles, 2006; Shin and Engelhardt, 2013).

### 2.2.5 Steel column splices

Column splices in steel MRFs are typically located at story mid-height, or at four feet above the floor level, and can be either bolted or welded with butt splices. Assuming that the column is in double curvature, this will place the splice near the location of minimal moment, since the inflection point is assumed to be located near the mid-story point. However, due to column plastic hinging and in-cycle column flexural strength deterioration, the location of the column inflection point will change, leading to increased flexural demands at the splice location. Furthermore, due to cyclic hardening, the inelastic flexural demands on the splices may be up to  $1.4M_{pe}$  of the corresponding column, depending on the axial stress present within the column.

Figure 2.19 shows a typical splice detail, the moment-curvature relation of this splice

is shown in Figure 2.20. Observed from this figure, it is fairly common that significant nonlinearity will occur in the range of the column  $40\text{--}60\%M_y$ , due to the residual stresses from cutting and welding. Depending on the cross section geometry and story shear demands, flexural yielding typically spreads far beyond the splice location within the column (Bruneau and Mahin, 1991; Shaw, 2013). A failure mode that can cause rapid flexural strength deterioration in welded column splices is column flange weld fracture as shown in Figure 2.21. Fracture may propagate into the column web as shown in the same figure.

Bruneau and Mahin (1991) found that partial joint penetration (PJP) welds often resulted in brittle failures of column splice connections, while more desirable ductile failure modes were often observed when properly designed and executed CJP welds were used. It was observed that a fracture in the splice weld propagate to the column, leading to fracture of the column web. However, recent research by Shaw (2013) has shown that when high-toughness weld materials are used, column splice connections with PJP welds and additional fillet reinforcement welds can exhibit a desirable ductile performance. The above observations are made for splice connections that are subjected to pure bending, and do not consider the axial or shear forces present on the splice (Bruneau et al., 1987; Bruneau and Mahin, 1991; Shaw, 2013).

Pre-Northridge column splices consist of PJP welds of roughly half the thickness of the smaller column section being connected, as shown in Figure 2.22a. Experimental findings from the early 1990s (Bruneau and Mahin, 1991) suggest that when such connections are subjected to tensile forces due to flexural demands and/or axial loading during the steel moment-frame system earthquake response, they can only carry a small portion of the column flexural and/or axial tension capacity of the smallest column section being connected. This can be seen from Figure 2.22b that illustrates the deduced moment-curvature relation from a typical pre-Northridge column splice that utilized heavy steel wide-flange sections with PJP welds. From this figure, the moment-curvature relation is practically linear up to the point that brittle fracture occurs through the weld (see Figure 2.22c). In these connections, once a

crack develops in the tension flange of the column splice, it progresses through the whole section almost instantaneously. Based on experimental observations of Bruneau and Mahin (1991) the erection plate does not normally help restrain or stabilize the failure once initiated.

## 2.2.6 Column base connections

### Exposed column base connections

Exposed column base connections are a typical base connection method for steel MRFs, often designed according to AISC Design Guide 1 (Fisher and Kloiber, 2006). Typical details for exposed column base connections are shown in Figure 2.23. The baseplate transfers forces to the foundation in the presence of flexure and axial loads through a combination of baseplate yielding on the compression side of the plate, and tension which is developed in the anchor rods on the tension side of the plate.

As discussed in Gomez (2010) there are three typical yield mechanisms observed in exposed column base connections subjected to axial compression and bending: flexural yielding on the compressive side of the plate, flexural yielding on the tensile side of the plate, and axial yielding of the anchor rods. The first yield moment will be the moment at which the first one of these components reaches its yield capacity. However, since flexural yielding on the compression side of the base plate is not sufficient to form a failure mechanism, there will be an increase in strength in the cases where flexural compression yielding is the first yield moment. In these cases, the ultimate moment will be controlled by the minimum of the moments causing yielding in the anchor rods or flexure on the tension side of the plate. Other possible failure modes could include breakout of the concrete or tension pull out of the anchor rods.

As observed in Figure 2.24 exposed column base plates follow a pinched hysteretic response under reversed-cyclic loading, similar to that of a self-centering connection as shown in Figure 2.24b. The pinching is due to elongation of the anchor rods under tension, such that bearing contact is lost between rod nut and the top of the base plate in reversed-cyclic

loading. Grout damage has been observed at lateral deformations consistent with design basis earthquakes, and at increasing lateral drift levels, in-cycle deterioration in stiffness is observed due to the base plate yielding in flexure and the anchor rods yielding in tension. The deterioration in stiffness resulting from disengagement of the anchor rods from the base plate due to yielding in tension will be recaptured at increasing lateral deformations, as the anchor rods will be re-engaged.

Fracture of the anchor rods in tension is a brittle failure mode, this damage state is associated with grout crushing at the base plate edges. Both of these failure modes are shown in Figure 2.25. Depending on the level of the applied compressive axial load, the initial stiffness of the column base connection will vary. Under high axial loads, the primary failure mode occurs when the concrete foundation exceeds its ultimate bearing capacity.

### **Embedded column base connections**

Embedded column base connections are characterized by having a portion of the column cast into the concrete foundation in an attempt to create a fully fixed boundary condition at the base. The axial loading and bending moments present on the column are supported by a combination of horizontal and vertical bearing of both the baseplate and the embedded portion of the column, as seen in Figure 2.26. Grilli (2015) tested 5 embedded column bases, the salient findings are: the observed flexural strength increases with increasing embedment depths; damage in one loading direction will affect the response in the opposite loading direction; there is an observed increase in strength with increased flange width; axial tension is found to have a limited impact on the flexural strength, while there is an observed increase in strength due resulting from axially compressive loading; and that embedded column bases have significant plastic deformation capacity.

Figure 2.27 illustrates deduced moment-drift relations for typical embedded type column base connections under constant axial load coupled with lateral deformations. Nonlinear behaviour of the embedded column base occurs at low drift demands, in elastic range of

the loading protocol, due to small cracks that typically form near the corners of the steel column. At larger lateral deformations a gap adjacent to the tension flange opens. Diagonal cracks near the steel column corners are also apparent. Upward bulging in the bearing zone between these cracks is also observed. Due to the gap opening the hysteretic response of the embedded column base connection is typically pinched. Eventually, flexural cracks develop on the sides and top of the concrete footing on the tension side of the connection. Shear cracks also develop in the concrete panel. These failure mechanisms are shown schematically in Figure 2.28. With the increased lateral loading amplitude, the flexural strength of the connection deteriorates due to the reduction in the moment resisted by bearing ahead of the column flanges. This is shown in Figure 2.27.

Grilli (2015) identified a number of failure modes that are present for embedded column bases, the possible brittle failure modes include tension break out of the top of the concrete, and joint shear failure of the column. Possible ductile failure modes include: compression break out of the bottom of the concrete, concrete crushing / plate yielding, and horizontal bearing failure of the concrete.

The damage progression due to seismic loading in each of the structural components in steel MRFs were explored in this section. It is important to quantify the relevant deterioration mechanisms for each structural component in order to accurately capture the component behaviour in the process of developing nonlinear component models. The subsequent section will review the available component models for the nonlinear modelling of buildings with steel MRFs as the lateral load resisting system for performance-based earthquake seismic evaluations.

## 2.3 Available nonlinear component models for structural components in steel moment-resisting frame systems

For the development of nonlinear structural models with applications in performance-based seismic assessments there currently exists two primary documents for practising engineers, ASCE-41-13 (ASCE, 2014) as previously discussed, and ATC-72, *Modeling and acceptance criteria for seismic design and analysis of tall buildings* (PEER/ATC, 2010). However, many other researchers have contributed to the development of component models suitable for use in the nonlinear analysis of steel MRFs, and there are several available component modelling recommendations that are not included as a part of these documents.

Listed by component, an overview is provided for each available component models for the nonlinear modelling of steel MRFs. The limitations of the ASCE-41-13 provisions are then discussed in terms of the current state-of-the-art nonlinear modelling procedures. Where limitations in the current ASCE-41-13 provisions are encountered these areas are identified, such that they will then be addressed in the development of an updated set of component modelling recommendations for steel MRFs in Chapter 3.

### 2.3.1 Steel beams

This section first provides an overview of the available component models for the nonlinear modelling of beams in steel MRFs in the context of performance-based earthquake engineering. Following the overview and brief discussion of each of the component models, the limitations of the ASCE-41-13 provisions are provided with reference to the current state-of-the-art modelling procedures and the observed deterioration mechanisms discussed in Section 2.2.

The ASCE-41-13 (ASCE, 2014) provisions provide recommendations for the nonlinear modelling of beams as a part of both fully-restrained and partially-restrained beam-to-column

connections. The component modelling parameters are based off of the previously described ASCE-41-13 general component model shown in Figure 2.29. The parameters given that define the plastic deformation in the ASCE-41-13 component models are provided as a function of the yield deformation (i.e.,  $\Delta_p = \text{const.} * \Delta_y$ ); and the slope of the component model from BC with reference to Figure 2.29, is provided based on a strain-hardening ratio,  $3\%K_e$ , where  $K_e$  is the effective elastic stiffness (although other values are allowed if justifiable based on experimental evidence). Currently, no guidance is given for beams that do not meet the lateral-bracing requirements in ANSI/AISC 360-10 (AISC, 2010b).

The parameters provided for modelling the nonlinear behaviour of beams in fully- and partially-restrained moment connections, as provided in Table 9-6 of ASCE-41-13, are based off of FEMA-273 (FEMA, 1997b) and FEMA-355D (FEMA, 2000). The component response parameters are provided based on test data as either a simple linear-regression as a function of the beam depth,  $d$ , or as a mean value when there was insufficient experimental data. Furthermore, the response parameters were determined from tests with reversed-cyclic loading histories, and are therefore based on the first-cycle envelope. The beam component models were developed based on  $Q_u = 0.80Q_{max}$ , where  $Q_u$  is the maximum strength of the component model and  $Q_{max}$  is the maximum strength from test data, as shown in Figure 2.30. Importantly, ASCE-41-13 provides no guidelines for the modelling the effects of the composite slab on the response of the steel beams in fully- and partially-restrained beam-to-column connections.

Uang and Fan (2001) developed multiple-regression equations based on analysis of 55 of beams in RBS connections test specimens in order to assess the lateral bracing requirements in the plastic-hinge region. In the regression analysis the web-slenderness ratio,  $h/t_w$ , was used to assess the web-local buckling, the flange-slenderness ratio,  $b_f/2t_f$ , was used to assess flange-local buckling, and the ratio of the unbraced length to radius of gyration,  $L_b/r_y$ , was used to assess lateral-torsional buckling. A power form of the regression equations was used to estimate the pre-peak plastic rotation,  $\theta_p$ . The  $\theta_p$  values deduced from experimental data

were based on the rotation at  $80\%M_{max}$  on the descending portion of the first-cycle envelope. Additionally, Uang and Fan (2001) found that the slab does provide lateral stability in the positive loading direction, but not in the negative loading direction.

ATC-72 (PEER/ATC, 2010) provides component modelling recommendations for beams as a part of fully-restrained beam-to-column connections based on the work done by Lignos and Krawinkler (2009, 2011). The analysis was divided based on beams with RBS connections, and beams with other-than-RBS connections from a database of nearly 300 tests (Lignos and Krawinkler, 2012). The response parameters of the component models are based off of the multivariate regression analysis of test data taken from beams in fully-restrained connections subjected to monotonic loading protocols. Since the equations of the component models consider several input variables, sufficient parameters are provided to capture the local, global, and lateral-torsional slenderness of the steel beam components. As such, the component models are able to inherently capture the deterioration mechanisms based on each of the respective instabilities represented by parameters such as the web-slenderness ratio,  $h/t_w$ , and the ratio of the unbraced length to radius of gyration,  $L_b/r_y$ . Lignos and Krawinkler (2009) found the web local-slenderness to have a dominant effect over the flange local-slenderness on the rotation capacity. A calibrated parameter to model component deterioration based on the modified Ibarra-Medina-Krawinkler (IMK) deterioration model (Lignos and Krawinkler, 2009, 2011) is provided as a part of the component models. Therefore, the component deterioration can be explicitly modelled as a part of nonlinear dynamic analysis procedures. Estimations of the residual strength present in steel beams, and the observed rotation at which gravity load carrying capacity is lost are provided as well. As noted in Lignos and Krawinkler (2009) the residual region is not a true plateau in strength, however for practical purposes it can be modelled as so.

Additionally, provided with each of the equations are the standard deviations, so that the variability of the component response can be quantified as a part of the performance-based seismic assessment framework. The ATC-72 provisions do not explicitly provide any

component models for steel beams based on the first-cycle envelope curve. Provided instead are a set of reduction factors, such that an estimation of the first-cycle envelope based on the monotonic backbone can be developed. However, the component models developed in this manner are approximate, and do not inherently capture the effects of cyclic loading, in particular the increased strength of steel beams due to cyclic-hardening. As discussed in Lignos and Krawinkler (2009), the parameters defining the plastic deformations and the post-yield slope in the ATC-72 component models are modified to remove their dependency on the elastic response; this leads to more stable response parameters.

Recently Elkady and Lignos (2014) have developed provisions for the construction of component models for steel beams in fully-restrained connections that consider the effects of the composite slab. This work is based on an experimental database of 22 composite steel beams in RBS connections (Engelhardt et al., 2000; Ricles et al., 2004; Tremblay et al., 1997; Uang et al., 2000). The modelling recommendations for composite steel beams are based on calibrated adjustment factors applied to the component model of the bare steel beams. The adjustment factors take into account the asymmetric response of composite steel beams under reversed-cyclic loading, and are able to capture important deterioration effects in composite steel beams, such as crushing of the concrete slab. However, since the modelling recommendations are provided as a modification based on the bare steel component behaviour, if the component model is based on the first-cycle envelope curve, as provided in ATC-72 or ASCE-41-13, they will inherit the limitations that have already been noted for these cases.

Elkady and Lignos (2015b) developed updated recommendations for the modelling of beams as a part of partially-restrained beam-to-column connections. These recommendations are based on the 5 single-plate shear-tab beam-to-column connections tested by Liu and Astaneh-Asl (2000); Liu (2000). The advantage of the approach taken by Elkady and Lignos (2015b) is that the slab binding effects are included in the component model, which has

been overlooked in previous component models (Liu and Astaneh-Asl, 2004; Wen et al., 2013). The peak flexural strength of the component model can be calculated from engineering mechanics, however all other strength and deformation response parameters are calibrated based on mean values from the database of tests subjected to reversed-cyclic loading protocols. Therefore, the component model is based on the first-cycle envelope curve, and furthermore due to the limited test data that was available, the variability in the response parameters due to connection geometry, and material properties are not captured by the component model. However, as noted by Liu and Astaneh-Asl (2000) the material properties and slab reinforcement were seen to have a limited effect on the flexural capacity of the beams in single-plate shear-tab beam-to-column connections. Elkady and Lignos (2015b) have provided COVs with each of the component model response parameters.

### **Limitations in the ASCE-41-13 provisions for the modelling of beams in steel moment-resisting frames**

The issues with the beam specific component models in ASCE-41-31 for the nonlinear modelling of steel MRFs are summarized as follows. First the beam force-deformation parameters developed in FEMA-355D are based on a limited set of experimental data that was available at the time of their development. Second, the component models are a function of  $d$  only, therefore they will not be able to inherently capture the deterioration mechanisms that are associated with local, global, and lateral-torsional instabilities that are primarily attributed to cross-section slenderness as well as member slenderness. Third, the component models are based on  $Q_u = 0.80Q_{max}$  from reversed-cyclic test data only. The implications are that the component models will under-predict the peak strength, and post-peak plastic deformation; and over-predict the pre-peak plastic deformation. The under-prediction of the peak strength is an important consideration in properly tracing weak-story collapse mechanisms in nonlinear analysis procedures. The under-prediction of the post-peak plastic deformation leads to a very steep slope in the descending region of the force-deformation

envelope that can lead to convergence issues for numerical solvers. Furthermore, only component models based on the first-cycle envelope are provided, making the provisions in ASCE-41-13 suitable only for nonlinear static analysis procedures, and not suitable for nonlinear dynamic analysis procedures that can model explicitly the in-cycle and cyclic deterioration in strength and stiffness of various structural components.

The fourth issue is that the variability of the input parameters are not explicitly provided as a part of ASCE-41-13 (statistical parameters are given in FEMA-355D for each of the beam connections). Therefore, there is practically no rational way for quantifying the modelling uncertainty in the nonlinear building models, which is an important part of providing a reliable performance-based seismic assessment. For beams as a part of pre-Northridge fully-restrained WUF-B connections, the effects of beam depth and tensile stress of the steel on the plastic deformation capacity are overlooked, as discussed in FEMA-355D (FEMA, 2000). The final issue with regards to the nonlinear modelling of beams as a part of fully- and partially-restrained beam-to-column connections is that the effects of the composite slab were overlooked in the current provisions.

The ASCE-41 provisions for the nonlinear modelling of steel beams in MRFs should be updated to address the aforementioned limitations. See Section 3.3 for explicit recommendations for the nonlinear modelling of beams in steel MRFs for performance-based seismic evaluations.

### **2.3.2 Steel columns**

This section will provide an overview of the component models available in the nonlinear modelling of steel columns in MRFs in the context of performance-based seismic evaluation. Afterwards, a summary of the current limitations in ASCE-41-13 with respect to the modelling of columns is given, and the major research needs to address these limitations.

ASCE-41-13 (ASCE, 2014) provides a set of recommendations for the nonlinear modelling of steel columns under seismic loading. The deformation parameters provided for the nonlinear

modelling recommendations in ASCE-41-13 for steel columns in MRFs are based off of the conservative formulations provided in FEMA-237 (FEMA, 1997b). The component models provided for steel columns in MRFs are suitable only for nonlinear static analysis procedures. Of importance, is to note that ASCE-41-13 specifies that columns with an axial load greater than  $50\%P_{cr}$  should be treated as force-controlled elements, where  $P_{cr}$  is the lower-bound compressive strength of the column. The component models for columns in ASCE-41-13 are broadly separated based on local slenderness ratios and axial load ratios, but otherwise provide no differentiation in the component response based on the member slenderness. The effective flexural yield strength of columns modelled according to the ASCE-41-13 provisions are based off of the AISC interaction equations for columns under the combined effects of axial forces and bending moments. The peak strength of the component is based off of a 3% strain hardening ratio. No statistical parameters are given to assess the variability of the inputs to the component model. No guidelines are provided for columns under bi-directional loading or varying axial loads. Furthermore, only steel wide-flange columns are considered in the recommendations, whereas no specific guidance for HSS columns is provided.

Lignos and Krawinkler (2009, 2010) developed a set of recommendations for the nonlinear modelling of HSS columns for earthquake engineering applications. These response parameters based on the modified IMK model were developed from a dataset of over 100 square HSS columns using multivariate regression analysis, utilizing parameters to represent the axial load ratio present on the column, the effective yield stress of the steel, and the local slenderness of the HSS column. Based on the statistical analysis, the axial load ratio was found to have a dominant effect on the response of the response of HSS columns. Furthermore, a parameter is provided based on the modified IMK model for the explicit modelling of component deterioration as a part of nonlinear response history analysis procedures. Each of the equations are provided with the standard deviation in order to address the variability of the input parameters.

No explicit component models are provided in ATC-72 for the nonlinear modelling of wide-flange columns, due to a lack of experimental data available at that time. The modelling recommendations for columns in ATC-72 state that they are to be modelled according to the provisions provided for beams in other-than-RBS fully-restrained beam-to-column connections based on the monotonic backbone curve, and to modify the results to account for the P-M interactions due to the axial load present on the column. Therefore, the effect of axial loading on the in-cycle and cyclic deterioration are not captured in the component model. As previously mentioned, a set of reduction factors are provided that can be applied to the component model based on the monotonic backbone curve to approximate the component response based on the first-cycle envelope curve.

### **Limitations in the ASCE-41-13 provisions for the modelling of columns in steel moment-resisting frames**

Many of the limitations observed regarding the nonlinear modelling of beams according to the ASCE-41-13 provisions previously discussed can be made for the modelling of column components in steel MRFs, including: a lack of component models suitable for nonlinear dynamic analysis procedures; component models are based on limited test data; a steep post-peak slope can lead to convergence issues in numerical solvers; the component models do not inherently capture all local, global, and lateral-torsional instability-related deterioration mechanisms; and that there are no statistical parameters provided to assess the variability in the component response.

Furthermore, ASCE-41-13 specifies that columns with an axial load greater than 50%  $P_{cr}$  should be treated as force controlled, as noted in Section 2.2.3, an appreciable level of plastic deformation is observed in columns under these loading conditions. Therefore, this limit should be revised based on existing experimental data. The constant 3% strain hardening in ASCE-41-13 is not reflective of the post-yield behaviour of columns, as the hardening is dependant on the slenderness of the component as well as the axial load present on the column.

No guidelines are provided for columns under bi-directional loading or varying axial loads. As outlined in Section 2.2.3 recent test data has shown the influence of bi-directional loading and varying axial loads on wide-flange columns. A further issue is that the ASCE-41-13 provides no guidance for the modelling of HSS columns. Lignos and Krawinkler (2009) has addressed this limitation for HSS columns based on the monotonic backbone curve.

Therefore, the major research needs are to develop state-of-the-art component models for wide-flange beam columns based on both the first-cycle envelope and the monotonic backbone curve that address the issues outlined above. Additionally, a component model is to be developed for HSS columns based on the first-cycle envelope curve. Recommendations for bi-directional loading and columns subjected to varying axial loads are to be provided as well.

### **2.3.3 Beam-to-column joint panel zones**

Krawinkler et al. (1971); Krawinkler (1978) studied the behaviour of beam-to-column joint panel zones in steel MRFs. They developed mathematical relations based on material properties and panel zone geometry in order to estimate the shear strengths and distortions at yield of the panel zone volume (yield strength) and yield of the column flanges (full plastic strength). Additionally, formulas are provided for the effective elastic stiffness and full plastic distortion. Gupta and Krawinkler (1999) furthered this work to develop component models based on the mathematical relations developed by Krawinkler et al. (1971); Krawinkler (1978). Two component models are suggested: a parallelogram model, and a scissor model. See Figure 2.31 for visual representations of these panel zone models. Gupta and Krawinkler (1999) found that although the parallelogram model adds significant complexity to the nonlinear building model, it provides a more realistic representation of the panel zone behaviour, and is therefore recommended. Since the panel zone behaviour is controlled through rotational spring elements, it is not possible to explicitly capture the effects of axial loading on the panel zone behaviour.

The panel zone behaviour proposed by Wang (1988) closely agrees with that of Krawinkler et al. (1971). The major differences in the behaviour proposed by Wang (1988) are a reduction in the effective shear area of the panel zone, and an decreased full plastic distortion.

Kim and Engelhardt (2002) proposed panel zone force-deformation relations based on both the cyclic and monotonic response of beam-to-column joint panel zones. These were developed to address the observation that the behaviour predicted by Krawinkler et al. (1971) may over estimate the shear strength capacity for columns with thick flanges ( $t_f > 2.5$  cm). As well, it was noted that the panel zone model by Wang (1988) tends to under-predict the panel shear strength due to the reduced effective shear area. The monotonic model is was found to provide a reasonable prediction of test data regardless of the column flange thickness considered (flange thickness up to  $t_f = 4.5$  cm). It is noted that in practice column flanges may be up to 13 cm, therefore additional test data is required to validate the models in these cases.

The cyclic model proposed in Kim and Engelhardt (2002) is developed based on the observation that panel zone behaviour is not accurately represented through bilinear force-deformation relation. The models are shown to provide a reasonable prediction of the available test data. Additionally, Kim and Engelhardt (2002) provided recommendations to model the composite floor slab by increasing the effective depth of the panel zone to account for the slab. Considerations are made for both interior and exterior composite panel zones. The composite panel zone model is shown to provide a reasonable prediction of the available test data. Noted limitations are the lack of considerations for: shear buckling of the panel zone; and the deterioration in strength due to instability or fracture in the surrounding beams and/or columns.

The current ASCE-41-13 (ASCE, 2014) nonlinear modelling recommendations for beam-to-column joint panel zones in MRFs are based on the recommendation provided in Gupta and Krawinkler (1999). It is recommended that the Krawinkler parallelogram model be

used in order to more accurately capture the panel zone behaviour. The ASCE-41-13 recommendations overlook the effects of the composite slab on panel zone behaviour. Therefore, it is recommended that the recommendations to consider the composite slab effects from Kim and Engelhardt (2002) be integrated with the Krawinkler parallelogram model. A notable limitation of the parallelogram model is that since the behaviour is modelled through a rotational spring, the effects of the axial load present in the column cannot be explicitly captured, additional research is required to quantify these effects. Furthermore, the effects of the column flange thickness on the formulations developed by Krawinkler et al. (1971) should be investigated more thoroughly in order to assess if they provide an accurate prediction for column sizes that are typically employed in modern steel construction practice. None of the currently proposed panel zone models take account of the shear buckling deterioration mechanisms that has been observed, or deterioration due to instability or fracture in the surrounding beams and/or columns.

### **2.3.4 Column splice connections**

As stated in FEMA-355C (FEMA, 2000), with regards to the analysis of pre-Northridge MRFs, special attention needs to be paid to the analysis of column splice connections. If fracture of the weld occurs, there will be a rapid deterioration in the load carrying capacity of the splice connection. However, since column splices are designed as force-controlled structural elements they do not require explicit modelling.

Stillmaker et al. (2015) have developed fracture mechanics based design formulas for use of estimating the capacity of columns splices with PJP welds. The design formulas are developed on the basis of characterizing the stress at which fracture of the PJP weld will occur in terms of the toughness capacity of the weld, therefore the condition of fracture is dependent on the flange stress exceeding this capacity. Calibrated design formulas are then developed based on finite element fracture mechanics simulations carried out in Shaw et al. (2015). These formulas are applicable for both use in modern construction of splices with

PJP welds, and can be used for the analysis of pre-Northridge splice connections. Stillmaker et al. note that the equations are developed based on limited set of test data, and as well the finite element simulations do not represent all effects that will be present in physical splice connections. As well, the recommendations do not take into account the explicit modelling of cyclic degradation of the material toughness.

Modelling recommendations for pre-Northridge splices are to be provided based on a post-analysis verification procedure. This procedure is to be developed based on the one provided in Stillmaker et al. (2015), while the parameters are calibrated based on experimental data from Bruneau et al. (1987); Bruneau and Mahin (1991).

For post-Northridge column splices, due to the high fracture toughness of the weld metal, the splice welds should be able to develop their full yield strength as per ANSI/AISC 341-10 (AISC, 2010a). Therefore, no explicit modelling recommendations are to be developed for steel column splices. However the limit state of splice connections under combined axial force and bi-axial moment should always be verified post-analysis.

### **2.3.5 Column base connections**

#### **Exposed column bases**

No guidelines are provided in ASCE-41-13 for the modelling of exposed column base connections in steel MRFs, provided below are available recommendations for the modelling of these structural components.

Kanvinde et al. (2012); Gomez (2010) developed mathematical equations to predict the response of exposed column bases designed according to AISC Design Guide 1 (Fisher and Kloiber, 2006). The attractiveness of these formulations is that they are mechanics-based, relatively simple to implement, and consider a range of geometric and material properties of the base connection. These equations were compared against test data from Gomez (2010) and Picard and Beaulieu (1985). It was found that the equations provide a reasonably good prediction of the effective elastic stiffness, flexural yield strength, and peak strength for the

tests considered. Additionally COVs are provided in order to show the uncertainty in the predicted parameters compared to the test data. The limitations of the proposed equations are that: they are not applicable to connection details that are significantly different than the ones studied; simplified strain distributions are used to approximate the behaviour in the footings, and uplift of the footings due to anchor rod tension are neglected; and the formulas neglect soil-foundation interactions.

As a part of an assessment based on the full-scale 4-story structure tested on the E-Defense shake table (Suita et al., 2008), Lignos et al. (2013) studied the effects of modelling exposed column bases as a strategy to increase the collapse capacity. The exposed column base connection was modelled through the use of a self-centring material, where the parameters of the component model were calibrated based on available experimental data for HSS column base connections. An effective yield strength of  $60\%M_p$  of the column was chosen for the exposed column base connection based on available experimental data for exposed column base connections. Based on nonlinear analysis procedures Lignos et al. (2013) observed a notable increase in the collapse capacity of the structure when the simulated effects of the base plate connection were modelled.

Zareian and Kanvinde (2013) carried out a case study on 2-, 4-, 8- and 12-story steel MRFs modelled with varying levels of column base connection flexibility. Using the equations developed in Kanvinde et al. (2012), the column base connections were modelled as linear elastic elements. Through a comparison with pinned and fixed conditions at the base, it was found that models with fixed base connections had a greater collapse capacity than the models with flexible base connections. Additionally, for mid- and high-rise buildings, they found that for design level events, the median peak story drift ratios could exceed 2.5% when the base flexibility is considered.

Very recently Rodas et al. (2016) have developed a component model to simulate the behaviour of exposed column base connections. A set of parameters calibrated based on

the definitions of the original Ibarra-Medina-Krawinkler (Ibarra and Krawinkler, 2005) deterioration model are provided. The formulations given in Rodas et al. (2016) build on the self-centring nature of the component noted earlier and characterize the response in terms of a moment-rotation relation. The response parameters related to the effective elastic stiffness, yield strength, and peak strength are determined based on the mathematical equations provided in Kanvinde et al. (2012). In order to simplify the estimation of the deformation-related parameters, calibrated values based on data from Gomez (2010) are utilized. Additionally, calibrated parameters are provided in order to explicitly model the deterioration in stiffness, and estimate the pinched hysteresis. The noted limitations of this model are: due to the model being posed in terms of a moment-rotation relation, the effects of axial load present in the column cannot be explicitly modelled; no considerations are made for columns in axial tension or bi-axial bending; and the effects of weld detailing and anchor rod layouts are not addressed. Furthermore, all of the limitations that are noted for the equations developed by Kanvinde et al. (2012) are applicable here as well.

Due to the timing of the component model developed by Rodas et al. (2016), it was not possible to incorporate these recommendations into those provided in Chapter 3. The model developed in Chapter 3 for exposed column base connections is consistent with the recommendations provided in Rodas et al. (2016), however the parameters dealing with cyclic deterioration are not incorporated.

### **Embedded column bases**

No guidelines are provided in ASCE-41-13 for the modelling of embedded column base connections. Provided below are applicable research for developing recommendations for the modelling of these structural components.

Grilli (2015) developed mechanics-based procedures for estimating the peak strength of embedded column bases, based on the connection geometry and material properties. The other modelling parameters can then be determined based on the analysis of the available test

data, and defined with respect to their relation to  $Q_u$ . Based on this approach, component modelling recommendations, respecting the failure mechanisms outlined in Grilli (2015), are provided in Chapter 3 for embedded column base connections.

## 2.4 Summary

The development of phenomenological component models requires that the relevant deterioration mechanisms for each of the respective structural component are properly captured by the component model. Therefore, this chapter provides a summary of the damage progression for each of the structural components that one has to consider modelling in steel MRFs for their performance-based seismic assessment. Following this, a review of each of the available component models is provided. As a part of the component model review, the limitations in the ASCE-41-13 nonlinear modelling guidelines for steel MRFs are noted.

Based on the thorough review of the available literature, the current ASCE-41-13 provisions do not provide guidance for: assessing the variability of the input parameters on the component model response; the component models are generally based on limited test data that was from at least 20 years ago; constructing component models suitable for nonlinear dynamic analysis procedures that can explicit model cyclic and in-cycle deterioration in strength and stiffness; consideration for the effects of the composite slab on the response of both beams and panel zones; constructing state-of-the-art component models for beams in pre-Northridge WUF-B connections; non-conforming beams; state-of-the-art modelling of columns with an axial load ratio greater than  $50\%P_{cr}$ ; the modelling of columns subjected to varying axial loads, or bi-directional loading; the nonlinear modelling of steel column splices, as well as column base connections.

The aforementioned issues will be addressed through the proposed recommendations provided in Chapter 3.

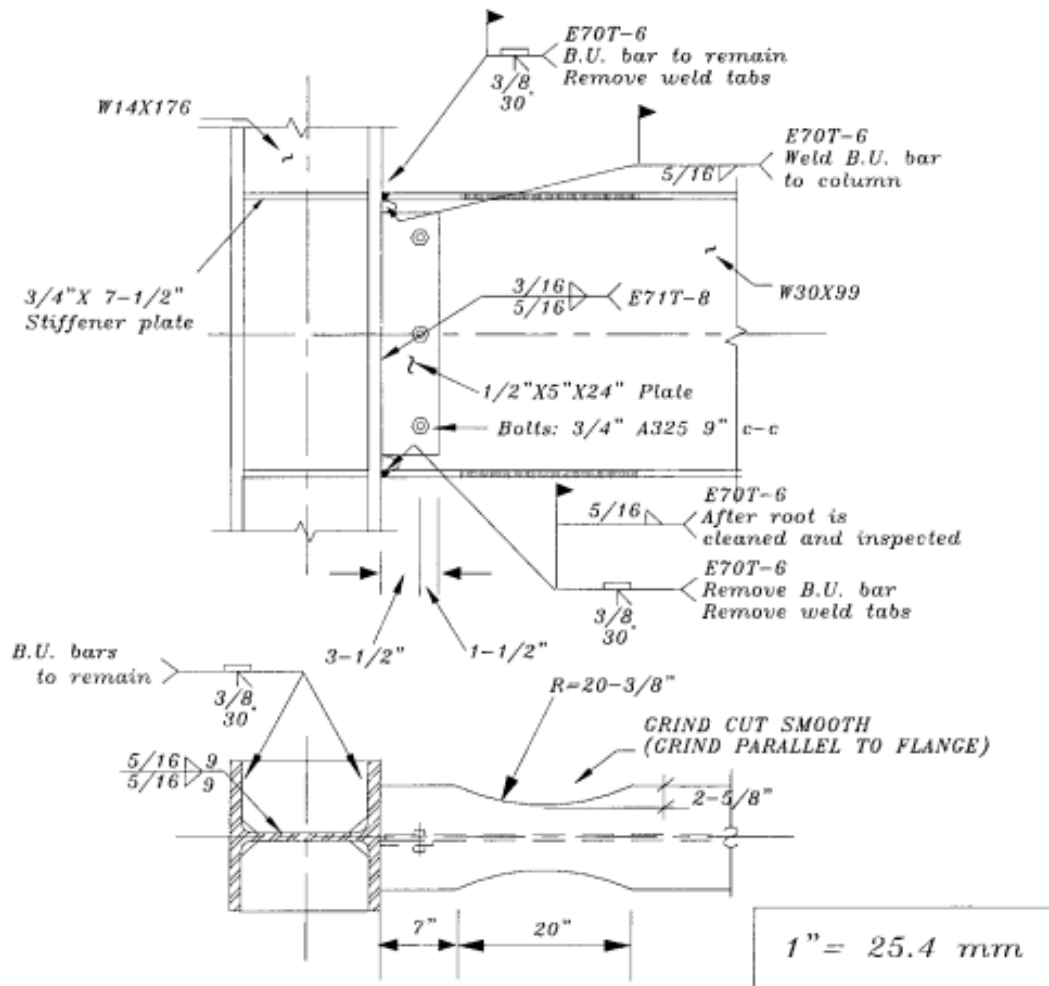


Figure 2.1: Connection details and geometry of beams in RBS connections, from Uang and Fan (2001).

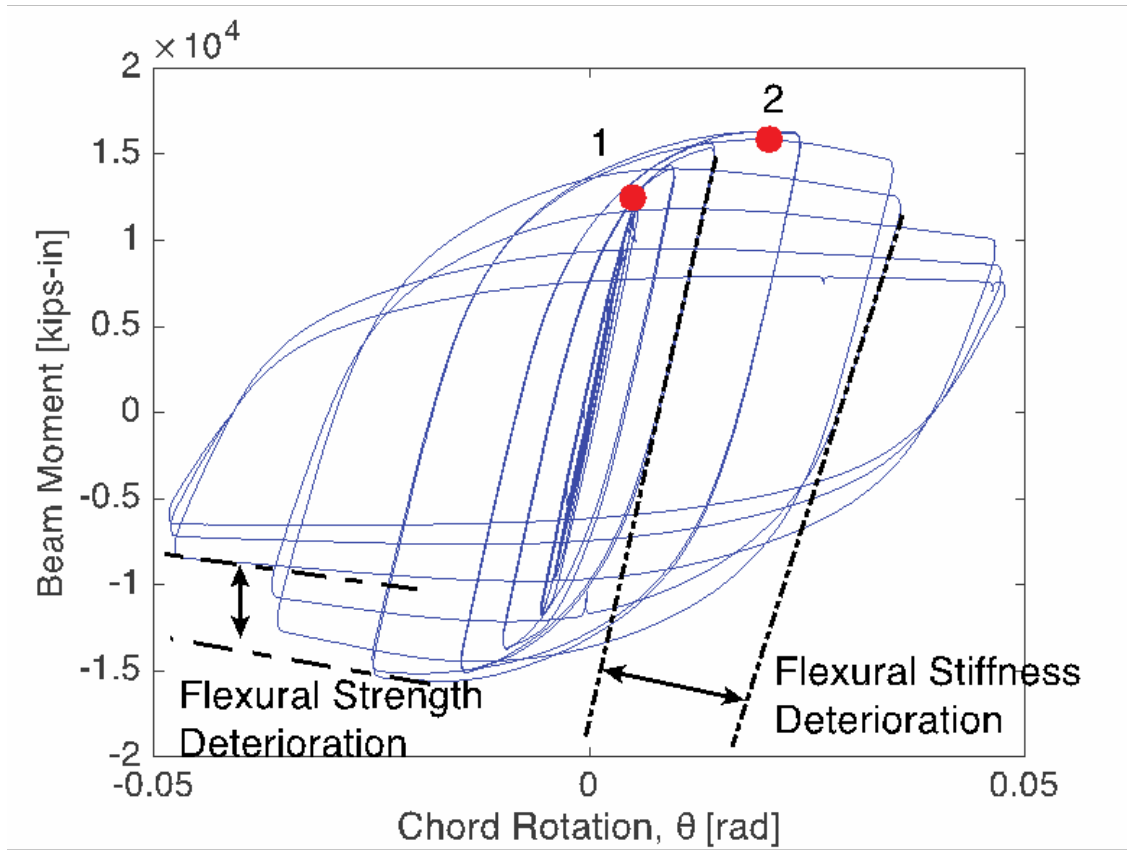
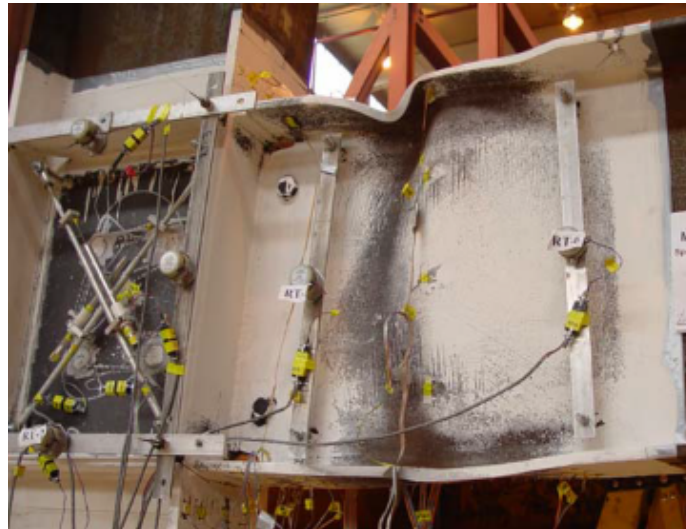


Figure 2.2: Deduced moment-rotation relation for bare beam with RBS, from FEMA (2000).



(a) local buckling

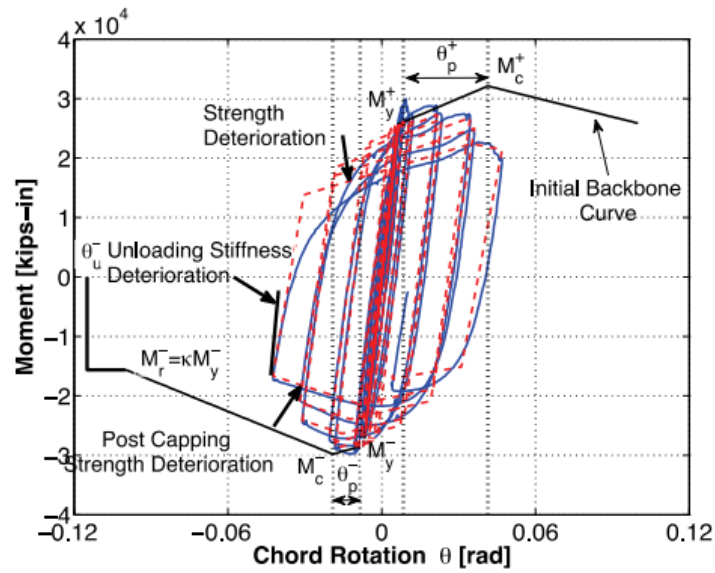


(b) lateral-torsional buckling



(c) ductile tearing

Figure 2.3: Typical damage progression for bare beam with RBS, from FEMA (2000) and Zhang and Ricles (2006).



(a) deduced moment-rotation relation of composite slab with RBS



(b) deck local buckling



(c) concrete slab cracking and crushing

Figure 2.4: Deduced moment-chord rotation and typical damage progression for composite beams with RBS. From Elkady and Lignos (2014), FEMA (2000), and Zhang and Ricles (2006).

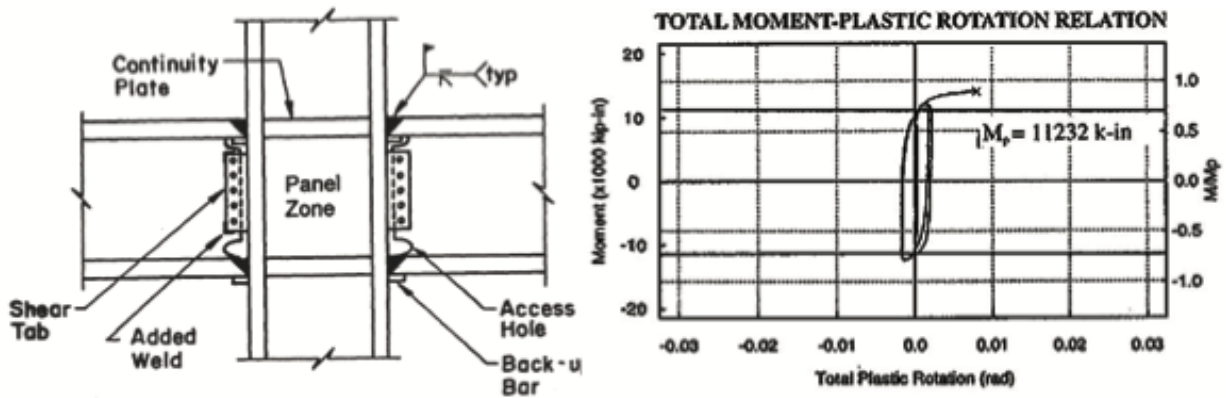


Figure 2.5: Left: Typical connection detail for pre-Northridge beam-to-column connection (WUF-B). Right: deduced moment-rotation relation of a steel beam as part of a Pre-Northridge beam-to-column connection. From FEMA (1997a) and Lu et al. (2000).



(a) fracture across welded beam top flange

(b) fracture in heat affected zone

Figure 2.6: Typical failure modes observed in steel beams as part of pre-Northridge welded-flange-bolted-web beam-to-column connections, from FEMA-289 (FEMA, 1997a).

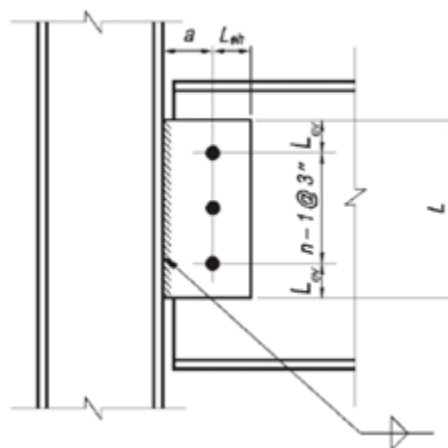
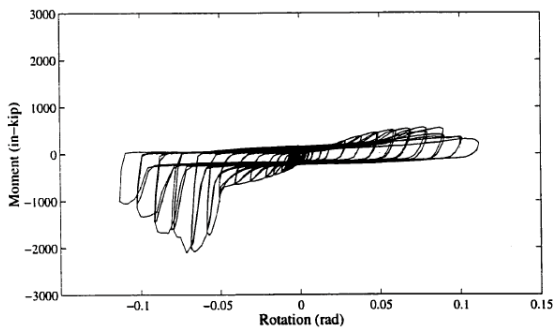
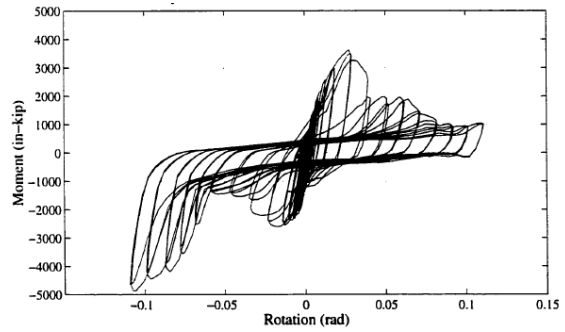


Figure 2.7: Typical shear tab connection. From FEMA (2000).



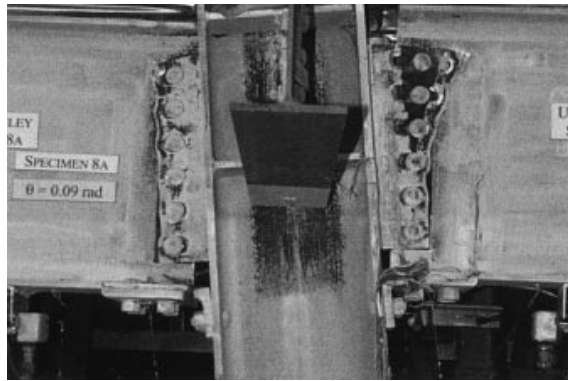
(a) bare steel beam



(b) composite steel beam

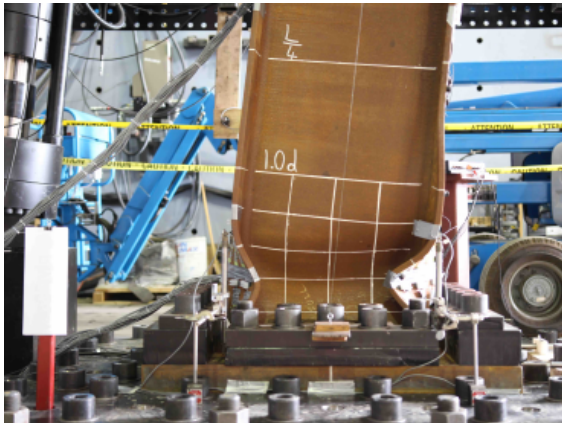


(c) crushing of concrete slab

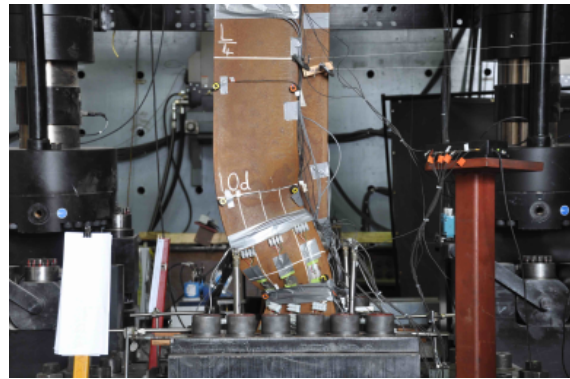


(d) net section failure

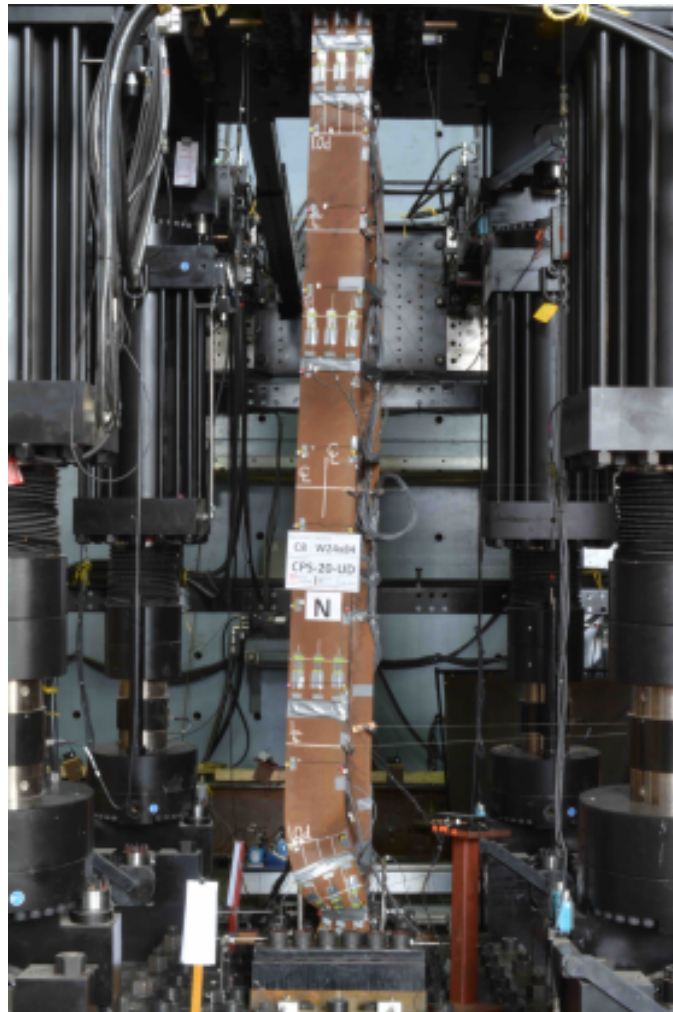
Figure 2.8: Typical deduced beam moment-chord rotation relations of single plate shear-tab beam-to-column connections including damage progression, from Liu (2000) and Liu and Astaneh-Asl (2004).



(a) local buckling

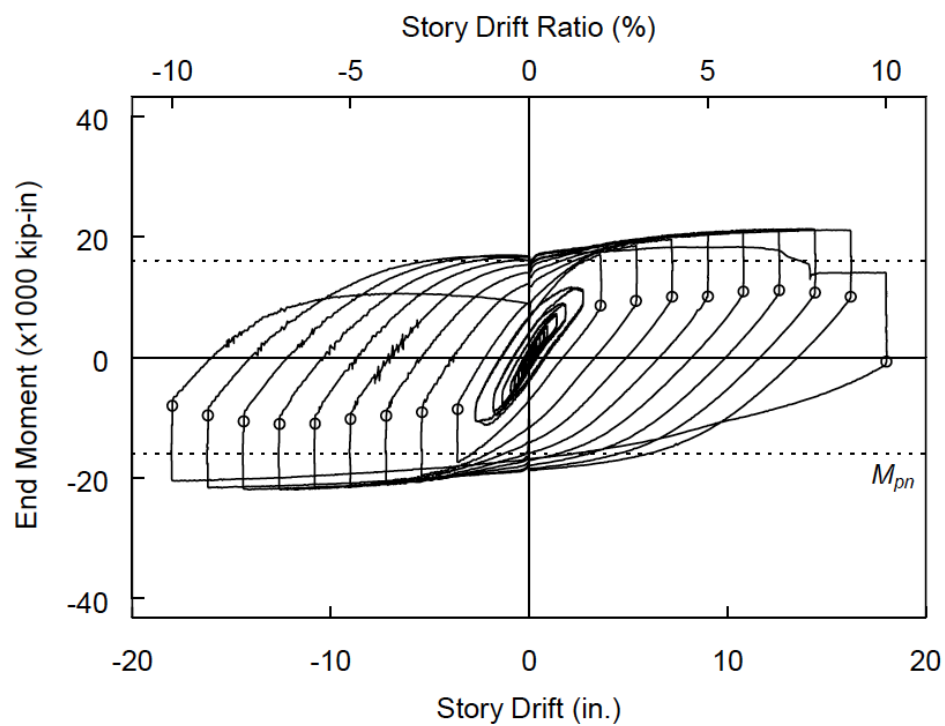


(b) local buckling coupled with lateral torsional buckling



(c) lateral torsional buckling for W24X84,  $P_g/P_{ye} = 0.20$ ,  $L/r_y = 80$ .

Figure 2.9: Typical damage progression in deep slender wide flange steel columns under cyclic loading, from Elkady and Lignos (2016).



(a) deduced column end moment-story drift relation for W14X176

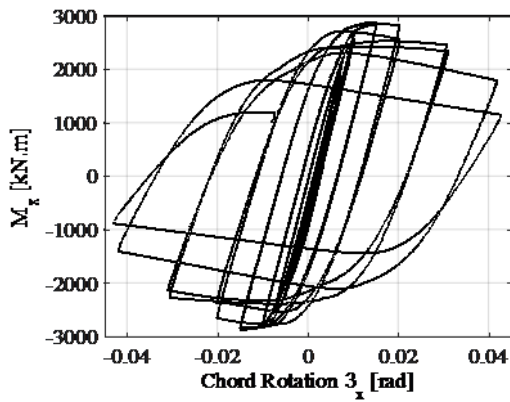


(b) local buckling—global view

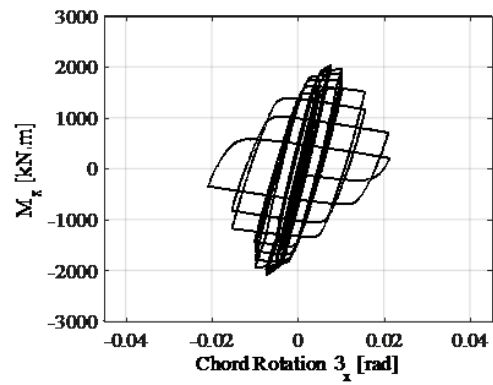


(c) local buckling—local view

Figure 2.10: Typical deduced moment rotation relation of stocky wide flange columns including damage progression, from Newell and Uang (2006).



(a) W24X146,  $P_g/P_{ye} = 0.20$ ,  $L/r_y = 50$



(b) W24X146,  $P_g/P_{ye} = 0.50$ ,  $L/r_y = 50$

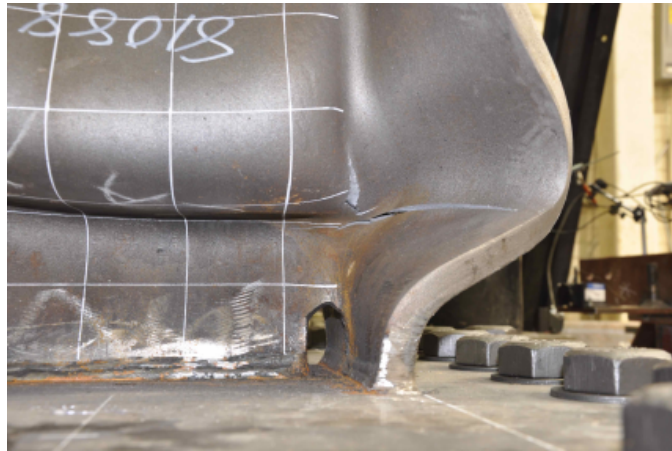
Figure 2.11: Deduced column end moment-chord rotation relation for deep and slender wide flange steel columns under constant compressive axial load ratios, from Elkady and Lignos (2016).



(a) severe axial shortening



(b) k-area flange fracture



(c) k-area fracture initiation

Figure 2.12: Failure modes associated with large deformations in steel wide flange steel columns; (a) loss of column axial load carrying capacity; (b) and (c) fracture due to high distortion in the k-area, from Suzuki and Lignos (2015).

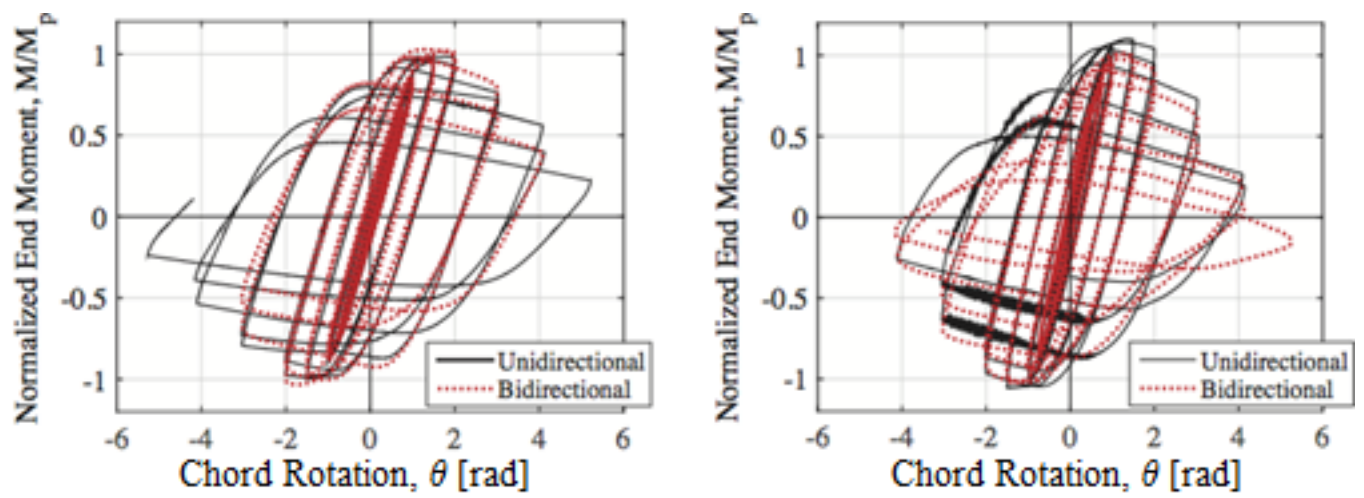
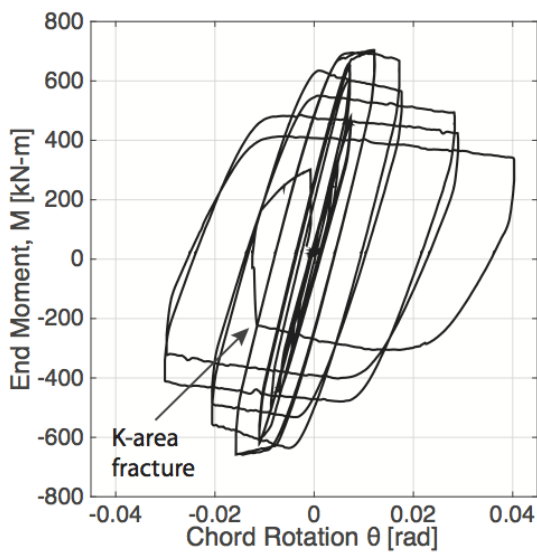
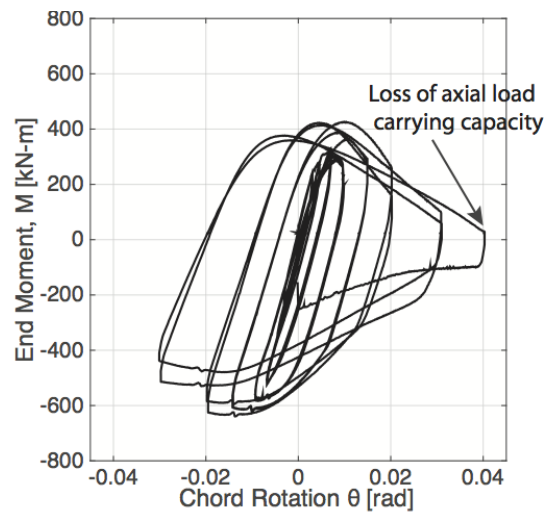


Figure 2.13: Comparison of unidirectional loading with bidirectional loading. Left: W24X146  $P_g/P_{ye} = 0.2$ ; right: W24X84  $P_g/P_{ye} = 0.2$ . From Elkady and Lignos (2016).

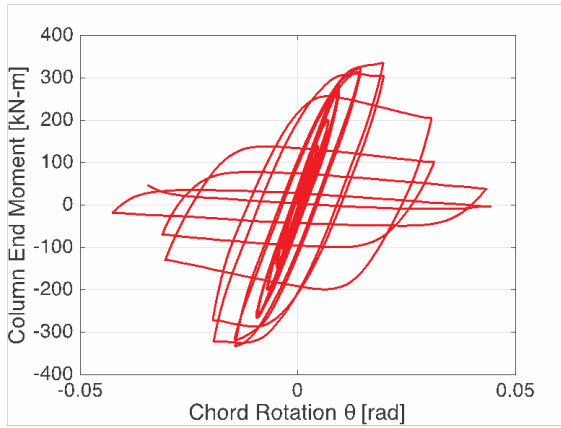


(a)  $P_g/P_{ye} = 0.30$

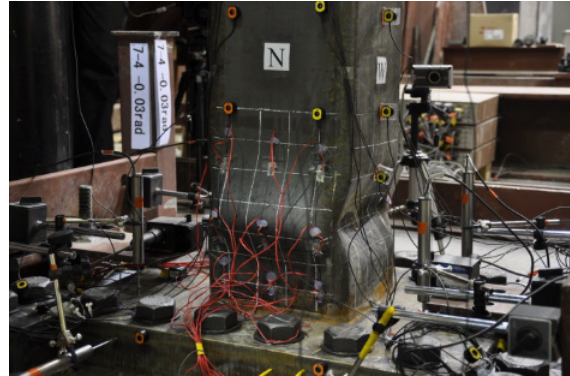


(b)  $P/P_{ye} = -0.15$  to  $0.75$ ,  $P_g/P_{ye} = 0.30$

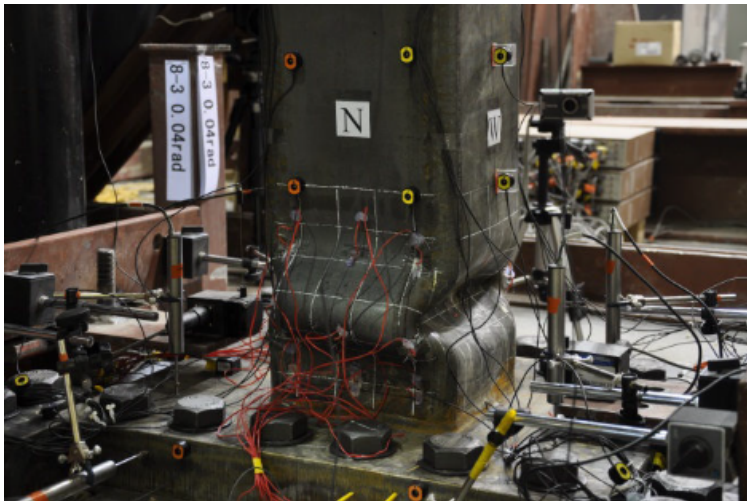
Figure 2.14: Deduced column end moment-chord rotation relation for W14X61 wide-flange steel columns under constant compressive axial load ratio and varying axial load coupled with symmetric lateral loading protocols. Images from ATC (2016), data from Suzuki and Lignos (2015) and Lignos et al. (2016).



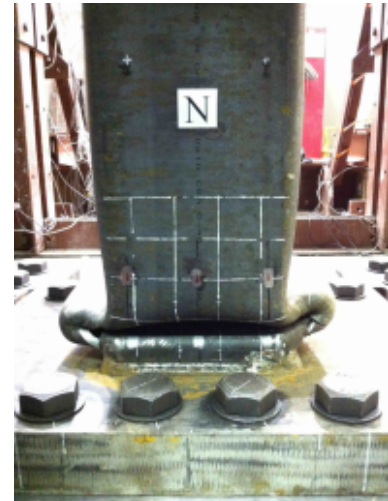
(a) HSS10X10X3/8,  $P_g/P_{ye} = 0.30$



(b) onset of local buckling



(c) progression of local buckling

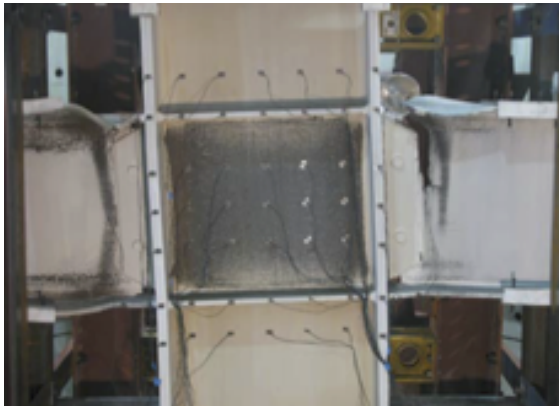


(d) severe column axial shortening

Figure 2.15: Typical deduced column end moment-chord rotation relation of HSS steel columns including damage progression Suzuki and Lignos (2015).



Figure 2.16: Elephant foot local buckling mechanism, from Suzuki and Lignos (2015).



(a) panel zone shear yielding



(b) panel zone shear buckling

Figure 2.17: Typical hysteretic response of beam-to-column joint panel zone, from Engelhardt et al. (2000) and Newell and Uang (2006).

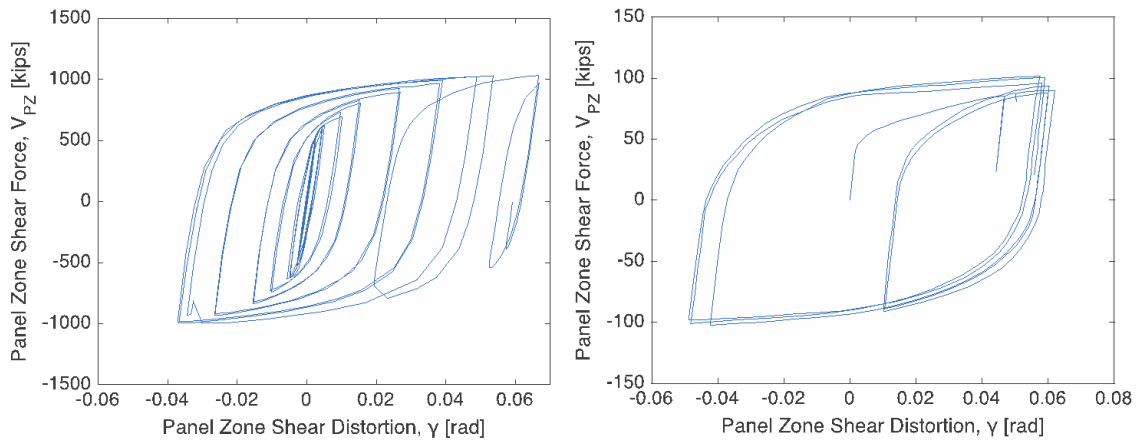
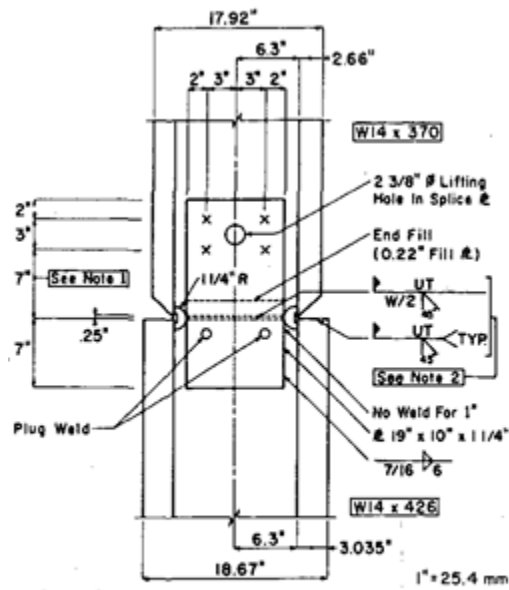


Figure 2.18: Typical hysteretic response of beam-to-column joint panel zone. Image from ATC (2016), data from Engelhardt et al. (2000), and Krawinkler et al. (1971).



- NOTES:**
1. Provide 7" as specified instead of 3" as on standard detail.
  2. A certified inspector is to be present during construction and perform ultrasonic testing of the weld.

Figure 2.19: Typical column splice details. From Bruneau and Mahin (1990).

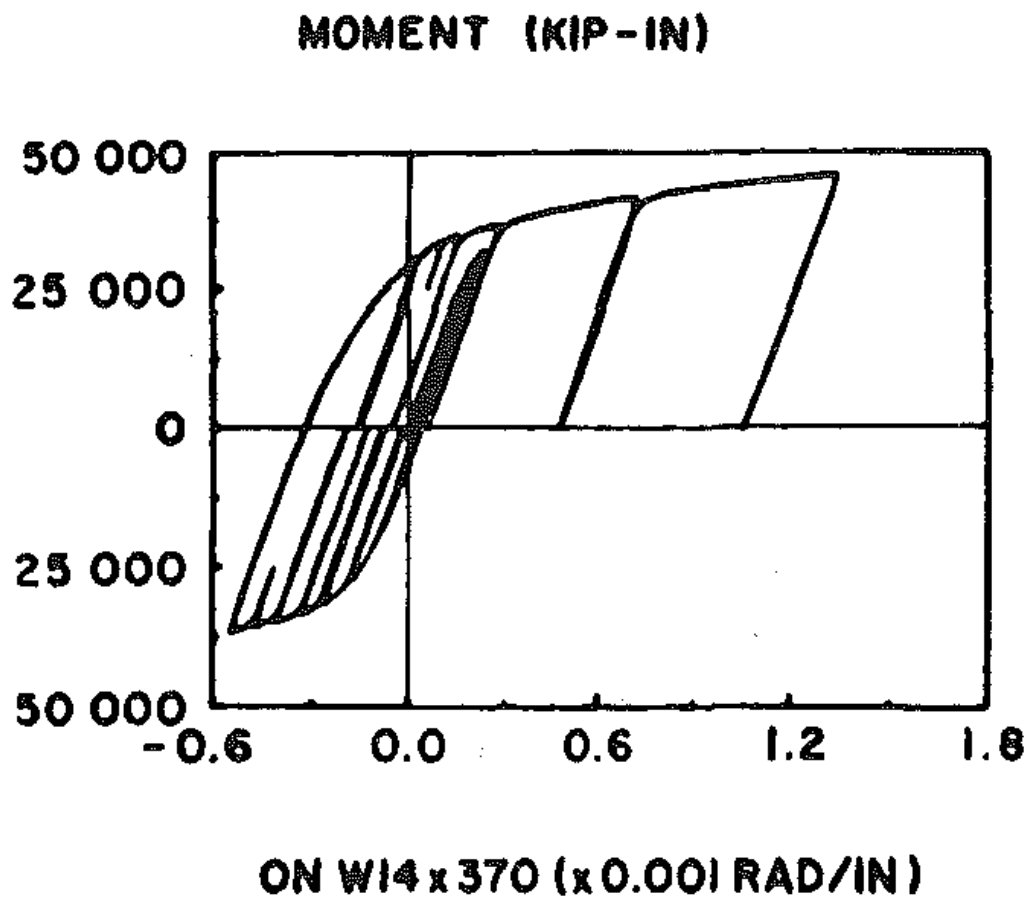


Figure 2.20: Typical moment curvature relation for complete joint penetration welded splice. From Bruneau and Mahin (1991).

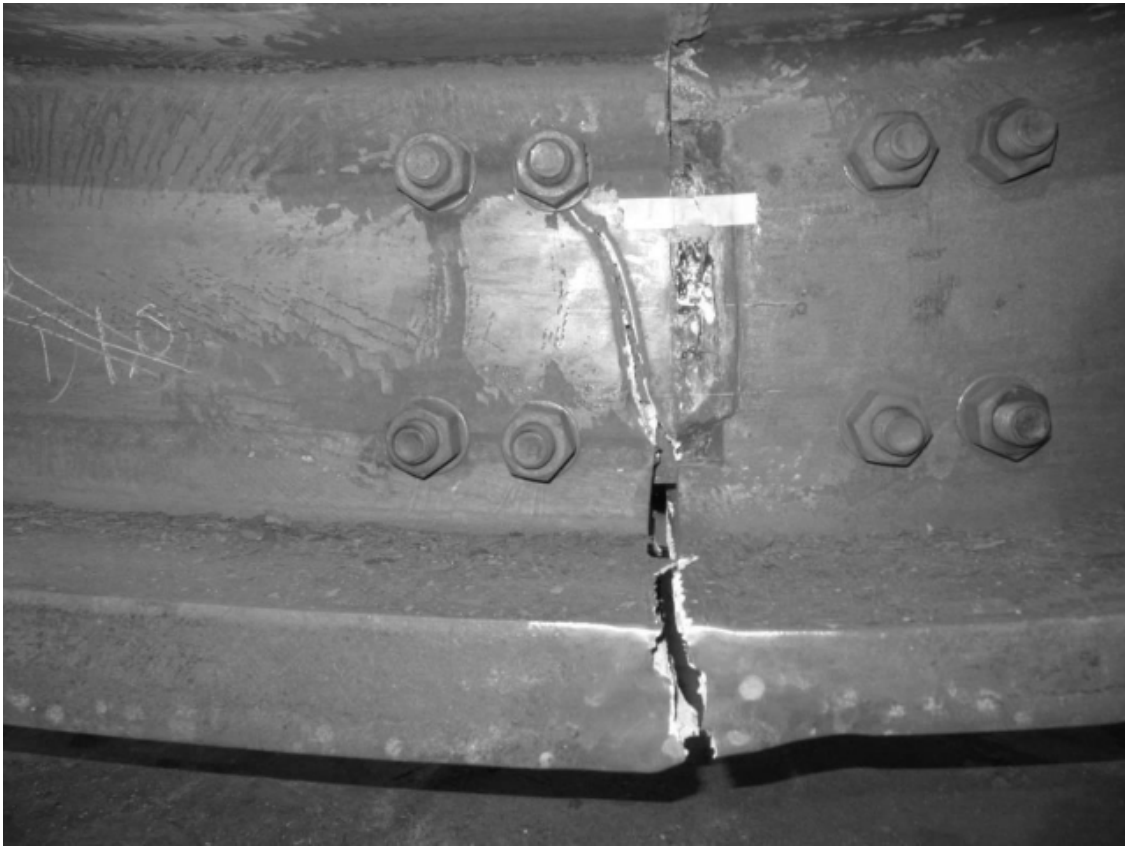
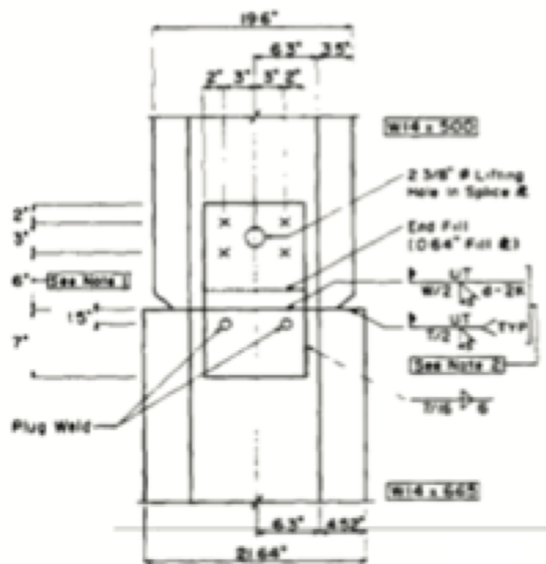
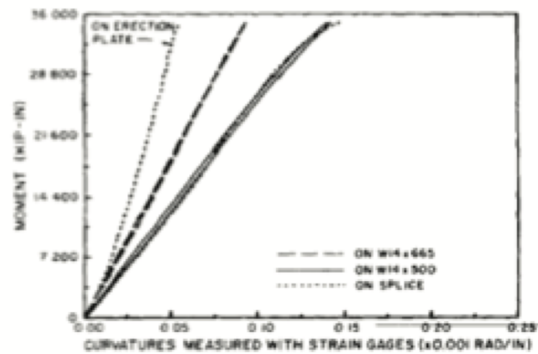


Figure 2.21: Weld fracture in welded column splice. From Shaw (2013).



(a) typical detail



(b) moment-curvature relation



(c) damage progression

Figure 2.22: Typical detail, moment-curvature relation and damage progression for pre-Northridge column splice connections, from Bruneau and Mahin (1991).

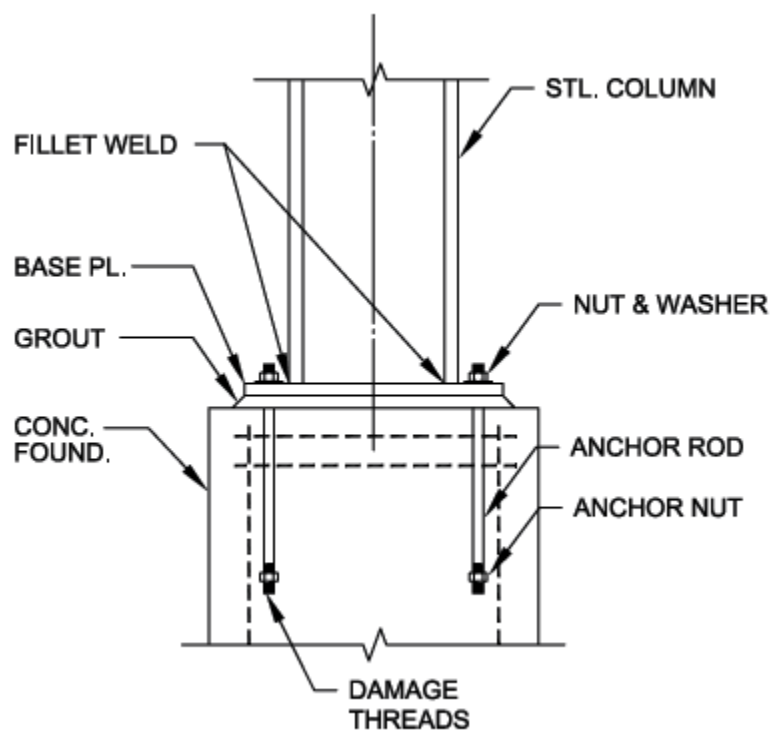
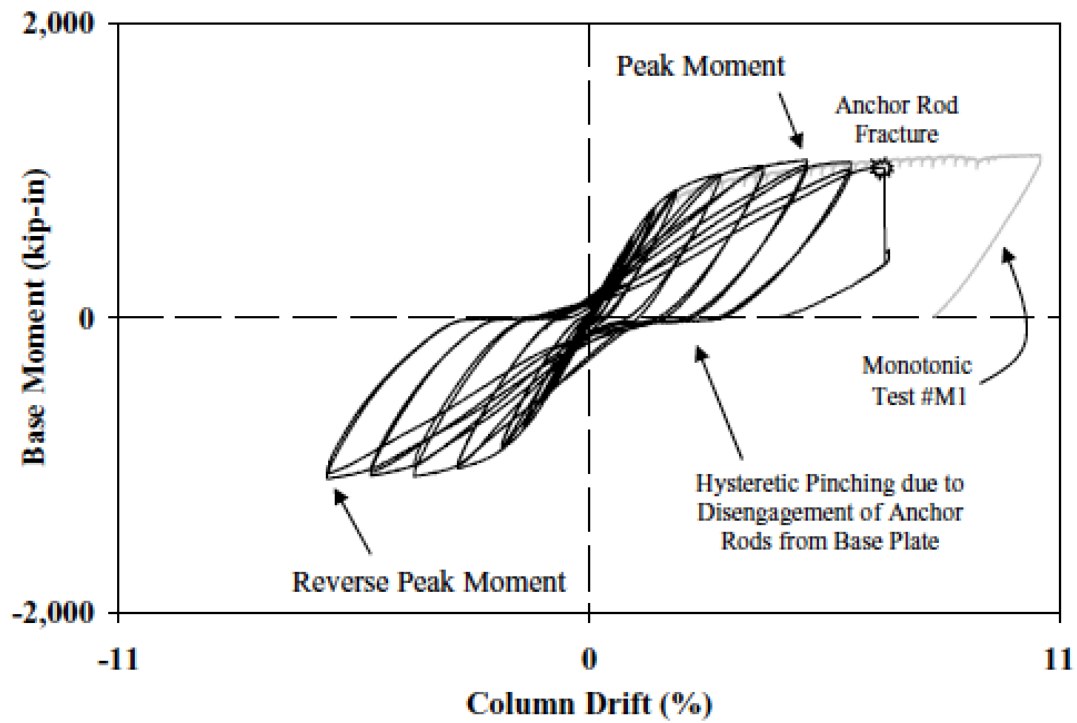
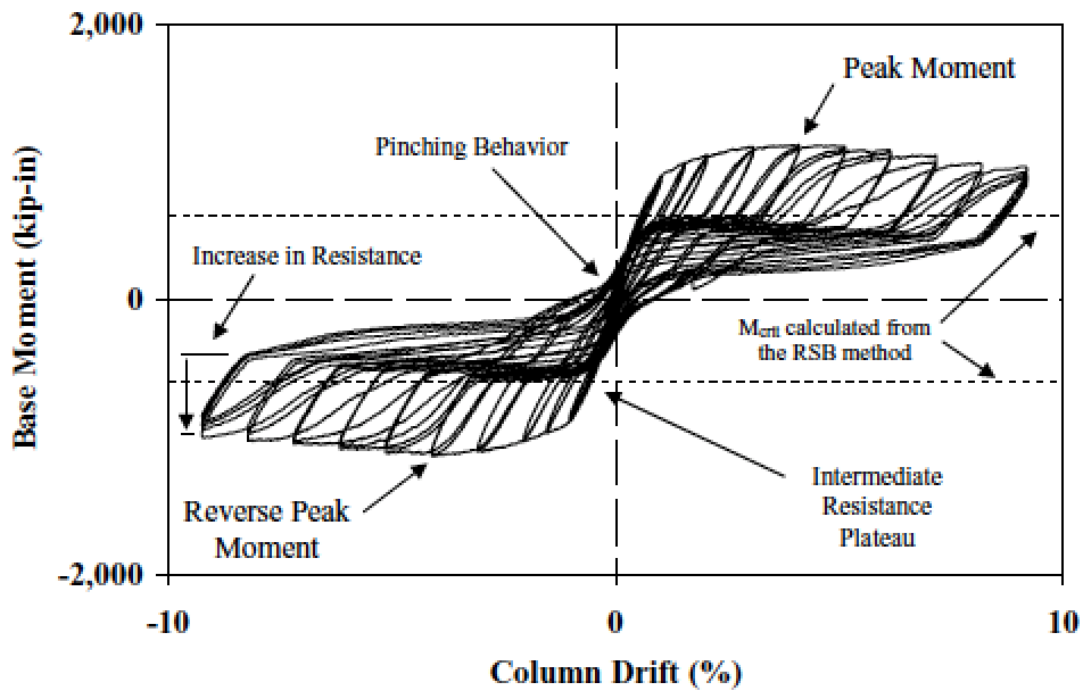


Figure 2.23: Typical exposed column base details. From Fisher and Kloiber (2006).



(a) exposed column base connection,  $P = 0$



(b) exposed column base connection,  $P = 92.5$  kips

Figure 2.24: Damage progression of exposed column base connections, from Gomez (2010).

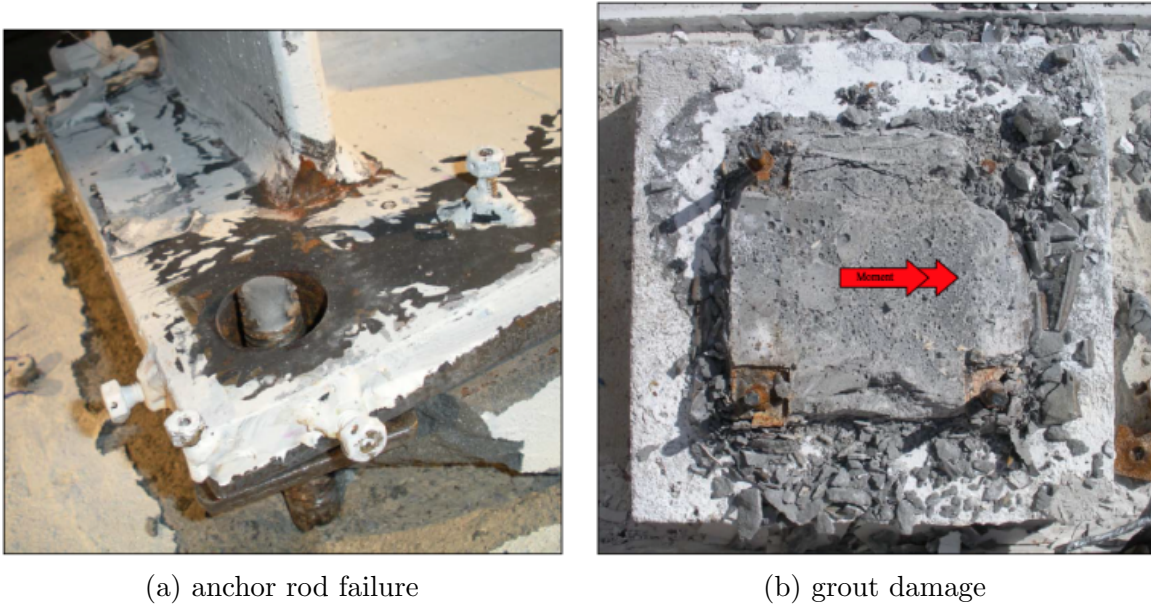


Figure 2.25: Hysteretic response of exposed column base connections, from Gomez (2010).

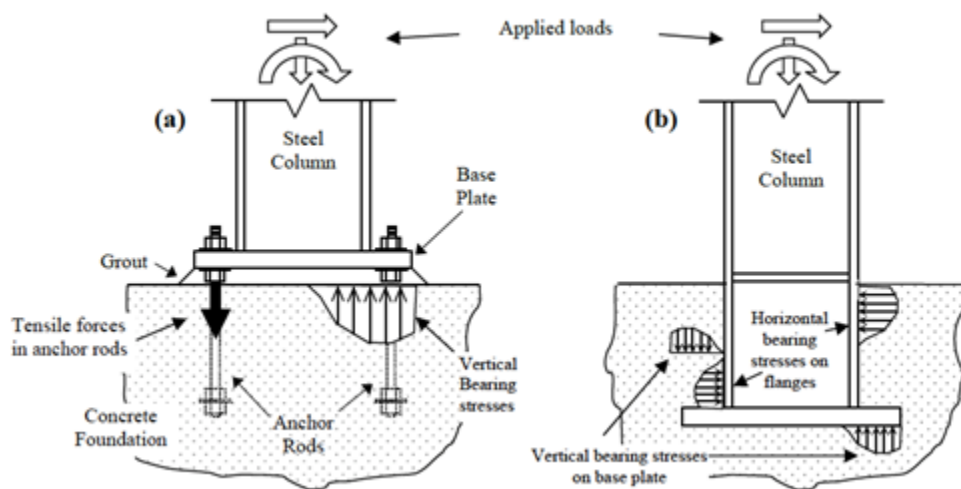


Figure 2.26: Typical embedded column base details and force transfer mechanisms, from Grilli (2015).

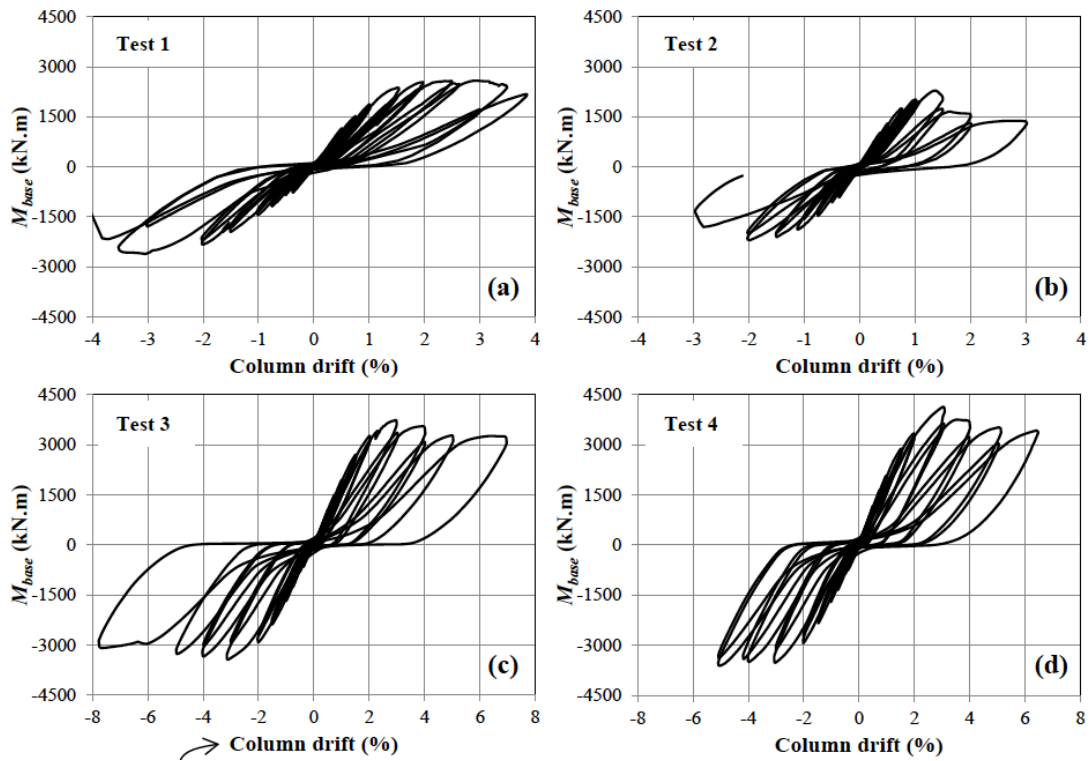


Figure 2.27: Moment drift relations for embedded type column base connections, from Grilli (2015).

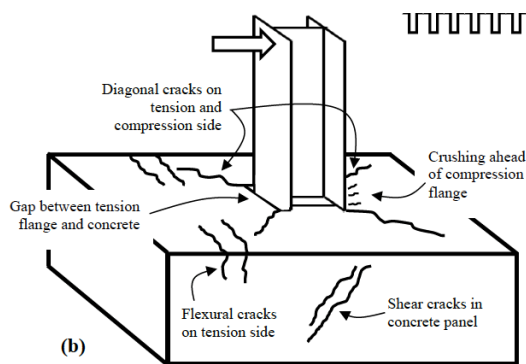


Figure 2.28: Typical failure modes observed in embedded column base connections, from Grilli (2015).

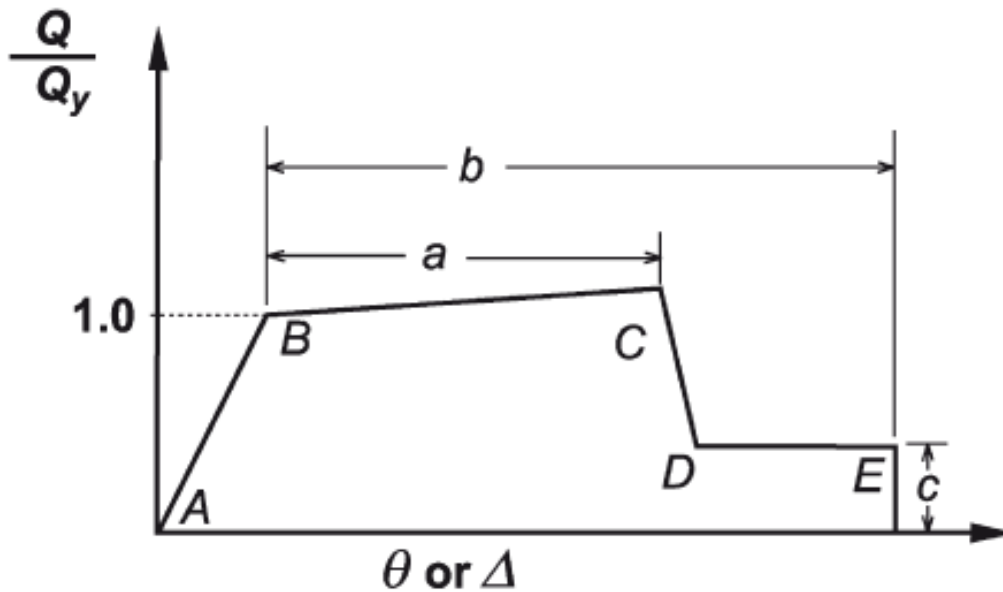


Figure 2.29: The general component model for the modelling of steel frame components based on ATC-114 (ASCE, 2014).

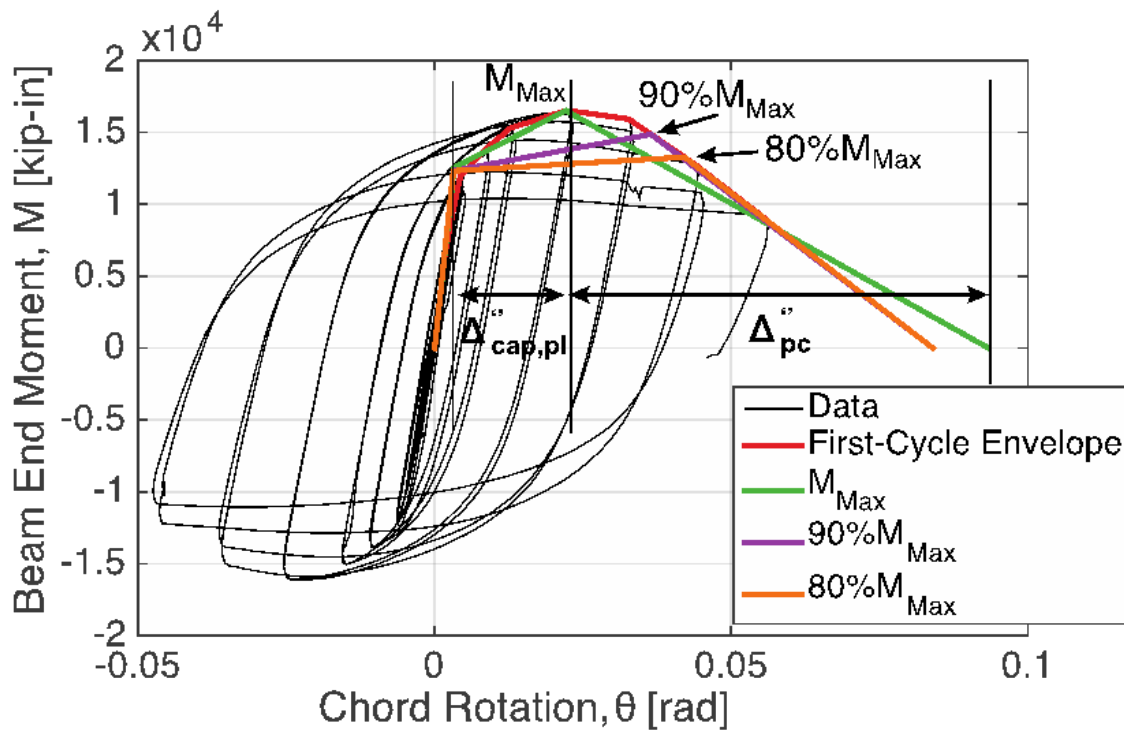


Figure 2.30: Methods used to develop the first-cycle envelope, from ASCE (2014) data from FEMA (2000).

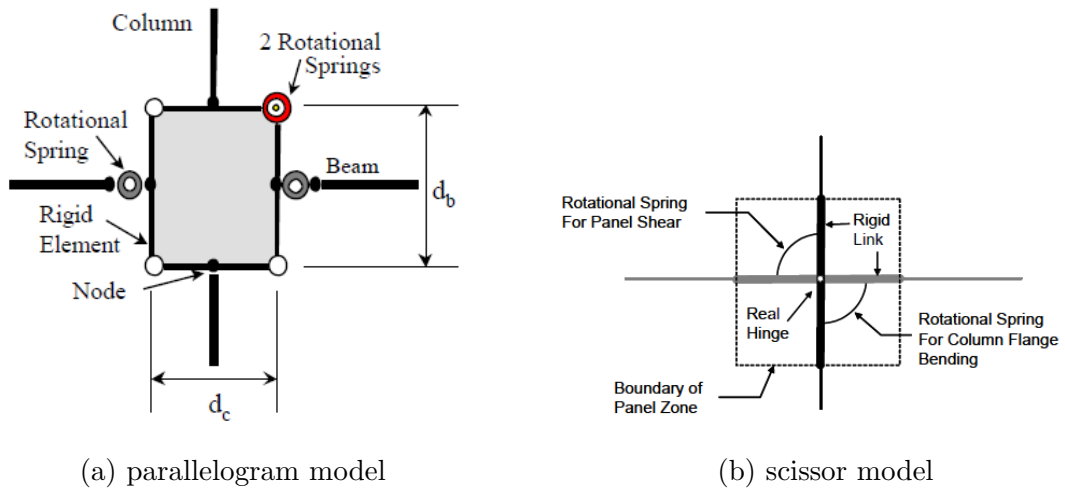


Figure 2.31: Comparison of panel zone modelling options. Image (a) from Gupta and Krawinkler (1999), (b) from Charney and Downs (2004)

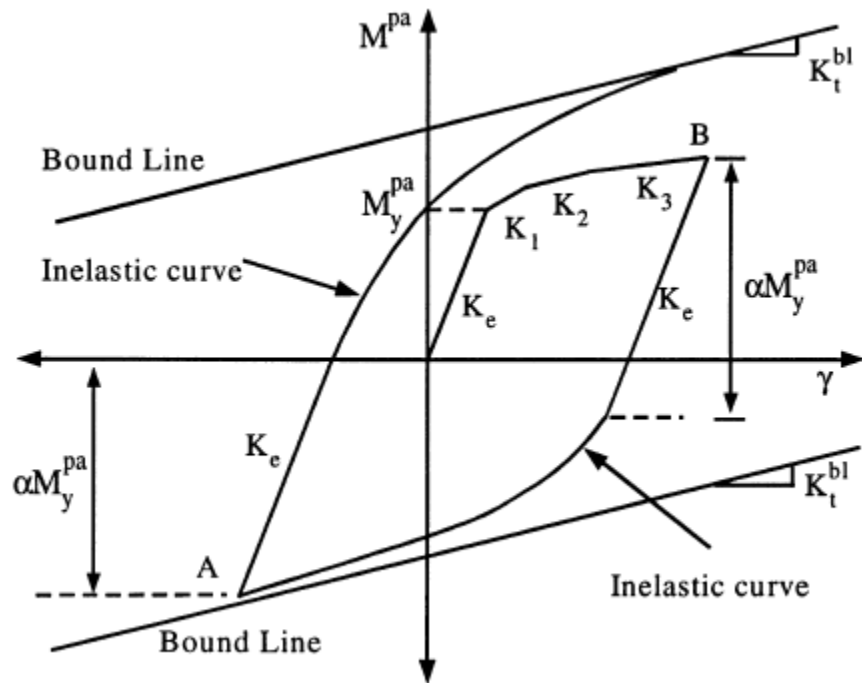


Figure 2.32: Idealized cyclic panel zone behaviour. From Kim and Engelhardt (2002).

# Chapter 3

## Development of Nonlinear Modelling Recommendations for Steel Moment-Resisting Frame Systems

### 3.1 Introduction

This chapter addresses the limitations of the ASCE-41-13 provisions through the development of a set of guidelines for the nonlinear modelling of steel MRF components. The development of each of the component models follows a general procedure that can be summarized as follows:

1. Develop a test database for each of the respective components based on available literature
2. Extract the response parameters from the experimental data according to a rationale-based procedure
3. Develop predictive equations for each of the response parameters based on the definitions of the ATC-114 component model
4. Analyse and evaluate the regression equations through statistical testing and comparison

with experimental data

First an overview of the methodology that was followed in the component model development procedure will be presented, including details on the extraction of response parameters from experimental data, and an overview of the statistics used. Following this are the proposed recommendations for the nonlinear modelling of each of the structural components considered for the performance-based seismic assessment of steel MRFs.

## **3.2 Methodology for the development of component models**

### **3.2.1 Data collection**

This section will provide an overview of each of these steps in the development of the updated component models that are to be used as a part of the ATC-114 provisions for steel MRFs. The first of these steps is the collection of experimental data. The experimental data for each of the component models was either directly obtained, or through digitization of the deduced force-deformation relations if the test data was not available. The digitization was done manually using the tool Digitizer (Lignos and Krawinkler, 2007) as a computer-based aid.

For each of the steel MRF structural components described in Section 2.2, the response due to earthquake loading can be described in terms of four regions: the elastic region, the post-yield region, the post-buckling region, and the residual region. The elastic region represents the state of the structural component prior to the initiation of yielding. The post-yield region represents the state of the member after the component has yielded, the component may increase in load carrying capacity due to hardening, and has not yet begun to deteriorate in strength or stiffness. The post-buckling region represents the post-buckling behaviour of the structural component, where local, global, or lateral-torsional buckling has

initiated, leading to a deterioration in strength and stiffness. The deterioration will continue with increasing cyclic amplitudes until a stabilization of the component force-deformation response occurs, this is the residual region. Finally the ultimate deformation of the component will be reached at the point that the component can no longer sustain the applied gravity loading, or ductile tearing occurs.

The relation between the force and deformation of a structural component in each of the four regions is in general nonlinear, however linear approximations can be made for each of these regions. This multi-linear approach is taken for both the ASCE-41-13 (ASCE, 2014) and the ATC-114 (ATC, 2016) component models, as shown in Figure 3.1. With reference to Figure 3.1, the component response is represented as follows: the elastic region is represented by the effective elastic stiffness of the component,  $K_e$ , up to the effective yield strength,  $Q_y^*$ ; the post-yield region is represented by the slope up to the peak strength,  $Q_u$  (or  $Q_u^*$  for the first-cycle envelope), and the deformation in this region denoted by  $\Delta_p$  for the monotonic backbone or  $\Delta_p^*$  for the first-cycle envelope; the post-buckling region is represented by the behaviour in the descending portion of either the monotonic backbone,  $\Delta_{pc}$ , or first-cycle envelope,  $\Delta_{pc}^*$ ; the residual region is represented by the plateau in strength once the residual strength,  $Q_r$ , is reached (or  $Q_r^*$  for the first-cycle envelope); and finally, the ultimate deformation is given as  $\Delta_{ult}$  for the monotonic backbone and  $\Delta_{ult}^*$  for the first-cycle envelope. Therefore, a calibrated value for each of the aforementioned parameters must be provided in order to fully define the component model for each structural component.

To obtain an estimate of the ultimate deformation, generally some form of extrapolation was used to predict the ultimate rotation from the test data, as shown in Figure 3.2. The capping, or peak, moment is defined in the component models as the ratio of the yield strength to the peak strength,  $a = Q_u/Q_y^*$  (or  $a^*$  for the first-cycle envelope).

Based on the above, a general procedure for determining the response parameters from cyclic data can be developed. The response parameters from the test data are then taken from this tri-linear curve as shown in Figure 3.2. For the test data under consideration,

the procedure is broken into two steps: the first step is to establish the first-cycle envelope curve, and the second step is to fit an idealized tri-linear curve. The idealized tri-linear curve consists of the elastic slope, the slope up to the peak strength of the envelope curve, and the slope of the descending portion of the envelope curve. Two MATLAB (The MathWorks, Inc., 2015) scripts were developed for these purposes, a summary of the procedures are given as follows:

**Establishment of the first-cycle envelope curve:**

- Find the yield moment and rotation for the positive loading direction
- Find the point of maximum moment and corresponding rotation, this becomes the maximum moment and the rotation at the maximum moment for the positive loading direction
- Find the corner points of the moment-rotation curve between the maximum and the yield point for the positive loading direction
- Find the corner points of the moment-rotation curve after the maximum point for the positive loading direction
- Repeat steps 1–4 to obtain the points for the negative loading direction

**Fitted idealized tri-linear curve:**

- Determine the elastic slope using principle mechanics
- Determine the point of maximum moment, take this as  $M_{max}^*$  and the corresponding rotation as  $\theta_{100\%}^*$
- Fit a line from the point of maximum moment to intersect through the elastic slope, then set the slope of this line such that the positive and negative areas between this line and the first-cycle envelope are equal within a specified tolerance
- Take the intersection between the line fitted in step 2 and the elastic slope as the yield moment,  $M_y^*$ , and yield rotation,  $\theta_y^*$
- Take the pre-peak plastic rotation,  $\theta_p^* = \theta_{100\%}^* - \theta_y^*$

- Use the final two points of the first-cycle envelope to do a linear extrapolation to zero moment
- Use a similar procedure as in step 2 to fit a line from the point of maximum moment with the descending portion of the first-cycle envelope curve
- Take the ultimate rotation,  $\theta_{ult}^*$ , as the rotation at the end point of the line fitted in the previous step
- If the line fitted in the descending region has a very shallow slope, generally in the case that the component was not tested far into the post-peak region, take the ultimate rotation as the rotation at the last point of the first-cycle envelope
- Take the post-peak plastic rotation,  $\theta_{pc}^* = \theta_{ult}^* - \theta_{100\%}^*$

### 3.2.2 Regression analysis

Once the database for the structural component under consideration is established, according to the procedures described in Section 3.2.1, the predictive equations for each of the response parameters are developed. The equations are developed through a multiple-regression analysis.

The component properties included in the regression analyses should relate to the damage progression observed for each of the components in Chapter 2. The chosen predictors are related to both the geometric and material properties of the component under consideration, and in the case of columns, the axial load present on the column. More specifically, the predictors are as follows:

- Geometric parameters: Parameters related to the local slenderness of a cross-section are used to represent a component's susceptibility to local instability, and include parameters such as the web and flange depth-to-thickness ratios,  $h/t_w$  and  $b_f/2t_f$ , respectively. For beam and column components in steel MRFs, the initiation of global instability is dependant on the un-braced length of the component,  $L_b$  and the radius of gyration in the weak-axis,  $r_y$ . Through a moment-curvature analysis, the plastic rotation capacity of beam and column components are dependant on the length of the

component under consideration,  $L$ , as well as the depth,  $d$ .

- Axial load ratios for column components: As shown from experimental observation and statistical analyses, the response of steel columns is heavily dependant on the axial loading on the component. Furthermore, as discussed in Section 2.2 the moment-rotation response is not as dependent on the transient portion of the axial load as it is the constant gravity load. Therefore the ratio of the gravity load to the expected axial yield strength is used,  $P_g/P_{ye}$ .
- Material properties: Both the plastic deformation and hardening of steel MRF components are dependant on the respective steel material. Therefore the effects of this parameter should be considered in the component model, the expected yield stress can be normalized by the elastic modulus,  $E/F_{ye}$ , to obtain a unit-less parameter.

A stepwise multiple-regression analysis is then carried out on a set of predictors for each of the response variables using the software MATLAB (The MathWorks, Inc., 2015). The regression equations provide a prediction for each of the parameters that are a part of the component models' multi-linear force-deformation relation.

### Stepwise multiple-regression analysis

The power form of the regression equation is used in the development of the component models, therefore the response parameters are calculated as

$$y = c \left( \prod_i^n x_i^{\beta_i} \right) \epsilon, \quad (3.1)$$

where  $y$  is the response parameter,  $c = e^{\beta_0}$  is the constant term (intercept in the case of a linear interpolation),  $x_i$  are the predictors,  $\beta_i$  are the coefficients of the predictors, and  $\epsilon$  is the error term. Therefore, when taking the natural logarithm of both sides

$$\log(y) = \beta_0 \log(e) + \left( \sum_i^n \beta_i \log(x_i) \right) + \log(\epsilon). \quad (3.2)$$

The regression is then carried out on the log-transformed data using the least-squares method to determine the estimates for the coefficients of the predictors (Chatterjee and Hadi, 2015).

The power form of the equation provides a better estimation of the experimental data than the linear, or other forms, of the regression equation. Additionally, the power form of the regression equation is preferred because it aligns with the physical constraint that the predicted parameters can never be less than zero. In the cases where there is limited test data, a full regression analysis is not appropriate, and therefore the mean value of the response parameter is used to predict the component model parameter instead.

The initial set of predictors are chosen as geometric and material properties that have been shown to have an effect on the component response, as discussed in Chapter 2. Once the set of initial predictors is selected, a stepwise regression analysis is carried out in order to determine the final form of the regression equations. The set of predictors that gave rise to the equation with the greatest coefficient of determination, or  $R^2$  value, is chosen as the final equation. The coefficient of determination is a measure of the variance captured by the regression equation, an  $R^2$  value close to 1.0 means that the equation well predicts the experimental data. The significance of each predictor is determined based on the t-test, if the resulting  $p$ -value was lower than the significance level, or  $\alpha$  value, then the predictor is said to be insignificant, and thus *may* be excluded from the equation. The t-tests, and all other statistical tests, were evaluated considering  $\alpha = 0.05$ . Additionally, predictors were only included in the equations if their coefficient was shown to follow the expected response based on engineering mechanics, if this trend was not shown, then they were removed from the equations.

Predictors are removed from the equations due to a high degree of correlation, or collinearity, between predictors. If the collinearity could not be addressed in the equation through statistical methods, the individual predictor that leads to the equation with the highest coefficient of determination is chosen, and the other predictors are not included in the equation.

All of the regression equations that are developed are presented with their  $R^2$  value and coefficient of variation (COV). The COV is a measure of the variance of the residuals, and is calculated as follows assuming the power regression form is used

$$\text{COV} = \text{std}(e^\epsilon) / \text{mean}(e^\epsilon), \quad (3.3)$$

where  $\epsilon$  are the residuals for the particular equation.

Once a suitable regression equation is developed based on the above criteria, each equation is examined to evaluate whether the Gauss-Markov hypothesis for best linear unbiased estimators was fulfilled. The criteria of the Gauss-Markov hypothesis are (Chatterjee and Hadi, 2015):

1. The mean of the residuals is equal to zero
2. There is constant variance of the residuals
3. There is no correlation between the residuals and the predictors

If it is shown that the criteria had been fulfilled, then it is assumed that the presented equation represents the best estimate of the data possible.

The evaluation of the regression equations are done through a combination of visual inspection and statistical testing, as presented in Chatterjee and Hadi (2015). The regression equations are first checked using an F-test, any equation that returned a  $p$ -value over the  $\alpha$  level is disregarded. The F-test is used as an indicator of whether or not the regression equation can provide any explanatory power over the response parameter.

To evaluate the constant variance of the residuals, or homoskedasticity (if there is non-constant variance it is said to be heteroskedastic), the residuals are examined visually through a plot of the residuals versus the fitted values, and through plots of the residuals versus the predictors. The correlation between the residuals and the predictors is first evaluated through the use of the Durbin-Watson test, if the returned  $p$ -value is greater than the alpha value, the residuals are inspected to determine if there is correlation of the residuals. The

correlation is evaluated visually through the plot of the residuals versus fitted values, and a plot of the residuals versus each predictor. If there are apparent trends in the residuals, it is assumed that correlation between the residuals and predictors exists. When any of the model assumptions were violated, steps are taken to modify the regression equations in an attempt to satisfy the assumptions, specific details are outlined in the discussion at the end of each component model.

The residuals are also tested to see if they follow a normal distribution. Testing the normality of the residuals is done as a verification, such that the component models that are developed can be used in performance-based evaluations that may consider the statistical variation between component input parameters. For each equation, the evaluation of normality is done through a visual inspection of the QQ-plot, a histogram of the residuals, and through the Lilliefors test (The MathWorks, Inc., 2015). For the Lilliefors test, if the  $p$ -value returned is greater than the alpha value then it can be assumed that the residuals follow a normal distribution. A summary table is given for each regression equation that provides the following information for each predictor: the estimate of the coefficient, the  $p$ -value for the t-test, and the 95% confidence interval bounds. The tables also provide the  $p$ -values for the Durbin-Watson and Lilliefors test, as well as the COV and the  $R^2$  values.

As the final step in evaluating the component models, the predicted component behaviour based on the newly developed component models are visually compared with test data, as well as the predicted component behaviour based on existing modelling options. A table for each of the components is provided with certain sample cross-sections and the computed values for the component models.

Additional details are provided as a discussion of the statistics and behaviour for each of the components presented in this chapter. The subsequent sections provide the proposed nonlinear modelling recommendations for performance-based seismic assessments of new and existing steel MRFs.

## 3.3 Hinge model for beams as a part of fully-restrained beam-to-column moment connections

### 3.3.1 Monotonic backbone curve

The equations provided in Lignos and Krawinkler (2011) are modified in to be in line with the current recommendations for the ATC-114 component models. The modifications included a simplification of the predictor coefficients, and by removing the dependence on  $F_{ye}$  by assuming an effective yield stress of 55 ksi (345 MPa) for all components. As well, the equations for the pre-capping plastic rotation are modified to remove the dependence on the unbraced length, since due to the strict lateral-bracing requirements in ANSI/AISC 341-10 (AISC, 2010a) it was found that the response parameters are not strongly influenced by this quantity (Lignos and Krawinkler, 2009). The parameters of these component models are with reference to Figure 3.1.

1. Elastic stiffness,  $K_e$ : For steel beams this quantity refers to the effective elastic flexural stiffness of the component. For steel beams  $K_e$  can be computed using Equation 3.4 regardless of the connection type

$$K_e = \alpha_e EI/L, \quad (3.4)$$

where  $EI$  is the cross-section flexural stiffness of the bare steel beam,  $L$  is the assumed beam length (i.e., distance between column faces), and  $\alpha_e$  is the stiffness coefficient.

For a beam in double curvature, take  $\alpha_e = 6$ . Commercial structural analysis software may assume that the structural members are “infinitely” rigid, in these cases for practical purposes, it is suggested to make the hinge stiffness 10 times stiffer than that of a steel beam in double curvature; therefore take  $\alpha_e = 60$  (Ibarra et al., 2005). If the hinge stiffness is modified, the stiffness of the beam must be modified as well. Assuming

the characteristic beam stiffness is the moment-rotation relation in double curvature, the effective beam flexural stiffness is as follows

$$EI^* = EI / (1 - 6/\alpha_e). \quad (3.5)$$

2. Effective yield strength,  $Q_y^*$ : For steel beams this quantity refers to the effective flexural yield strength,  $M_y^*$ , and is computed based on Equation 3.6

$$M_y^* = \beta R_y Z F_y, \quad (3.6)$$

$\beta$  is a parameter to represent the effects of cyclic hardening on the yield moment, and should be taken as follows:

$$\beta = \begin{cases} 1.1 & \text{for beams with RBS connections } (\sigma = 0.12) \\ 1.2 & \text{for beams with non-RBS connections } (\sigma = 0.21) \end{cases}. \quad (3.7)$$

$F_y$  is the nominal yield stress;  $R_y$  is the yield ratio coefficient based on the steel material type, taken from Tables 9-1, 9-2, and 9-3 of ASCE-41-13 ASCE (2014); and  $Z$  is the plastic section modulus of the beam. In the case that a beam with a RBS is specified, the plastic section modulus should be reduced according to Equation 3.8.

$$Z_{,RBS} = Z - 2c_{RBS}t_f(d - t_f), \quad (3.8)$$

where  $c_{RBS}$  is the depth of the flange cut-out,  $t_f$  is the beam flange thickness, and  $d$  is the beam depth.

3. Peak strength,  $Q_u$ : This quantity is the peak flexural strength of the steel beam,  $M_{max}$ , under monotonic loading adjusted for the effects of cyclic hardening. The capping moment can be found using the relationship between the yield moment and the capping

moment given in Equation 3.9

$$M_{max} = 1.1M_y^* \text{ (COV} = 0.10\text{)}, \quad (3.9)$$

The modification factor represents the effects of cyclic hardening on the component's strength.

4. Plastic deformation up to the peak strength,  $\Delta_p$ : This quantity refers to the pre-peak plastic rotation,  $\theta_p$ , the pre-peak plastic rotation for beams with non-RBS connections can be estimated as

$$\theta_p = 0.07(h/t_w)^{-0.3}(b_f/2t_f)^{-0.1}(L/d)^{0.3}(c_{unit}^1 d/533)^{-0.7} \text{ (COV} = 0.30\text{)}, \quad (3.10)$$

The following equations is provided for beams with RBS connections

$$\theta_p = 0.09(h/t_w)^{-0.3}(b_f/2t_f)^{-0.1}(L/d)^{0.1}(c_{unit}^1 d/533)^{-0.8} \text{ (COV} = 0.30\text{)}, \quad (3.11)$$

In these equations  $h/t_w$  is the web depth-to-thickness ratio of the beam;  $b_f/2t_f$  is the flange depth-to-thickness ratio of the beam;  $L/d$  is the beam's shear-span-to-depth ratio; and we have the following definition for  $c_{unit}^1 = 25.4$  if  $d$  is in inches and  $c_{unit}^1 = 1.0$  if  $d$  is in mm.

5. Plastic deformation of the descending portion of the monotonic backbone,  $\Delta_{pc}$ : For flexural hinges, this quantity refers to the post-peak plastic rotation,  $\theta_{pc}$ . The following equation should be used for beams with non-RBS connections

$$\theta_{pc} = 4.6(h/t_w)^{-0.5}(b_f/2t_f)^{-0.8}(c_{unit}^1 d/533)^{-0.3} \text{ (COV} = 0.30\text{)}, \quad (3.12)$$

and for beams with RBS connections

$$\theta_{pc} = 6.5(h/t_w)^{-0.5}(b_f/2t_f)^{-0.9} \text{ (COV} = 0.30\text{)}. \quad (3.13)$$

6. Residual strength,  $Q_r$ : The residual flexural strength,  $M_r$ , for steel beams due to stabilization of the buckle size can be assumed as

$$M_r = 0.4M_y^*. \quad (3.14)$$

This value is based on a relatively small set of data points from which an average of  $M_r/M_y^*$  could be made with confidence regardless of the steel beam-to-column moment connection type (Lignos and Krawinkler, 2011).

7. Ultimate deformation,  $\Delta_{ult}$ : For steel beams with flexural hinging this quantity represents the ultimate rotation capacity that is likely to be controlled by ductile tearing due to cracks that may develop in the steel base material or the shear capacity of the connection. For all sections and regardless of the connection type, the ultimate rotation is given as  $\theta_{ult} = 0.2$  (COV = 0.3).
8. Reference cumulative plastic rotation,  $\Lambda$ : This parameter is provided for use of explicit modelling of cyclic deterioration based off of the modified IMK deterioration model. For beams with non-RBS connections

$$\Lambda = 85(h/t_w)^{-1.26}(b_f/2t_f)^{-0.525}(L_b/r_y)^{-0.130}(E/F_{ye})^{0.291} \text{ } (\sigma = 0.34), \quad (3.15)$$

with  $R^2 = 0.50$ . While for beams with RBS connections we have

$$\Lambda = 49(h/t_w)^{-1.14}(b_f/2t_f)^{-0.632}(L_b/r_y)^{-0.205}(E/F_{ye})^{0.391} \text{ } (\sigma = 0.35), \quad (3.16)$$

with  $R^2 = 0.49$ .

The equations that comprise the component models in this section are valid for the following ranges of values for beams with:

non-RBS connections	RBS connections
$20 \leq h/t_w \leq 55$	$21 \leq h/t_w \leq 55$
$4 \leq b_f/2t_f \leq 8$	$4.5 \leq b_f/2t_f \leq 7.5$
$20 \leq L_b/r_y \leq 80$	$20 \leq L_b/r_y \leq 65$
$2.5 \leq L/d \leq 7$	$2.3 \leq L/d \leq 6.3$
$4'' \leq d \leq 36''$	$21'' \leq d \leq 36''$
$(102 \text{ mm} \leq d \leq 914 \text{ mm})$	$(533 \text{ mm} \leq d \leq 914 \text{ mm})$
$444 \leq E/F_{ye} \leq 833$	$460 \leq E/F_{ye} \leq 763$

For steel materials other than ASTM A992 Gr. 50 or equivalent are used, the equations from Lignos and Krawinkler (2011) should be employed.

A comparison with the ASCE-41-13 provisions, as well as test data is provided in Section 3.3.6.

### 3.3.2 First-cycle envelope curve

#### Parameter trends

The dataset for beams as a part of fully restrained beam-to-column connections is taken from a test database of over 250 cyclic tests on steel beam-to-column sub-assemblies developed by Lignos and Krawinkler (2011); Lignos et al. (2013). The beams are separated by connection type into two broad categories: beams with RBS connections, and beams with non-RBS connections. The data for the component models based on the first-cycle envelope curve are obtained from experimental data on beams subjected to symmetric loading protocols through the use procedures described in Section 3.2.1.

For beams as a part of fully restrained moment connections the initial set of predictors were: web width-to-depth ratio,  $h/t_w$ ; the flange width-to-depth ratio,  $b_f/2t_f$ ; the unbraced length ratio,  $L_b/r_y$ ; the normalized yield stress ratio,  $\sqrt{E/F_y}$ ; the normalized beam depth,

$d/21$ ”; and span-to-depth ratio,  $L/d$ . For these equations the expected trends by mechanics are that the rotation capacity should decrease with  $h/t_w$ ,  $b_f/2t_f$  and  $L_b/r_y$ . For  $h/t_w$  and  $b_f/2t_f$  the decrease in rotational capacity is due to the earlier onset of local buckling that is expected to occur with decreased slenderness of the section. It is expected that there is a negative relationship between the plastic rotation capacity and  $L_b/r_y$  due to an earlier on-set of global instabilities that lead to deterioration in the flexural capacity of the beam.

Based on a moment-curvature analysis (ASCE, 2014), it is expected that the plastic rotational capacity should increase with length, and inversely with beam depth, therefore  $L/d$  is expected to have a positive coefficient. As well it is expected that the plastic rotation capacity should decrease with an increase in  $F_{ye}$ , as generally we would expect that higher yield stress steels exhibit less ductility. Therefore we would expect  $\sqrt{E/F_{ye}}$  to have a positive coefficient. For all of the equations where  $F_{ye}$  was found to be significant, the effect of this parameter was removed from the equation by considering an effective yield stress of 55 ksi, and modifying the constant parameter in each equation by the result. This is done in an effort to simplify the regression equations as the majority of the collected experiments were conducted with beams that were fabricated by A992 Gr. 50 steel or equivalent.

The following are observed trends based on the database of steel beams in fully-restrained beam-to-column connections subjected to reversed-cyclic loading histories.

For the set of beams in non-RBS connections, the dependence of the pre-peak plastic rotation based on  $h/t_w$ ,  $b_f/2t_f$ ,  $L_b/r_y$ , and  $L/d$  from experimental data are shown in Figure 3.3. Clear negative relations between  $\theta_p^*$  and each of  $h/t_w$  and  $b_f/2t_f$  are observed. As well, the positive relation between  $\theta_p^*$  and  $L/d$  can be observed. However, the relation between  $\theta_p^*$  and  $L_b/r_y$  is much less clear than the others, this is due to the strict lateral bracing requirements for beams in steel MRFs per ANSI/ASCE 341-10 (AISC, 2010a) (or earlier versions), such that global buckling is limited in these cases. Therefore when the strict lateral bracing requirement is followed, deterioration is typically initiated through local buckling of the flanges and web. This is not the case for non-conforming steel beams, however in these cases

the effect of  $L_b/r_y$  on the flexural strength of the beam is more dominant than it is on the plastic deformation capacity.

For the parameter trends on the post-peak plastic rotation,  $\theta_{pc}^*$ , shown in Figure 3.4 there are fewer tests considered than for the pre-peak plastic rotation. This is due to the limited number of tests that showed sufficient deformation in post-peak range to develop a reasonable estimation of this parameter. Comparing the dependence of  $\theta_{pc}^*$  on  $h/t_w$  and  $b_f/2t_f$  shown in Figure 3.4, it is seen that the post-peak plastic rotation is dependent on  $h/t_w$ , and not on  $b_f/2t_f$ . This observation can be made considering the large variation of data in the region of  $b_f/2t_f = 6.5$ . This finding is generally in-line with those of Lignos and Krawinkler (2009) for steel beams under monotonic loading. We can observe a negative relation with  $L_b/r_y$  because lateral-torsional buckling may be observed in the post-peak range. In general, it is expected that there is greater variance in the prediction of  $\theta_{pc}^*$  due to the limited set of test data, and the extrapolations performed in order to get an estimate of this parameter.

Looking now at the parameter trends on the pre-peak plastic rotation,  $\theta_p^*$ , for beams in RBS connections, as shown in Figure 3.5, the dominance of  $h/t_w$  on this parameter is evident. The eminence of the web-slenderness ratio on the performance of beams with RBS is due to the fact that the flanges are cut, and therefore will not contribute as heavily as the web in the plastic hinge region. Otherwise a negative relation between  $\theta_p^*$  and  $L_b/r_y$ ,  $b_f/2t_f$  can be observed.

Similar observations made for  $\theta_p$  for beams in RBS connections can be made for  $\theta_{pc}^*$ , as shown in Figure 3.6. Again the dominance of the parameter  $h/t_w$  on  $\theta_{pc}^*$  is evident, and a negative dependence with  $b_f/2t_f$  and a positive dependence with  $L/d$ .

### **Proposed component model**

The following component models are for beams in fully restrained beam-to-column connections, and are divided based on RBS and non-RBS connections. These component models are based on the first-cycle envelope, and are given with reference to Figure 3.1.

1. Elastic stiffness,  $K_e$ : The effective elastic flexural stiffness should be calculated according to Equations 3.4 and 3.5.
2. Effective yield strength,  $Q_y^*$ : The effective yield moment should be calculated according to Equation 3.6.
3. Peak strength,  $Q_u^*$ : this quantity refers to the peak flexural strength of a steel beam,  $M_{max}^*$ , under cyclic loading, and can be computed using Equation 3.17 which was derived from test data for all connection types

$$M_{max}^* = 1.15M_y^* \text{ (COV} = 0.10\text{)}. \quad (3.17)$$

4. Plastic deformation up to peak strength of the first-cycle envelope,  $\Delta_p^*$ : This quantity refers to the pre-peak plastic rotation,  $\theta_p^*$ , for flexural hinges adjusted for in-cycle deterioration in strength and stiffness. The pre-peak plastic deformation can be calculated using Equation 3.18 for non-RBS connections

$$\theta_p^* = 0.3(h/t_w)^{-0.3}(b_f/2t_f)^{-1.7}(L_b/r_y)^{-0.2}(L/d)^{1.1} \text{ (COV} = 0.34, R^2 = 0.78\text{)}, \quad (3.18)$$

Equation 3.19 is to be used for beams with RBS connections

$$\theta_p^* = 0.55(h/t_w)^{-0.5}(b_f/2t_f)^{-0.7}(L_b/r_y)^{-0.5}(L/d)^{0.8} \text{ (COV} = 0.39, R^2 = 0.55\text{)}. \quad (3.19)$$

5. Plastic deformation of the descending portion of the first-cycle envelope curve,  $\Delta_{pc}^*$ : This quantity refers to the post-peak plastic rotation,  $\theta_{pc}^*$  for flexural hinges adjusted for in-cycle deterioration in strength and stiffness. The post-peak plastic deformation can be computed using Equation 3.20 for beams with non-RBS connections

$$\theta_{pc}^* = 24.0(h/t_w)^{-0.9}(b_f/2t_f)^{-0.2}(L_b/r_y)^{-0.5} \text{ (COV} = 0.45, R^2 = 0.61\text{)}, \quad (3.20)$$

and Equation 3.21 is to be used for beams with RBS connections

$$\theta_{pc}^* = 20.0 (h/t_w)^{-0.8} (b_f/2t_f)^{-0.1} (L_b/r_y)^{-0.6} \quad (\text{COV} = 0.28, R^2 = 0.39). \quad (3.21)$$

6. Residual strength,  $Q_r^*$ : The residual flexural strength,  $M_r^*$ , for steel beams due to stabilization of the buckle size can be assumed to be,

$$M_r^* = 0.3M_y^*, \quad (3.22)$$

regardless of the beam-to-column moment connection type. This value is based on cyclic tests according to a standard symmetric cyclic loading protocol.

7. Ultimate deformation,  $\Delta_{ult}^*$ : For steel beams with flexural hinging the ultimate rotation capacity with reference to Figure 3.1 that includes the cyclic and in-cycle deterioration effects can be assumed  $\theta_{ult}^* = 0.08$  radians (COV = 0.30) regardless of the beam-to-column moment connection type.

The equations that comprise the component models in this section are valid for the following ranges of values for beams with:

non-RBS connections	RBS connections
$20 \leq h/t_w \leq 55$	$21 \leq h/t_w \leq 55$
$4 \leq b_f/2t_f \leq 8$	$4.5 \leq b_f/2t_f \leq 7.5$
$20 \leq L_b/r_y \leq 80$	$20 \leq L_b/r_y \leq 65$
$2.5 \leq L/d \leq 7$	$2.3 \leq L/d \leq 6.3$
$4'' \leq d \leq 36''$	$21'' \leq d \leq 36''$
$(102 \text{ mm} \leq d \leq 914 \text{ mm})$	$(533 \text{ mm} \leq d \leq 914 \text{ mm})$

For steel materials other than ASTM A992 Gr. 50 or equivalent are used, the equations provided in the tables of the following section should be employed (Section 3.3.2).

## Discussion of statistics for first-cycle envelope

For the  $\theta_p^*$  equation of beams in non-RBS connections, based on the values shown in Table 3.1, that there is no reason to expect auto-correlation in the residuals as a result of the Durbin-Watson test since  $p < 0.05$  for this test. For this same equation, the residuals are not normally distributed based on the result of the Lilliefors test since  $p > 0.05$ . However from an investigation of the QQ-plot and the histogram of the residuals shown in Figure 3.7, the residuals appear to be nearly normally distributed apart from two outlying values. From the inspection of the plot of the residuals versus fitted values shown in Figure 3.7, the residuals exhibit a constant variance. Therefore, it is concluded that although the residuals may not be normally distributed, the assumptions of the Gauss-Markov hypothesis are fulfilled. Since  $R^2 = 0.782$  value for this equation the equation for  $\theta_p^*$  for beams in non-RBS connections will provide a fairly reasonable prediction of the expected component response.

The equation for  $\theta_{pc}^*$  for beams in non-RBS connections passes both the Durbin-Watson and Lilliefors tests (i.e.,  $p < 0.05$ ), as seen in Table 3.2. These observations are supported by an inspection of the plot of residuals versus fitted values and the QQ-plot, as shown in Figure 3.8. Therefore, we conclude that the Gauss-Markov hypothesis is fulfilled, and the residuals are normally distributed. Given that  $R^2 = 0.610$  value for the equation for  $\theta_{pc}^*$ , this equations will provide a reasonably accurate prediction of the post-capping plastic rotation for beams with non-RBS connections.

The equation for  $\theta_p^*$  for beams with RBS is shown to follow a normal distribution, since the Lilliefors test returns  $p > 0.05$ , however fails the Durbin-Watson test since  $p < 0.05$ . These results are shown in Table 3.3. The normality of the residuals is supported by inspection of the histogram of residuals and the QQ-plot as shown in Figure 3.9, where in the later plot it is seen that the residuals closely follow the normal distribution. From the inspection of the residuals plotted against the predictors shown in Figure 3.10 there is no obvious correlation between the residuals and the predictors, and therefore it can be concluded that the conditions of the Gauss-Markov hypothesis are fulfilled. Given that  $R^2 = 0.550$ , the equation provides a

reasonable estimation of the component pre-plastic rotation response for beams with RBS.

The statistical values for the equation of  $\theta_{pc}^*$  are shown in Table 3.4 for beams with RBS. From this table, it is observed that since  $p < 0.05$  for both the Lilliefors and Durbin-Watson tests, the residuals are not normally distributed, and that there is auto-correlation in the residuals. Based on an inspection of the QQ-plot and the histogram of residuals shown in Figure 3.11, it is observed that there are a number of outlying tests that lead to the violation of the assumption of normality. With regards to the correlation between the residuals and the predictors, there is no observable correlation as seen in Figure 3.12. From an inspection of the plot of residual values versus fitted values shown in Figure 3.11, there are number of outlying data points that lead to a non-constant variance in the residuals. Therefore, the Gauss-Markov hypothesis is not fulfilled for this equation. Based on the above observations, and the  $R^2 = 0.387$  value suggests that the equation for  $\theta_{pc}^*$  could lead to inaccuracies in the prediction of the expected component response. However it represents the best available prediction for the post-capping plastic rotation given the available test data.

A comparison with the ASCE-41-13 provisions, as well as test data is provided in Section 3.3.6.

### 3.3.3 Composite steel beams

The following component model is based off of the provisions in ATC-114 (ATC, 2016). A summary table of the values used to modify the component models from Elkady and Lignos (2014) is provided in Table 3.5.

The beam hinge model discussed in the previous section does not account for the non-symmetric hysteretic behaviour of composite steel beams due to the presence of the floor slab. Therefore, the component modelling approach for composite steel beams must be modified to account for the presence of the slab. The recommendations summarized herein are based on work of Elkady and Lignos (2014) that assessed the effect of the composite action on steel moment-resisting frames under earthquake loading. This was based on available test data from

full-scale cyclic tests on composite fully restrained beam-to-column connections. Figure 3.13a shows a typical calibration of the input model parameters of a widely used point plastic hinge deterioration model (Ibarra et al., 2005) with test data from full-scale beams with RBS conducted by Ricles et al. (2004). Based on these calibrations, the monotonic and first-cycle envelope curves for bare steel beams may be adjusted to include the composite effects due to the presence of the floor slab. Figure 3.13b illustrates schematic representations of the adjusted monotonic backbone and cyclic envelope curves for a composite beam in comparison with those for a bare steel beam. The adjusted monotonic backbone and first-cycle envelope curves are non-symmetric. The following scaling factor adjustments should be considered to adjust the monotonic and/or first-cycle envelope curves of bare steel beams to include composite effects.

The following component parameters are given with reference to the component model shown in Figure 3.1, the adjusted model is shown in Figure 3.13b.

1. Effective moment of inertia,  $I_{c,b}$ : For composite steel beams this quantity refers to the moment of inertia of the composite section, averaged in both the positive and negative loading directions. The modification factor should be taken as

$$I_{c,b} = 1.4I_b \text{ (COV} = 0.12\text{)}, \quad (3.23)$$

where  $I_b$  is the moment of inertia of the bare steel beam.

This adjustment is a conservative assumption given that the employed test data consisted of cruciform configurations in which the frame continuity is neglected. Prior experimental studies that utilized the frame action including composite effects (Cordoba and Deierlein, 2005; Nakashima et al., 2007; Nam and Kasai, 2012) have shown that this factor may be in the order of two times the respective moment of inertia of the bare beam.

2. Effective yield strength,  $Q_y^*$ : For composite steel beams this quantity refers to the flexural yield strength of the composite steel beam. Due to the asymmetry of the composite steel beam, the adjustment factors are separate for the positive and negative loading directions. In the positive loading direction,  $M_y^{*+}$  should be found according to Section I3 of ANSI/AISC 360-10 (AISC, 2010b) as follows:

- (a) Consider full composite action between the concrete slab and the steel beam
- (b) The effective width of the composite beam should be calculated based on ANSI/AISC 360-10 (AISC, 2010b) Section I3.1a:

$$b_{eff} = \min \left( \begin{array}{l} \text{one-eighth of the girder center-to-center of supports,} \\ \text{one-half the distance to the centerline of the adjacent girder,} \\ \text{distance to the edge of the slab} \end{array} \right)$$

- (c) The effective stress before concrete crushing is taken as 0.85 of the specified concrete stress  $f'_c$ .

The effective flexural yield strength in the negative loading direction (ie. slab in tension) may be increased so that  $M_y^{*-} = 1.10M_y^*$ , where  $M_y^*$  is the effective flexural yield strength of the bare steel beam. This increase is attributed to the steel slab reinforcement.

3. Peak strength,  $Q_u$  (or  $Q_u^*$  for a first-cycle envelope curve): This quantity refers to the peak flexural strength of the composite steel beam,  $M_{max}$  (or  $M_{max}^*$ ) in the positive and negative loading direction. For the positive loading direction, take

$$M_{max}^+ = 1.30M_y^* \text{ (COV} = 0.10\text{)}. \quad (3.24)$$

In the negative loading direction, take  $M_{max}^-$  in accordance with Equation 3.9 or Equation 3.17 based on the monotonic backbone curve or the first-cycle envelope curve,

respectively.

4. Plastic deformation up to peak strength of the monotonic backbone curve,  $\Delta_p$  (or  $\Delta_p^*$  for a first-cycle envelope curve): For composite steel beams, this quantity refers to the adjusted pre-peak plastic rotation,  $\theta_p$  (or  $\theta_p^*$ ), to take into consideration the effects of the composite action. For the positive loading direction use

$$\theta_p^+ = 1.80\theta_p \text{ (COV} = 0.20\text{)}, \quad (3.25)$$

where  $\theta_p$  (or  $\theta_p^*$ ) is the pre-peak plastic rotation of the bare steel beam.

5. Plastic deformation of the descending portion of the monotonic backbone curve,  $\Delta_{pc}$  (or  $\Delta_{pc}^*$  for a first-cycle envelope curve): For composite steel beams, this quantity refers to the adjusted pre-peak plastic rotation,  $\theta_{pc}$  (or  $\theta_{pc}^*$ ), to take into consideration the effects of the composite action. For the positive loading direction use

$$\theta_{pc}^+ = 1.35\theta_{pc} \text{ (COV} = 0.15\text{)}, \quad (3.26)$$

where  $\theta_{pc}$  (or  $\theta_{pc}^*$ ) is the post-peak plastic rotation of the bare steel beam.

6. The residual strength,  $Q_r$  (or  $Q_r^*$ ), and ultimate deformation,  $\Delta_{ult}$  (or  $\Delta_{ult}^*$ ), for composite steel beams should be taken as the same values calculated according to the component models based on the respective monotonic backbone or first-cycle envelope curve.

### 3.3.4 Beams as a part of pre-Northridge WUF-B connections

#### Parameter trends

The updated component model for steel beams in pre-Northridge beam-to-column connections is presented in this section. The data for beams with pre-Northridge connections is taken from

the FEMA/SAC joint testing program (SAC/FEMA, 1996) as well as from the beam database described in Section 3.3.2 for beams in pre-Northridge WUF-B connections. Modelling recommendations are provided only for a first-cycle envelope curve, as there is no monotonic test data available for pre-Northridge WUF-B beam-to-column connections. In addition, the beams in this data set fractured very early in their loading history (FEMA, 2000), such that little cyclic degradation occurred.

From Figure 3.14 the pre-peak plastic rotation is clearly dependent on the beam depth. As discussed in FEMA-355D (FEMA, 2000), there was a clear difference in behaviour between beams with depths larger than 21" and lower yield stresses.

### Proposed component model

The parameters of this component model are given with reference to Figure 3.1 for the response based on the first-cycle envelope curve.

1. Elastic stiffness,  $K_e$ : The effective elastic flexural stiffness should be calculated according to Equations 3.4 and 3.5.
2. Effective yield strength,  $Q_y^*$ : This quantity is the effective yield flexural moment,  $M_y^*$ , and should be calculated according to Equation 3.27

$$M_y^* = R_y S_x F_y \text{ (COV} = 0.19\text{)}, \quad (3.27)$$

$S_x$  is the section modulus of the bare steel beam,  $F_y$  is the nominal yield stress of the steel beam, and  $R_y$  is the yield ratio coefficient based on the steel material type based on Tables 9-1, 9-2, and 9-3 of ASCE-41-13 ASCE (2014).

3. Peak strength,  $Q_u^*$ : The capping strength represents the maximum flexural strength of the steel beam under cyclic loading,  $M_{max}^*$ , use the value given in Equation 3.28

$$M_{max}^* = 1.1 R_y Z_x F_y \text{ (COV} = 0.23\text{)}, \quad (3.28)$$

where  $Z_x$  is the plastic section modulus of the beam.

4. Plastic deformation up to peak strength of the first-cycle envelope,  $\Delta_p^*$ : This quantity is the pre-peak plastic rotation,  $\theta_p^*$ , Equation 3.29 should be used to calculate  $\theta_p^*$

$$\theta_p^* = \begin{cases} 0.046 - 0.0013d \geq 0 & \text{if } d < 24'' \text{ and } F_t/F_y < 0.6. \text{ (COV} = 0.50) \\ 0.008 \text{ radians} & \text{if } d \geq 24'' \text{ and } F_t/F_y \geq 0.6. \text{ (COV} = 0.64) \end{cases} \quad (3.29)$$

where  $F_t$  is the nominal tensile stress of the steel beam, and  $d$  is the beam depth.

5. Plastic deformation of the descending portion of the first-cycle envelope curve,  $\Delta_{pc}^*$ : This quantity is the post-peak plastic rotation,  $\theta_{pc}^*$ , and should be calculated according to Equation 3.30

$$\theta_{pc}^* = \begin{cases} -0.003 + 0.0007d \geq 0 & \text{if } d < 24'' \text{ and } F_t/F_y < 0.6 \text{ (COV} = 1.1) \\ 0.035 - 0.0006d \geq 0 & \text{if } d \geq 24'' \text{ and } F_t/F_y \geq 0.6 \text{ (COV} = 1.1) \end{cases} \quad (3.30)$$

6. Residual strength,  $Q_r$ : The residual flexural strength should be taken as  $M_r^* = 0.2M_y^*$  (COV = 0.50).
7. Ultimate deformation,  $\Delta_{ult}^*$ : The ultimate rotation capacity,  $\theta_{ult}$ , of the beam is based on the rotation at which components could no longer sustain their gravity loading, and should be calculated according to Equation 3.31

$$\theta_{ult}^* = \begin{cases} 0.050 & \text{if } d < 24'' \text{ and } F_t/F_y < 0.6. \text{ (COV} = 0.45) \\ 0.035 & \text{if } d \geq 24'' \text{ and } F_t/F_y \geq 0.6. \text{ (COV} = 0.50) \end{cases} \quad (3.31)$$

## Discussion of statistics

The linear form of the regression equation is used, as it is found to provide a higher coefficient of determination versus the power form for beams as a part of pre-Northridge WUF-B beam-

to-column connections. It is found that for this equation  $d$  was the only significant variable, this finding is consistent with the those of FEMA (2000). The results of the regression analysis compare well with the component model provided by FEMA-355D (FEMA, 2000), therefore it was decided to maintain a similar format and values for the component model. As well, it is decided to maintain the use of the chord rotation at which the gravity load can no longer be supported,  $\theta_g$  from FEMA-355D, to represent the ultimate rotation capacity. The difference between the proposed component model and the model provided in FEMA 355-D is that a lower pre-peak plastic rotation is found. The reduced  $\theta_p^*$  is due to the use of the maximum flexural capacity as the point of peak flexural strength, versus 80% of the maximum flexural capacity that had been used in the previous approach.

As shown in Table 3.6 for  $\theta_p^*$  from the Lilliefors test the equation has normally distributed residuals, this result is supported by the observation of the histogram of residuals and QQ-plot from Figure 3.15. The Durbin-Watson test returns  $p < 0.05$ , therefore there is reason to suspect correlation between the residuals and the predictors. This result is supported by an examination of Figure 3.16, where there is evidence that the proposed equation will over-estimate true values at beam depths near 24 inches. The  $R^2$  value with a low COV shows that there can be a reasonable level of confidence placed in this equation. Given the high COV for Equation 3.30 for  $\theta_{pc}^*$ , there should not be a high degree of accuracy expected for this parameter. However, given the tendency of pre-Northridge connections to fail in a brittle manner this result can be justified.

A comparison with the ASCE-41-13 provisions, as well as test data is provided in Section 3.3.6.

### **3.3.5 Non-conforming beams as a part of fully-restrained beam-to-column moment connections**

The following is from the ATC-114 recommendations (ATC, 2016). Steel beams that do not meet the requirements for lateral bracing and cross sectional slenderness for highly

ductile members per ANSI/AISC 360-10 (AISC, 2010b) may be modelled based on the recommendations discussed in Section 3.3.1 for the monotonic backbone or Section 3.3.2 for the first-cycle envelope. However, the effective yield flexural strength,  $M_y^*$ , of a non-conforming steel beam should be adjusted based on the beam unbraced length,  $L_b$ , such that the effects of lateral torsional buckling on the beam flexural yield strength should be explicitly captured. This should be done in accordance with Sections F2 to F5 of ANSI/AISC 360-10 (AISC, 2010b) provisions for doubly symmetric compact wide flange members bent about their strong axis and based on their web and flange depth-to-thickness ratios. Shown in Figure 3.17 schematically is the adjusted effective yield flexural strength,  $M_y^*$  of a steel beam with respect to its unbraced length.

### 3.3.6 Comparison with existing modelling options and experimental data

#### Steel beams in fully-restrained beam-to-column connections

Figure 3.18 shows a comparison between experimental data, the ASCE-41-13 component model, and the proposed component model for beams in fully-restrained beam-to-column connections (noted as “1st Cycle Env.”). In these figures, beams with RBS and non-RBS connections are shown, including steel beam cross-sections ranging from W18 to W36. Based on this figure and the table of computed model parameters, Table 3.7, the main observations are as follows:

- The post-yield hardening in the proposed component models is based on the ratio between  $a^* = M_{max}^*/M_y^*$ , as opposed to the 3% strain hardening value suggested in ASCE-41-13. This change is made since experimental data has shown that 3% strain hardening is not true in all cases, and therefore  $a^* = M_{max}^*/M_y^*$  is a more stable parameter versus using the 3% strain hardening ratio. This observations is in agreement with work by Lignos and Krawinkler (2011).

- As shown in Figures 3.5 and 3.3, the pre-peak plastic rotation,  $\theta_p^*$  is strongly dependent on the web and flange local slenderness ratios. The proposed component models capture this dependency, however the ASCE-41-13 component model express the plastic rotation solely in terms of the beam depth,  $d$ .
- As discussed in Section 3.2.1 the proposed component model uses a peak moment based on the maximum moment of each test, whereas the previous component model in ASCE-41-13 used a peak moment based on 80% of the post-maximum moment. Therefore, typically the pre-peak plastic rotation,  $\theta_p^*$ , will be lower for the proposed component models compared to the ASCE-41-13 component models, “ $a$ ”. In Figures 3.18a and 3.18b, for beams with depths less than 21”, the pre-peak plastic rotation seems to be fairly well represented, however for depths greater than 21”, as seen in Figures 3.18c to 3.18f,  $\theta_p^*$  is over estimated by the ASCE-41-13 component models. This indicates that there may be some bias in the parameters “ $a$ ” and “ $b$ ” towards smaller beams sizes in the ASCE-41-13 provisions.
- The pre-peak plastic rotation, or “ $a$ ” value in ASCE-41-13, for steel beams is dependant solely on the depth of the bare steel beam,  $d$ . This is contrary to experimental data that has shown that there are clear relationships between the plastic rotation and the local slenderness ratios, the proposed component models are able to capture these effects.
- The flexural strength of a steel beam deteriorates gradually with the increasing lateral loading amplitude regardless of the beam size and connection type. As seen for the various cross-sections and connections in Figure 3.18, this is captured fairly well based on the post-peak plastic deformation,  $\theta_{pc}^*$  as computed from the proposed modelling recommendations.
- Typically a lower pre-peak plastic rotation,  $\theta_p^*$ , is found from the proposed recommendations versus those in ASCE-41-13. This is to be expected, since as discussed in Section 2.3.1 the peak flexural strength  $M_{max}$  is based on the maximum flexural strength from experimental data, and not based on 80% $M_{max}$ . From Figure 3.18 we can

see that the ASCE-41-13 component model over predicts the experimental  $\theta_p^*$  for beams depths greater than 21". This may indicate that there is a bias in the ASCE-41-13 component model provisions for steel beams with smaller depths.

- The large discontinuity in flexural strength of steel beams based on the ASCE-41 component model is not reflected in the experimental data for steel beams as part of fully restrained beam-to-column connections regardless of the respective beam depth. As seen in Figure 3.18, in all cases the experimental deterioration in strength is more gradual than predicted by the ASCE-41-13 component model. Historically, this discontinuity caused numerical instabilities in nonlinear structural analysis software that is being used by the engineering profession (ASCE, 2014).

A table of computed component model parameters based on the first-cycle envelope for beams in fully-restrained beam-to-column connections are given in Table 3.7 for both non-RBS and RBS connections. Based on the values found in these tables, the main observations are:

- The mean ratio between the pre-peak plastic rotation for the first-cycle envelope and monotonic backbone,  $\theta_p^*/\theta_p$ , is found to be 0.65 for the proposed component models. This value is in agreement with the "Option 3" modelling recommendation of  $\theta_p^*/\theta_p = 0.70$  proposed in PEER/ATC-72-1 (PEER/ATC, 2010).
- The mean ratio between the total inelastic deformation to the deformation that loss of gravity load carrying capacity is expected to occur is,  $\theta_{ult}^*/\theta_{ult}$  is approximately 3.5. This finding is fairly consistent with that of Chapter 16 of ASCE-7-16 (ASCE, 2016).
- Generally beams in non-RBS connections provide a higher pre- and post-peak plastic rotation,  $\theta_p^*$  and  $\theta_{pc}^*$ , at beam depths  $d < 30"$ , and for  $d > 30"$  the values found are comparable between the two connection types.

### Composite steel beams

The following discussion is provided from ATC (2016). Figure 3.19 illustrates a comparison of the monotonic and first-cycle envelope curves based on the proposed nonlinear modelling

recommendations for composite steel beams.

The ASCE-41-13 component model (ASCE, 2014) is also superimposed in the same figure. From Figure 3.19, it is evident that the current ASCE-41 component model considerably overestimates the pre-peak plastic deformation  $\theta_p^*$  of composite beams when the slab is in tension (i.e., negative loading direction). The same component model seems to underestimate by 20%, on average, the flexural strength of a composite beam when the slab is in compression (i.e., positive loading direction). This can be fairly important for the nonlinear evaluation of steel moment-frame systems because the flexural strength of steel beams is directly related with the employed strong-column/weak-beam ratio. The computation of the effective yield flexural strength of a composite beam when the slab is in compression based on Section I3 of ANSI/AISC 360-10 (AISC, 2010b) seems to be effective in terms of adjusting the component backbone curve for the composite beam effects. This is consistent with what was found in recent studies by Elkady and Lignos (2014).

### **Beams in pre-Northridge WUF-B connections**

Figure 3.20 illustrates a number of examples for steel beams as part of pre-Northridge beam-to-column connections. The connection type in most cases was welded flange unreinforced web with a bolted shear tab (WUF-B). In few of the examples shown in the same figure, a weld reinforcement was used in the shear tab (i.e., WUF-W). Superimposed in the same figure are the nonlinear modelling recommendations discussed in this chapter as well as the current ASCE-41-13 recommendations (ASCE, 2014). The following observations hold true:

- For steel beams that experience fracture at chord rotations larger than 1.5% radians their effective yield strength is in general under predicted by both nonlinear modelling approaches (see Figures 3.20a and 3.20c). This is generally observed in steel beams with depths,  $d < 18''$ , which are not typically used in typical steel MRFs. This is attributed to cyclic hardening prior to the occurrence of fracture, which is not captured by Equation 3.27. In such cases (i.e.,  $d \leq 18''$ ) an upper bound analysis is also suggested

in which the flexural strength of the respective beam should be computed based on Equation 3.6 (i.e., full plastic resistance).

- For steel beams with  $d < 24''$  (see Figure 3.20c) the first-cycle envelope curve based on both modelling recommendations is more-or-less the same for all practical purposes. The use of the proposed nonlinear model discussed in this chapter is likely to eliminate problems associated with numerical instabilities within a nonlinear analysis software because it does not include the instantaneous vertical drop in flexural strength that the ASCE-41-13 component model does.
- The ASCE-41-13 component model seems to underestimate the pre-peak plastic rotation,  $\theta_p^*$  (i.e., parameter “ $a$ ”) of steel beams with  $d > 30''$  by 50%, on average, as seen in Figures 3.20a, 3.20b, 3.20d, 3.20f.

## 3.4 Column hinge model

### 3.4.1 Steel wide-flange columns

The component models for wide-flange columns were developed as a part of this thesis. The database for the wide-flange steel columns was developed in Elkady (2016). The database was in part based on detailed finite element studies performed as a part of Elkady and Lignos (2015a) and the ATC-114 project (ATC, 2016), in addition to experimental data, that are all summarized in Elkady (2016). The database consists of over 160 data points for columns subjected to both reversed-cyclic and monotonic loading protocols, with a wide range of geometric properties, and compressive axial load ratios ranging from 0% to 75%.

As all of the columns considered in the database had an expected yield stress of  $F_{ye} = 55$  ksi, it was not possible to explore the variation in this parameter, therefore the equations should be used only for ASTM A992 Gr. 50 steel or equivalent.

Experimental data with constant compressive and varying axial load on nominally identical steel columns (MacRae, 1989; Newell and Uang, 2006; Suzuki and Lignos, 2015; Lignos et al.,

2016) indicate that the post-buckling behaviour of steel columns is influenced more by the constant compressive axial load, or gravity load,  $P_g$ , rather than the transient component. The transient component is due to the dynamic overturning effect during earthquakes, and can be significant in end columns of the MRF. Therefore, the predictive equations for the model parameters discussed below are based on the gravity axial load ratio,  $P_g/P_{ye}$ , in which  $P_{ye}$  is the expected axial yield strength of the steel column. The proposed column hinge parameters do not include any reduction due to P-Delta effects. The experimental and analytical data that were utilized were processed such that the deduced moment reflected the actual moment within the column hinge.

### Parameter trends

It is found that for all equations, due to the collinearity between the predictors, the flange width-to-depth ratio,  $b_f/2t_f$ , was not included in the equations for the wide-flange columns. This is because in all cases the equations including the web width-to-depth ratio was found to provide a higher  $R^2$  value than flange web width-to-depth ratio. An illustration of the relation between the web and flange width-to-depth ratios can be seen in Figure 3.21, the high level of correlation between these two predictors is clearly seen. Therefore, a suitable set of predictors was chosen as  $h/t_w$ ,  $L_b/r_y$ , and  $P_g/P_{ye}$ .

Note that this observation was made for the database under consideration. Care should be taken when implementing the following equations for built-up-sections in which the correlation between the flange and web width-to-depth ratios may not be maintained.

With regards to the deformation related parameters of the component model, from mechanics, it is expected that there would be a negative relation between the web-slenderness and both the pre- and post-peak plastic rotations. This is due to an earlier onset of local buckling in the former case, and accelerated deterioration due to local buckling and axial shortening in the later. A negative relation is also predicted for the pre- and post-peak plastic rotations based on  $L_b/r_y$ , due to greater tendency for global instabilities. Finally, a reduced

rotation capacity with increased axial loading is expected, and therefore a negative relation between the pre- and post-peak plastic rotations and  $P_g/P_{ye}$ .

With regards to the ratio of the peak moment to the yield moment,  $M_{max}/M_y^*$ , it is expected that sections that buckle earlier will develop lower hardening, and therefore would expect a negative relation between  $h/t_w$  or  $L_b/r_y$  and  $M_{max}/M_y^*$ . Similarly, as columns under greater axial loads are shown to deteriorate more rapidly, thus a lower hardening ratio is expected in these cases as well. Therefore a negative relation between  $P_g/P_{ye}$  and  $M_{max}/M_y^*$  is expected.

The following is a discussion on the observed parameter trends for steel columns under combined axial force and lateral drift demands, subjected to both monotonic and reversed-cyclic loading protocols.

Due to the large set of test data, the trends on the pre-peak plastic rotation,  $\theta_p$ , for steel wide-flange columns under monotonic loading shown in Figure 3.22 are clearly seen. From this figure, it can again be seen the correlation between  $h/t_w$  and  $b_f/2t_f$ . There is a strong negative relation between  $\theta_p$  and both  $h/t_w$  and  $P_g/P_{ye}$ . However, it is observed that there is little difference in the pre-peak plastic rotation for columns loaded with 35%  $P_g/P_{ye}$  and 50%  $P_g/P_{ye}$ . The dependence of  $\theta_p$  on  $L_b/r_y$  is much less pronounced, this can be attributed to the observation that for seismically compact cross-sections within the limits of highly ductile members as per AISC 360-10 (AISC, 2010b), typically global instabilities do not occur until after the initiation of local buckling. The general trends observed in Figure 3.23 for columns under reversed-cyclic loading are similar to those observed for columns under monotonic loading, however we observe an increased dependence of  $\theta_p^*$  on  $h/t_w$  in the cyclic loading case versus the monotonic loading case. For both monotonic and cyclic loading, since the variance in the response of the pre-peak plastic rotation decreases with increasing  $P_g/P_{ye}$ , it is observed that the axial load ratio has a dominant effect over the pre-peak plastic rotation.

Figure 3.24 shows the trends on the post-peak plastic rotation,  $\theta_{pc}$ , for columns under monotonic loading. Due to the increased variance on  $\theta_{pc}$  a larger spread in the data than

with  $\theta_p$  is observed. The variance is due to the extrapolation procedures used to estimate this parameter, as well as multiple deterioration mechanisms that may be acting on the column section that reduce the dependence on any single parameter. Similarly with  $\theta_p$ , strong negative trends on  $h/t_w$  and  $L_b/r_y$  are observed for  $\theta_{pc}$ . There is an increase in dependence on  $L_b/r_y$  in  $\theta_{pc}$  over what was observed for  $\theta_p$ . This is expected since typically the initiation of global instabilities occur after that of local buckling of the column flanges and web. Again the general observations made with regards to the post-peak plastic rotation for columns under reversed-cyclic loading are similar to those made for columns under monotonic loading protocols, as shown in Figure 3.25. Similarly with the pre-peak plastic rotation, for both monotonic and cyclic loading the variance in the response of the post-peak plastic rotation decreases with increasing  $P_g/P_{ye}$ , and therefore it can be concluded the axial load ratio has a dominant effect over the post-peak plastic rotation as well.

Figure 3.26 shows the trends for the hardening ratio  $M_{max}/M_y^*$  based on the monotonic backbone curve. A major difference in the observed trends between hardening ratio and the pre- and post-peak plastic rotations is that there is a limited influence of the applied axial load on the hardening ratio, and that there are therefore strong influences from both  $h/t_w$  and  $L_b/r_y$  on this parameter. Figure 3.27 shows the trends based on the first-cycle envelope curve. For each of  $h/t_w$ ,  $L_b/r_y$ , and  $P_g/P_{ye}$  the basic trends on the hardening ratio are similar to those of wide-flange columns subjected to monotonic loading. Comparing the data from the monotonic tests, as shown in Figure 3.26, to those of the cyclic tests, it is observed that the cyclic tests show less variation in the hardening ratio. This is because cyclic hardening has a dominant effect. As well, looking at the cyclic test data, a number of tests with 50% axial load ratio exhibit relatively high rates of hardening. In these cases, it is expected that the columns yielded very early, yet were still able to reach an appreciable level of maximum flexural capacity.

In summary, all of the response parameters of wide-flange columns subjected to both monotonic and reversed-cyclic lateral drift demands have a negative relation with the local

and global slenderness ratios, as well as with the axial load ratio. However, what varies is the influence of each of the parameters on the response variables. The following sections will provide the component models that have been developed, and a discussion of the statistics of the predictive equations.

### Monotonic backbone curve

The following component model is based on the monotonic backbone, and is intended to be used for nonlinear response history analysis procedures of steel frame buildings with the use of component models that are able to explicitly capture the effects of cyclic hardening and component deterioration in strength and stiffness. The parameters of this component model are with reference to Figure 3.1.

1. Elastic stiffness,  $K_e$ : This quantity is given in terms of the effective elastic flexural stiffness,  $K_e$ . The column hinge may be modelled with a finite flexural stiffness, or as rigid-plastic based on Equations 3.4 and 3.5.

Based on experimental findings from Suzuki and Lignos (2015) and Elkady and Lignos (2015a, 2016) the assumed plastic hinge length  $L_h = 1.4d_c$ ; where  $d_c$  is the steel column depth. This agrees with the seismic design criteria for steel columns according to the New Zealand seismic code NZS (1997).

2. Effective yield strength,  $Q_y^*$ : For steel columns this quantity refers to the effective yield moment,  $M_y^*$ , and can be computed using Equation 3.32 based on the axial load ratio and the interaction equations provided by AISC that are modified to account for the effects of cyclic hardening on the hysteretic behaviour.

$$M_y^* = \begin{cases} 1.15R_yZF_y(1 - P_g/2P_{ye}) & \text{if } P_g/P_{ye} \leq 0.20 \text{ (COV} = 0.10) \\ 1.15R_yZF_y(9/8)(1 - P_g/P_{ye}) & \text{if } P_g/P_{ye} > 0.20 \text{ (COV} = 0.10). \end{cases} \quad (3.32)$$

Where  $Z$  is the plastic section modulus of the column;  $F_y$  is the nominal yield stress of

the steel;  $R_y$  is the yield ratio coefficient depending on the steel material type and can be computed based on Table A3.1 per AISC-341-10 (AISC, 2010a); and  $P_g/P_{ye}$  is the ratio of the applied gravity load on the column to the effective axial yield strength of the column.

3. Peak strength,  $Q_u$ : For steel columns this quantity refers to the maximum flexural moment of the section under monotonic loading adjusted for the effects of cyclic hardening,  $M_{max}$ , and can be computed using Equation 3.33

$$M_{max} = aM_y^*, \quad (3.33)$$

The coefficient  $a$  reflects the hardening ratio of the column,  $M_{max}/M_y^*$ , and can be calculated using Equation 3.34 for monotonic backbone models

$$a = 12.5 (h/t_w)^{-0.2} (L_b/r_y)^{-0.4} (1 - P_g/P_{ye})^{0.4} \geq 1.0 \quad (\text{COV} = 0.10, R^2 = 0.76). \quad (3.34)$$

If  $P_g/P_{ye} > 0.3$  or if  $h/t_w < 15$  then  $a \leq 1.3$ . The local slenderness of the column is represented through the web length-to-depth ratio of the steel column,  $h/t_w$ ; and the global slenderness of the column is represented through the ratio of the unbraced length to radius of gyration,  $L_b/r_y$ ; and  $P_g/P_{ye}$  is the ratio of the applied gravity load to the axial yield strength of the column.

4. Plastic deformation up to peak strength of the monotonic backbone,  $\Delta_p$ : For steel columns this quantity refers to the the pre-peak plastic rotation,  $\theta_p$  can be calculated using Equation 3.35

$$\theta_p = 294 (h/t_w)^{-1.7} (L_b/r_y)^{-0.7} (1 - P_g/P_{ye})^{1.6} \leq 0.20 \quad (\text{COV} = 0.39, R^2 = 0.89), \quad (3.35)$$

5. Plastic deformation of the descending portion of the monotonic backbone,  $\Delta_{pc}$ : For

steel columns this quantity refers to the the post-peak plastic rotation,  $\theta_{pc}$ ; it indicates the post-buckling behaviour of steel columns. The post-peak plastic rotation can be computed using Equation 3.36

$$\theta_{pc} = 90 (h/t_w)^{-0.8} (L_b/r_y)^{-0.8} (1 - P_g/P_{ye})^{2.5} \leq 0.30 \text{ (COV} = 0.26, R^2 = 0.91), \quad (3.36)$$

6. Residual strength,  $Q_r$ : The residual flexural strength for columns can be computed from Equation 3.37

$$M_r = (0.5 - 0.4P_g/P_{ye}) M_y^* \text{ (COV} = 0.27), \quad (3.37)$$

7. Ultimate deformation,  $\Delta_{ult}$ : For steel columns with flexural hinging this quantity represents the ultimate rotation capacity that is likely to be controlled by loss of the column axial carrying capacity. With reference to the monotonic curve it is recommended to take

$$\theta_{ult} = 0.15 \text{ radians (COV} = 0.46). \quad (3.38)$$

The range of sections for which the equations are applicable are:

$$3.71 \leq h/t_w \leq 57.5$$

$$1.82 \leq b_f/2t_f \leq 8.52$$

$$38.4 \leq L_b/r_y \leq 120$$

$$0 \leq P_g/P_{ye} \leq 0.60$$

Steel wide flange columns under compressive axial load ratios  $P_g/P_{ye} > 0.60$  that have  $h/t_w > 43$  and  $KL_b/r_y > 120$  must be treated as force-controlled elements as per ASCE-41-13 (ASCE, 2014). Steel columns utilizing stocky cross-sections that experience gravity loads

$P_g > 0.60P_{ye}$  have a finite plastic deformation capacity, which is not zero. However, columns with gravity loads over  $0.6P_{ye}$  may be under designed for gravity loads (Bech et al., 2015), therefore, column yielding should be restricted in these cases.

### Discussion of statistics for the monotonic backbone

A summary of the statistics for the  $\theta_p$  equation is show in Table 3.8, the diagnostic plots can be seen in Figure 3.28. Since the  $p$ -value returned for Durbin-Watson test on the residuals of both the  $\theta_p$  and  $\theta_{pc}$  equations was less than 0.05, it is seen that there is correlation between the residuals and the predictors.

Examining Figure 3.29 it is observed the residuals are correlated with the axial load ratio. As a strategy to mitigate the observed corellation between the residuals and the axial load ratio, the equations were split for tests with  $P_g/P_y \leq 0.20$ , and tests with  $P_g/P_y \geq 0.20$ . However, the correlation was still statistically significant in some cases when using the modified form. It was therefore decided to keep the equations in the current format because the level of expression complexity did not substantially improve the accuracy of the predictive equation. In order to the address concerns of an over-prediction of the response parameters, a limit is placed on the pre- and post-capping plastic rotations.

From an inspection of the plot of fitted values versus test data for  $\theta_p$  shown in Figure 3.28b, the scatter in data can be seen for values of  $\theta_p > 0.10$  or so, these values would generally correspond to columns with thick webs and flanges combined with low axial load ratios. In these cases (i.e., the values above the line in Figure 3.28b for  $\theta_p > 0.10$ ) the equation shows a tendency to underpredict the test data, however this is acceptable since it represents a safe prediction.

From the results of the Lilliefors test as seen in Table 3.8 for the equation on  $\theta_p$ , the residuals are normally distributed. The normal distribution of the residuals is well supported by visual inspection of the histogram of residuals in Figure 3.28, additionally it can be seen that the residuals show constant variance. The equation's ability to predict the test data is

reflected by a relatively high  $R^2 = 0.892$ , therefore the equation for  $\theta_p$  will give a reasonably good prediction of the true component response.

A summary of the statistical results for the equation for  $\theta_{pc}$  is shown in Table 3.9. From this table, the  $p$ -value returned from the Lilliefors test is less than 0.05, and therefore the test for the normality of the residuals is not passed. Examining the QQ-plot and the plot of the residuals versus the fitted value of Figure 3.30, the residuals show a constant variance and a near normal distribution, apart from one outlying test that may have a strong influence on the results of the Lilliefors test. A similar correlation between the residuals and the axial load ratio found in the regression analysis of  $\theta_p$  is also found for  $\theta_{pc}$ , as seen in Figure 3.31. The same conclusion with respect to this issue is made as above by placing a limit on the maximum values that can be obtained through observations based on experimental data. Given the relatively high  $R^2 = 0.907$  that is obtained for the regression on  $\theta_{pc}$  it is concluded that the equation reasonably well predicts the component response.

Once again, the equation for  $a = M_{max}/M_y^*$  shows a similar correlation between the residuals and the axial load ratio as suggested a  $p$ -value less than 0.05 returned from the Durbin-Watson test as shown in Table 3.10. From the QQ-plot and the histogram of residuals in Figure 3.32 it is concluded that the residuals are not normally distributed, however they are close, as supported by  $p = 0.046$  from the Lilliefors's test that is very near to 0.05. In addition to the correlation of the residuals with the axial load ratio, it is seen from Figure 3.33 that there is an increase in the variance of the residuals at 50% axial load ratio, therefore it is expected that the equation may provide less accuracy at higher axial load ratios. An  $R^2 = 0.764$  indicates that the equation will provide a reasonably good prediction of the true component response.

### **First-cycle envelope curve**

This component model is based off experimental data taken from the first-cycle envelope of wide-flange columns, it is intended to be used for nonlinear static analyses. The parameters

of this component model are given with reference to Figure 3.1.

1. Elastic stiffness,  $K_e$ : This quantity is given in terms of the effective elastic flexural stiffness,  $K_e$ . The column hinge may be modelled with a finite flexural stiffness, or as rigid-plastic based on Equations 3.4 and 3.5
2. Effective yield strength,  $Q_y^*$ : For steel columns this quantity refers to the effective yield moment,  $M_y^*$ , and can be computed using Equation 3.32 for steel columns under cyclic loading.
3. Peak strength,  $Q_u^*$ : For steel columns this quantity refers to the maximum yield moment,  $M_{max}^*$ . The capping, or maximum moment of the steel column under cyclic loading can be computed using the Equation 3.33. For cyclic loading, the hardening coefficient  $a^*$  should be calculated using Equation 3.39

$$a^* = 9.5 (h/t_w)^{-0.4} (L_b/r_y)^{-0.16} (1 - P_g/P_{ye})^{0.2} \geq 1.0 \text{ (COV} = 0.07, R^2 = 0.87), \quad (3.39)$$

As well, if  $P_g/P_{ye} > 0.3$  or if  $h/t_w < 15$  then  $a \leq 1.3$ . The local slenderness of the column is represented through the web length-to-depth ratio of the steel column,  $h/t_w$ ; and the global slenderness of the column is represented through the ratio of the unbraced length to radius of gyration,  $L_b/r_y$ ; and  $P_g/P_{ye}$  is the ratio of the applied gravity load to the axial yield strength of the column.

4. Plastic deformation up to peak strength of the first-cycle envelope,  $\Delta_p^*$ : For steel columns this quantity refers to the pre-peak plastic rotation,  $\theta_p^*$ , and can be calculated using Equation 3.40

$$\theta_p^* = 15 (h/t_w)^{-1.6} (L_b/r_y)^{-0.3} (1 - P_g/P_{ye})^{2.3} \leq 0.10 \text{ (COV} = 0.31, R^2 = 0.89), \quad (3.40)$$

5. Plastic deformation of the descending portion of the first-cycle envelope,  $\Delta_{pe}^*$ : For steel

columns this quantity refers to the post-peak plastic rotation,  $\theta_{pc}^*$ , and can be calculated using Equation 3.41

$$\theta_{pc}^* = 14 (h/t_w)^{-0.8} (L_b/r_y)^{-0.5} (1 - P_g/P_{ye})^{3.2} \leq 0.10 \text{ (COV} = 0.42, R^2 = 0.78), \quad (3.41)$$

6. Residual strength,  $Q_r^*$ : The residual moment,  $M_r^*$ , for columns can be computed from Equation 3.42

$$M_r^* = (0.4 - 0.4P_g/P_{ye}) M_y^* \text{ (COV} = 0.35), \quad (3.42)$$

7. Ultimate deformation,  $\Delta_{ult}^*$ : For steel columns with flexural hinging this quantity represents the ultimate rotation capacity,  $\theta_{ult}^*$  that is likely to be controlled by loss of the column axial carrying capacity. With reference to the first-cycle envelope curve it is recommended to take

$$\theta_{ult}^* = 0.08 (1 - 0.6P_g/P_{ye}) \text{ radians (COV} = 0.51), \quad (3.43)$$

The range of sections for which the equations are applicable are:

$$3.71 \leq h/t_w \leq 57.5$$

$$1.82 \leq b_f/2t_f \leq 8.52$$

$$38.4 \leq L_b/r_y \leq 120$$

$$0 \leq P_g/P_{ye} \leq 0.60$$

Steel wide flange columns under compressive axial load ratios  $P_g/P_{ye} > 0.60$  that have  $h/t_w > 43$  and  $KL_b/r_y > 120$  must be treated as force-controlled elements as per ASCE-41-13 (ASCE, 2014). Steel columns utilizing stocky cross-sections that experience gravity loads  $P_g > 0.60P_{ye}$  have a finite plastic deformation capacity, which is not zero. However, columns

with gravity loads over  $0.6P_{ye}$  may be under designed for gravity loads (Bech et al., 2015), therefore, column yielding should be restricted in these cases.

### Discussion of statistics for the first-cycle envelope

The diagnostic plots for the regression on  $\theta_p^*$  are shown in Figure 3.34. Table 3.11 provides the statistics for the regression of  $\theta_p^*$ . For the equation for the pre-peak plastic rotation, the Durbin-Watson test is not passed, as the  $p$ -value returned is less than 0.05. From an investigation of Figure 3.35, there is a correlation between the axial load ratio and the residuals, similar to what was observed in the regression equations developed based on the monotonic backbone curve. A similar strategy of splitting the equations at  $P_g/P_{ye} = 0.20$  was explored. However, for the modified equations, the correlation between the residuals and predictors is still statistically significant in certain cases. Therefore, limits are placed on the maximum values based on observations from experimental data in order to limit the maximum values that may be obtained from the equations. This limit can be justified, since as shown in Figure 3.34b for values of  $\theta_p^*$  near 0.05 the equation overpredicts the test data (i.e., data points are below the red line).

Despite the aforementioned issues, with reference to  $R^2 = 0.886$ , as shown in Table 3.11, the equation for  $\theta_p^*$  can be expected to provide a reasonably good prediction of the component response. Since the Lilliefors test returned  $p > 0.05$ , and supported from an inspection of the QQ-plot and the histogram of residuals shown in Figure 3.34, it is concluded that the residuals are normally distributed.

The regression equation for the post-peak plastic rotation,  $\theta_{pc}^*$ , shown in Table 3.12. From Table 3.12,  $p > 0.05$  returned from the Durbin-Watson test indicates that there is no correlation between the residuals and the predictors. From an inspection of the plot of residuals versus predicted values from Figure 3.36, it is observed that there is a non-constant variance in the residuals. This observation is supported by the plot of the fitted values versus test data, where the increase in variance can be observed as  $\theta_{pc}^*$  increases. For this reason a

limit on the maximum value of  $\theta_{pc}^*$  based on an analysis of the test data is provided, such that the values obtained from the equations are not unreasonably large. The residuals follow a normal distribution based on the results of the Lilliefors test shown in the same table, and an evaluation of the QQ-plot and the histogram of residuals as shown in Figure 3.36. Given the  $R^2 = 0.775$  obtained from the regression analysis, it can be concluded that this equation will provide a reasonably well prediction of the post-capping plastic rotation.

The diagnostic plots for the regression on  $a^* = M_{max}^*/M_y^*$  are shown in Figure 3.37. Based on the results of the Durbin-Watson test (i.e.,  $p < 0.05$ ), as shown in Table 3.13, the regression on  $a^* = M_{max}^*/M_y^*$  once again shows a correlation between the residuals and the predictors. This conclusion is supported by inspection of the residuals in Figure 3.38. A similar strategy of splitting the equations at  $20\%P_g/P_{ye}$  was explored, however again the equation is kept in its current format. A limit is placed on the minimum and maximum acceptable hardening ratios in accordance with the expected physical and experimental behaviour. Apart from the correlation of the residuals, the criteria for homoskedascity is satisfied based on an inspection of the plot of residuals versus fitted values (Figure 3.37a); and the normality of the residuals is satisfied for this equation based on an inspection of the QQ-plot and the histogram of residuals (Figure 3.37c and d). Based on the  $R^2 = 0.865$ , the equation will provide a reasonably accurate prediction of  $a^* = M_{max}^*/M_y^*$ .

### Comparison with existing modelling options

The following is a discussion for steel wide-flange columns based on a comparison between experimental data, the ASCE-41-13 provisions, and the proposed recommendations. Figures 3.39 and 3.40 show a comparison between the nonlinear component models and experimental data for columns subjected to monotonic lateral drift demands and reversed-cyclic drift demands, respectively. For the cases shown in these figures, the columns were subjected to constant axial force demands as indicated. The main observations are as follows:

- As seen in Figure 3.39 for the component model based on the monotonic backbone and

test data from steel columns subjected to monotonic loading, the proposed component models represent fairly well the experimental data, including the response in the post-peak range. These observations are made regardless of the applied axial load ratio. The observed differences between the predicted effective yield strength and the experimental data is due the difference between the expected and measured yield stress, and how the proposed component model only approximates the effects of kinematic hardening on the monotonic response of steel columns.

- From Figures 3.40a to 3.40d, the proposed first-cycle envelope curve represents relatively well the measured response of the steel columns regardless of the cross-sectional local slenderness ratio and the applied compressive axial load ratio. Based on the same figures, the ASCE-41-13 component model overestimates by a considerable amount the pre-peak plastic deformation of steel columns subjected to  $P_g/P_{ye} = 0.20$  and  $0.30$ , as shown in Figure 3.40. This is attributed to the fact that the ASCE-41 component model does not capture the cross-section local slenderness effects on the parameter “a”. In addition, the ASCE-41 component model does not directly capture the effect of global slenderness ratio on the pre-peak plastic deformation parameter “a”. This is only done through the calculation of  $P_{cr}$  but this load is not relevant for triggering global-out-of-plane instabilities associated with lateral torsional buckling of a steel column under lateral loading.
- From Figures 3.39b and 3.40d, steel columns that utilize cross sections within the limits of highly ductile members as per AISC-341-10 (AISC, 2010a) and subjected to  $P_g/P_{ye} = 0.50$  (i.e.,  $P/P_{cr} > 0.50$ ) have a appreciable plastic deformation capacity that is significantly underestimated by the ASCE-41-13 component model. ASCE-41-13 provisions specify that columns with  $P/P_{cr} > 0.50$  as force-controlled elements. However, experimental evidence (Suzuki and Lignos, 2015; Lignos et al., 2016) confirmed with detailed finite element studies (Elkady and Lignos, 2015a) indicates that they should be treated as deformation-controlled elements.

A table of computed component model parameters based on the monotonic backbone curve for wide-flange steel columns is given in Table 3.14, and in Table 3.15 for the parameters based on the first-cycle envelope curve. These tables include both the computed plastic rotation values, as well as the hardening ratios. The values are calculated for axial load ratios of 5%, 20%, and 50%, and the main observations are as follows:

- The pre-peak plastic deformation  $\theta_p^*$  of the first-cycle envelope curve of wide-flange columns is, on average, two to three times smaller than the corresponding value of the idealized monotonic curve. This difference decreases while the applied compressive axial load increases, this observation is in-line with the observation that the cyclic response is less dependent on the axial load ratio made in Section 3.4.1.
- The ratio between the mean value of the total plastic deformation of a monotonic curve with respect to that of a first-cycle envelope curve for the same cross-section is, on average, 2.8. This value is consistent with what is currently reported in Chapter 16 of ASCE 7-16 (ASCE, 2016) for deformation-controlled elements (i.e., recommended value is 3.0).
- From Tables 3.14 and 3.15, steel columns with  $L_b/r_y = 80$  that utilize cross-sections near the current compactness limits for highly ductile member as per AISC-341-10 (AISC, 2010a) have a finite plastic deformation capacity even when they are subjected to  $P_g/P_{ye} = 0.50$  (i.e.,  $P/P_{cr} > 0.50$ ). This indicates that columns subjected to axial load ratios in that range should not be treated as force-controlled elements as currently suggested by ASCE-41-13 (ASCE, 2014). This agrees with recent findings of the ASCE-41 steel subcommittee Bech et al. (2015).
- From Figures 3.41 and 3.42, stocky columns (i.e.,  $h/tw < 15$ ) have a relative large plastic deformation capacity regardless of the applied axial compressive load ratio. This is consistent with prior experimental data by Newell and Uang (2006).
- From Figures 3.41 and 3.42, the scatter in the computed pre- and post-peak plastic deformation capacity of steel columns becomes smaller for higher levels of axial com-

pressive load. This indicates that the higher the applied axial load ratio the smaller the influence of the cross-sectional slenderness on the column behaviour. This is in-line with the observations made in Section 3.4.1 with regards to the experimental data.

### **Bidirectional loading**

The following recommendations for columns subjected to combined axial load and bidirectional lateral drift demands are provided based on the recommendations in ATC-114 for steel columns in MRFs (ATC, 2016). Figure 3.43 shows a comparison of the first-cycle envelope curves of nominally identical steel column specimens (i.e., W24X146 and W24X84) that were subjected to a constant compressive axial load coupled with symmetric unidirectional and bidirectional lateral loading as discussed in Section 2.2.3. From this figure, the pre- and post-peak plastic deformation of these columns was nearly identical in both cases. Therefore, the proposed modelling recommendations for nonlinear modelling of columns subjected to unidirectional loading may be used to assess the nonlinear behaviour of wide-flange columns subjected to bidirectional lateral loading.

### **End columns**

The following recommendations for end columns are the same as those provided in ATC-114 for steel columns in MRFs (ATC, 2016). End columns in steel moment-frame systems may experience large variations in their axial load demands due to the transient component coming from the dynamic overturning moment effects. Figure 3.44 shows the experimental data in terms of average first-cycle envelope curves from full-scale tests on steel columns subjected to varying axial load in addition to lateral drift demands. Figure 3.44a refers to a steel column that utilized a W14X233 cross section, with data from (Newell and Uang, 2006). The initially applied axial load ratio due to gravity in this case was  $P_g/P_{ye} = 0.15$ ; however, the applied axial load ratio varied from -0.15 to 0.75 during the test. Similarly, Figure 3.44b refers to a steel column that utilized a W16x89 cross section. The initial gravity offset was

$P_g/P_{ye} = 0.50$ . This load ratio varied from 0.25 to 0.75 throughout the lateral loading history, with data from Lignos et al. (2016).

Superimposed in the same figure are the predicted first-cycle envelope curves based on the nonlinear modelling recommendations discussed above by using the gravity offset  $P_g/P_{ye}$  as a reference axial load ratio in the predictive equations summarized in Section 2.2.3 and not the transient component as suggested by the ASCE-41-13 recommendations. This is also consistent with the recommendations discussed in Bech et al. (2015). From Figure 3.44, the proposed equations predict the first-cycle envelope of end columns fairly well regardless of the cross-sectional compactness ratio.

The effective and peak flexural strength of the column utilizing the W14x233 cross-section are underpredicted by about 25% as shown in Figure 3.44a. This is due to the fact that this cross-section is fairly stocky (i.e.,  $h/t_w = 10.7$ ,  $b_f/2t_f = 4.62$ ) and it did not buckle locally during the lateral loading history. Therefore, cyclic hardening was significant in this case. However, for more slender but still seismically compact cross-sections such as the one in Figure 3.44b (i.e., W16X89:  $h/t_w = 25.9$ ,  $b_f/2t_f = 5.92$ ) the predicted effective yield and peak strength of the steel column is fairly close to the one measured from the test. In this case, the formation of local buckling near the member base occurred early in the lateral loading history; therefore, the member did not harden cyclically by much.

From Figure 3.44, the ASCE-41 component model treats both members as force-controlled elements because the transient component of the axial load demand exceeds the  $P/P_{cr} = 0.50$  limit. From the same figure, it is evident that the same members can be treated as deformation-controlled elements even though they experience high axial load demands.

### 3.4.2 Hollow structural steel columns

#### Monotonic backbone curve

The monotonic backbone component model is taken from Lignos and Krawinkler (2009, 2010), and was modified such that the parameter  $F_{ye}$  was normalized by considering  $E/F_{ye}$ . For

details on the parameter trends see Lignos and Krawinkler (2009).

The parameters of this component model are with reference to Figure 3.1.

1. Elastic stiffness,  $K_e$ : This quantity is given in terms of the effective elastic flexural stiffness,  $K_e$ . The column hinge may be modelled with a finite flexural stiffness, or as rigid-plastic based on Equations 3.4 and 3.5
2. Effective yield strength,  $Q_y^*$ : For steel HSS columns this quantity refers to the effective yield moment,  $M_y^*$ , and can be computed using Equation 3.32 for steel columns under monotonic loading.
3. Peak strength,  $Q_u$ : For steel HSS columns this quantity refers to the maximum flexural moment of the section under monotonic loading adjusted for the effects of cyclic hardening,  $M_{max}$ , and can be computed using the hardening ratio,  $a$ , that can be computed according to Equation 3.44. The peak moment is defined as

$$M_{max} = a * M_y^*, \quad (3.44)$$

where the hardening ratio,  $a$ , is calculated as

$$a = 0.04 (D/t)^{-0.3} (1 - P_g/P_{ye})^{1.3} (E/F_{ye})^{0.75} \geq 1.0, \quad (\text{COV} = 0.23, R^2 = 0.66), \quad (3.45)$$

where  $D/t$  is the slenderness ratio of the HSS column, and  $P_g/P_{ye}$  is the ratio of the applied gravity load on the column to the expected axial yield strength of the column, and  $E/F_{ye}$  is the ratio of elastic modulus to the expected yield stress of the steel HSS column.  $a$  should always be less than 1.3.

4. Plastic deformation up to the peak strength,  $\Delta_p$ : For steel columns this quantity refers to the the pre-peak plastic rotation,  $\theta_p$ , the pre-peak plastic rotation can be determined

according to the following equation

$$\theta_p = 0.3 (D/t)^{-0.95} (1 - P/P_{ye})^{1.1} (E/F_{ye})^{0.1} \quad (\text{COV} = 0.26, R^2 = 0.70). \quad (3.46)$$

5. Plastic deformation of the descending portion of the monotonic backbone,  $\Delta_{pc}$ : For steel columns this quantity refers to the the pre-peak plastic rotation,  $\theta_{pc}$ , the post-peak plastic rotation should be determined using the following equation

$$\theta_{pc} = 5.4 (D/t)^{-1.2} (1 - P/P_{ye})^{3.0} (E/F_{ye})^{0.14} \quad (\text{COV} = 0.35, R^2 = 0.70). \quad (3.47)$$

6. Residual strength,  $Q_r$ : This quantity is taken as the residual moment for HSS columns,  $M_r$ , and can be computed from Equation 3.48

$$M_r = (0.5 - 0.6P_g/P_{ye}) M_y^* \geq 0 \quad (\text{COV} = 0.34). \quad (3.48)$$

7. Ultimate deformation,  $\Delta_{ult}$ : This quantity is taken as the ultimate rotation for HSS columns,  $\theta_{ult}$ , the ultimate deformation for HSS steel columns can be taken as the value from Equation 3.49 regardless of section size

$$\theta_u = 0.10 \text{ radians} \quad (\text{COV} = 0.45). \quad (3.49)$$

This value is based on a database of steel HSS columns from Lignos and Krawinkler (2010, 2012).

8. Reference cumulative plastic rotation,  $\Lambda$ : This parameter is provided for use of explicit modelling of cyclic deterioration based off of the modified IMK deterioration model.

$$\Lambda = 860 (D/t)^{-2.49} (1 - P/P_{ye})^{3.51} (E/F_{ye})^{0.20} \quad (R^2 = 0.84). \quad (3.50)$$

The range of sections for which the equations are applicable are:

$$20 \leq D/t \leq 40$$

$$0 \leq P_g/P_{ye} \leq 0.60$$

$$400.0 \leq E/F_y \leq 725.0$$

Furthermore, hollow structural steel columns under compressive axial load ratios,  $P_g/P_{ye} > 0.60$  and with  $D/t > 33$  must be treated as force-controlled elements per ASCE 41-13 (ASCE, 2014).

### Parameter trends for the first-cycle envelope

The database for the regression analysis of first-cycle envelopes for square HSS columns is developed from over 100 experimental tests on square HSS columns from Lignos and Krawinkler (2010, 2012).

Given the symmetry of square HSS the only geometric property that is found to be significant is the HSS depth-to-thickness ratio,  $D/t$ . The dependency of the response parameters on the yield stress ( $\sqrt{E/F_{ye}}$ ) is explored, as well as the axial load ratio,  $P_g/P_{ye}$ .

Figure 3.45 shows the trends on the pre-peak plastic rotation,  $\theta_p^*$ . From these figures we see that  $\theta_p^*$  has a relatively strong negative relation on the depth-to-thickness ratio of the HSS,  $D/t$ . There is a less substantial positive relation between  $\theta_{pc}^*$  and  $\sqrt{E/F_{ye}}$ , and a comparatively weak relation between the  $P_g/P_{ye}$  and  $\theta_{pc}^*$ . From this it is concluded that the pre-peak plastic rotation is more dependant on the depth-to-thickness ratio, versus the applied axial load.

The trends on  $\theta_{pc}^*$  can be seen in Figure 3.46. There is increased scatter in the data for the post-peak plastic rotation due to the use of an extrapolation to predict the ultimate rotation. As well there are fewer tests considered in the post-peak range, as many tests did not show sufficient post-peak plastic deformation to be considered in this range. From the

plot of  $\theta_{pc}^*$  versus  $P_g/P_{ye}$  shown in Figure 3.46, we can see that the post-peak plastic rotation is heavily dependent on the axial load ratio. Visually, there are no obvious trends in  $\theta_{pc}^*$  with either  $D/t$  or  $\sqrt{E/F_{ye}}$ . However, from the trend lines plotted based on each parameter a negative relation for both of these parameters can be seen.

From the evaluation of the trends on the hardening ratio,  $M_{max}^*/M_y^*$  shown in Figure 3.47, there are relatively higher levels of hardening generally observed in HSS columns with low local slenderness, low axial load ratios, and lower yield stress steels. This is due to the larger pre-peak plastic rotation that is expected in these cases, therefore leading to a higher hardening ratio. Generally,  $D/t$  and  $P_g/P_{ye}$  have similar levels of influence on  $a^*$ . This can be seen in Figure 3.47, where a column with  $D/t = 35$  (i.e., relatively slender cross-section), only subjected to  $P_g/P_{ye} = 0.3$  exhibits relatively lower levels of hardening. Similarly, columns with  $D/t$  near 15 (i.e., relatively stocky cross-section) subjected to  $P_g/P_{ye} = 0.4$  will likewise exhibit relatively lower levels of hardening.

### First-cycle envelope curve

The parameters of this component model are given with reference to Figure 3.1.

1. Elastic stiffness,  $K_e$ : This quantity is given in terms of the effective elastic flexural stiffness,  $K_e$ . The column hinge may be modelled with a finite flexural stiffness, or as rigid-plastic based on Equations 3.4 and 3.5
2. Effective yield strength,  $Q_y^*$ : For steel HSS columns this quantity refers to the effective yield moment,  $M_y^*$ , and can be computed using Equation 3.32 for steel columns under cyclic loading.
3. Peak strength,  $Q_u^*$ : For steel HSS columns this quantity refers to the maximum flexural moment of the section under monotonic loading adjusted for the effects of cyclic hardening,  $M_{max}^*$ , and can be computed using the hardening ratio,  $a^*$ , that can be computed according to Equation 3.44.

4. Plastic deformation up to the peak strength,  $\Delta_p^*$ : For steel columns this quantity refers to the the pre-peak plastic rotation,  $\theta_p^*$ , the pre-peak plastic deformation can be calculated using Equation 3.51

$$\theta_p^* = 0.1 (D/t)^{-1.1} (1 - P_g/P_{ye})^{1.4} (E/F_{ye})^{0.3} \quad (\text{COV} = 0.53, R^2 = 0.53). \quad (3.51)$$

5. Plastic deformation of the descending portion of the monotonic backbone,  $\Delta_{pc}^*$ : For HSS columns this quantity refers to the the pre-peak plastic rotation,  $\theta_{pc}^*$ , the post-peak plastic deformation can be computed using Equation 3.52

$$\theta_{pc}^* = 2.8 (D/t)^{-1.3} (1 - P_g/P_{ye})^{2.6} (E/F_{ye})^{0.17} \quad (\text{COV} = 0.27, R^2 = 0.71). \quad (3.52)$$

6. Residual strength,  $Q_r^*$ : This quantity is taken as the residual moment for HSS columns,  $M_r^*$ , and can be computed from Equation 3.53.

$$M_r^* = (0.4 - 0.6P_g/P_{ye}) M_y^* \geq 0 \quad (\text{COV} = 0.40). \quad (3.53)$$

7. Ultimate deformation,  $\Delta_{ult}^*$ : This quantity is taken as the ultimate rotation for HSS columns,  $\theta_{ult}^*$ , the ultimate deformation for HSS steel columns can be taken as the value from Equation 3.54 regardless of section size.

$$\theta_{ult}^* = 0.08 (1 - P_g/P_{ye}) \text{ radians} \quad (\text{COV} = 0.50). \quad (3.54)$$

This value is based on a database of steel HSS columns from Lignos and Krawinkler (2010, 2012).

The range of sections for which the equations are applicable are:

$$20 \leq D/t \leq 40$$

$$0 \leq P_g/P_{ye} \leq 0.60$$

$$400.0 \leq E/F_{ye} \leq 725.0$$

Furthermore, hollow structural steel columns under compressive axial load ratios,  $P_g/P_{ye} > 0.60$  and with  $D/t > 33$  must be treated as force-controlled elements per ASCE 41-13 (ASCE, 2014).

### Discussion of statistics

For all the equations the regression is carried out using  $\sqrt{E/F_{ye}}$ . However for the component models, the square-root was simplified by modifying the final exponent.

The diagnostic plots for the regression analysis of  $\theta_p^*$  for HSS columns is shown in Figure 3.48, and the table of statistical values is provided in Table 3.16. For  $\theta_p^*$  the result of the Durbin-Watson test provided in Table 3.16 would suggest that there is correlation between the predictors and the residuals (i.e.,  $p < 0.05$ ). However from an inspection of the plots of the residuals versus the predictors shown in Figure 3.49, no clear trend is observed. Therefore it is concluded that correlation between the residuals and predictors is not a significant issue for this equation. Since the Lilliefors test returned  $p > 0.05$  the residuals are normally distributed, this result is supported from an inspection of the QQ-plot and the histogram of residuals in Figure 3.49. Furthermore, from an inspection of the plot of the residuals versus the fitted values in this same figure, the residuals show a constant variance, and thus the criteria for the Gauss-Markov hypothesis are fulfilled. Given that  $R^2 = 0.504$ , the equations are expected provide a reasonable estimation of the true component response for  $\theta_p^*$ .

For the  $\theta_{pc}^*$  equation, it is found that the  $\sqrt{E/F_{ye}}$  term was not significant and may therefore be excluded from the equation in the principle of model parsimony. From the results

of the Durbin-Watson test and the Lilliefors test shown in Table 3.17 it is concluded that the residuals show no correlation with the predictors, and are normally distributed (i.e.,  $p > 0.05$  in both cases). This findings are supported by an inspection of the plots of the residuals versus fitted values and the QQ-plot, as shown in Figure 3.50. Given that  $R^2 = 0.701$  and  $COV = 0.242$ , the equations will provide a reasonably good estimation of the true component response for  $\theta_{pc}^*$ .

The regression equation for  $a^* = M_{max}^*/M_y^*$  is seen to have normally distributed residuals based on a  $p > 0.05$  from the Lilliefors test provided in Table 3.18. This is reinforced by an inspection of the QQ-plot and the histogram of residuals in Figure 3.51. Furthermore, the residuals show a constant variance as seen from the plot of the residuals versus fitted values in Figure 3.51. Since  $p > 0.05$  from the Durbin-Watson test, this implies that there is no correlation of the residuals. Given that  $R^2 = 0.134$  and  $COV = 0.084$ , the equation for  $a^* = M_{max}^*/M_y^*$  for HSS columns is expected to provide limited accuracy with respect to the prediction of hardening ratio, however it represents the best prediction given available test data. This is due in part to a lack of experimental data in which there is an appreciable level of hardening for HSS columns.

### **Comparison with experimental data**

This section provides illustrative comparisons of the proposed nonlinear modelling recommendations for steel HSS columns. The comparison is done with available experimental data. Figure 3.52 includes the deduced column end moment-chord rotation relation for a range of HSS steel columns subjected to reversed cyclic lateral loading. In all cases the compressive axial load was kept constant throughout the loading history. In addition, Figure 3.53 shows the trends of pre- and post-peak plastic deformations with respect to the cross-section local slenderness ratio,  $D/t$  for steel columns utilizing HSS cross-sections. Tables 3.19 and 3.20 provide estimates of the plastic deformation parameters and hardening ratio that define the monotonic backbone and the first-cycle envelope curves, respectively,

for selective HSS columns. These columns are subjected to  $P_g/P_{ye} = 0.05, 0.20, 0.50$ . The following observations can be made:

- From Figure 3.52, the proposed modelling recommendations capture relatively well the pre- and post-peak plastic deformation capacities,  $\theta_p^*$  and  $\theta_{pc}^*$ , respectively, for both slender (i.e., see Figure 3.52a) and highly compact (see Figure 3.52b) HSS columns.
- From Figure 3.52 and Tables 3.19 and 3.20, slender HSS columns ( $D/t > 27$  or so) do not seem to harden cyclically for axial load ratios  $P_g/P_{ye} > 0.20$ . This is attributed to the early occurrence of local buckling. For highly ductile HSS members (see Figure 3.52b), the amount of hardening is appreciable.
- The ratio between the mean value of the total plastic deformation  $\theta_p$  with respect to  $\theta_p^*$  is, on average, 2.0. This value is smaller than what is currently reported in Chapter 16 of ASCE 7-16 (ASCE, 2016) for deformation-controlled elements (i.e., recommended value is 3.0).
- From Figure 3.53a, the influence of  $D/t$  ratio on the pre-buckling behaviour of HSS columns is significant even in cases that the applied compressive axial load is fairly large (i.e.,  $P_g/P_{ye} > 0.20$ ). On the other hand, from Figure 3.53b and Tables 3.19 and 3.15, the applied  $P_g/P_{ye}$  dominates the post-buckling behaviour of HSS columns.

### 3.5 Beam-to-column joint panel zone

Due to the observed hysteretic behaviour of beam-to-column joint panel zones, a tri-linear non-deteriorating component model is recommended to represent the component response. The component model is non-deteriorating due to shear buckling being a stable failure mechanism (Krawinkler, 1978).

### 3.5.1 Bare steel beam-to-column joint panel zones

The component model recommended for ATC-114 is the Krawinkler parallelogram model (Krawinkler et al., 1971; Krawinkler, 1978; Gupta and Krawinkler, 1999), and it is intended to be used for both nonlinear static and response history analysis procedures. The parameters of the component model are given with reference to the component model shown in Figure 3.54a and 3.1.

1. Yield strength,  $Q_y$ : For beam-to-column joint panel zones this quantity refers to the first yield moment,  $M_y$ . The first yield moment corresponds to the moment that shear yielding is initiated in the panel zone volume, therefore Equation 3.55 should be used to calculate  $M_y$

$$M_y = V_y d_b. \quad (3.55)$$

The yield shear strength of the beam-to-column joint panel zone can be estimated as

$$V_y = 0.60 R_y F_y d_c t_p, \quad (3.56)$$

where  $F_y$  is the nominal yield stress of the column web;  $R_y$  is the yield ratio coefficient based on the steel material type, taken from Tables 9-1, 9-2, and 9-3 of ASCE-41-13 ASCE (2014);  $d_c$  is the column depth; and  $t_p$  is the thickness of the panel zone, including the thickness of the column web, as well as any doubler plates that may be present.

2. Yield deformation,  $\Delta_y$ : For beam-to-column joint panel zones this quantity refers to the yield distortion,  $\gamma_y$ . The yield distortion can be calculated as

$$\gamma_y = \frac{R_y F_y}{\sqrt{3}G}, \quad (3.57)$$

where  $G$  is the shear modulus of the panel zone.

3. Plastic strength,  $Q_p$ : For beam-to-column joint panel zones this quantity refers to the

full plastic moment,  $M_p$ . The plastic moment corresponds to the moment at which yielding of the column flanges will occur, it can be calculated as

$$M_p = V_p d_b. \quad (3.58)$$

The full plastic shear strength,  $V_p$ , can be calculated according to

$$V_p = \begin{cases} 0.6R_y F_y d_c t_p \left(1 + \frac{3b_c t_{cf}^2}{d_b d_c t_p}\right) & P_r \leq 0.75P_c \\ 0.6R_y F_y d_c t_p \left(1 + \frac{3b_c t_{cf}^2}{d_b d_c t_p}\right) \left(1.9 - \frac{1.2P_r}{P_c}\right) & P_r > 0.75P_c, \end{cases} \quad (3.59)$$

where  $b_c$  is the width of the column flange,  $t_{cf}$  is the thickness of the column flange.  $P_r$  is the required compressive strength, and  $P_c$  is the available column axial strength per AISC 341-10 (AISC, 2010a).

4. Plastic deformation,  $\Delta_p$ : For beam-to-column joint panel zones this quantity refers to the plastic distortion,  $\gamma_p$ . Based on experimental observations from Gupta and Krawinkler (1999), the following relationship is proposed

$$\gamma_p = 4\gamma_y. \quad (3.60)$$

5. Strain hardening,  $\alpha$ : Based on work by Krawinkler et al. (1971); Krawinkler (1978) a strain hardening value of 3% is recommended. In recent studies (Suzuki and Lignos, 2015; Elkady and Lignos, 2014, 2015b) 1% strain hardening was found to be more appropriate. This matter deserves more attention in future research studies associated with the hysteretic behaviour of beam-to-column panel zone joints.

Figure 3.54b illustrates an example of the idealized tri-linear relation of a panel zone compared to experimental data from Engelhardt et al. (2000). From this figure it is apparent that the panel zone model provides a reasonable prediction of the experimental data.

### 3.5.2 Composite beam-to-column joint panel zones

To account for the presence of the slab on the beam-to-column joint panel zone, an adjustment is made based on the effective depth of the composite beam using the following equations. The following parameters are given with respect to Figure 3.54a. A definition of each of the properties under consideration is shown in Figure 3.55.

1. Yield strength,  $Q_y$ : the following yield strength should be used in lieu of the yield strength given in Equation 3.55

$$M_y^* = V_y d_{eff}, \quad (3.61)$$

where the effective depth,  $d_{eff}$ , is based on work by Kim and Engelhardt (2002).  $d_{eff}$  is based on whether or not the slab will be in tension or compression. For a negative bending moment, the slab is in tension and can the effective should be taken as

$$d_{eff}^- = d_b - t_f, \quad (3.62)$$

where  $d_b$  is the depth of the bare steel beam and  $t_f$  is the thickness of the beam flange. If the slab is in compression the effective depth can be taken as

$$d_{eff}^+ = d_b - d_{rib} + 0.5t_s - 0.5t_f, \quad (3.63)$$

where  $d_{rib}$  is the depth of the rib of the steel deck,  $t_s$  is the total depth of the concrete slab. It should be noted that for interior panel zones the behaviour will be symmetric, however for exterior panel zones the behaviour will be asymmetric since only one side of the panel zone will benefit from the composite slab effects.

2. Plastic strength,  $Q_p$ : the following plastic strength should be used in lieu of the plastic

strength given in Equation 3.58

$$M_p = V_p d_{eff}, \quad (3.64)$$

where  $d_{eff}$  is as defined above.

3. Strain hardening,  $\alpha$ : Based on work by Krawinkler et al. (1971); Krawinkler (1978) a strain hardening value of 3% is recommended.

## 3.6 Beams as a part of partially-restrained beam-to-column connections

The model based off of work done by Liu and Astaneh-Asl (2004), and is presented as in ATC-114 for steel MRFs (ATC, 2016). The component model is based off of the first-cycle envelope taken from a symmetric loading protocol on experimental test data of steel beams in single-plate shear-tab connections. This component model is intended to be used for all analyses due to limited test data available based off of the monotonic backbone. The idealized force-deformation relation can be seen in Figure 3.56, the following parameters are given with reference to this figure.

1. Peak positive and negative moment capacity,  $M_{max}^+$  and  $M_{max}^-$ : This parameter refers to the maximum flexural strength,  $M_{max}$ , for beams with single-plate shear-tab beam-to-column connections, in the positive and negative loading directions.

The maximum positive flexural strength is to be calculated using the following procedure

- (a) Use the governing limit state for a bolt in shear and first determine how many bolts should be allocated to carry the design shear load. These bolts should be assigned as shear elements, beginning with the top bolt.

- (b) Starting at the top of the bolt group, distribute the shear to the bolts based on their shear capacity.
- (c) Assume that the remaining bolt elements resist the bending moment. Based on the appropriate stress distribution, calculate the capacity,  $T$ , of the remaining bolt elements in tension for the governing failure mode.
- (d) Compute the compressive capacity of the concrete slab using

$$C = 0.85f'_c b_{eff} a, \quad (3.65)$$

where  $f'_c$  is the compressive strength of the concrete,  $b_{eff}$  is the bearing width against the column face, and  $a = r$  for the deck parallel to the shear connection, and  $a = 0.6r$  for the deck perpendicular to the shear connection. Where  $r$  is the depth of concrete above the top of the deck rib. For reference to the above parameters see Figure 3.57.

- (e) Use the following to determine the force resisted by the connection

$$F = \min (C, T) \quad (3.66)$$

- (f) By equilibrium of the axial forces,  $C = T$ . Recompute either  $C$  and solve for  $a$  using Equation 3.65, or  $T$  and solve for the number of bolts in tension required for equilibrium.
- (g) Use the resulting forces and distribution to find  $M_{max}^+$ .
- (h) To compute the negative bending capacity of a simple connection with composite slab,  $M_{max}^-$ , conservatively a bare steel connection should be assumed. Similar to  $M_{max}^+$ , a number of bolt-elements required to compute the gravity shear is calculated. The main difference compared to the computation of  $M_{max}^+$  is that the bolts in the middle section of the shear tab are now the ones carrying the shear.

2. Flexural strength,  $M_{slip}$ : This parameter refers to the flexural strength at which bolt slipping of the connection occurs,  $M_{slip}$ . Based on averages from test data (Liu and Astaneh-Asl, 2004) for composite connections use  $M_{slip} = 0.25M_{max}^+$ . Or for bare connections use  $M_{slip} = 0.55M_{max}^+$ .
3. Residual strength,  $M_{drop}$ : The residual flexural strength is associated with crushing of the concrete, therefore there is no drop for bare connections. For composite connections use the following value  $M_{drop} = 0.55M_{max}^+$ .
4. Plastic deformation up to peak strength of the first-cycle envelope,  $\theta_{max}$ : This parameter refers to the rotation at maximum strength,  $\theta_{max}$ , in either the positive or negative loading directions. For composite connections use the following values:

$$\theta_{max}^+ = 0.03 \text{ radians (COV} = 0.20) \quad (3.67)$$

$$\theta_{max}^- = 0.02 \text{ radians (COV} = 0.20) \quad (3.68)$$

For bare beams use instead:

$$\theta_{max}^+ = \theta_{max}^- = 0.05 \text{ radians (COV} = 0.35). \quad (3.69)$$

5. Deformation at bolt slip,  $\theta_{slip}$ : This parameter refers to the rotation at which bolt slipping occurs,  $\theta_{slip}$ . Use the value  $\theta_{slip} = 0.0042$  radians (COV = 0.30).
6. Ultimate deformation,  $\theta_{ult}$ : In many cases, beam failure occurs at larger rotations than the ones at which beam binding occurs.  $\theta_{ult}$ . This typically occurs at a chord rotation of 1.5% radians after beam binding occurs and it is sustained for about 4% radians till connection failure occurs Therefore take the ultimate rotation as  $\theta_{ult} = \theta_{bind} + 0.04$ .
7. Binding strength,  $M_{bind}^-$ : The binding moment,  $M_{bind}^-$ , is a result of binding of the concrete slab on the steel column face, and will occur when the connection experiences

a negative moment. Therefore use the following adjustment  $M_{bind}^- = 2.35M_{max}^-$ . To properly model the binding behaviour, a gap element is required to be modelled with  $M_{bind}^-$  and  $\theta_{ult}$  in addition to the element which carries the cyclic behaviour of the component. This effect can be simulated with two nonlinear spring elements combined in series as discussed in Elkady and Lignos (2015b) and shown in Figure 3.58. The first spring utilizes the envelope curve discussed above, and the second one utilizes a gap element.

## 3.7 Column splice connections

The component modelling recommendations for column splice connections are divided based on pre- and post-Northridge steel splice connections. The following recommendations were developed as a part of ATC-114 (ATC, 2016).

### 3.7.1 Pre-Northridge connections

Based on experimental data from Bruneau et al. (1987); Bruneau and Mahin (1991) the controlling stress of the pre-Northridge column splice connection is likely less than the specified design stress, due to the low toughness of the weld metal. Therefore, the modelling recommendations for pre-Northridge column splices is as follows:

1. Carry out the nonlinear analysis on the structure of interest.
2. Calculate the critical stress at each column splice connection, according to Equation 3.70.

The critical stress,  $\sigma_{cr}$  can be calculated as follows:

$$\sigma_{cr} = \frac{K_{IC}}{F(a_0/t_{f,u}) \cdot \sqrt{\pi a_0}} \leq F_{u,e} (1 - a_0/t_{f,u}) \leq F_{ye}, \quad (3.70)$$

where  $K_{IC}$  is the stress intensity factor for a mode I crack,  $a_0$  is the internal flaw created by the unfused portion of the flange,  $F_{u,e}$  is the least ultimate strength of the weld and

base metals,  $t_{f,u}$  is the thickness of the upper column flanges, and  $F_{ye}$  is the expected yield stress of the upper column flange. We have the following definition for  $F(a_0/t_{f,u})$ :

$$F(a_0/t_{f,u}) = (2.3 - 1.6a_0/t_{f,u}) (4.6a_0/t_{f,u}). \quad (3.71)$$

The recommended values for  $a_0/t_{f,u}$  and  $K_{IC}$  are:

$$a_0/t_{f,u} = 0.5 \quad (3.72)$$

$$K_{IC} = 107 \text{ ksi}\sqrt{\text{in.}} \quad (3.73)$$

3. Evaluate the stress at the splice due to the combination of: the maximum tensile stress acting on the weld at the splice location,  $\sigma_{tension}$ ; and the tensile stress on the weld from bending in both the strong- and weak-axes,  $\sigma_{bending,x/y}$ . The combination of these three stresses should be less than the critical stress, therefore we have

$$\sigma_{tension} + \sigma_{bending,x} + \sigma_{bending,y} \leq \sigma_{cr}. \quad (3.74)$$

### 3.7.2 Post-Northridge connections

Since column splice connections designed according to modern design and seismic provisions are specified with high fracture toughness, the connection should have adequate toughness to obtain their expected yield strength (AISC, 2005b). As the column splice connections are specified as force-controlled elements, inelastic deformations are not expected in these components. However, the forces and moments on the splice should be checked post-analysis in order to verify that the expected splice strength is not exceeded.

## 3.8 Column base connection hinge model

This section discusses how a first-cycle envelope curve can be constructed for column base connections as part of steel moment-resisting frame systems. The following component models were developed based on the work of Gomez (2010), Kanvinde et al. (2012), Grilli and Kanvinde (2015), Trautner et al. (2015). The proposed recommendations have been developed based on data from large- and full-scale experiments on exposed and embedded column base connections. Because of lack of monotonic tests, the input model parameters to compute a first-cycle envelope curve of a column base connection are only provided. These parameters are statistically calibrated to median values. The variability in the same parameters is described in terms of a COV, if available.

### 3.8.1 Exposed column base connections

#### Data analysis

The exposed column base component model is based off of work by Kanvinde et al. (2012), and the AISC Design Guide 1 (Fisher and Kloiber, 2006), while calibrated parameters are taken from test data (Gomez, 2010; Trautner et al., 2015; Picard and Beaulieu, 1985). The experiments consisted of column base connections subjected to symmetric loading protocols, therefore the following component model is based on the first-cycle envelope.

Due to the limited number of test specimens it was not suitable to develop regression equations to predict the component model parameters. Therefore the parameters and statistics for the exposed column base component model are based off of the mean of the available test data. Since the three predicted failure modes are ductile there is no differentiation made between the failure modes, and the mean of all failure modes is used to obtain an estimate of the ultimate rotation.

## Component model

The component model is based on the first-cycle envelope, and is intended to be used for all analyses due to the lack experimental data. The parameters of this component model are with reference to Figure 3.1.

1. Effective yield strength,  $Q_y^*$ : This parameter refers to the first yield moment is to be calculated using the rectangular stress block (RSB) approach, as suggested in AISC Design Guide 1 Fisher and Kloiber (2006) and Kanvinde et al. (2012).

First the critical eccentricity,  $e_{crit}$ , should be calculated using Equation 3.75,

$$e_{crit} = N/2 - P/(2Bf_{max}). \quad (3.75)$$

$P$  is the compressive axial load demand on the base plate,  $B$  is the base plate width, and  $N$  is the base plate length.  $f_{max}$  is the maximum bearing stress, and can be calculated using Equation 3.76 as follows

$$f_{max} = 0.85f'_c\sqrt{A_2/A_1} \leq 1.7f'_c. \quad (3.76)$$

In the above equation,  $f'_c$  is the concrete compressive stress,  $A_1$  is the area of the base plate, and  $A_2$  is the effective concrete area.

For  $e < e_{crit}$  the only possible failure mode is flexural yielding on the compressive side of the plate. However, for moments such that  $e > e_{crit}$  there are three possible failure modes: (a) flexural yielding of the compressive side of the plate,  $M_y^{pl,c}$ , (b) flexural yielding of the tension side of the plate,  $M_y^{pl,t}$  and (c) tensile yielding of the anchor rods,  $M_y^{rod}$ . The first yield moment will be taken as the minimum of the three moments according to Equation 3.77

$$M_y^* = \min (M_y^{pl,c}, M_y^{pl,t}, M_y^{rod}). \quad (3.77)$$

The two situations of  $e < e_{crit}$  and  $e > e_{crit}$  are shown in Figure 3.59.

2. Yield deformation,  $\Delta_y$ : This parameter refers to the rotation at first yield of the plate,  $\theta_y$ , and is used to estimate the effective elastic stiffness of the exposed column base,  $K_e$ . The rotation at first yield is found by summing the contributions of the four deformation mechanisms: flexural yielding on both the compressive and tension sides, axial yielding of the anchor rods, and the deformation of the concrete.

First, the deflection of the anchor rods may be calculated using Equation 3.78

$$\delta_{rod} = (T_{rod}L_{total}^{rod}) / (A_{rod}E_{rod}), \quad (3.78)$$

where we can find the tension in the rod,  $T_{rod}$ , through Equation 3.79

$$\begin{aligned} T_{rod} &= T/2 \\ &= 1/2f_{max}B \left( (N - g) - \sqrt{(N - g)^2 - \frac{2(M + P(N/2 - g))}{f_{max}B}} \right) - P \end{aligned} \quad (3.79)$$

$L_{total}^{rod}$  is the total length of the anchor rods from top of base plate to the nut-washer assembly at the bottom; and  $A_{rod}$ ,  $E_{rod}$  are the gross area and modulus of elasticity of the anchor rods.

The deflection on the tension side of the plate can be calculated according to Equation 3.80

$$\delta_{plate}^{tension} = (TL_{tension}^3/3E_{plate}I_{plate}) + (TL_{tension}/A_{plate}^S G_{plate}), \quad (3.80)$$

the moment of inertia of the plate,  $I_{plate}$ , and the shear area,  $A_{plate}^S$ , can be calculated

as

$$I_{plate} = Bt_p^3/12 \quad (3.81)$$

$$A_{plate}^S = (5/6)Bt_p. \quad (3.82)$$

In the above equations  $L_{tension}$  is the distance between the edge of the column flange and the centreline anchor rod, as shown in Figure 3.60, and  $E_{plate}, G_{plate}$  are the modulus of elasticity and shear modulus of the base plate, respectively.  $T$  is force in the anchor rods.

The deflection on the compressive side of the plate can be calculated according to Equation 3.83 if  $Y \geq m$

$$\delta_{plate}^{compression} = f_{max}B \left( \frac{M^4}{8E_{plate}I_{plate}} + \frac{m^2}{2A_{plate}^S G_{plate}} \right), \quad (3.83)$$

or Equation 3.84 if  $Y < m$

$$\begin{aligned} \delta_{plate}^{compression} = & \frac{f_{max}B}{8E_{plate}I_{plate}} (m^4 - 1/3(m - Y)^3(3m + Y)) \\ & + \frac{f_{max}BY}{A_{plate}^S G_{plate}} (m - Y + Y^2/2). \end{aligned} \quad (3.84)$$

$Y$  is the length of the stress block, and can be calculated according to Equation 3.85,

$$Y = \begin{cases} N - 2M/P & \text{if } e \leq e_{crit} \\ (N - g) - \sqrt{(N - g)^2 - \frac{2(M+P(N/2-g))}{f_{max}B}} & \text{if } e > e_{crit} \end{cases} \quad (3.85)$$

$M$  is the moment demand in the column base, and in the above equations the parameters are as defined in Figures 3.59 and 3.60  $m$  is flap length,  $g$  is the base plate edge distance.

Finally, the concrete deformation can be found using Equation 3.86

$$\delta_{concrete} = \frac{f_{max}}{E_{concrete}} d_{footing}, \quad (3.86)$$

where the modulus of elasticity of the concrete is  $E_{concrete}$ , and  $d_{footing}$  is the depth of the footing. For  $f'_c$  in ksi,  $E_{concrete} = 4700\sqrt{f'_c}$ .

Now using all four deformation components, the rotation of the plate at first yield can be calculated using Equation 3.87

$$\theta_y^* = (\delta_{rod} + \delta_{plate}^{tension} + \delta_{plate}^{compression} + \delta_{concrete}) / (s + N/2). \quad (3.87)$$

Where  $s$  is the base plate edge distance.

The effective elastic flexural stiffness can be found using Equation 3.88

$$K_e = M_y^* / \theta_y^*. \quad (3.88)$$

3. Peak strength,  $Q_u^*$ : This parameter represents the maximum flexural strength of the exposed base plate,  $M_{max}^*$ . The maximum moment depends on the yield mechanism of the plate, if the yield mechanism is either axial yielding of the anchor rods or flexural yielding on the tension side of the plate there is no increase in strength. Only in the case of flexural yielding on the compressive side of the plate would we expect an increase in the flexural strength of the connection. Therefore, we take the maximum strength as given in Equation 3.89

$$M_{max}^* = \min(M_y^{rod}, M_y^{plate,ten}) \quad (\text{COV} = 0.03). \quad (3.89)$$

The COV is calculated based off of a comparison with test data from Gomez (2010).

4. Plastic deformation up to the peak strength of the first-cycle envelope,  $\Delta_p^*$ : The pre-peak

plastic rotation was found by taking the mean value from test data. Use the value given in Equation 3.90

$$\theta_p^* = 0.065 \text{ radians (COV} = 0.42\text{)}. \quad (3.90)$$

A comparison with the experimental data can be seen in Figure 3.61. From the comparison with the test data we can see that the proposed component model provides a reasonable approximation of the exposed column base connection moment-rotation response. In the case of yielding of the compressive side of the plate as the first yield mechanism, as seen in Figures 3.61a and 3.61b, the rate of hardening up to the peak flexural strength is much higher in the test data. Therefore, the component response is generally under predicted until the ultimate deformation is reached. Thus if base plate yielding is allowed, the moment demands at the base of the column could be under estimated. Since no parameters are provided to estimate the deterioration in the stiffness, the pinched hysteresis is not captured in the current component model.

Very recently, Rodas et al. (2016) developed a hysteretic model to characterise the cyclic behaviour of exposed column base connections, for a further discussion of this model see Section 2.3.5.

## 3.8.2 Embedded column based connections

### Data analysis

The data analysis was performed on 5 test specimens taken from Grilli (2015), following the same procedure as outlined in Section 3.8.1. Due to the low number of test specimens it was not suitable to develop a regression equations, and therefore only the mean of each response parameter along with the COV are reported. The following component model is based on the first-cycle envelope, and due to the lack of monotonic data.

## Component model

The component models for embedded column bases are based off of work done by Grilli (2015). The parameters of this component model are with reference to Figure 3.1.

1. Effective yield moment,  $Q_y^*$ : This parameter refers to the effective flexural yield moment, and is calculated by taking a factor of the maximum expected flexural capacity according to Equation 3.91

$$M_y^* = 0.7M_{max}^*, \quad (\text{COV} = 0.10), \quad (3.91)$$

where  $M_{max}^*$  can be found according to the procedure outlined as follows.

2. Peak strength,  $Q_u^*$ : This parameter refers to the maximum flexural column base strength,  $M_{max}^*$ , and is found according to the procedure summarized in Grilli (2015).

The procedure is as follows:

- (a) Find the horizontal bearing moment,  $M_{HB}$ , according to Equation 3.92

$$M_{HB} = \min(M_{HB}^{bearing}, M_{HB}^{shear}), \quad (3.92)$$

where the moment corresponding to bearing failure can be calculated from Equation 3.93

$$M_{HB}^{bearing} = \beta\beta_1 f'_c b_j (d_L d_{effective} - (d_L^2 + d_U^2)/2). \quad (3.93)$$

$f'_c$  is the concrete compressive strength,  $b_j$  is the width of the joint,  $b_f$  is the effective joint width,  $d_L$  and  $d_U$  represent the bearing dimensions, as shown in Figure 3.62, and  $B$  is the base plate width. The constants  $\beta$  and  $\beta_1$  represent the effects of confinement and an equivalent rectangular stress block, respectively, and in Equation 3.93 can be taken as  $\beta = 2.0$  and  $\beta_1 = 0.85$ . Additionally

$$b_j = (b_f + B)/2, \quad (3.94)$$

and

$$d_{effective} = d_{ref} \leq d_{embed}. \quad (3.95)$$

$d_{effective}$  is the effective embeddment depth, and  $d_{ref}$  is the reference embeddment depth. The definition for  $d_{ref}$  is given in Equation 3.96

$$d_{ref} = C/\rho = C \left( \frac{E_{concrete}}{4E_{steel}I_{col}} \right)^{-1/4}, \quad (3.96)$$

and based on calibrated test data take  $C = 1.77$ .  $E_{concrete}$ ,  $E_{steel}$  are the modulus of elasticities of the concrete and steel, respectively, and  $I_{col}$  is the moment of inertia of the column.

The moment at which failure occurs in the column panel zone in shear can be estimated according to Equation 3.97, and is a function of the strength of the steel web, and inner and outer concrete struts. We get

$$M_{HB}^{shear} = (V_{steel}d_w) + (V_{strut,inner}h) + (1.25V_{strut,outer}h), \quad (3.97)$$

where we can calculate

$$V_{steel} = 0.6F_{ye}^{column}t_w \left( d_{effective} - \frac{d_U + d_L}{2} \right). \quad (3.98)$$

The expected yield stress is  $F_{ye}^{column}$ , and  $t_w$  is the thickness of the web of the column.  $d_U$  and  $d_L$  represent the bearing dimensions as shown in Figure 3.62.

For the inner and outer strut strengths we have Equations 3.99 and 3.100

$$V_{strut,inner} = 1.7\sqrt{f'_c}b_f(d_{effective} - (d_U + d_L)/2) \leq 0.5f'_c b_f h \quad (3.99)$$

$$V_{strut,outer} = 1.7\sqrt{f'_c}b_0(d_{effective} - (d_U + d_L)/2), \quad (3.100)$$

in which  $f'_c$  is the concrete compressive strength and  $b_0$  is the outer joint panel

zone.

After  $M_{HB}^{shear}$  and  $M_{HB}^{bearing}$  have been calculated,  $M_{HB}$  should be calculated according to Equation 3.92.

(b) The vertical bearing failure mode is to be determined as follows

$$M_{VB} = \min (M_{VB}^b, M_{VB}^c, M_{VB}^t, M_{VB}^y), \quad (3.101)$$

where  $M_{VB}^b$  is bearing failure of the concrete above or below the base plate,  $M_{VB}^c$  is concrete breakout below the compression toe of the base plate,  $M_{VB}^t$  is concrete breakout above the tension flap of the base plate, and  $M_{VB}^y$  is yielding of the baseplate. Bearing failure can be estimated using Equation 3.102

$$M_{VB}^b = (f_{VB}^b - P/(NB)) 0.21BN^2 = (1.7f'_c - P/(NB)) 0.21BN^2, \quad (3.102)$$

where the  $f_{VB}^b = 1.7f'_c$ . The moment at which concrete breakout will occur can be estimated through Equation 3.103

$$M_{VB}^{t,c} = \left( \eta \frac{40}{9} \frac{1}{\sqrt{d_{cover}}} \sqrt{f'_c} A_{35} + 0.3P \right) 0.7N, \quad (3.103)$$

based on calibrated test data take  $\eta = 1.5$ .  $d_{cover}$  is the depth of concrete in which breakout is considered, it is suggested that  $d_{cover}$  be taken according to Equation 3.104

$$d_{cover} = d_{embed}. \quad (3.104)$$

$A_{35}$  is the failure cone taken by projecting from the edges of the stress block at 35 degrees.

The moment at which yielding of the baseplate will occur can be estimated using

Equation 3.105

$$\begin{aligned} M_{VB}^y &= (f_{VB}^y - P/(BN)) 0.21BN^2 \\ &= \left( \frac{t_{plate}^2 F_y^{plate}}{2\eta^2} - P/(BN) \right) 0.21BN^2, \end{aligned} \quad (3.105)$$

$t_{plate}$  is the thickness of the baseplate, and  $F_y^{plate}$  is the specified yield stress of the baseplate.

(c) Next compute the parameter  $a$  according to Equation 3.106, then calculate  $M_{max}$

$$a = 1 - d_{embed}/d_{ref} \geq 0, \quad (3.106)$$

where  $d_{ref}$  was calculated using Equation 3.96. Use Equation 3.107 to determine if the column base will fail in horizontal or vertical bearing,

$$\begin{aligned} M_{VB}/a \leq M_{HB}/(1-a) & \quad \text{failure due to vertical bearing} \\ M_{VB}/a > M_{HB}/(1-a) & \quad \text{failure due to horizontal bearing} \end{aligned} \quad (3.107)$$

In the case of failure due to vertical bearing calculate  $M_{max}^*$  according to Equation 3.108

$$M_{max}^* = \begin{cases} M_{VB}^t/a & \text{if concrete breakout on tension side} \\ M_{HB} & \text{if concrete breakout on the compressive side} \\ M_{HB} + M_{VB}^b & \text{if concrete crushing or baseplate yielding} \\ \text{or } M_{HB} + M_{VB}^t & \end{cases} \quad (3.108)$$

In the case of failure due to horizontal bearing calculate  $M_{max}^*$  according to Equation 3.109

$$M_{max}^* = \max(\kappa M_{HB}, M_{VB}, M_{HB}/(1-a)), \quad (3.109)$$

the degradation factor,  $\kappa$ , can be found using Equation 3.110

$$\kappa = \left( \frac{M_{VB}(1-a)}{M_{HB}a} \right)^{-2} \leq 1.0. \quad (3.110)$$

3. Plastic deformation up to the peak strength of the first-cycle envelope,  $\Delta_p^*$ : This parameter refers to the pre-peak plastic rotation, and is to be taken according to calibrations based on test data, the value is given as

$$\theta_p^* = 0.015 \text{ radians (COV} = 0.48). \quad (3.111)$$

4. Plastic deformation on the descending portion of the first-cycle envelope,  $\Delta_{pc}^*$ : This parameter refers to the post-peak plastic rotation, and is based on calibrations from test data. There were two types of observed failure modes, ductile and brittle. The ductile failure modes are: compression break out of the bottom of the concrete, concrete crushing or baseplate yielding, and horizontal bearing failure of the concrete. The brittle failure modes are: tension breakout of the top of the concrete or joint shear failure of the steel column. Take  $\theta_{pc}^*$  according to Equation 3.112

$$\theta_{pc}^* = \begin{cases} 0.09 \text{ radians} & \text{if ductile failure} \\ 0.03 \text{ radians} & \text{if brittle failure} \end{cases} \quad (3.112)$$

5. Ultimate deformation,  $\Delta_{ult}^*$ : the ultimate rotation is taken from the observed test data, the follow values are recommended:

$$\theta_{ult}^* = \begin{cases} 0.06 \text{ radians} & \text{if ductile failure} \\ 0.03 \text{ radians} & \text{if brittle failure} \end{cases} \quad (3.113)$$

6. Residual strength,  $Q_r^*$ : at this point in time it is unknown if any residual strength exists.

Therefore it should be assumed that the residual strength of the component is equal to zero.

From the mean of the available tests, it was found that at the ultimate rotation the strength had deteriorated to around 75% of  $M_{max}^*$  (COV = 0.16), the  $\theta_{pc}^*$  values given in Equation 3.112 reflect this slope. No COV is given for Equation 3.112 since the equations are based off of only 2 data points each. The component model provided is based on very limited test data, as more test data is made available the existing parameters should be verified, and more detailed equations can be developed based on mechanical principles or by regression analysis.

Examples of the component models compared with the experimental test data are shown in Figure 3.63. Generally the proposed component models provide a reasonable approximation of the first-cycle envelope for the considered tests, however given the limited data available this should be expected. The nonlinearities present at loads lower than the effective flexural yield strength cannot be captured by the current modelling approach. Furthermore, the asymmetric behaviour of the embedded column bases is not captured, for example in all tests there is lower effective elastic stiffness in the negative loading direction, as seen in Figure 3.63. This is due to the concrete deterioration in the negative loading direction as a result of the lateral drift in the positive direction. Additionally, parameters to predict the degradation in flexural stiffness should be provided in order to capture the pinched hysteresis that is observed in the deduced test data.

### 3.9 Summary

In order to advance the state of knowledge for the nonlinear modelling of steel MRF structural components for performance-based earthquake engineering, recommendations for state-of-the-art component models are proposed in this chapter. The recommendations provided in this chapter address the limitations noted in the ASCE-41-13 provisions, as discussed in

## Chapter 2.

The main conclusions with regards to the development of the component models are as follows:

### **Steel beams as a part of fully-restrained beam-to-column connections**

- From the statistical evaluation of beams in fully-restrained beam-to-column connections, for all connection types, the web depth-to-thickness ratio,  $h/t_w$ , was found to be the most important parameter in predicting the plastic rotation capacity. Other significant parameters were the flange depth-to-thickness ratio,  $b_f/2t_f$ , the shear span to depth ratio,  $L/d$ , and the ratio of the unbraced length to radius of gyration,  $L_b/r_y$ .
- The ratio of the effective flexural yield strength to plastic moment for beams in fully-restrained beam-to-column connections subjected to reversed-cyclic loading protocols is found to be  $M_y^*/M_{pe} = 1.15$ .
- The mean ratio of ultimate rotation based on the first-cycle envelope to monotonic backbone for bare steel beams in fully-restrained beam-to-column connections was found to be  $\theta_{ult}^*/\theta_{ult} = 0.65$ . This is comparable to the value of 0.70 assumed in ATC-72 (PEER/ATC, 2010).
- For steel beams in fully-restrained beam-to-column connections with a depth  $d > 21''$  the ASCE-41-13 component models were found to generally overestimate the pre-peak plastic rotation. For beams with  $d < 21''$ , the plastic deformation parameters seem to be more reasonably predicted, indicating that there may be some bias in the ASCE-41-13 provisions towards beams with smaller depths. The proposed component models are found to provide a reasonable estimation of test data, and are able to capture the gradual decrease in flexural strength in the post-peak region.

### **Steel beams as a part of pre-Northridge WUF-B connections**

- The component model for steel beams with  $d < 24''$  is practically similar to the one provided in ASCE-41-13 (ASCE, 2014). For beams with  $d > 24''$ , the recommendations are practically similar to those of FEMA-355D (FEMA, 2000).

- Generally, both ASCE-41-13 and the proposed recommendations will underestimate the pre-peak plastic rotation for beams in pre-Northridge WUF-B connections.
- For beams with  $d < 18''$ , an upper-bound flexural strength can be utilized in the modelling procedure, as typically such beams have an appreciable plastic deformation prior to fracture.

### **Wide-flange steel columns**

- The axial force exerted on steel wide-flange columns due to gravity loading,  $P_g$ , has a greater influence on the column force-deformation response than the transient component resulting from the dynamic overturning effects on columns force-deformation response. Therefore, the constant gravity load  $P_g$  can be used to predict the behaviour of steel columns in nonlinear modelling procedures.
- The parameter with a dominant effect on the force-deformation behaviour of steel wide-flange columns from a statistical evaluation is found to be the ratio of the applied axial load to expected yield strength,  $P_g/P_{ye}$ . This is true for columns subjected to both monotonic and reversed-cyclic loading histories. Both the web and flange depth-to-thickness ratios (i.e.,  $h/t_w$  and  $b_f/2t_f$ ) are found to be significant on the deformation and force related parameters, however it is observed that  $h/t_w$  has a dominant effect over  $b_f/2t_f$ . Due to the high correlation between the flange and web depth-to-thickness ratios for the sections considered in the database, only  $h/t_w$  is considered in each of the equations. As well, it is found that the global slenderness ratio,  $L_b/r_y$ , was significant in each of the response parameters.
- For steel wide-flange columns, in all cases the ASCE-41-13 component models overestimate the pre-peak plastic rotation for the first-cycle envelope curve. The proposed component models are found to provide a reasonable estimation of test data, and are able to capture the gradual decrease in flexural strength in the post-peak region.
- Each of  $h/t_w$ ,  $L_b/r_y$ , and  $P_g/P_{ye}$  are found to have a significant relation with the post-yield hardening ratio of steel wide-flange columns. This observation is true for columns

subjected to both monotonic and reversed-cyclic loading histories, and is converse to the constant 3% strain hardening assumed under ASCE-41-13 (ASCE, 2014).

- Steel wide-flange columns exhibit appreciable plastic deformation with axial loads up to 75% of their axial yield strength. However, due to the presence of geometric imperfections, columns loaded to 75% of  $P_{ye}$  may buckle. Therefore, the limit for force-controlled elements per ASCE-41-13 (ASCE, 2014) should be revised to columns with  $P_g/P_{ye} \geq 0.60$  that have  $h/t_w > 43$  and  $kL_b/r_y > 120$ .
- Based on observations from full-scale testing, nominally identical steel wide-flange columns subjected to uni- and bi-directional loading show practically similar force-deformation envelopes. Therefore, it is recommended to use the uni-directional provisions when modelling columns under bi-directional lateral drift demands.
- End columns in steel MRFs typically experience increased axial load demands during seismic events due to the dynamic overturning effect. Full-scale testing has shown that the constant gravity load however has a greater influence on the column force-deformation history than the transient component of the axially compressive load. As such, from full-scale experimental observations, columns with varying axially compressive loads of up to 75% $P_{ye}$  show appreciable plastic deformation capacity. Therefore, the constant gravity load,  $P_g$ , may be considered when modelling end columns in steel MRFs.
- The ratio between the mean value of the total plastic deformation of a monotonic curve with respect to that of a first-cycle envelope curve for the same cross-section is, on average, 2.8. This value is consistent with what is currently reported in Chapter 16 of ASCE 7-16 (ASCE, 2016) for deformation-controlled elements (i.e., recommended value is 3.0).

### **HSS columns**

- Based on the first-cycle envelope, the dominant parameter from the statistical evaluation of HSS columns in the pre-peak plastic region is found to be the HSS depth-to-thickness

ratio,  $D/t$ . The ratio of the elastic modulus to effective yield stress,  $E/F_y$ , is found to be significant in the pre-peak plastic deformation only. In the post-peak plastic region, the ratio of the axial gravity load to expected yield strength,  $P_g/P_{ye}$ , is found to be the dominant parameter.

- Relationships between the hardening ratio and each of the local slenderness, the expected yield stress, and the axial load ratio of HSS columns can be established. Therefore, the strain hardening is not a constant 3% as assumed in ASCE-41-13, and will vary with each of these three parameters.
- HSS columns should be considered as force-controlled elements for  $P_g/P_{ye} > 0.60$ , and  $D/t > 33$  per ASCE-41-13 (ASCE, 2014).

#### **Column splice connections**

- Using a fracture mechanics based design formula, the strength capacity of pre-Northridge column splices can be verified based on the maximum tensile stresses due to axial tension and bi-axial bending at the splice location.

#### **Column base connections**

- The average pre-peak plastic rotation capacity of exposed column base connections based on data deduced from tests under reversed-cyclic loading is approximately  $\theta_p^* = 0.065$  radians.
- The average pre-peak plastic rotation capacity of embedded column base connections based on data deduced from tests under reversed-cyclic loading is approximately  $\theta_p^* = 0.015$  radians. The average ultimate rotation is found to be approximately  $\theta_{pc}^* = 0.06$  radians for ductile failure modes, and  $\theta_{pc}^* = 0.03$  radians for brittle failure modes.

Predictor	Estimate	$p$ -Value	CI–	CI+
Constant	0.135	0.163	0.008	2.309
$h/t_w$	-0.231	0.230	-0.611	0.150
$b_f/2t_f$	-1.681	2.096e-05	-2.409	-0.953
$L_b/r_y$	-0.177	0.005	-0.299	-0.055
$L/d$	1.634	5.379e-08	1.108	2.160
Lillie $p$ -Val = 0.032    D-W $p$ -Val = 0.264 $R^2 = 0.782$ COV = 0.374				

Table 3.1: Summary of the results from the regression analysis of  $\theta_p^*$  for beams in non-RBS fully-restrained beam-to-column connections.

Predictor	Estimate	$p$ -Value	CI–	CI+
Constant	6.217e-06	0.039	7.727e-11	0.500
$h/t_w$	-0.744	0.054	-1.502	0.014
$\sqrt{E/F_y}$	4.345	0.007	1.376	7.315
$L_b/r_y$	-0.553	0.029	-1.042	-0.064
Lillie $p$ -Val = 0.5    D-W $p$ -Val = 0.733 $R^2 = 0.610$ COV = 0.357				

Table 3.2: Summary of the results from the regression analysis of  $\theta_{pc}^*$  for beams in non-RBS fully-restrained beam-to-column connections.

Predictor	Estimate	$p$ -Value	CI–	CI+
Constant	5.759	0.181	0.430	77.150
$h/t_w$	-0.247	0.341	-0.772	0.278
$b_f/2t_f$	-1.125	0.018	-2.047	-0.204
$d$	-1.211	0.001	-1.878	-0.544
$L_b/r_y$	-0.616	0.021	-1.134	-0.098
Lillie $p$ -Val = 0.5    D-W $p$ -Val = 0.010 $R^2 = 0.550$ COV = 0.359				

Table 3.3: Summary of the results from the regression analysis of  $\theta_p^*$  for beams in RBS fully-restrained beam-to-column connections.

Predictor	Estimate	$p$ -Value	CI–	CI+
Constant	1.483	0.650	0.258	8.536
$h/t_w$	-0.691	1.437e-04	-1.017	-0.365
$b_f/2t_f$	-0.216	0.580	-1.002	0.570
Lillie $p$ -Val = 0.025    D-W $p$ -Val = 0.001 $R^2 = 0.387$ COV = 0.278				

Table 3.4: Summary of the results from the regression analysis of  $\theta_{pc}^*$  for beams in RBS fully-restrained beam-to-column connections.

$\frac{I_c}{I_s}$	$\frac{M_y^+}{M_y^*}$	$\frac{M_y^-}{M_y^*}$	$\frac{M_{max}^+}{M_{max}}$	$\frac{M_{max}^-}{M_{max}}$	$\frac{M_r^+}{M_y^*}$	$\frac{M_r^-}{M_y^*}$	$\frac{\theta_p^+}{\theta_p}$	$\frac{\theta_p^-}{\theta_p}$	$\frac{\theta_{pc}^+}{\theta_{pc}}$	$\frac{\theta_{pc}^-}{\theta_{pc}}$	$\Lambda$	D <sup>+</sup>	D <sup>-</sup>
1.40	1.35	1.25	1.30	1.05	0.30	0.20	1.80	0.95	1.35	0.95	1.0	1.15	1.0

Table 3.5: Modification factors for composite steel beams, values from Elkady and Lignos (2014).

Predictor	Estimate	<i>p</i> -Value	CI-	CI+
Constant	0.048	1.837e-15	0.0392	0.0558
<i>d</i>	-1.369e-3	8.633e-07	-1.858e-03	-8.806e-04
Lillie <i>p</i> -Val = 0.063    D-W <i>p</i> -Val = 0.031    R <sup>2</sup> = 0.393 $\sigma$ = 0.012				

Table 3.6: Summary of the results from the regression analysis of  $\theta_p^*$  for beams in pre-Northridge WUF-B connections.

Sections	$h/t_w$	$b_f/2t_f$	$L_b/r_y$	$L/d$	$\theta_p^*$ [rad]	$\theta_{pc}^*$ [rad]	$\theta_p^*$ (RBS) [rad]	$\theta_{pc}^*$ (RBS) [rad]
W21X62	46.9	6.7	50.0	7.14 <sup>†‡</sup>	0.015	0.073	0.015	0.073
W21X147	26.1	5.4	50.0	6.79 <sup>†</sup>	0.024	0.128	0.022	0.119
W24X84	45.9	5.9	50.0	6.22	0.016	0.076	0.014	0.075
W24X207	24.8	4.1 <sup>†</sup>	50.0	5.84	0.033	0.142	0.024	0.127
W27X94	49.5	6.7	50.0	5.58	0.011	0.069	0.012	0.069
W27X217	28.7	4.7	50.0	5.28	0.022	0.120	0.019	0.101
W30X108	49.6	6.9	50.0	5.03	0.009	0.069	0.010	0.067
W30X235	32.2	5.0	50.0	4.79	0.018	0.108	0.016	0.092
W33X130	51.7	6.7	50.0	4.53	0.009	0.067	0.010	0.068
W33X241	35.9	5.7	50.0	4.39	0.013	0.096	0.013	0.092
W36X150	51.9	6.4	50.0	4.18	0.009	0.067	0.009	0.068
W36X210	39.1	4.5	50.0	4.09	0.017	0.093	0.013	0.088

Table 3.7: Modelling parameters for first-cycle envelope of beams as a part of fully-restrained beam-to-column connections, with  $L_b/r_y = 50$  and  $L = 150$  in. <sup>†</sup>Outside range of predictive equations for RBS connections. <sup>‡</sup>Outside range of predictive equations for non-RBS connections.

Predictor	Estimate	$p$ -Value	CI–	CI+
Constant	297.500	9.362e-24	116.000	763.200
$h/t_w$	-1.689	6.222e-39	-1.878	-1.499
$L_b/r_y$	-0.763	1.748e-07	-1.038	-0.487
$1 - P_g/P_y$	2.959	4.931e-57	2.728	3.190
Lillie $p$ -Val = 0.485   D-W $p$ -Val = $1.08e - 21$ $R^2 = 0.892$ COV = 0.386				

Table 3.8: Summary of the results from the regression analysis of  $\theta_p$  for wide-flange columns based on the monotonic backbone.

Predictor	Estimate	$p$ -Value	CI–	CI+
Constant	77.550	4.907e-27	40.360	149.000
$h/t_w$	-0.766	1.303e-22	-0.897	-0.635
$L_b/r_y$	-0.741	1.492e-12	-0.931	-0.551
$1 - P_g/P_y$	2.666	5.191e-72	2.506	2.825
Lillie $p$ -Val = 0.001   D-W $p$ -Val = $1.6e - 06$ $R^2 = 0.907$ COV = 0.261				

Table 3.9: Summary of the results from the regression analysis of  $\theta_{pc}$  for wide-flange columns based on the monotonic backbone.

Predictor	Estimate	$p$ -Value	CI–	CI+
Constant	15.200	4.788e-45	11.630	19.870
$h/t_w$	-0.184	2.750e-10	-0.238	-0.130
$L_b/r_y$	-0.429	1.137e-20	-0.507	-0.350
$1 - P_g/P_y$	0.411	8.244e-25	0.345	0.476
Lillie $p$ -Val = 0.046   D-W $p$ -Val = $1.340e - 18$ $R^2 = 0.764$ COV = 0.103				

Table 3.10: Summary of the results from the regression analysis of  $a = M_{max}/M_y^*$  for wide-flange columns based on the monotonic backbone.

Predictor	Estimate	$p$ -Value	CI–	CI+
Constant	13.890	1.012e-09	6.246	30.890
$h/t_w$	-1.629	5.497e-45	-1.790	-1.468
$L_b/r_y$	-0.252	0.035	-0.485	-0.018
$1 - P_g/P_y$	2.337	3.425e-53	2.141	2.533
Lillie $p$ -Val = 0.5   D-W $p$ -Val = $1.66e - 09$ $R^2 = 0.886$ COV = 0.307				

Table 3.11: Summary of the results from the regression analysis of  $\theta_p^*$  for wide-flange columns based on the first-cycle envelope.

Predictor	Estimate	$p$ -Value	CI–	CI+
Constant	14.600	1.142e-04	3.833	55.600
$h/t_w$	-0.896	2.958e-10	-1.158	-0.633
$L_b/r_y$	-0.489	0.015	-0.879	-0.098
$1 - P_g/P_y$	3.387	1.018e-46	3.066	3.708
Lillie $p$ -Val = 0.077   D-W $p$ -Val = 0.056 $R^2 = 0.775$ COV = 0.416				

Table 3.12: Summary of the results from the regression analysis of  $\theta_{pc}^*$  for wide-flange columns based on the first-cycle envelope.

Predictor	Estimate	$p$ -Value	CI–	CI+
Constant	9.857	1.200e-60	8.337	11.650
$h/t_w$	-0.369	7.985e-49	-0.402	-0.335
$L_b/r_y$	-0.167	3.072e-10	-0.216	-0.118
$1 - P_g/P_y$	0.084	9.250e-05	0.042	0.125
Lillie $p$ -Val = 0.217   D-W $p$ -Val = $5.080e - 09$ $R^2 = 0.865$ COV = 0.068				

Table 3.13: Summary of the results from the regression analysis of  $a^* = M_{max}^*/M_y^*$  for wide-flange columns based on the first-cycle envelope.

Sections	$h/t_w$	$L_b/r_y$	$P_g/P_{ye} = 0.05$			$P_g/P_{ye} = 0.20$			$P_g/P_{ye} = 0.50$		
			$M_{max}/M_y^*$	$\theta_p$	$\theta_{pc}$	$M_{max}/M_y^*$	$\theta_p$	$\theta_{pc}$	$M_{max}/M_y^*$	$\theta_p$	$\theta_{pc}$
W33X318	28.7	42.0	1.400	0.066	0.271	1.310	0.050	0.176	1.080	0.024	0.055
W27X307	20.6	45.7	1.450	0.109	0.300	1.350	0.083	0.215	1.120	0.039	0.066
W27X235	26.2	46.8	1.370	0.071	0.268	1.280	0.054	0.174	1.060	0.026	0.054
W24X146	33.2	51.8	1.250	0.044	0.204	1.170	0.034	0.133	1.000	0.016	0.041
W24X103	39.2	78.4	1.030	0.025	0.128	1.000	0.019	0.084	1.000	0.009	0.026
W24X84	45.9	80.0	1.000	0.019	0.111	1.000	0.014	0.073	1.000	0.007	0.022
W14X370	6.9 <sup>†</sup>	36.5 <sup>†</sup>	1.300	0.200	0.300	1.300	0.200	0.300	1.300	0.200	0.191
W14X233	10.7 <sup>†</sup>	38.0 <sup>†</sup>	1.300	0.200	0.300	1.300	0.200	0.300	1.300	0.135	0.130

Table 3.14: Modelling parameters for monotonic back bone curve of wide-flange columns, with  $L = 13$  feet  $F_{ye} = 55$  ksi. <sup>†</sup>Outside of the range of the predictive equations.

Sections	$h/t_w$	$L_b/r_y$	$P_g/P_{ye} = 0.05$			$P_g/P_{ye} = 0.20$			$P_g/P_{ye} = 0.50$		
			$M_{max}^*/M_y^*$	$\theta_p^*$	$\theta_{pc}^*$	$M_{max}^*/M_y^*$	$\theta_p^*$	$\theta_{pc}^*$	$M_{max}^*/M_y^*$	$\theta_p^*$	$\theta_{pc}^*$
W33X318	28.7	42.0	1.350	0.020	0.125	1.300	0.014	0.072	1.190	0.005	0.016
W27X307	20.6	45.7	1.520	0.034	0.156	1.470	0.023	0.090	1.300	0.008	0.020
W27X235	26.2	46.8	1.380	0.023	0.127	1.330	0.015	0.074	1.210	0.005	0.016
W24X146	33.2	51.8	1.230	0.015	0.140	1.190	0.010	0.058	1.080	0.003	0.013
W24X103	39.2	78.4	1.080	0.010	0.071	1.040	0.007	0.041	1.000	0.002	0.009
W24X84	45.9	80.0	1.010	0.008	0.062	1.000	0.005	0.036	1.000	0.002	0.008
W14X370	6.9 <sup>†</sup>	36.5 <sup>†</sup>	1.300	0.100	0.100	1.300	0.100	0.100	1.300	0.047	0.054
W14X233	10.7 <sup>†</sup>	38.0 <sup>†</sup>	1.300	0.100	0.100	1.300	0.068	0.100	1.300	0.023	0.037

Table 3.15: Modelling parameters for first-cycle envelope of wide-flange columns, with  $L = 13$  feet  $F_{ye} = 55$  ksi. <sup>†</sup>Outside of the range of the predictive equations.

Predictor	Estimate	<i>p</i> -Value	CI–	CI+
Constant	0.002	0.107	1.499e-06	3.889
<i>D/t</i>	-1.985	2.275e-07	-2.637	-1.333
$1 - P_g/P_y$	1.349	0.014	0.289	2.409
$\sqrt{E/F_y}$	2.798	0.018	0.511	5.084
Lillie <i>p</i> -Val = 0.313   D-W <i>p</i> -Val = 2.30e – 4   R <sup>2</sup> = 0.504   COV = 0.637				

Table 3.16: Summary of the results from the regression analysis of  $\theta_p^*$  of the first-cycle envelope component model for HSS columns.

Predictor	Estimate	<i>p</i> -Value	CI–	CI+
Constant	5.831	0.128	0.573	59.360
<i>D/t</i>	-1.340	7.302e-4	-2.034	-0.647
$1 - P_g/P_y$	2.001	1.485e-05	1.284	2.718
Lillie <i>p</i> -Val = 0.5   D-W <i>p</i> -Val = 0.217   R <sup>2</sup> = 0.701   COV = 0.242				

Table 3.17: Summary of the results from the regression analysis of  $\theta_{pc}^*$  of the first-cycle envelope component model for HSS columns.

Predictor	Estimate	<i>p</i> -Value	CI–	CI+
Constant	0.832	0.793	0.200	3.463
<i>D/t</i>	-0.100	0.248	-0.273	0.073
$1 - P_g/P_y$	0.116	0.301	-0.110	0.343
$\sqrt{E/F_y}$	0.233	0.246	-0.170	0.636
Lillie <i>p</i> -Val = 0.5   D-W <i>p</i> -Val = 0.544   R <sup>2</sup> = 0.134   COV = 0.084				

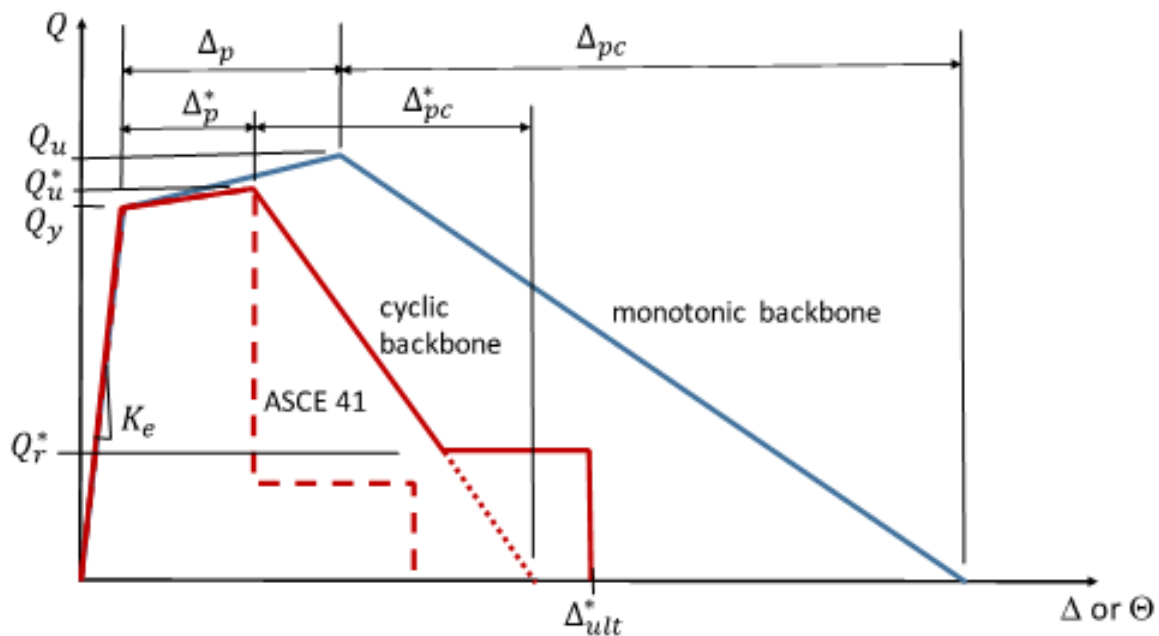
Table 3.18: Summary of the results from the regression analysis of  $a^* = M_{max}^*/M_y^*$  of the first-cycle envelope component model for HSS columns.

Sections	$D/t$	$E/F_y$	$P_g/P_{ye} = 0.05$			$P_g/P_{ye} = 0.20$			$P_g/P_{ye} = 0.50$		
			$M_{max}/M_y^*$	$\theta_p$	$\theta_{pc}$	$M_{max}/M_y^*$	$\theta_p$	$\theta_{pc}$	$M_{max}/M_y^*$	$\theta_p$	$\theta_{pc}$
HSS20X20X5/8	34.4	414	1.190	0.018	0.154	1.000	0.015	0.092	1.000	0.009	0.023
HSS20X20X3/8	57.3 <sup>†</sup>	414	1.020	0.011	0.084	1.000	0.009	0.050	1.000	0.005	0.012
HSS16X16X5/8	27.5	414	1.270	0.022	0.201	1.020	0.018	0.120	1.000	0.011	0.029
HSS16X16X3/8	45.8 <sup>†</sup>	414	1.090	0.014	0.109	1.000	0.011	0.065	1.000	0.007	0.016
HSS12X12X5/8	20.7	414	1.390	0.029	0.284	1.110	0.024	0.170	1.000	0.014	0.042
HSS12X12X3/8	34.4	414	1.190	0.018	0.154	1.000	0.015	0.092	1.000	0.009	0.023
HSS10X10X5/8	17.2 <sup>†</sup>	414	1.460	0.035	0.354	1.170	0.029	0.211	1.000	0.017	0.052
HSS10X10X3/8	28.7	414	1.260	0.021	0.192	1.000	0.018	0.115	1.000	0.011	0.028

Table 3.19: Modelling parameters for monotonic backbone of HSS columns, with  $L = 13$  feet  $F_{ye} = 70$  ksi. <sup>†</sup>Outside of the range of the predictive equations.

Sections	$D/t$	$E/F_y$	$P_g/P_{ye} = 0.05$			$P_g/P_{ye} = 0.20$			$P_g/P_{ye} = 0.50$		
			$M_{max}^*/M_y^*$	$\theta_p^*$	$\theta_{pc}^*$	$M_{max}^*/M_y^*$	$\theta_p^*$	$\theta_{pc}^*$	$M_{max}^*/M_y^*$	$\theta_p^*$	$\theta_{pc}^*$
HSS20X20X5/8	34.4	414	1.188	0.012	0.069	1.000	0.009	0.044	1.000	0.005	0.013
HSS20X20X3/8	57.3 <sup>†</sup>	414	1.020	0.007	0.035	1.000	0.005	0.023	1.000	0.003	0.007
HSS16X16X5/8	27.5	414	1.271	0.015	0.092	1.016	0.012	0.059	1.000	0.006	0.017
HSS16X16X3/8	45.8 <sup>†</sup>	414	1.090	0.008	0.047	1.000	0.007	0.030	1.000	0.003	0.009
HSS12X12X5/8	20.7	414	1.300	0.020	0.133	1.107	0.016	0.085	1.000	0.008	0.025
HSS12X12X3/8	34.4	414	1.188	0.012	0.069	1.000	0.009	0.044	1.000	0.005	0.013
HSS10X10X5/8	17.2 <sup>†</sup>	414	1.300	0.025	0.169	1.170	0.020	0.108	1.000	0.010	0.032
HSS10X10X3/8	28.7	414	1.255	0.014	0.087	1.003	0.011	0.056	1.000	0.006	0.016

Table 3.20: Modelling parameters for first-cycle envelope of HSS columns, with  $L = 13$  feet  $F_{ye} = 70$  ksi. <sup>†</sup>Outside of the range of the predictive equations.



**Definitions:**

- $Q$  - characteristic stress resultant (force or moment) in a structural component
- $Q_u$  - peak strength of the monotonic backbone
- $Q_u^*$  - peak strength of the cyclic backbone
- $Q_y$  - effective yield strength of the component
- $Q_r^*$  - residual strength of the cyclic backbone
- $\Delta$  or  $\Theta$  - characteristic deformation (displacement or rotation) in a structural component
- $\Delta_p$  - plastic deformation up to the peak strength of the monotonic backbone
- $\Delta_p^*$  - plastic deformation up to the peak strength of the cyclic backbone
- $\Delta_{pc}$  - plastic deformation of the descending portion of the monotonic backbone
- $\Delta_{pc}^*$  - plastic deformation of the descending portion of the cyclic backbone
- $\Delta_{ult}^*$  - ultimate deformation capacity at which point characteristic strength of the component is lost or where the component loses the resistance to resist vertical gravity loads
- cyclic backbone - idealized envelope of component response under cyclic loading
- monotonic backbone - idealized component response under monotonic loading
- ASCE 41 - Idealized component response under cyclic loading as specified in ASCE 41

Figure 3.1: General component model for the ATC-114 project, from ATC (2016).

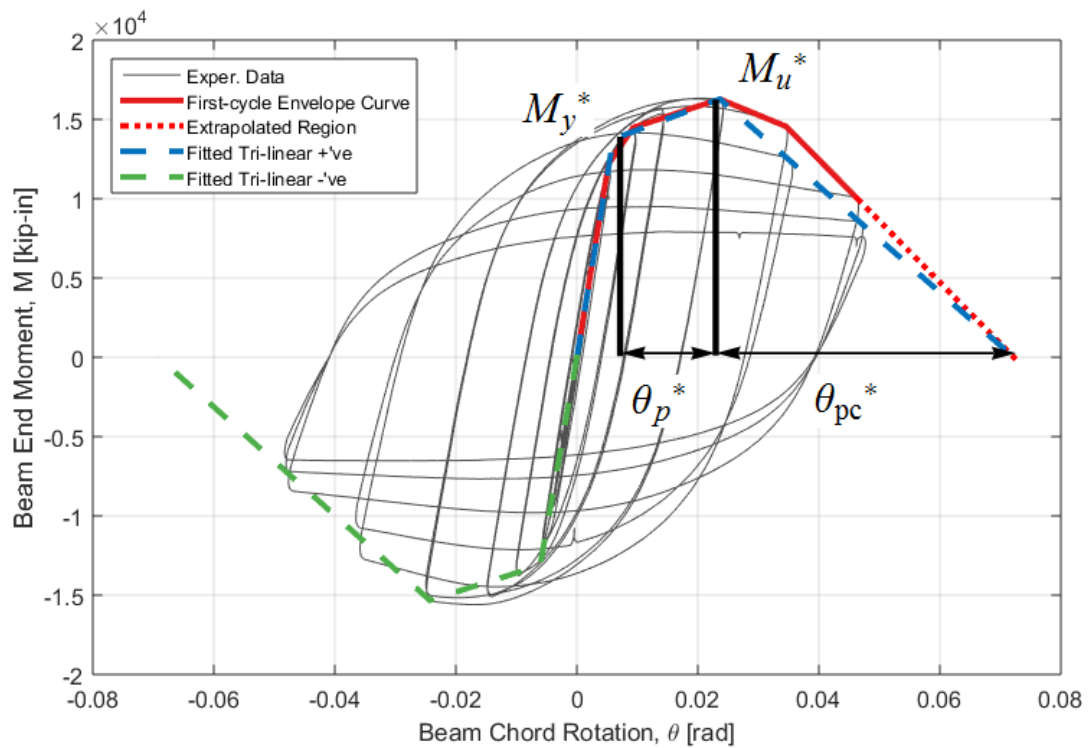


Figure 3.2: Deduced moment-rotation data, showing first-cycle envelope curve and fitted tri-linear curve, data from Yu et al. (2000).

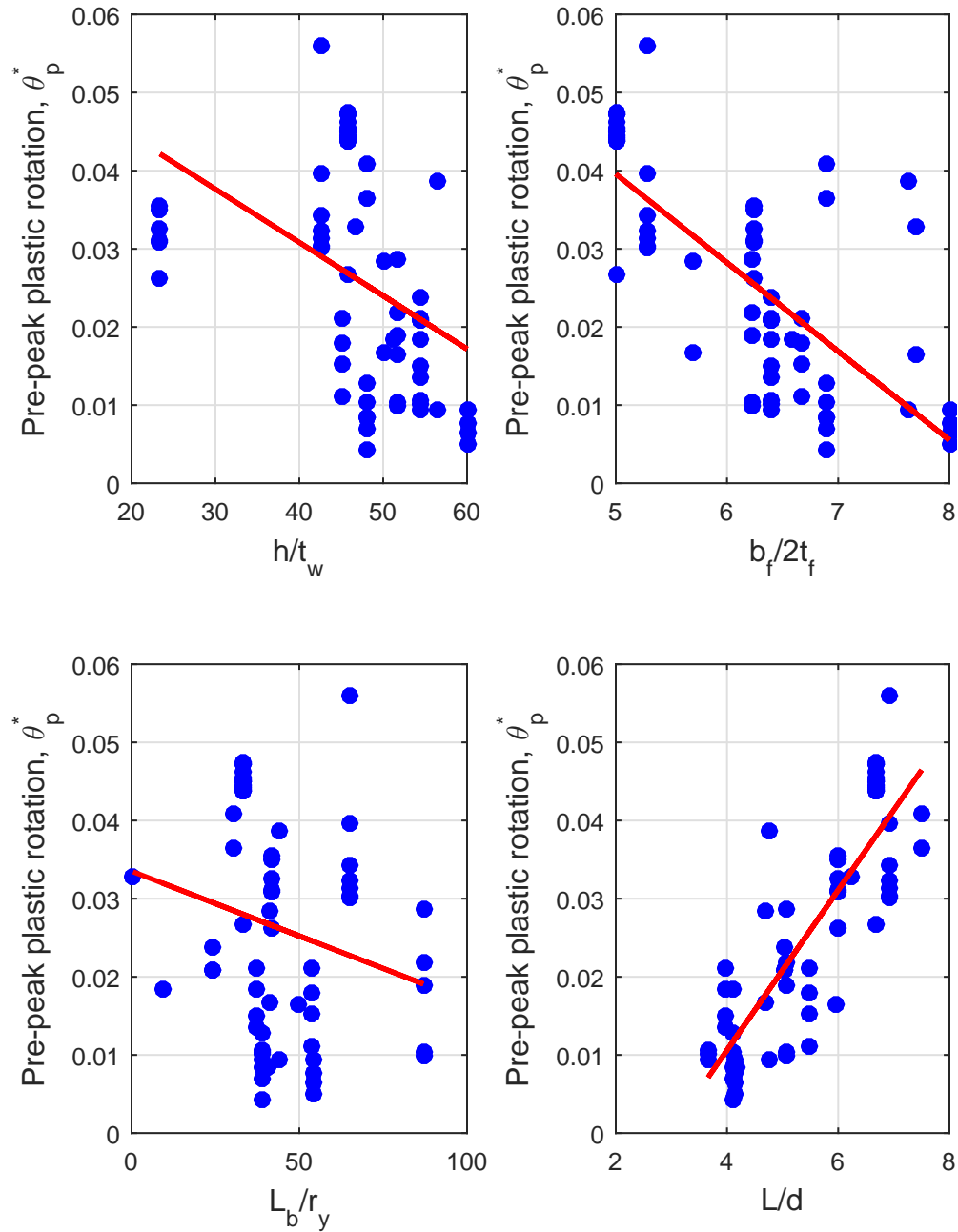


Figure 3.3: Trends on the pre-peak plastic rotation for steel beams with other-than-RBS connections based on the first-cycle envelope curve.

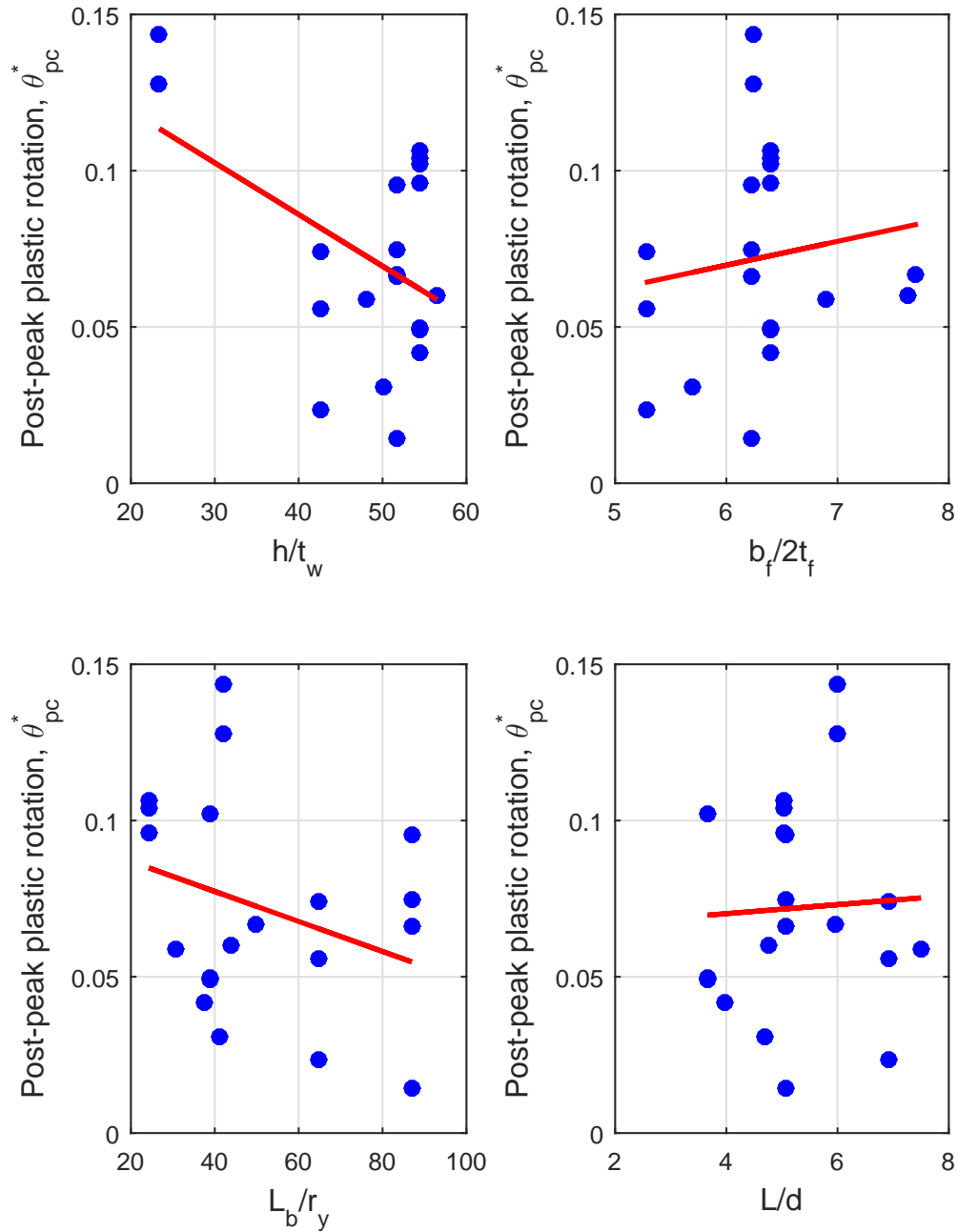


Figure 3.4: Trends on post-peak plastic rotation for steel with other-than-RBS connections based on the first-cycle envelope curve.

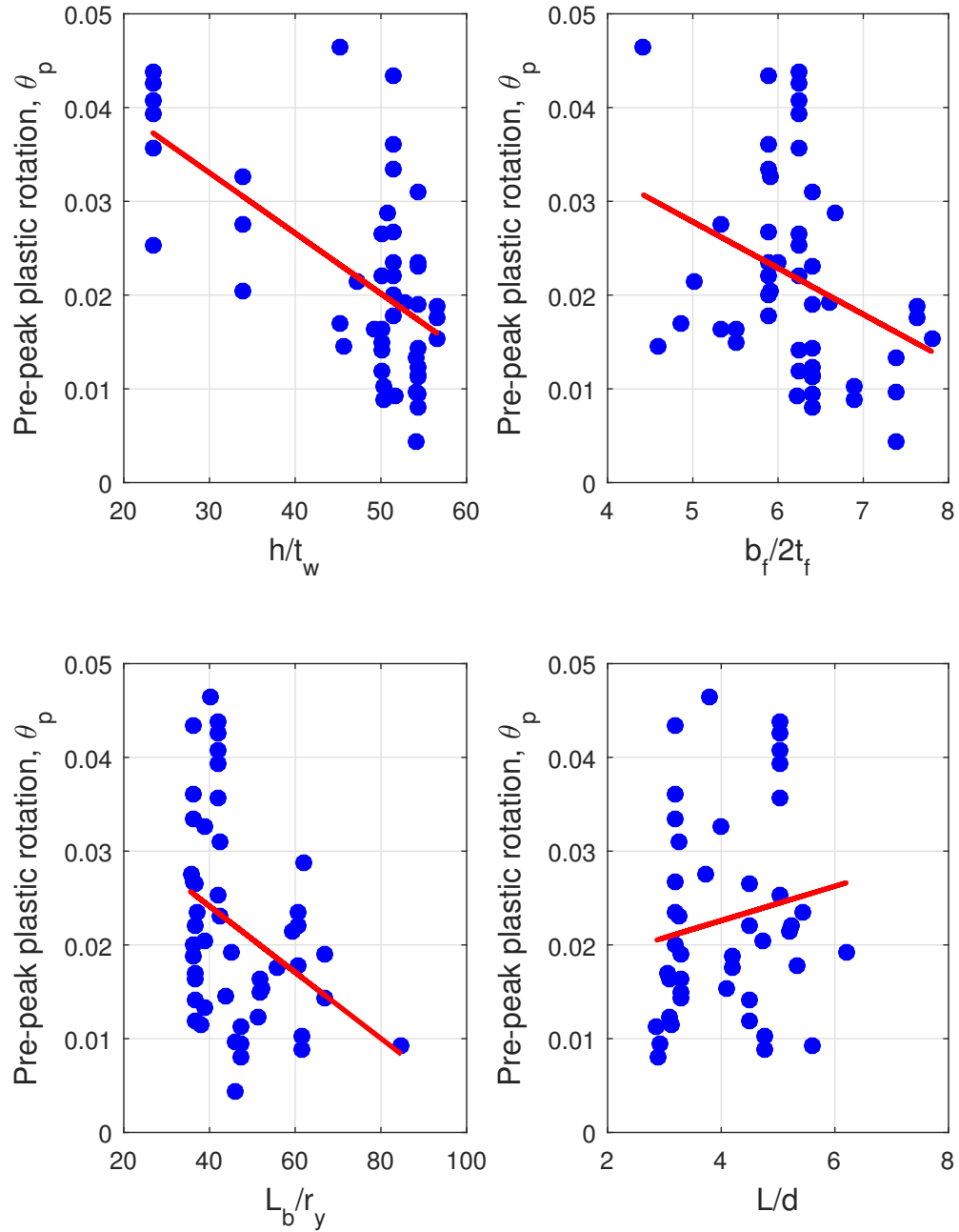


Figure 3.5: Trends on pre-peak plastic rotation for steel beams with RBS connections based on the first-cycle envelope curve.

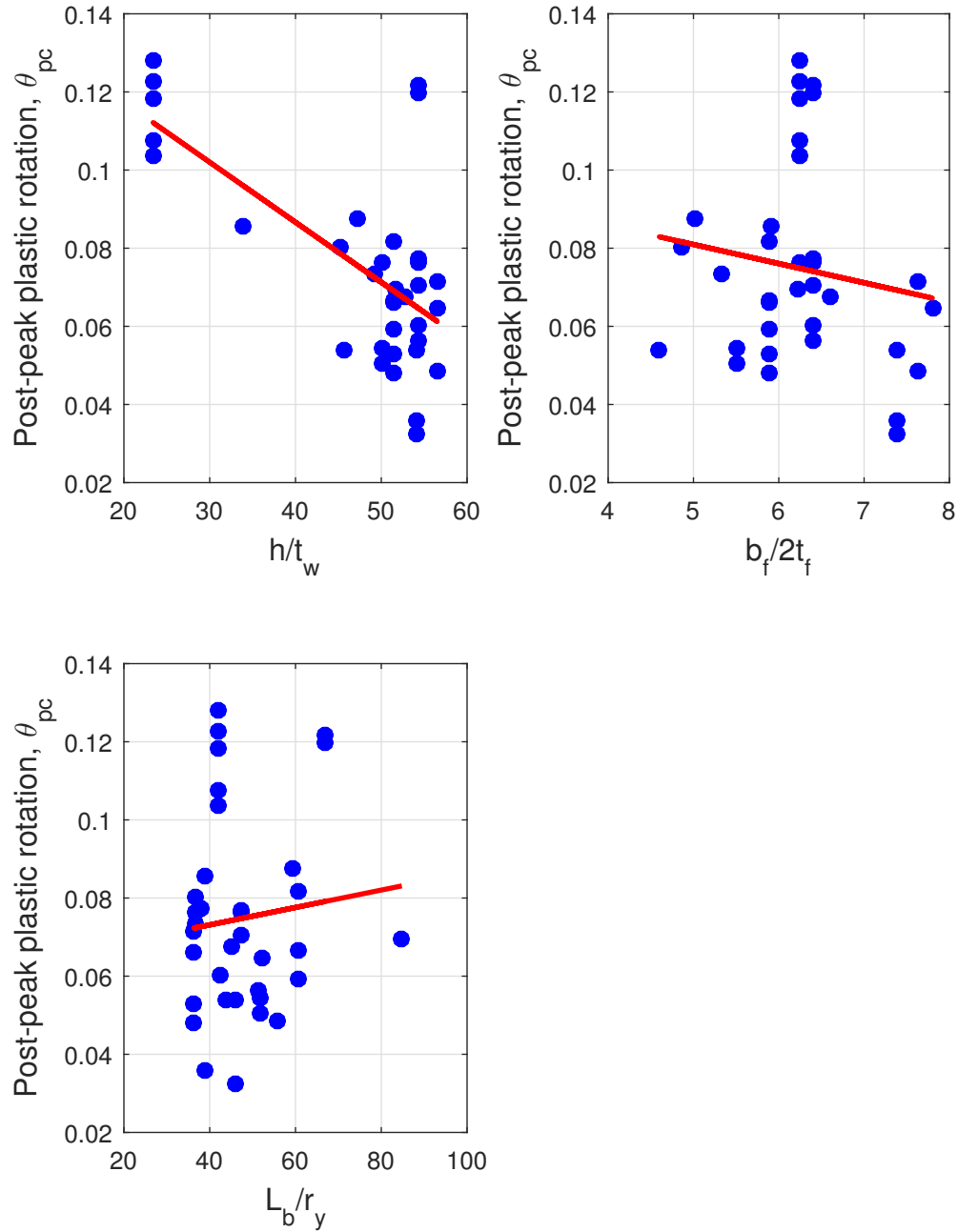


Figure 3.6: Trends on post-peak plastic rotation for steel beams with RBS connections based on the first-cycle envelope curve.

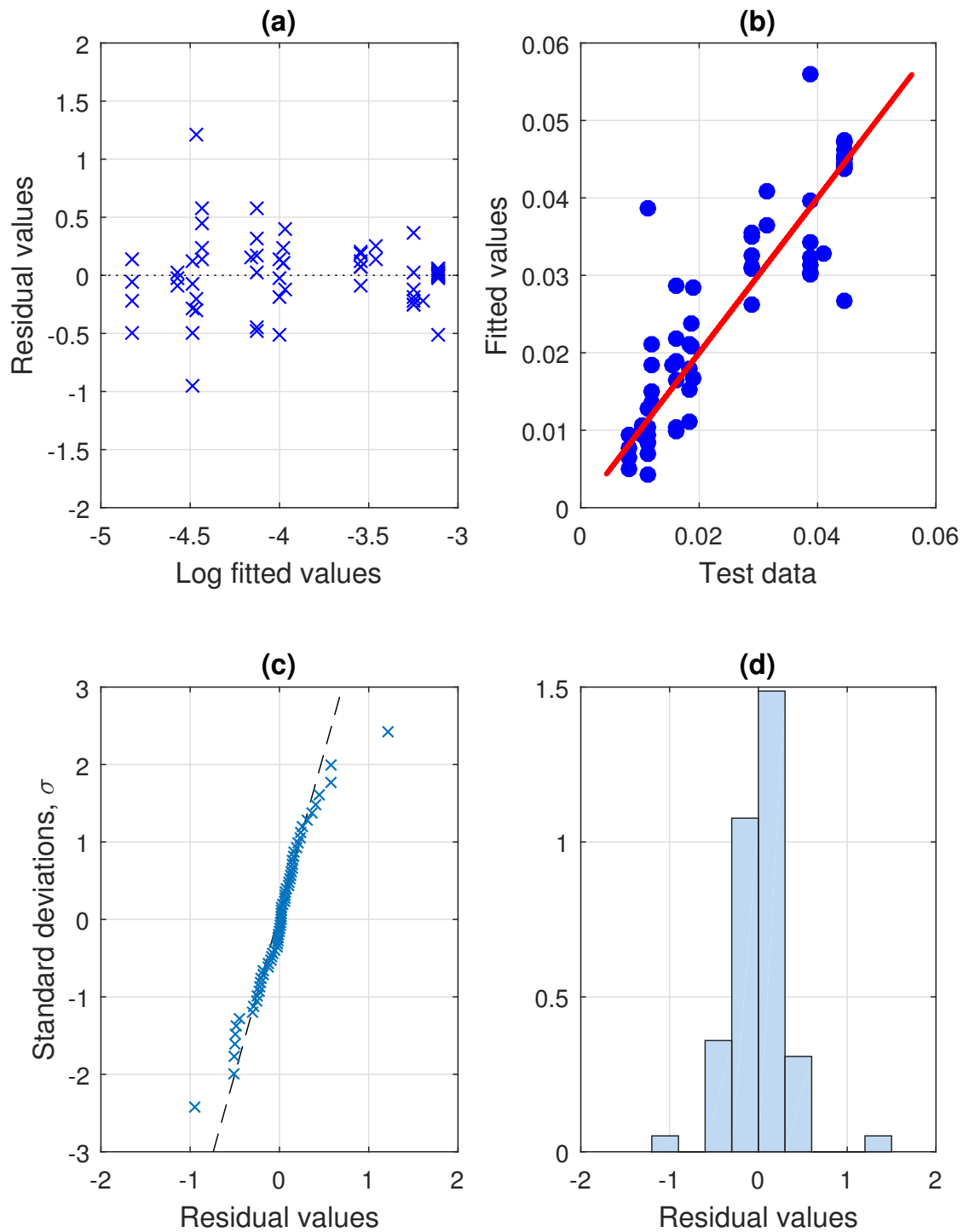


Figure 3.7: Diagnostics for the regression of  $\theta_p^*$  of the first-cycle envelope component model for beams with non-RBS connections. (a) Residuals versus fitted values; (b) Fitted values versus test data; (c) QQ-plot; (d) Histogram of residuals.

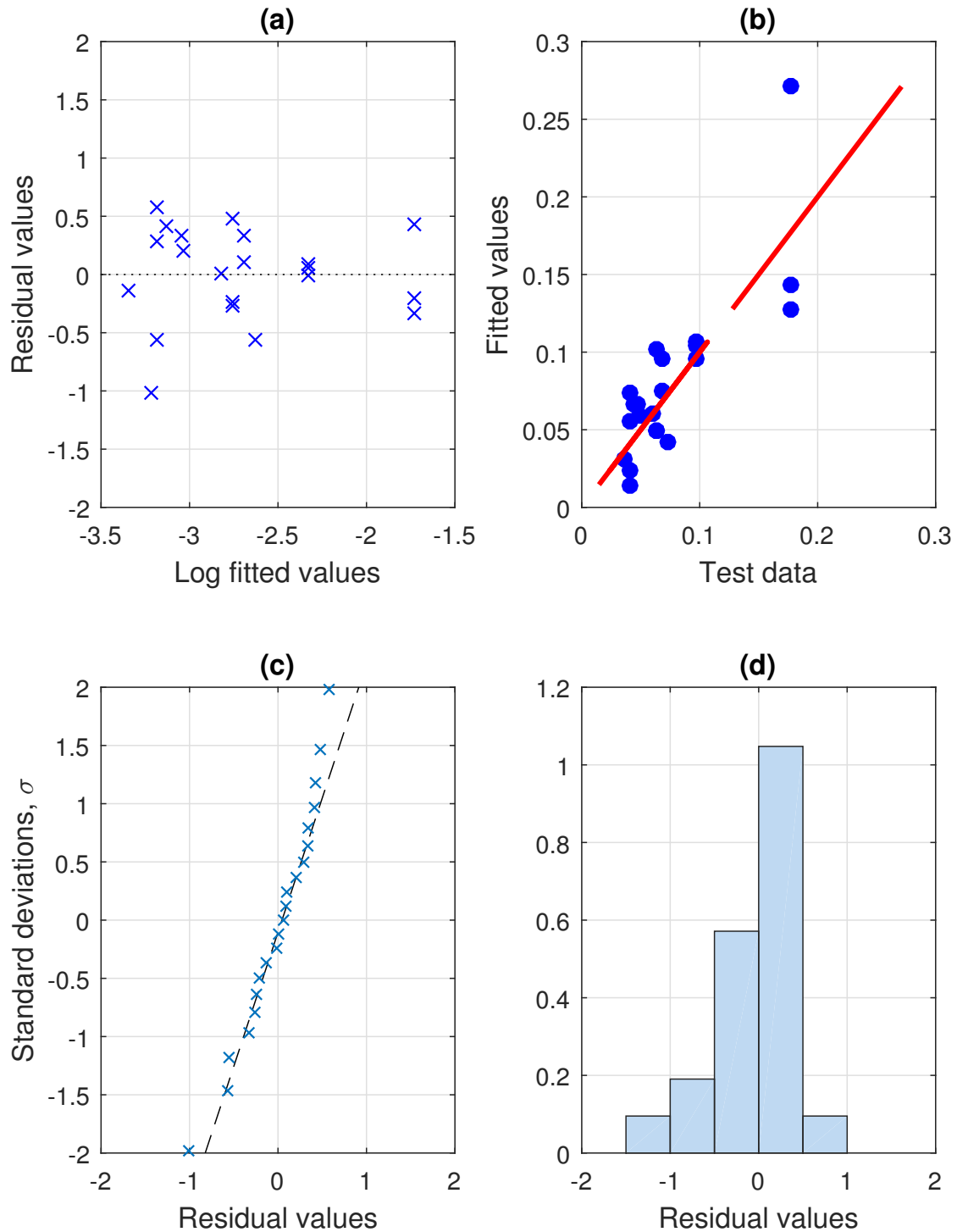


Figure 3.8: Diagnostics for the regression of  $\theta_{pc}^*$  of the first-cycle envelope component model for beams with non-RBS connections. (a) Residuals versus fitted values; (b) Fitted values versus test data; (c) QQ-plot; (d) Histogram of residuals.

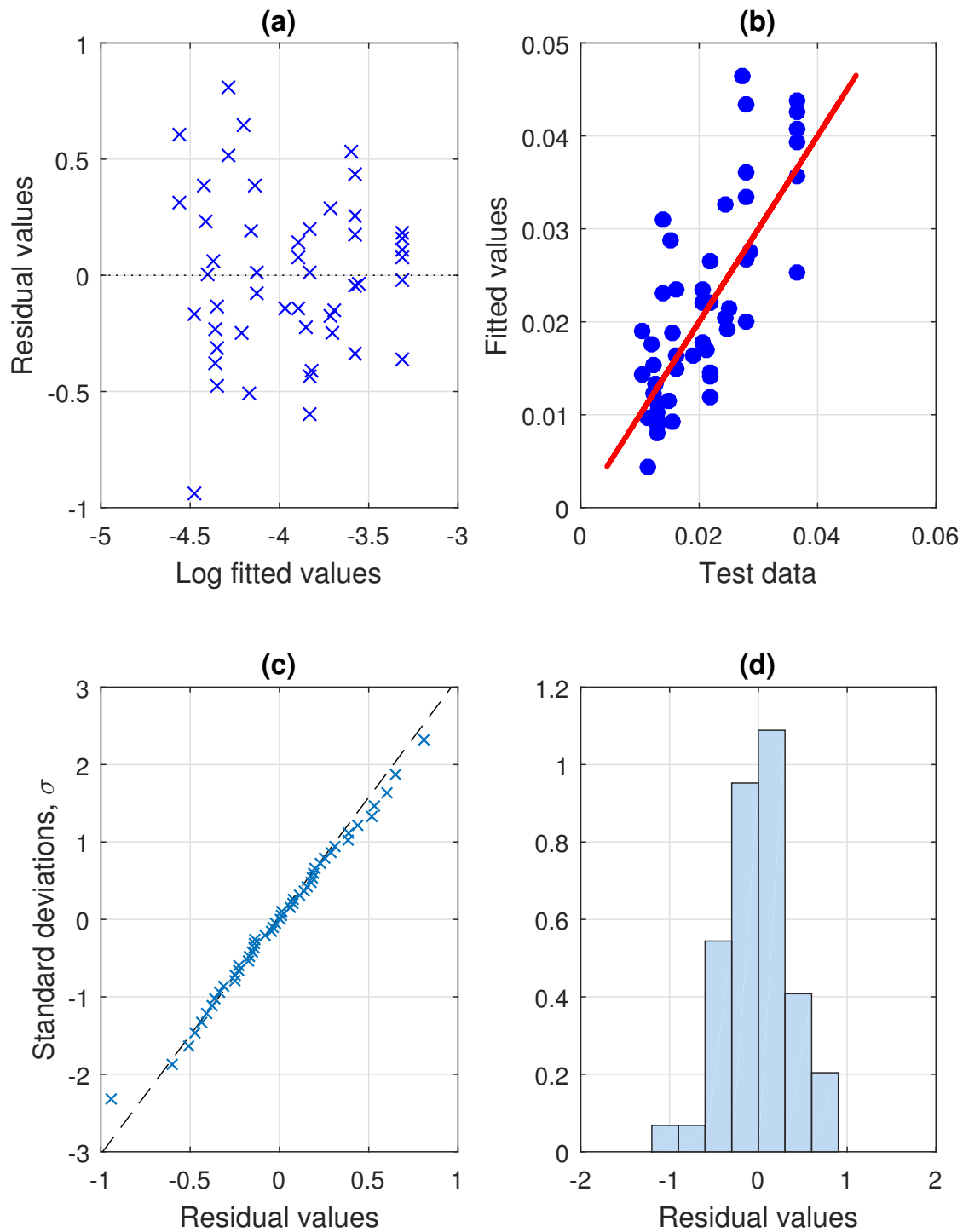


Figure 3.9: Diagnostics for the regression of  $\theta_p^*$  of the first-cycle envelope component model for beams with RBS connections. (a) Residuals versus fitted values; (b) Fitted values versus test data; (c) QQ-plot; (d) Histogram of residuals.

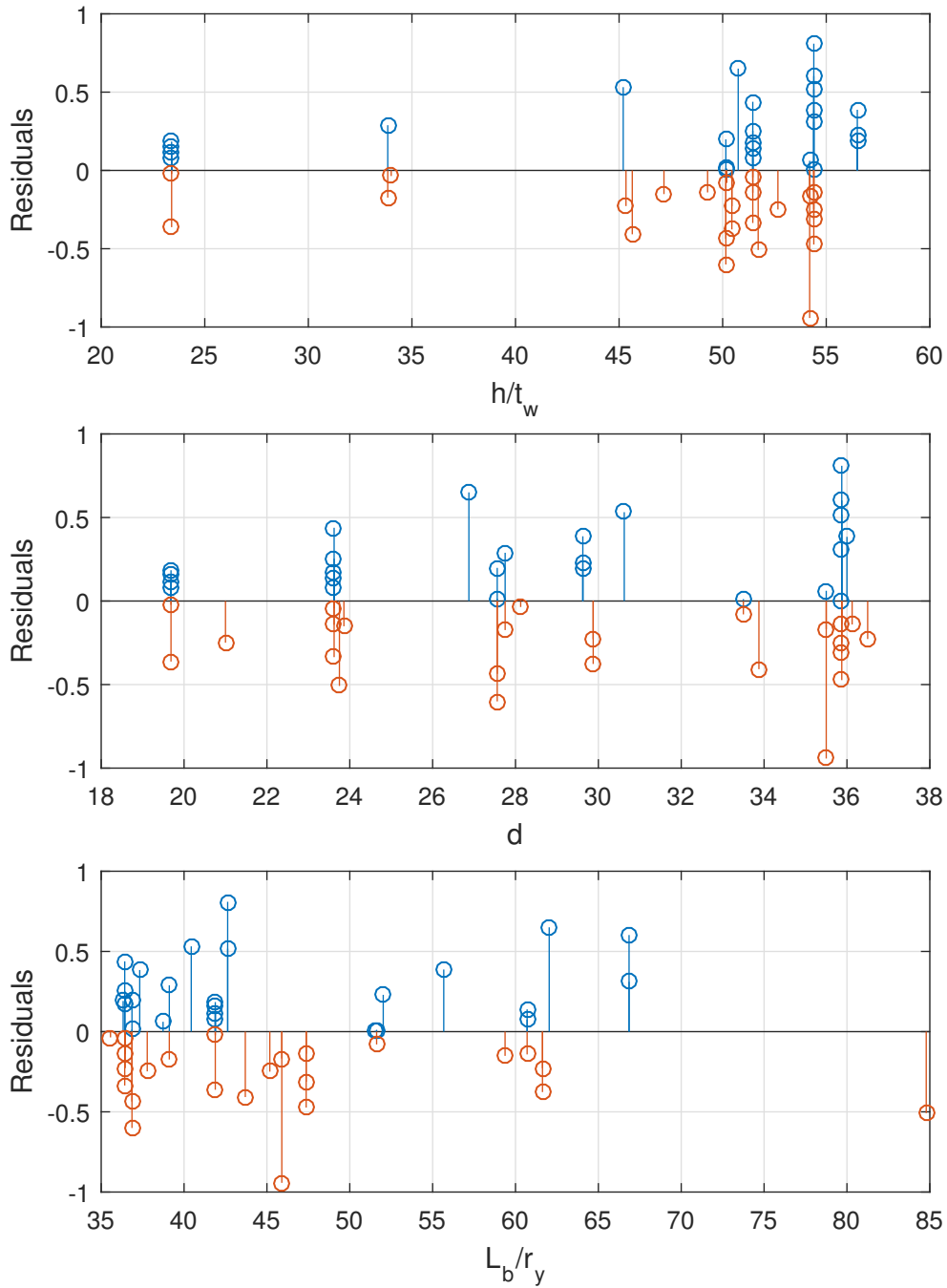


Figure 3.10: Plot of the residuals of the  $\theta_p^*$  equation for the first-cycle envelope component model for beams with RBS connections.

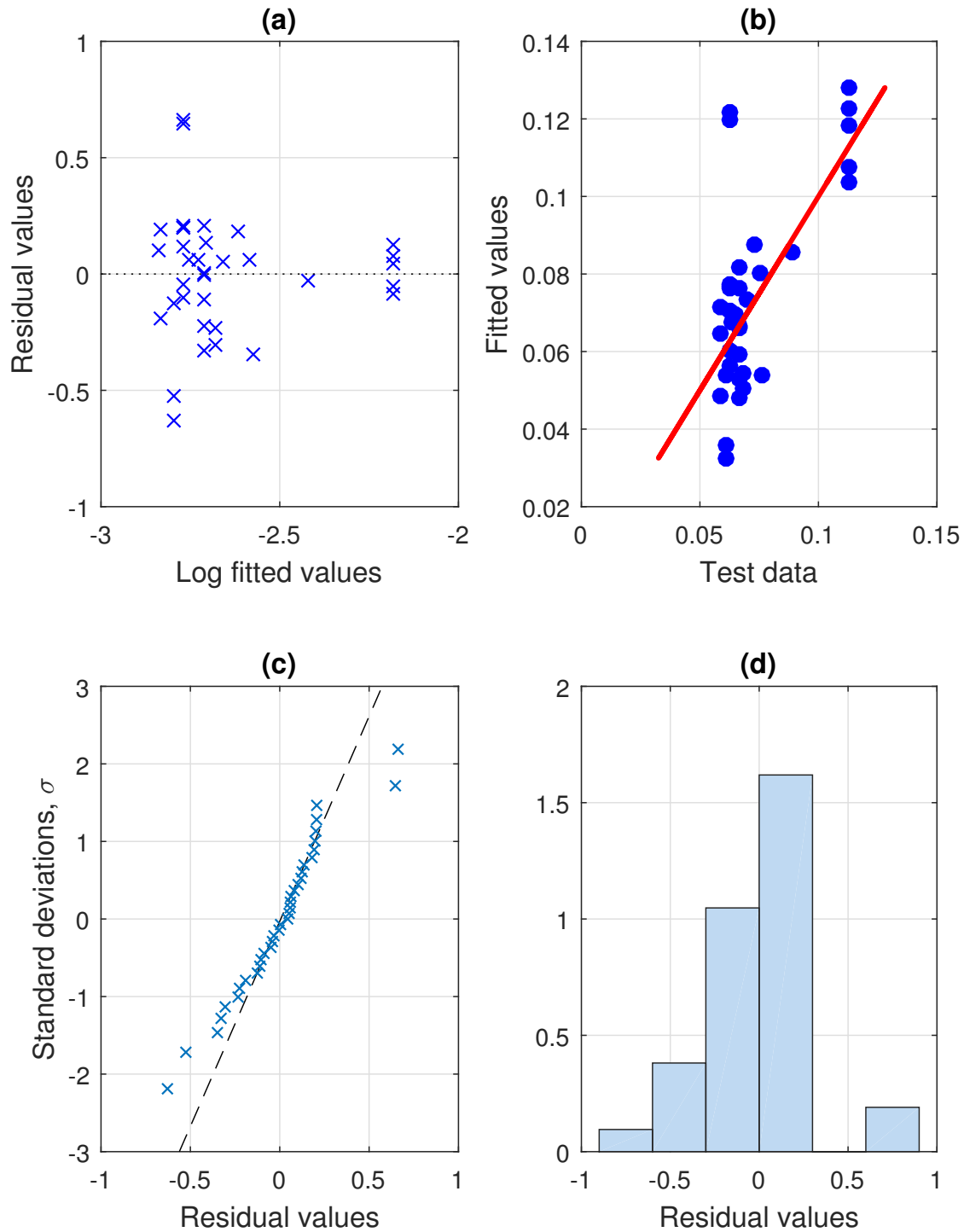


Figure 3.11: Diagnostics for the regression of  $\theta_{pc}^*$  of the first-cycle envelope component model for beams with RBS connections. (a) Residuals versus fitted values; (b) Fitted values versus test data; (c) QQ-plot; (d) Histogram of residuals.

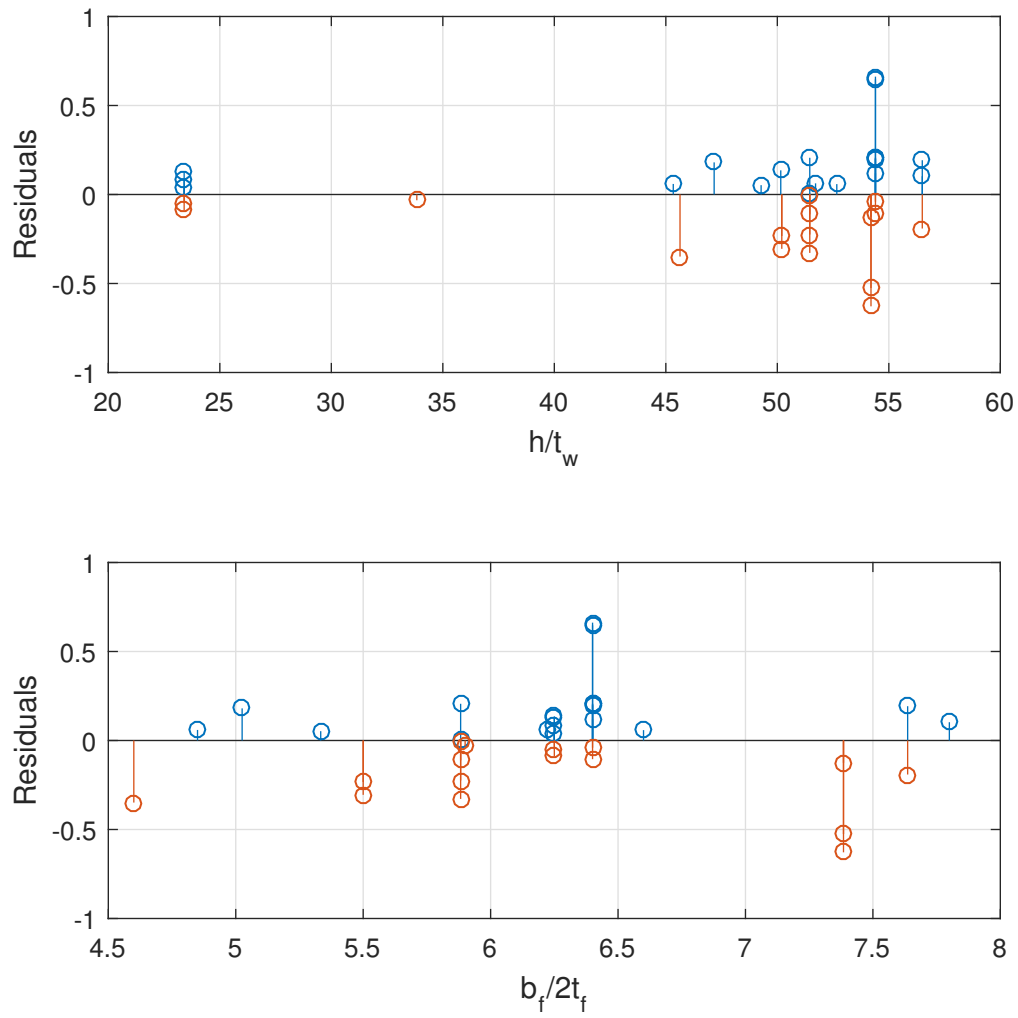
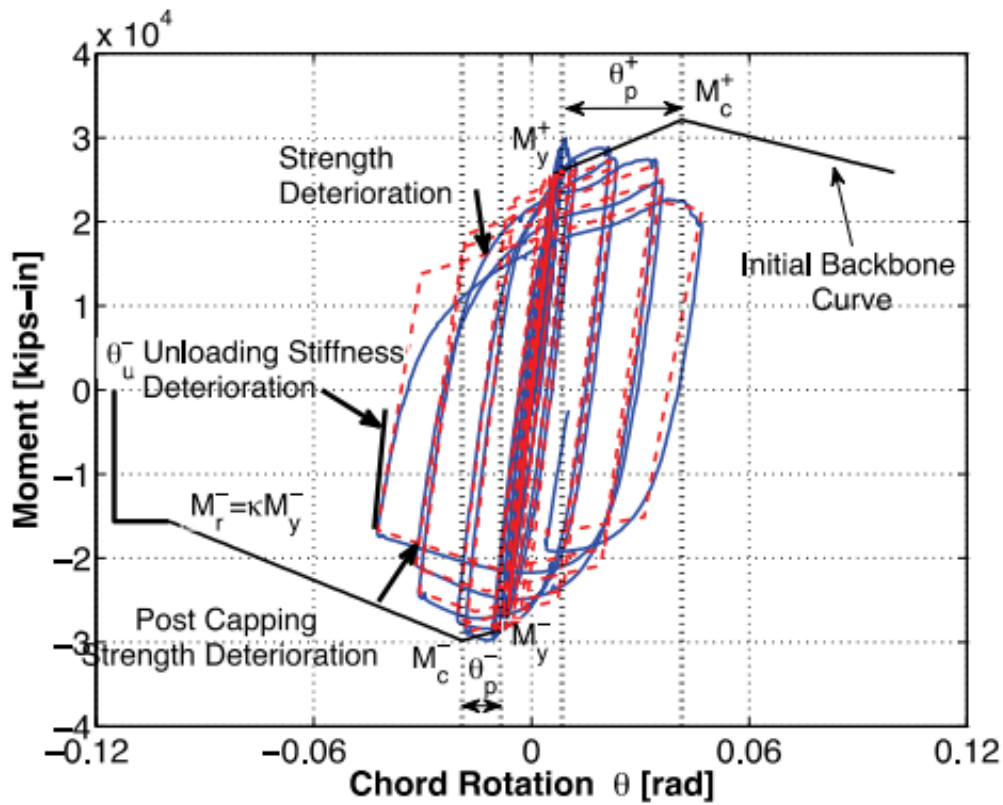
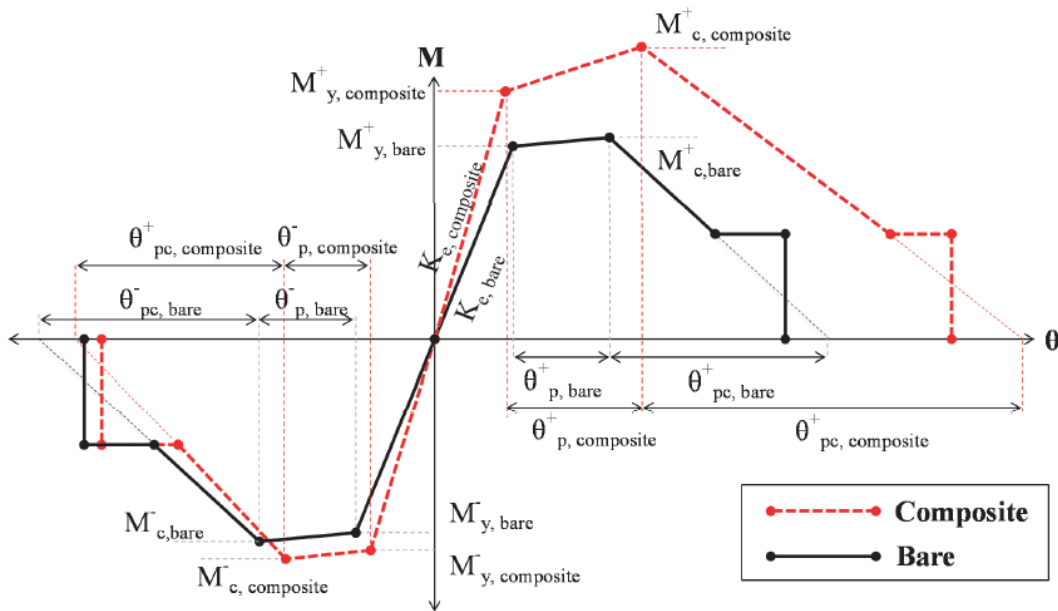


Figure 3.12: Plot of the residuals of the  $\theta_{pc}^*$  equation for the first-cycle envelope component model for beams with RBS connections.



(a) composite steel beam with RBS



(b) adjusted monotonic curve for composite beam effects

Figure 3.13: Composite effects on the hysteretic behaviour of steel beams. Images from Elkady and Lignos (2013, 2014), experimental data from Ricles et al. (2004).

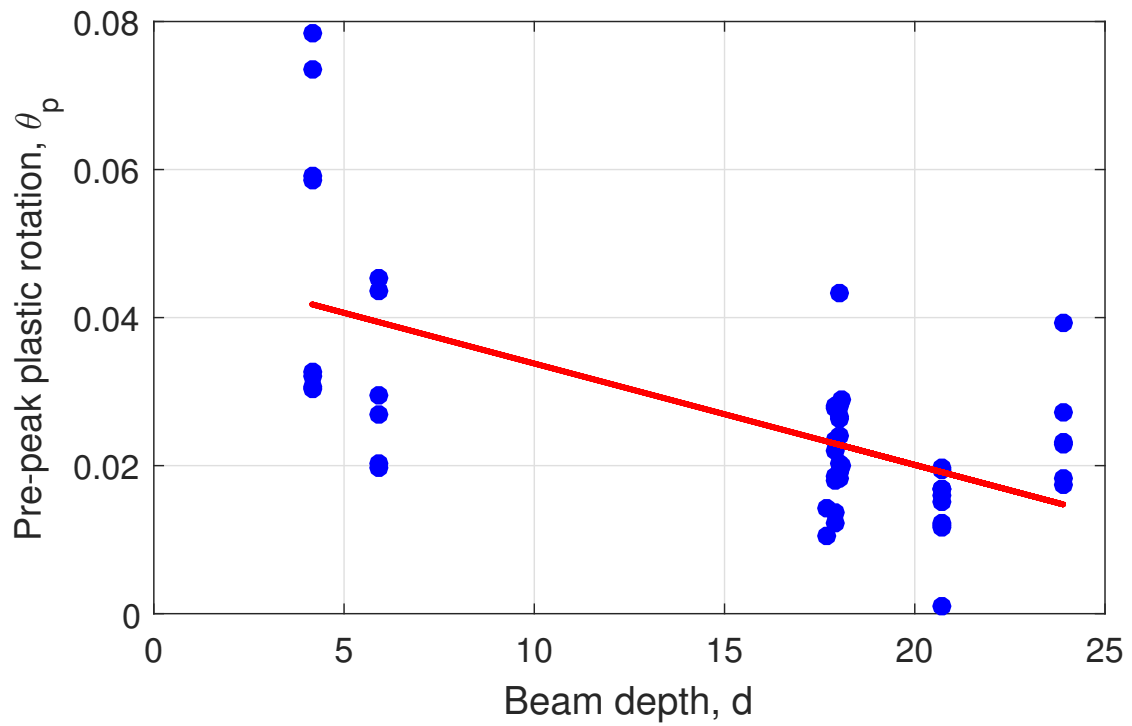


Figure 3.14: Trends on pre-peak plastic rotation for steel beams in pre-Northridge WUF-B connections.

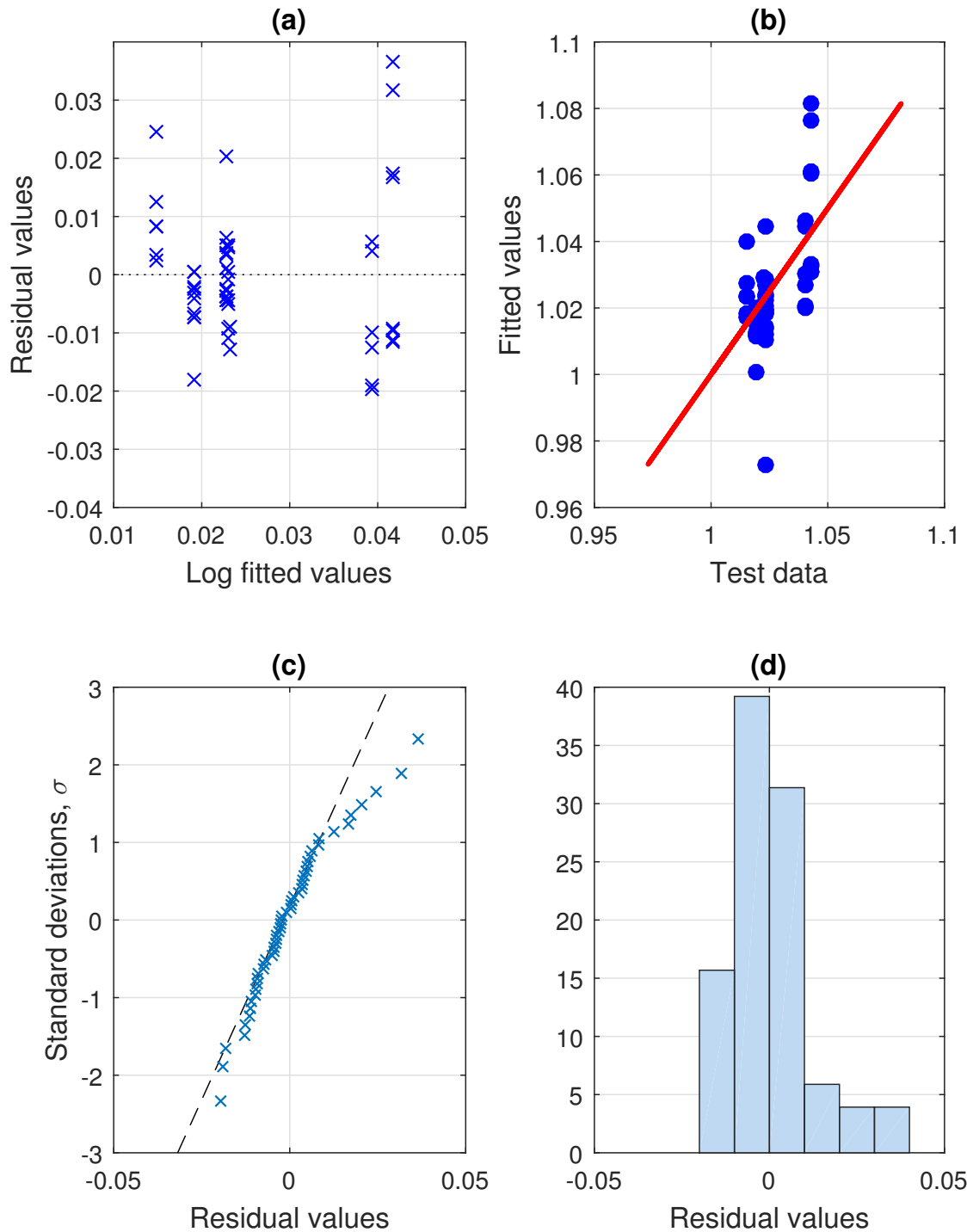


Figure 3.15: Diagnostics for regression of  $\theta_p$  for beams with pre-Northridge connections. (a) Residuals versus fitted values; (b) Fitted values versus test data; (c) QQ-plot; (d) Histogram of residuals.



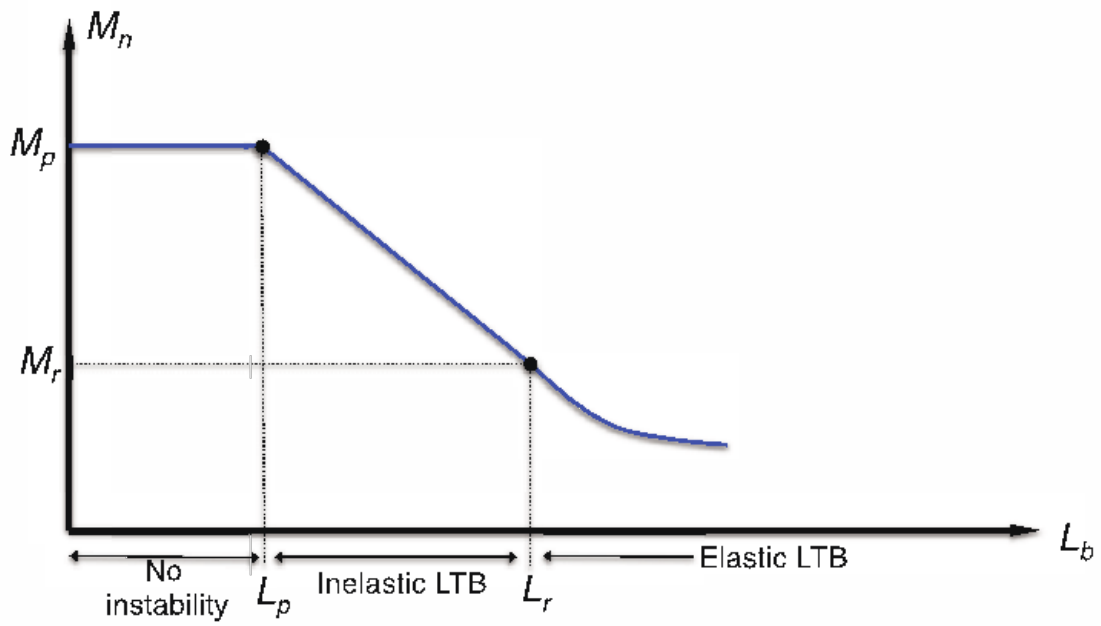
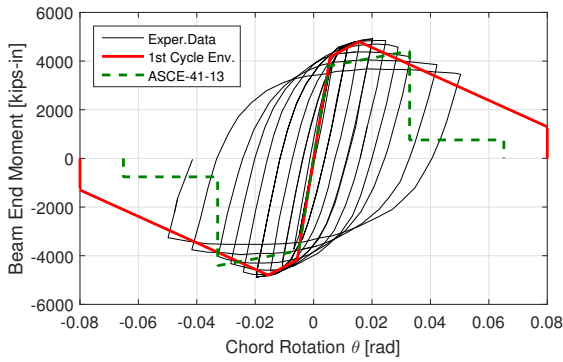
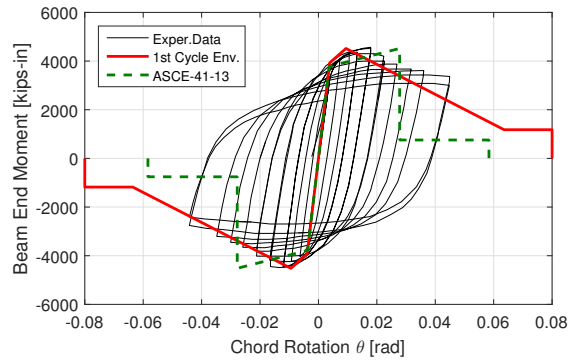


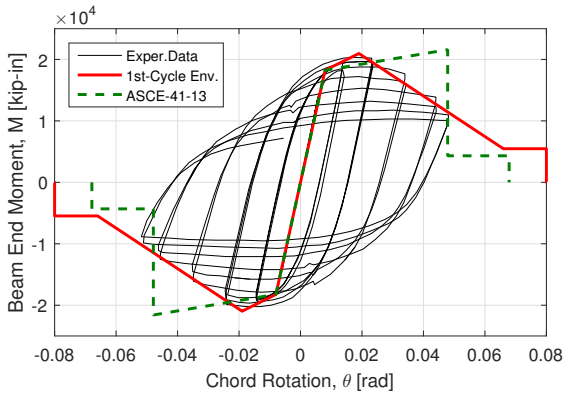
Figure 3.17: Flexural strength of bare steel beams with respect to their unbraced length, from ATC-114 (ATC, 2016).



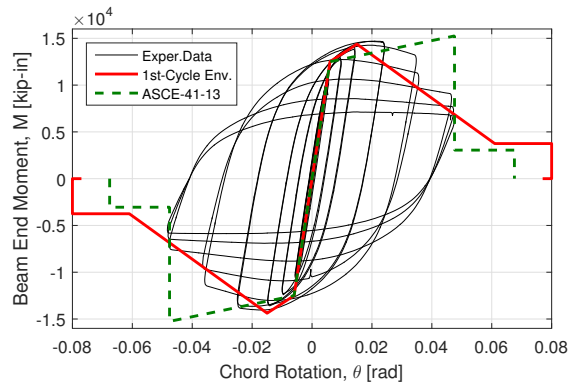
(a) W18X40 beam with WUF-B



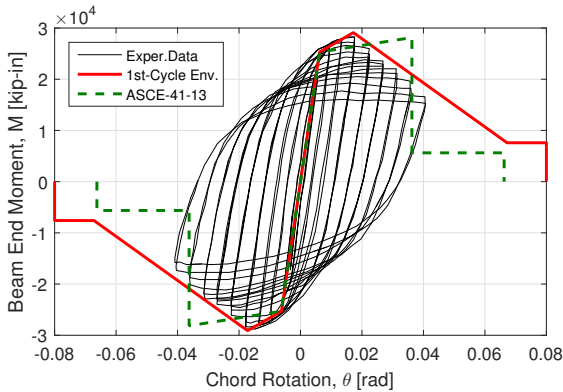
(b) W21X44 beam with WUF-B



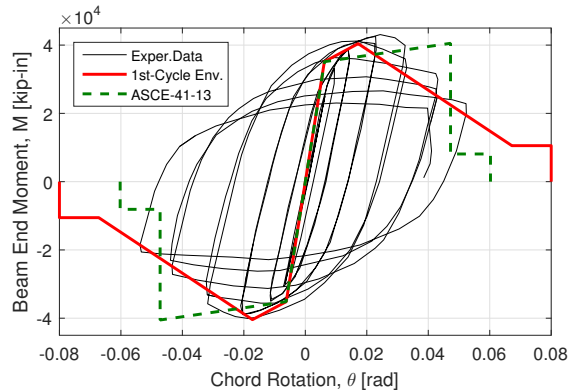
(c) W33X130 beam with RBS



(d) W30X99 beam with RBS



(e) W36X150 beam with welded flange plate



(f) W36X150 beam with WUF-W

Figure 3.18: Comparison of deduced beam moment-rotation response with predicted response from ASCE-41-13 and proposed ATC-114 component models. Data from: (a,b) Tsai and Popov (1988); (c) Popov et al. (1997); (d) Chi and Uang (2002); (e) Engelhardt et al. (2000); (f) Ricles et al. (2002); .

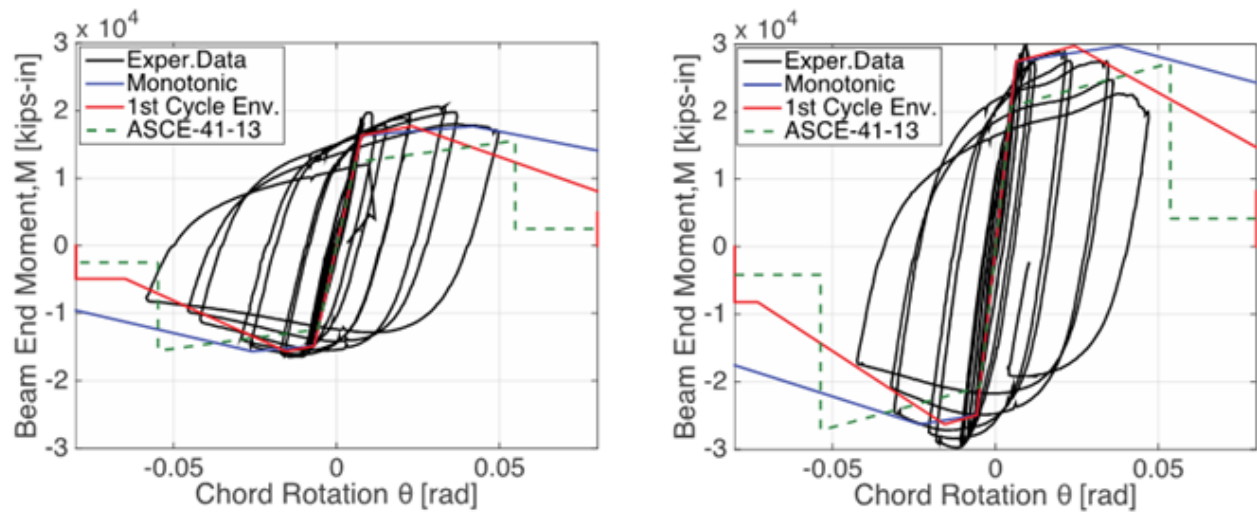


Figure 3.19: Comparisons of proposed modelling recommendations with ASCE-41-13 for composite steel beams, data from Zhang and Ricles (2006).

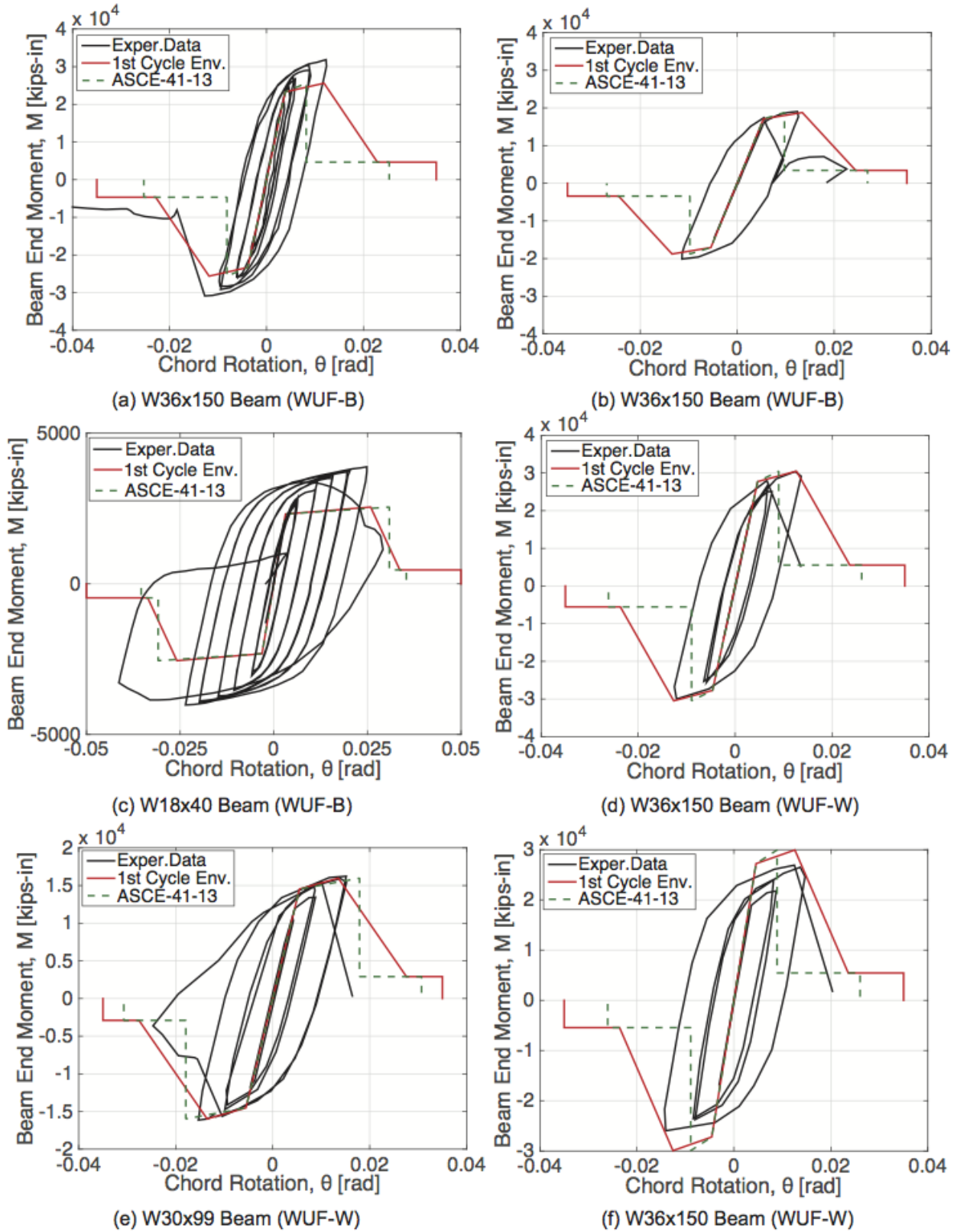


Figure 3.20: Comparisons of proposed modelling recommendations with ASCE-41-13 for steel beams as part of pre-Northridge beam-to-column connections. Data from FEMA (1997a); Tsai and Popov (1988); Engelhardt and Sabol (1994).

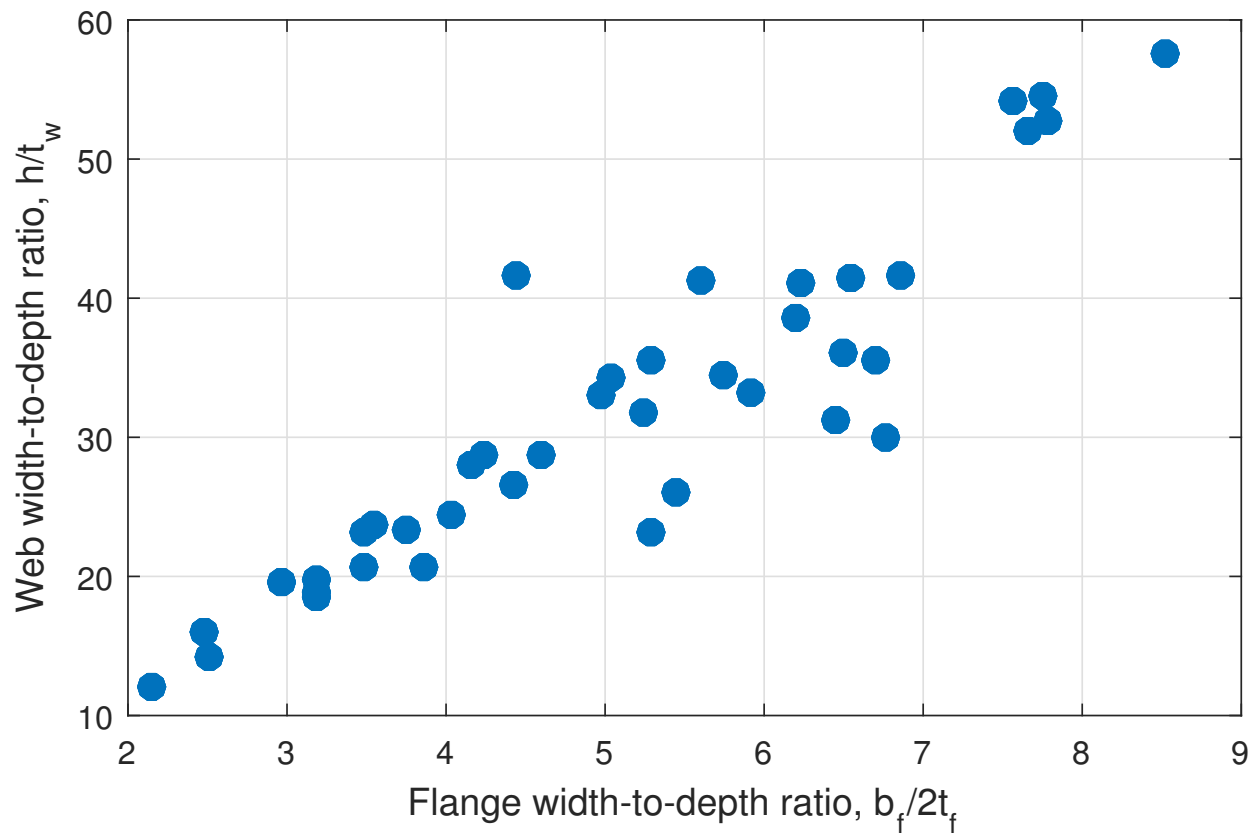


Figure 3.21: Plot of the web versus flange width-to-depth ratios from the database of steel wide-flange columns.

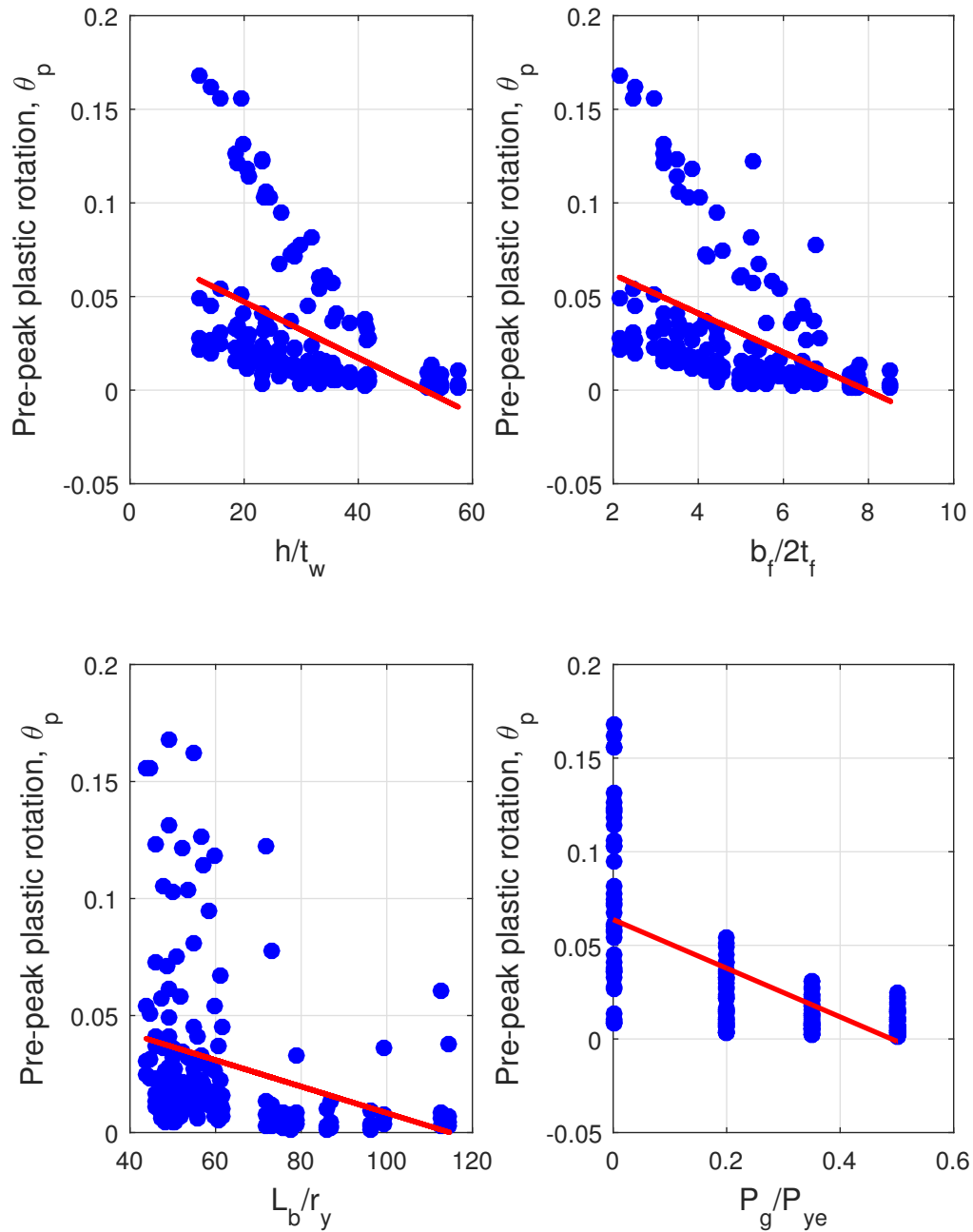


Figure 3.22: Trends on pre-peak plastic rotation,  $\theta_p$ , for steel wide-flange columns subjected to monotonic loading protocols.

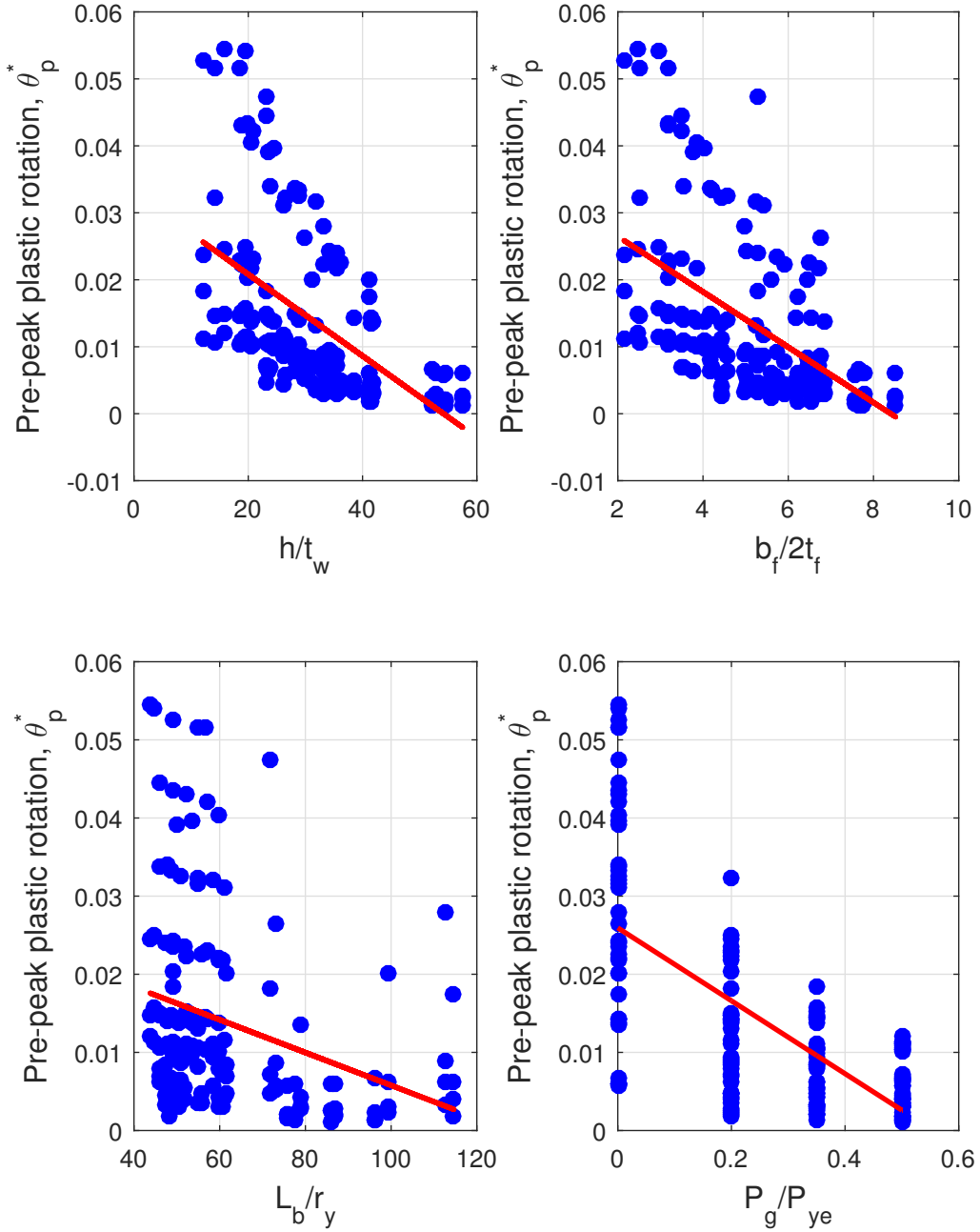


Figure 3.23: Trends on post-peak plastic rotation,  $\theta_p^*$ , for steel wide-flange columns subjected to symmetric cyclic loading protocols.

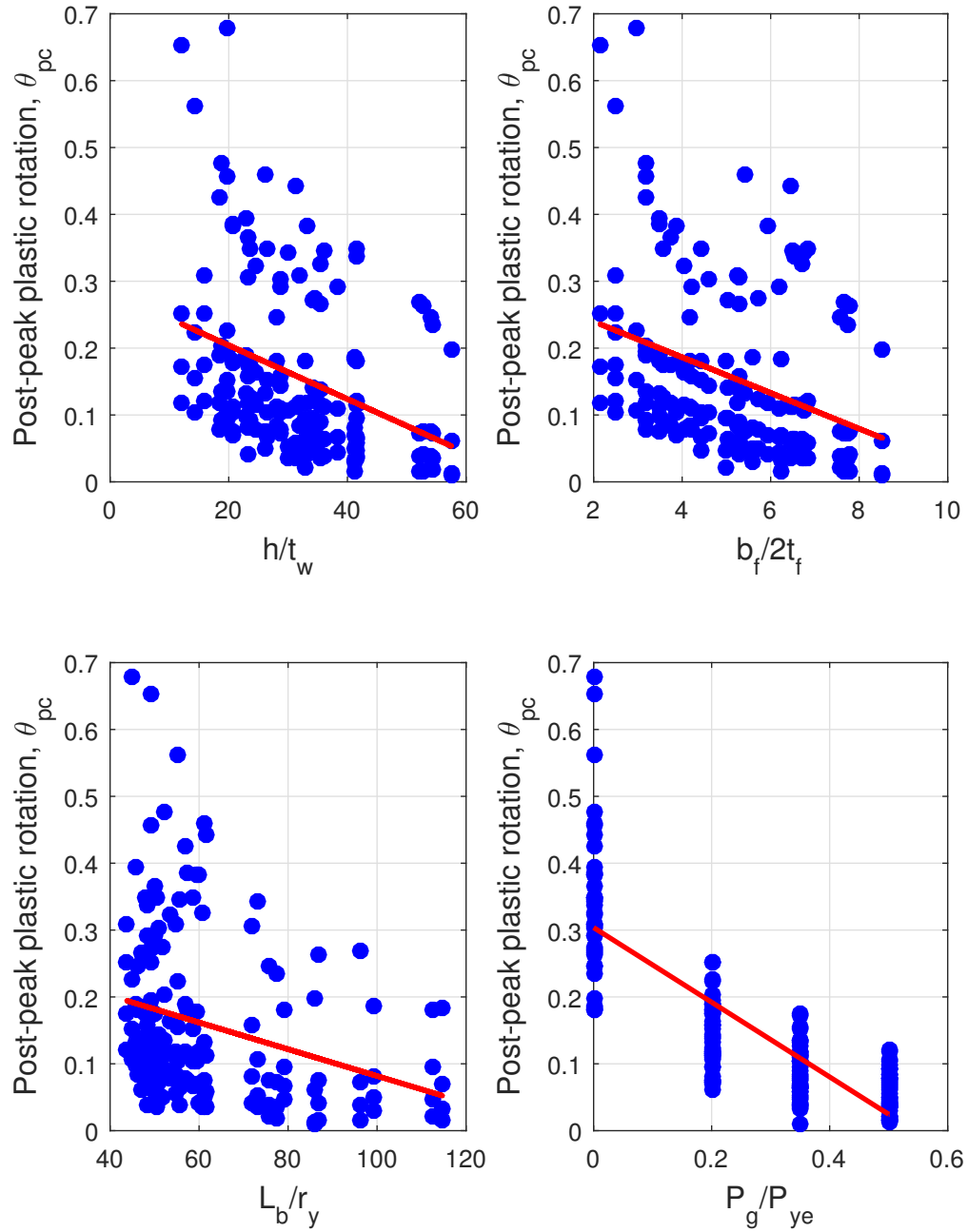


Figure 3.24: Trends on post-peak plastic rotation,  $\theta_{pc}$ , for steel wide-flange columns subjected to monotonic loading protocols.

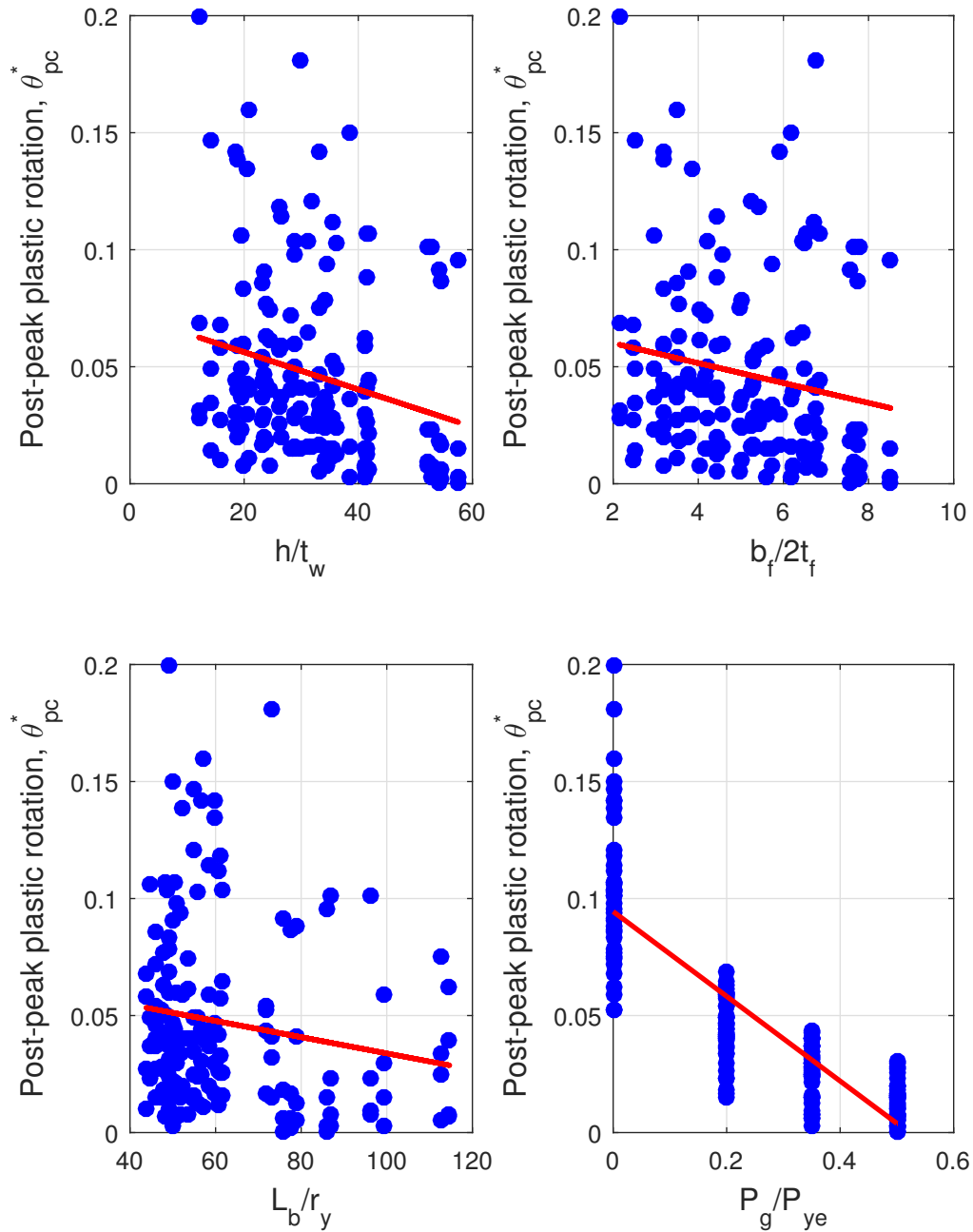


Figure 3.25: Trends on pre-peak plastic rotation,  $\theta_{pc}^*$ , for steel wide-flange columns subjected to symmetric cyclic loading protocols.

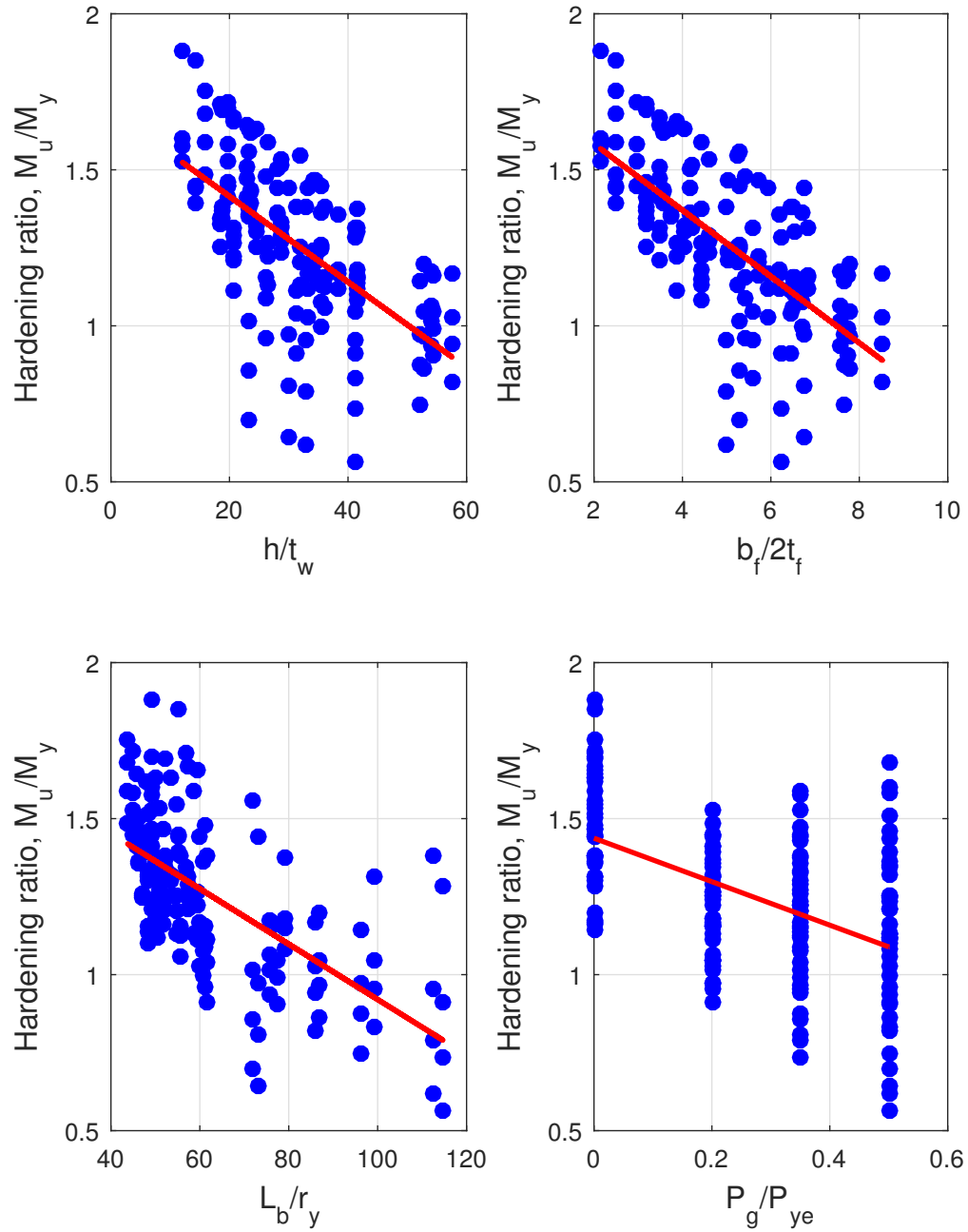


Figure 3.26: Trends on hardening ratio,  $a = M_{max}/M_y^*$ , for steel wide-flange columns subjected to monotonic loading protocols.

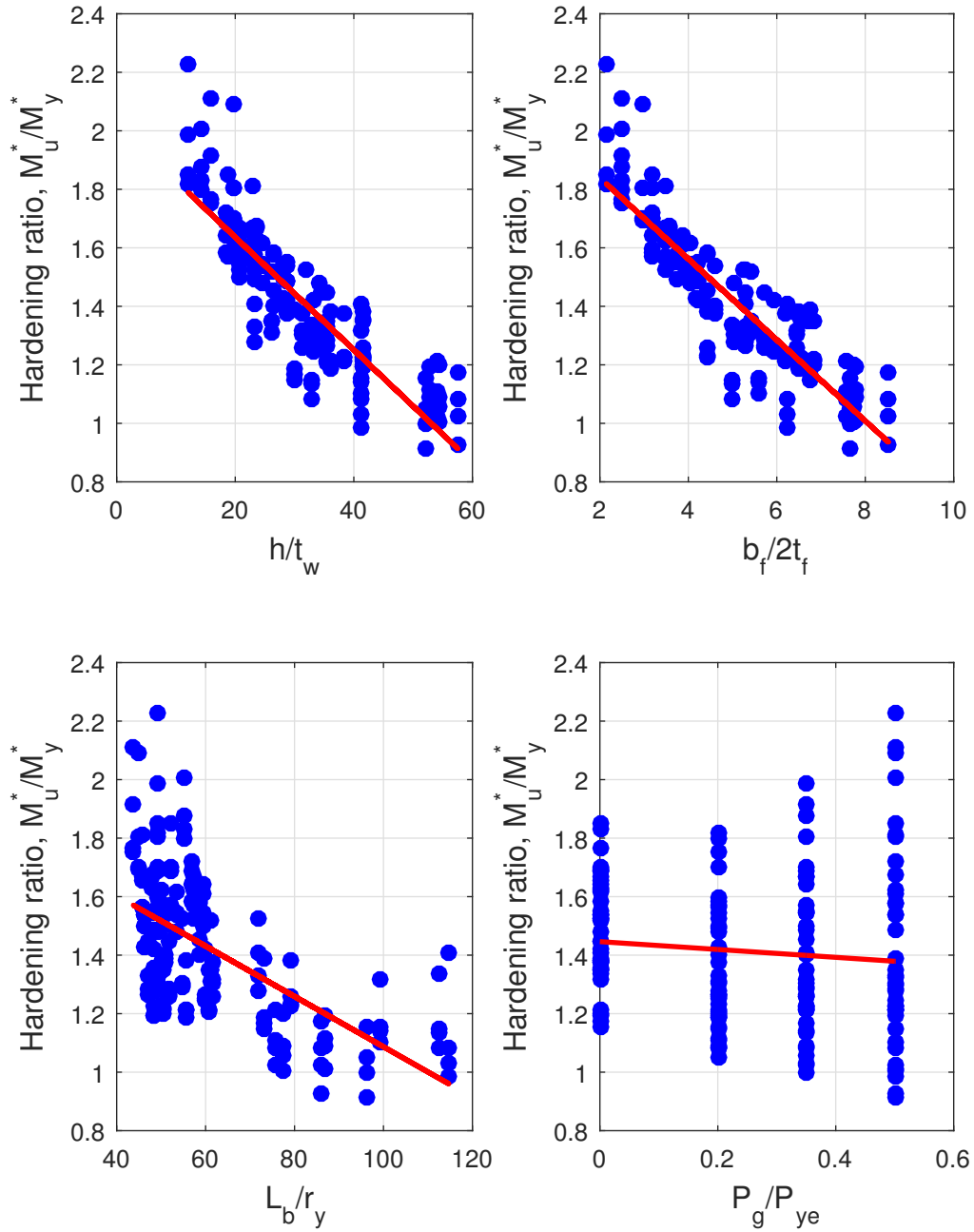


Figure 3.27: Trends on hardening ratio,  $a^* = M_{max}^*/M_y^*$ , for steel wide-flange columns subjected to symmetric cyclic loading protocols.

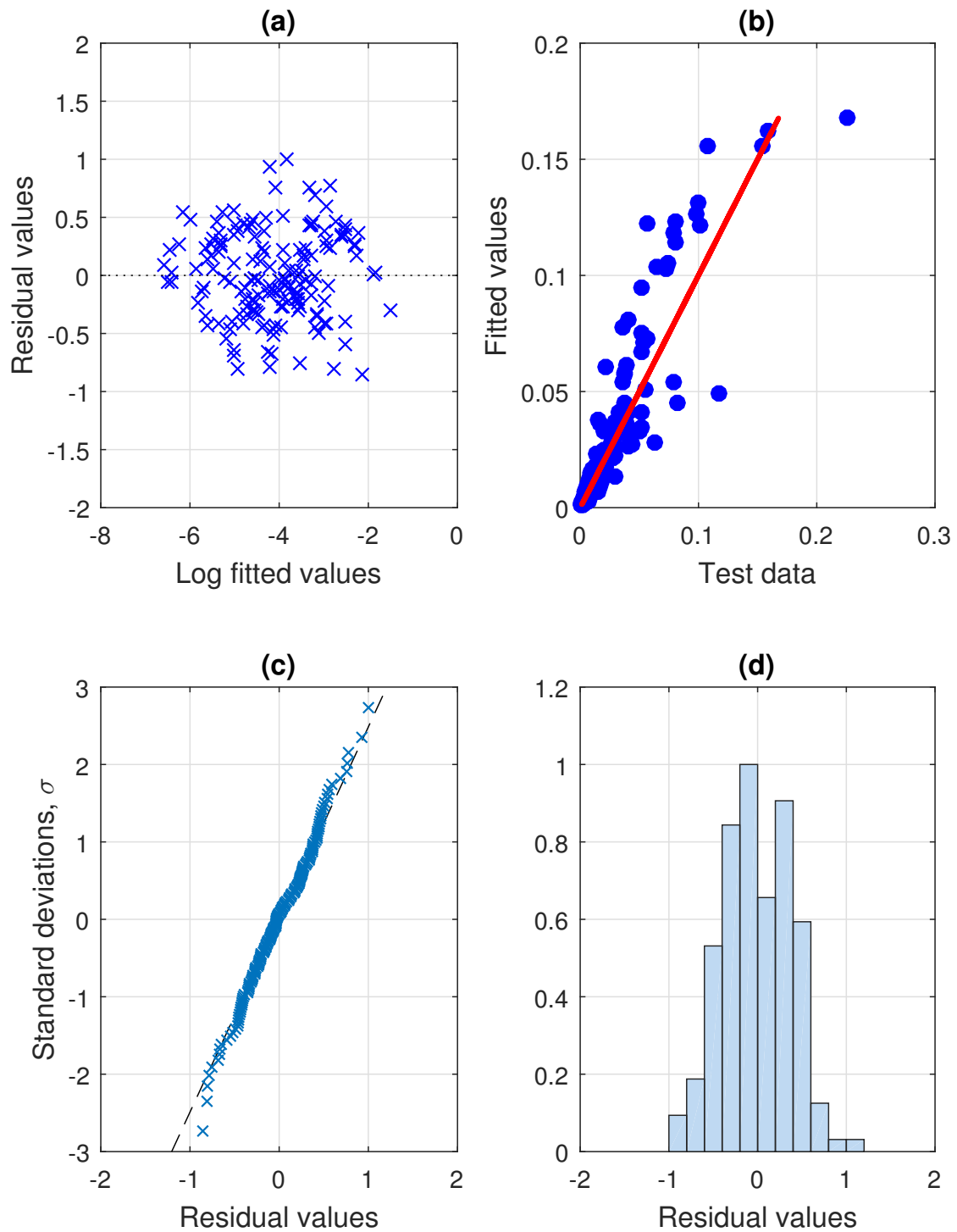


Figure 3.28: Diagnostics for the regression of  $\theta_p$  for the monotonic backbone component model for wide-flange columns. (a) Residuals versus fitted values; (b) Fitted values versus test data; (c) QQ-plot; (d) Histogram of residuals.

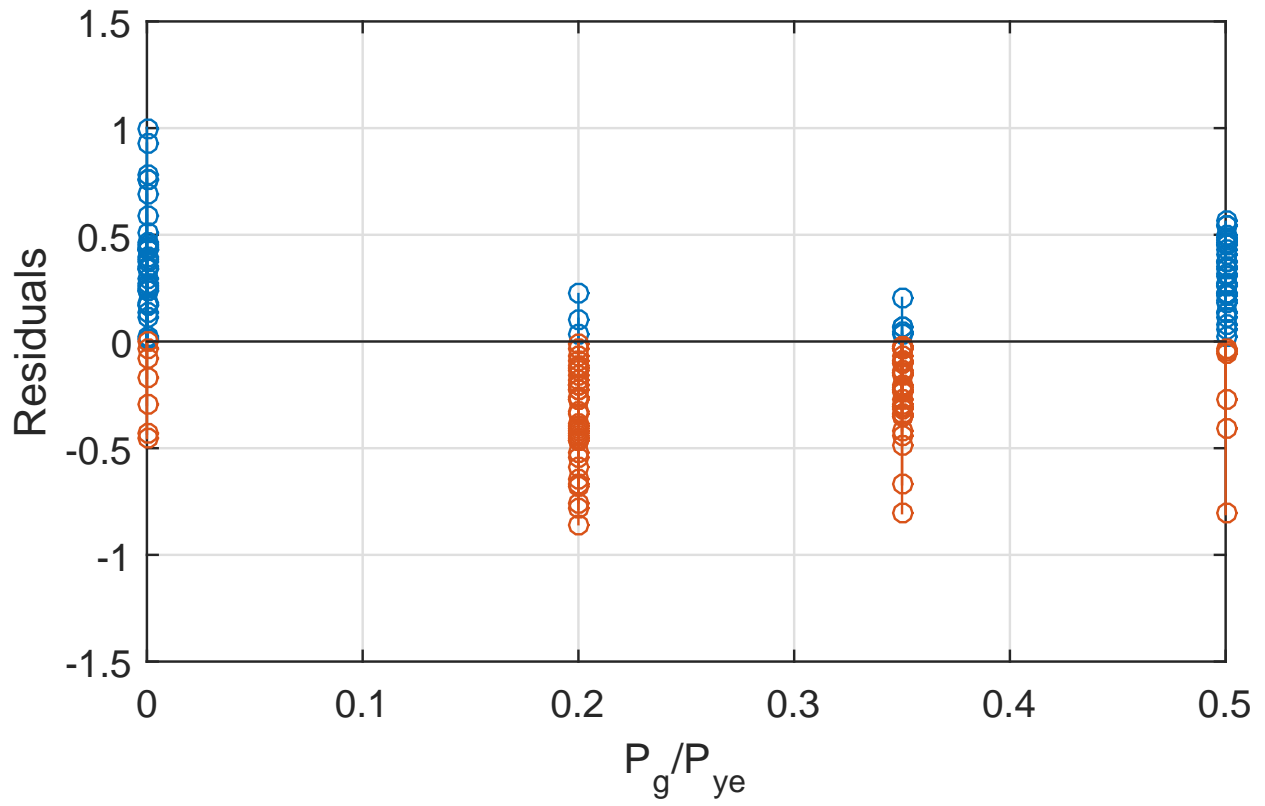


Figure 3.29: Plot of residuals versus  $P_g/P_{ye}$  for  $\theta_p$  for the monotonic backbone component model for wide-flange columns.

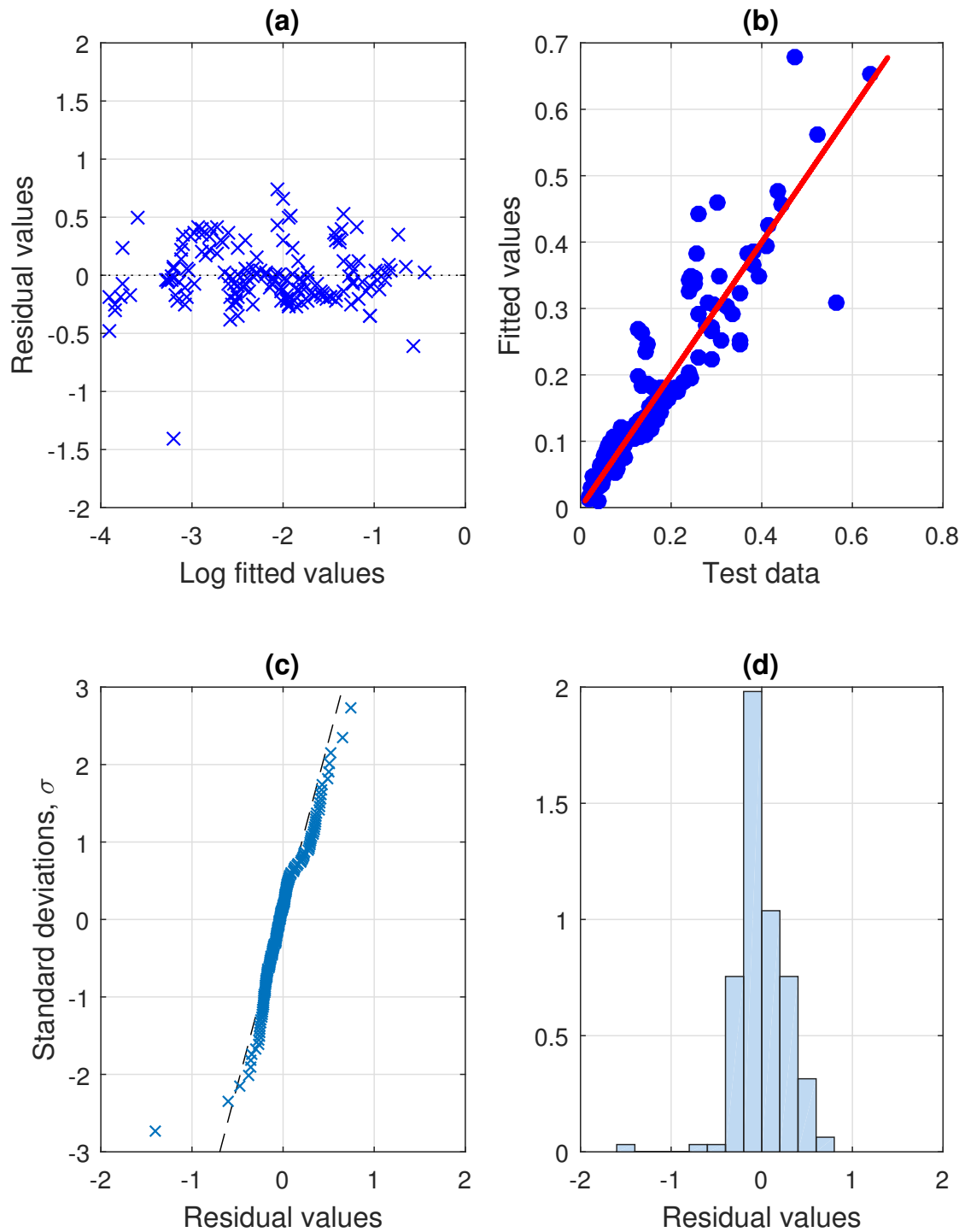


Figure 3.30: Diagnostics for the regression of  $\theta_{pc}$  for the monotonic backbone component model for wide-flange columns. (a) Residuals versus fitted values; (b) Fitted values versus test data; (c) QQ-plot; (d) Histogram of residuals.

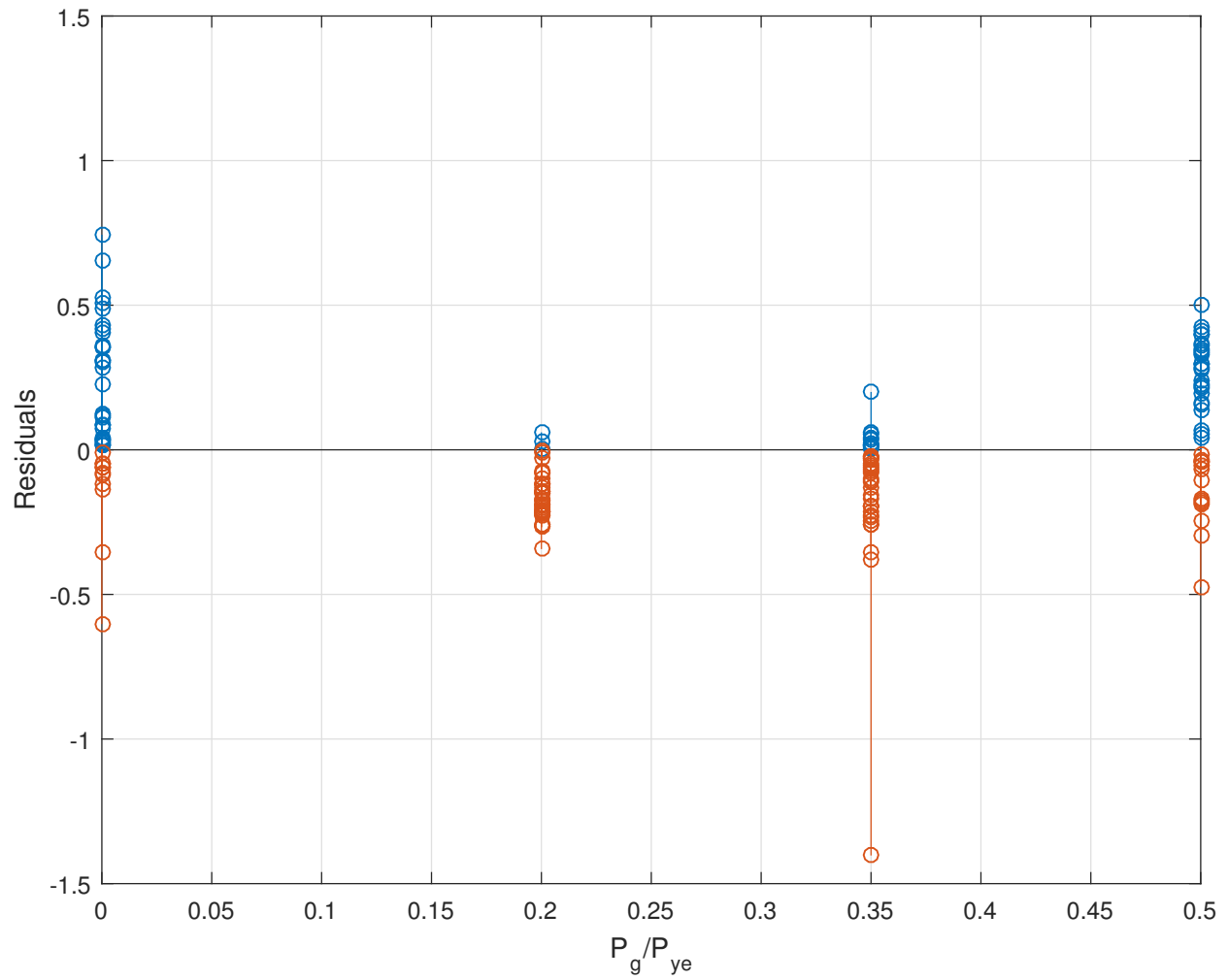


Figure 3.31: Plot of residuals versus  $P_g/P_{ye}$  for  $\theta_{pc}$  for the monotonic backbone component model for wide-flange columns.

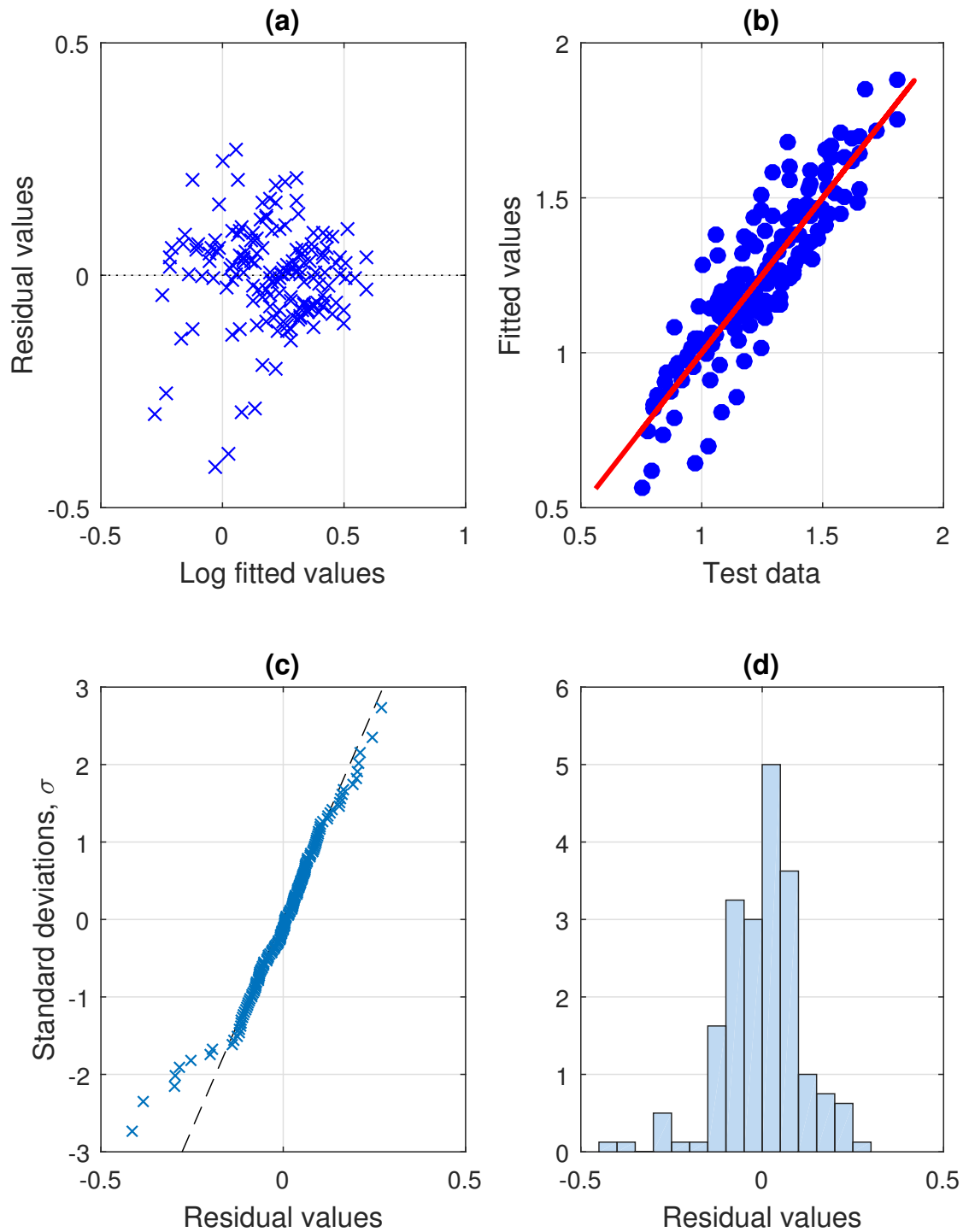


Figure 3.32: Diagnostics for the regression of  $a = M_{max}/M_y^*$  for the monotonic backbone component model for wide-flange columns. (a) Residuals versus fitted values; (b) Fitted values versus test data; (c) QQ-plot; (d) Histogram of residuals.

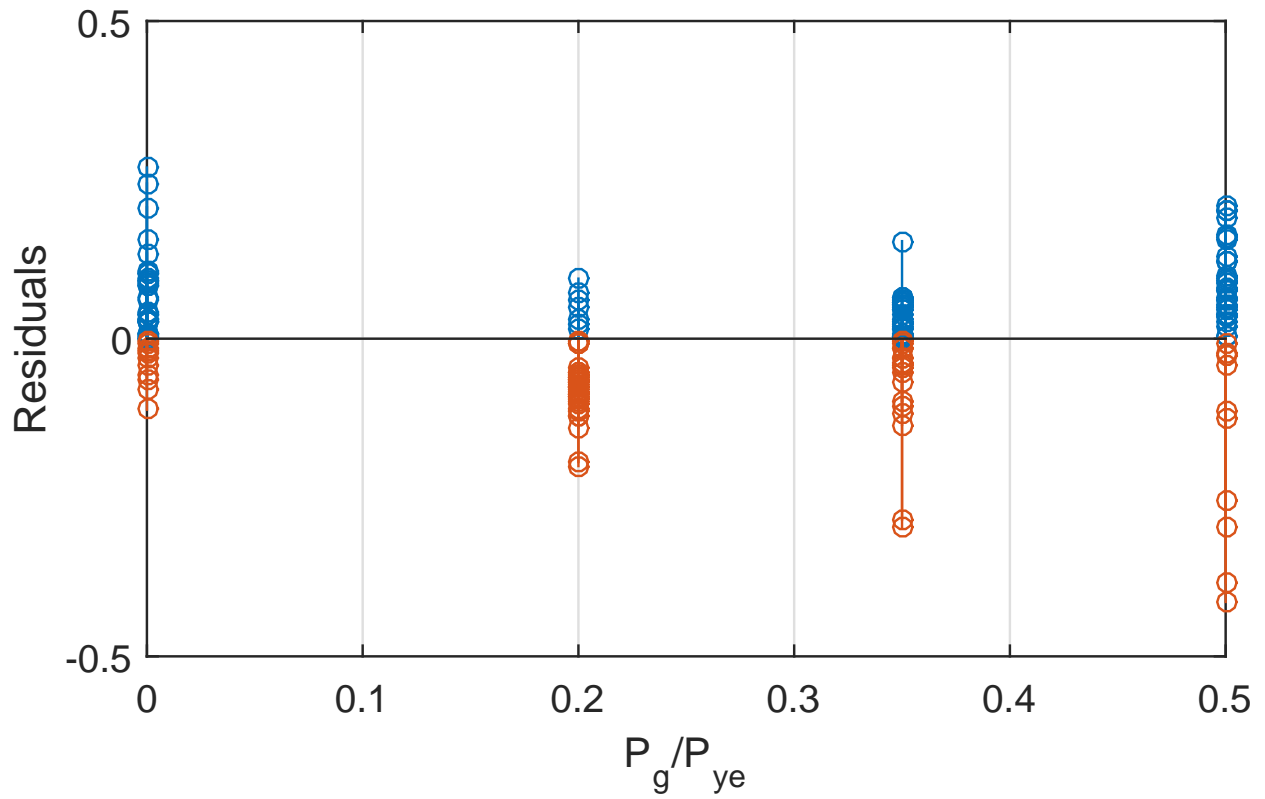


Figure 3.33: Plot of residuals versus  $P_g/P_{ye}$  for  $a = M_{max}/M_y^*$  for the monotonic backbone component model for wide-flange columns.

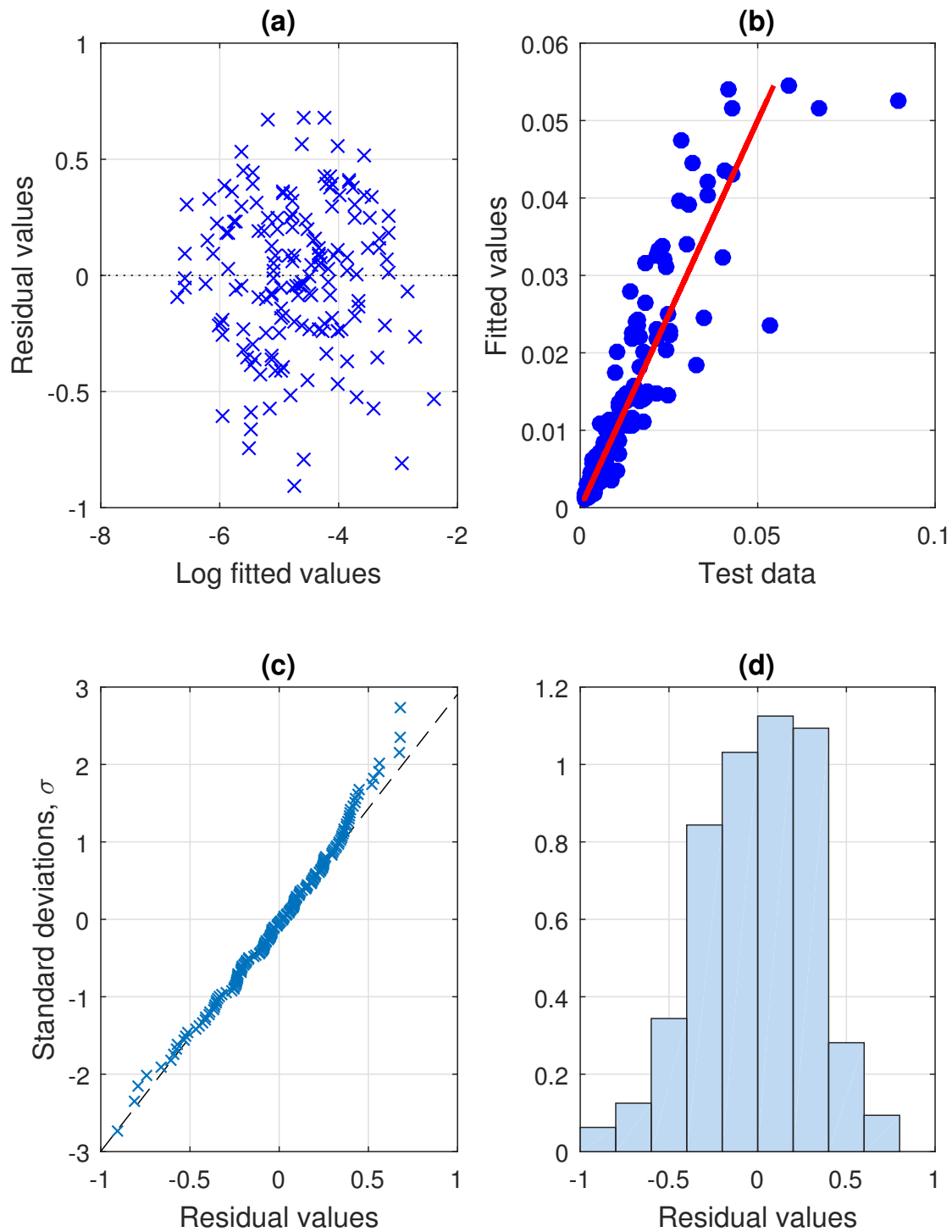


Figure 3.34: Diagnostics for the regression of  $\theta_p^*$  for the first-cycle envelope component model for wide-flange columns. (a) Residuals versus fitted values; (b) Fitted values versus test data; (c) QQ-plot; (d) Histogram of residuals.

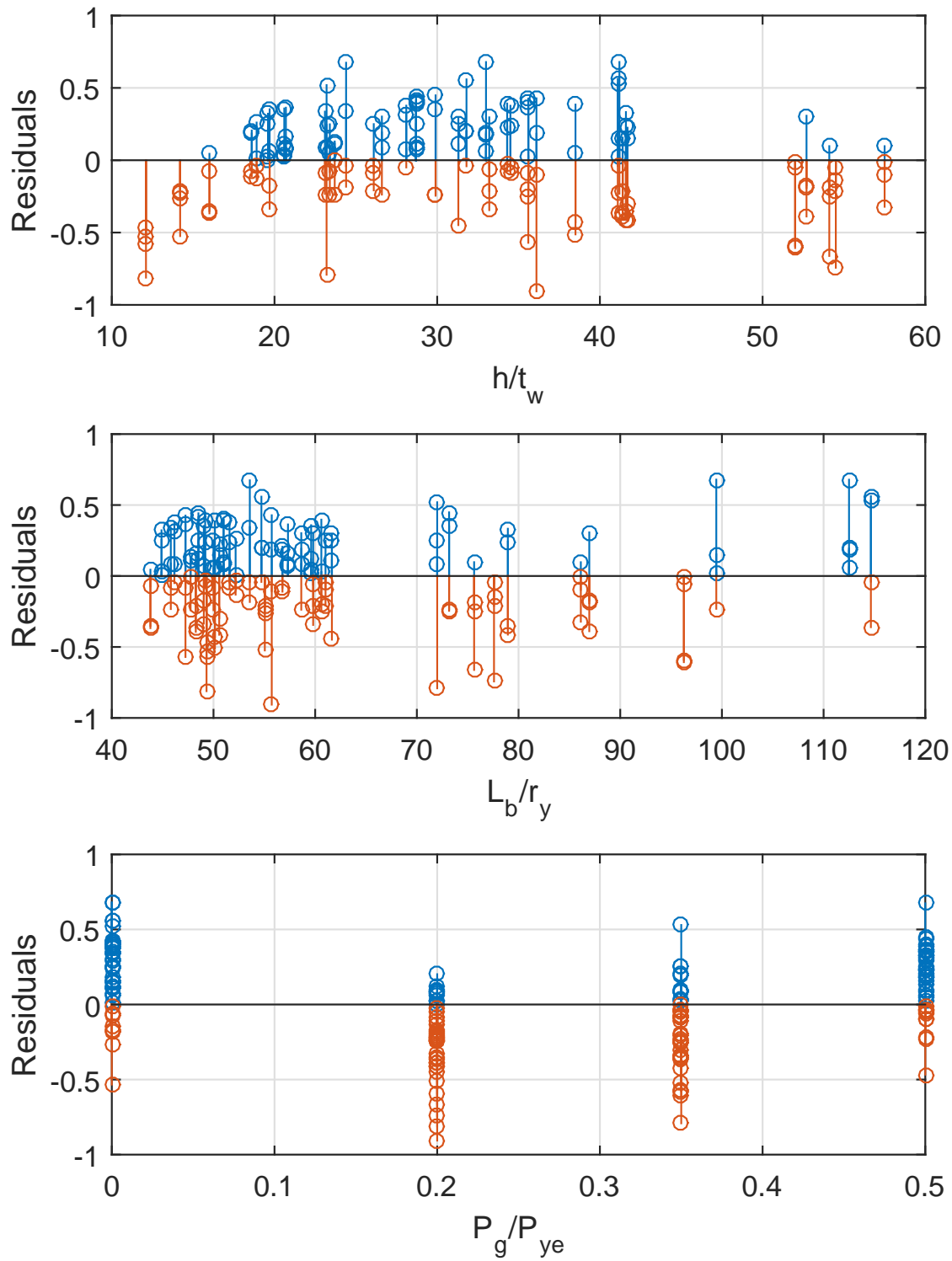


Figure 3.35: Plot of residuals versus predictors of  $\theta_p^*$  for the first-cycle envelope component model for wide-flange columns.

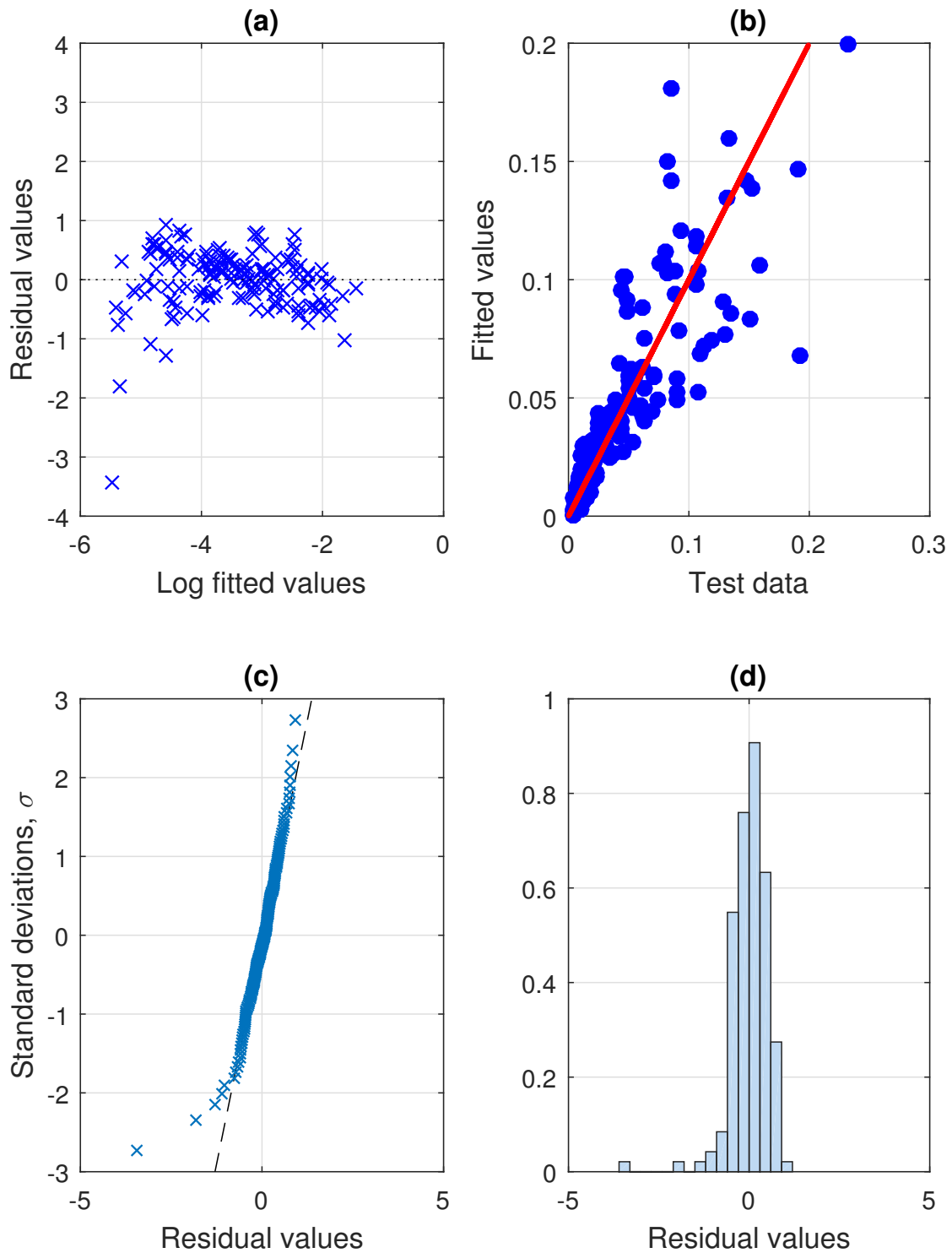


Figure 3.36: Diagnostics for the regression of  $\theta_{pc}^*$  for the first-cycle envelope component model for wide-flange columns. (a) Residuals versus fitted values; (b) Fitted values versus test data; (c) QQ-plot; (d) Histogram of residuals.

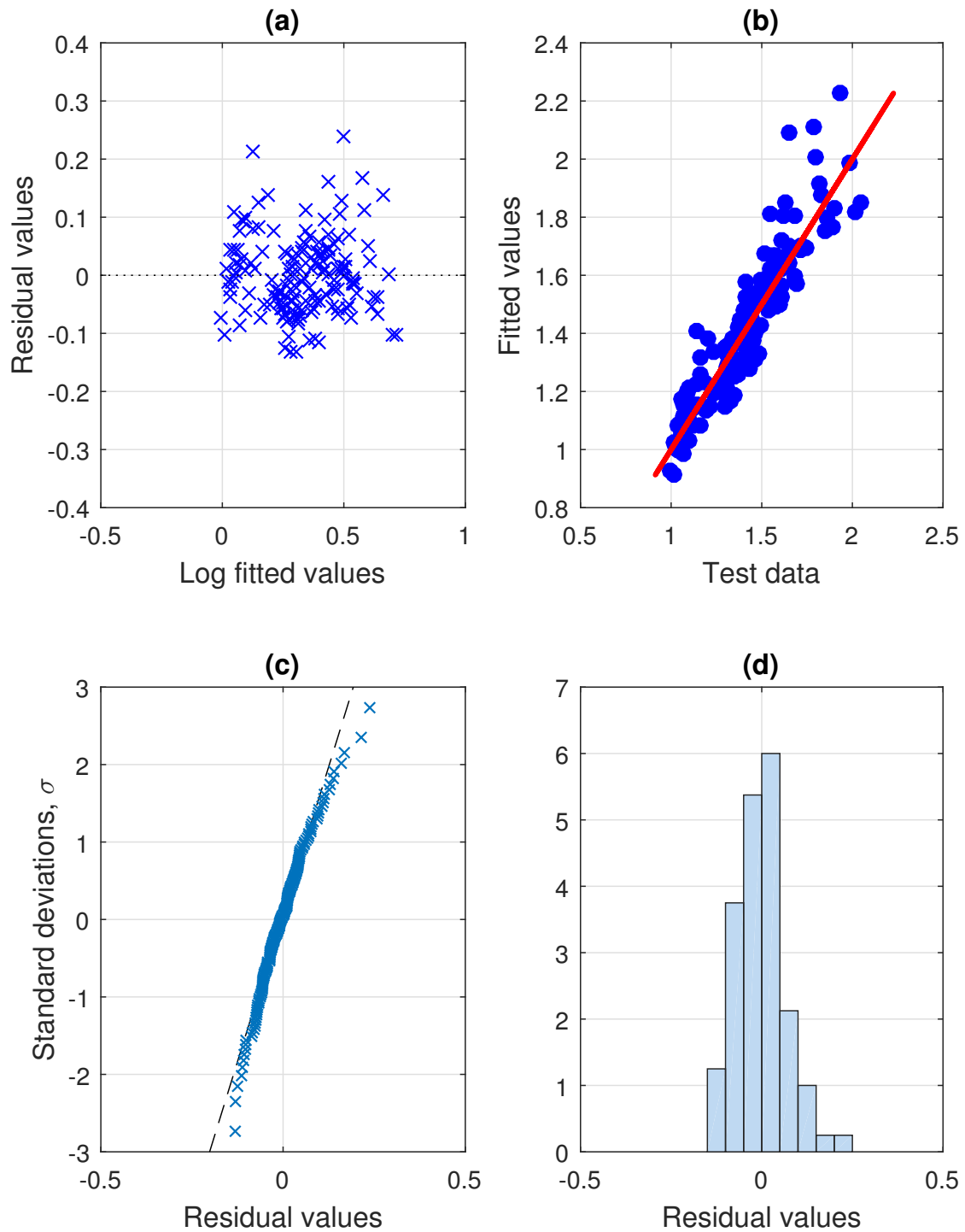


Figure 3.37: Diagnostics for the regression of  $a^* = M_{max}^*/M_y^*$  for the first-cycle envelope component model for wide-flange columns. (a) Residuals versus fitted values; (b) Fitted values versus test data; (c) QQ-plot; (d) Histogram of residuals.

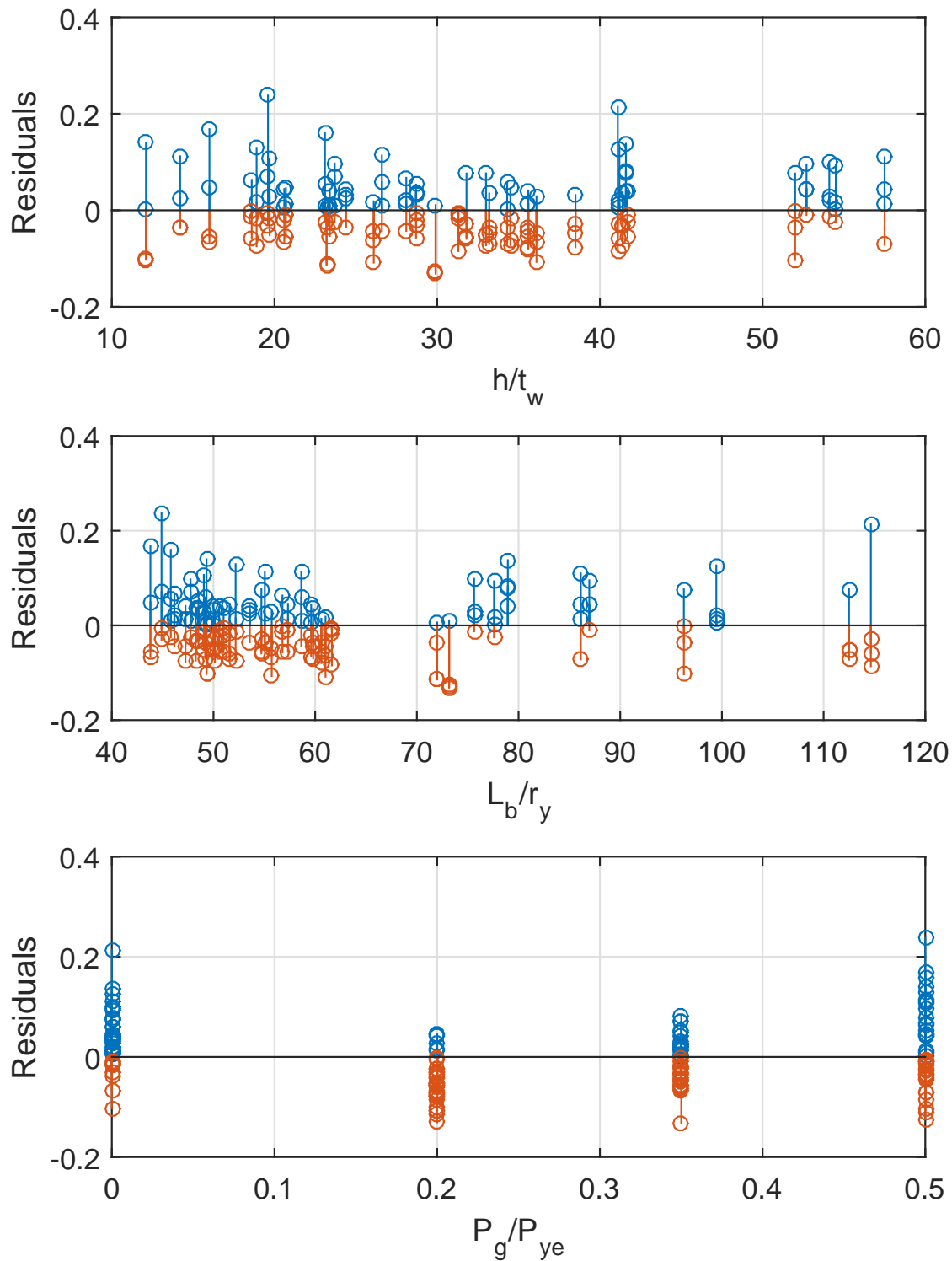
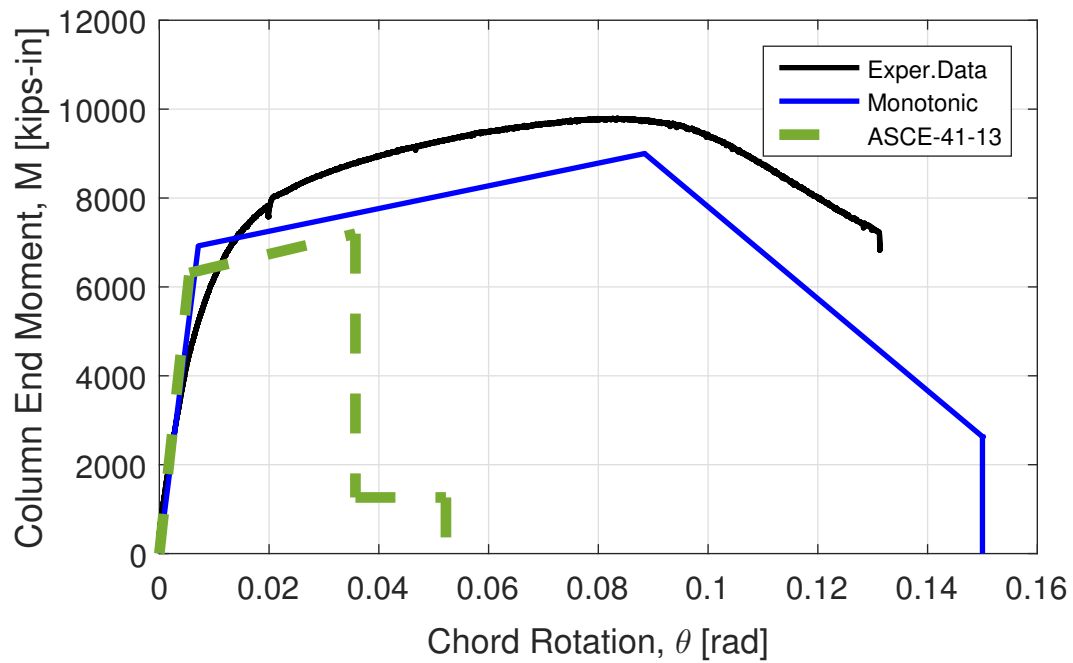
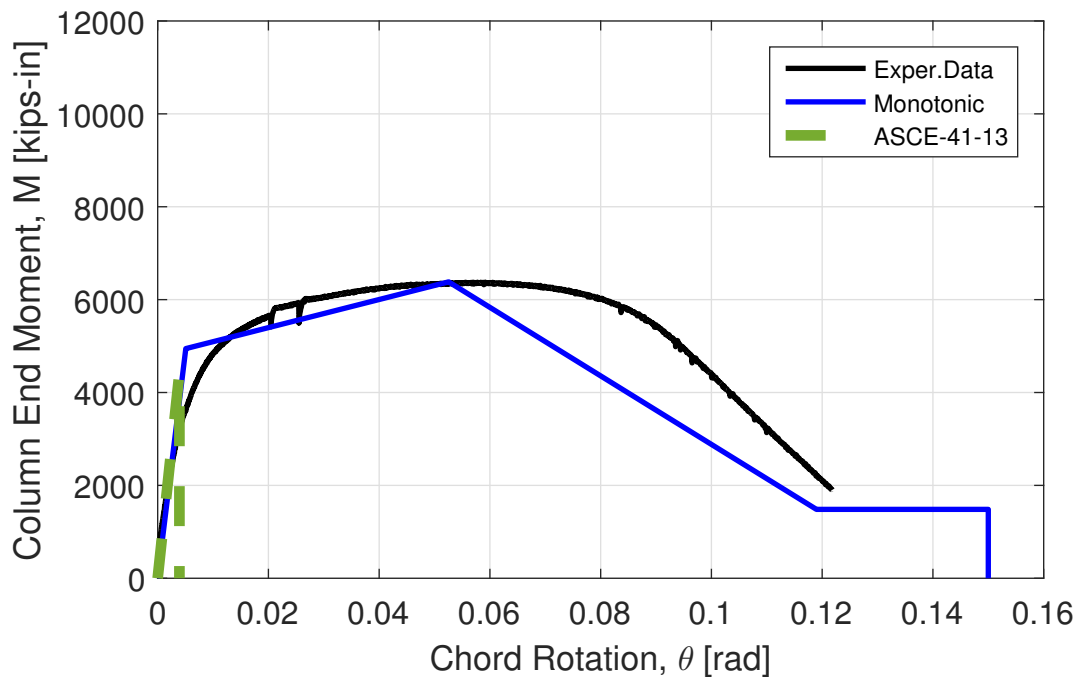


Figure 3.38: Plot of residuals versus predictors of  $a^* = M_{max}^*/M_y^*$  for the first-cycle envelope component model for wide-flange columns.

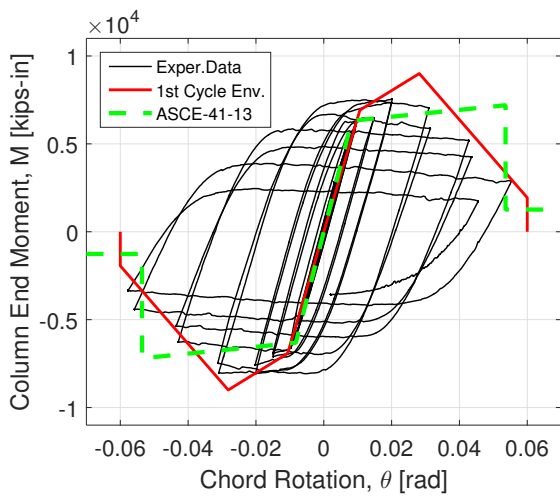


(a) W14X82  $P_g/P_{ye} = 0.30$

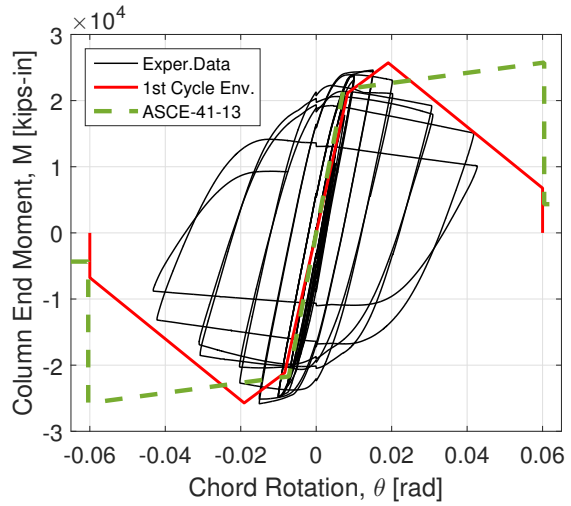


(b) W14X82  $P_g/P_{ye} = 0.50$

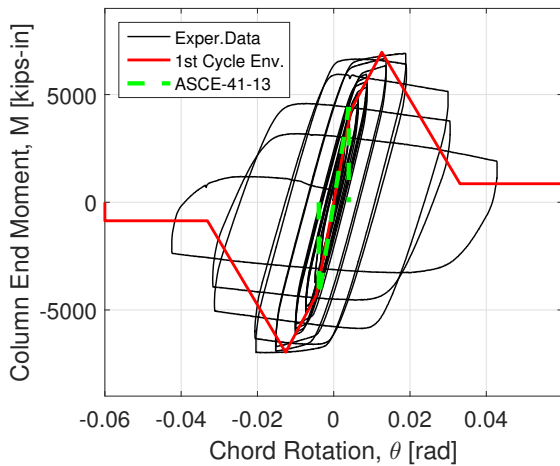
Figure 3.39: Comparison between test data and proposed ATC-114-1 monotonic backbone component model for wide-flange beam columns. Data from Suzuki and Lignos (2015).



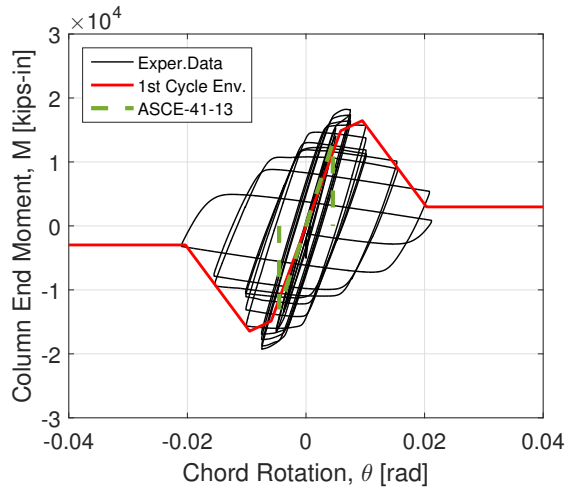
(a) W14X82  $P_g/P_{ye} = 0.30$



(b) W24X146  $P_g/P_{ye} = 0.20$



(c) W14X82  $P_g/P_{ye} = 0.50$



(d) W24X146  $P_g/P_{ye} = 0.50$

Figure 3.40: Comparison between test data and proposed ATC-114-1 component model based on the first cycle envelope for wide-flange beam columns. Data from Elkady and Lignos (2016), and Lignos et al. (2016).

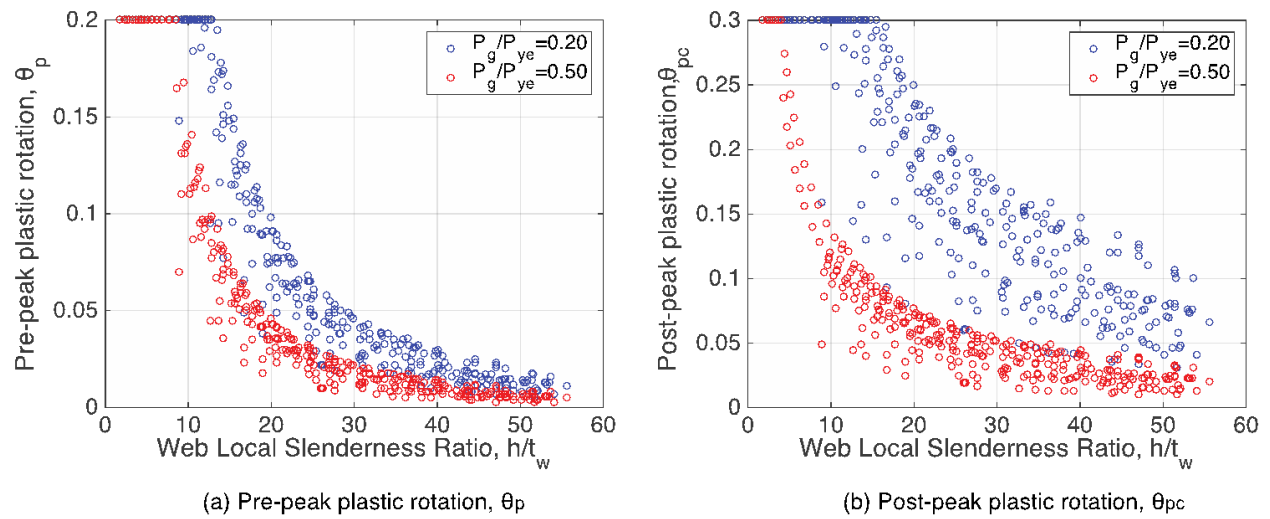


Figure 3.41: Trends of pre- and post-peak plastic deformations with respect to the cross-section web local slenderness ratio for modelling the monotonic backbone curve of steel wide-flange columns, from ATC (2016).

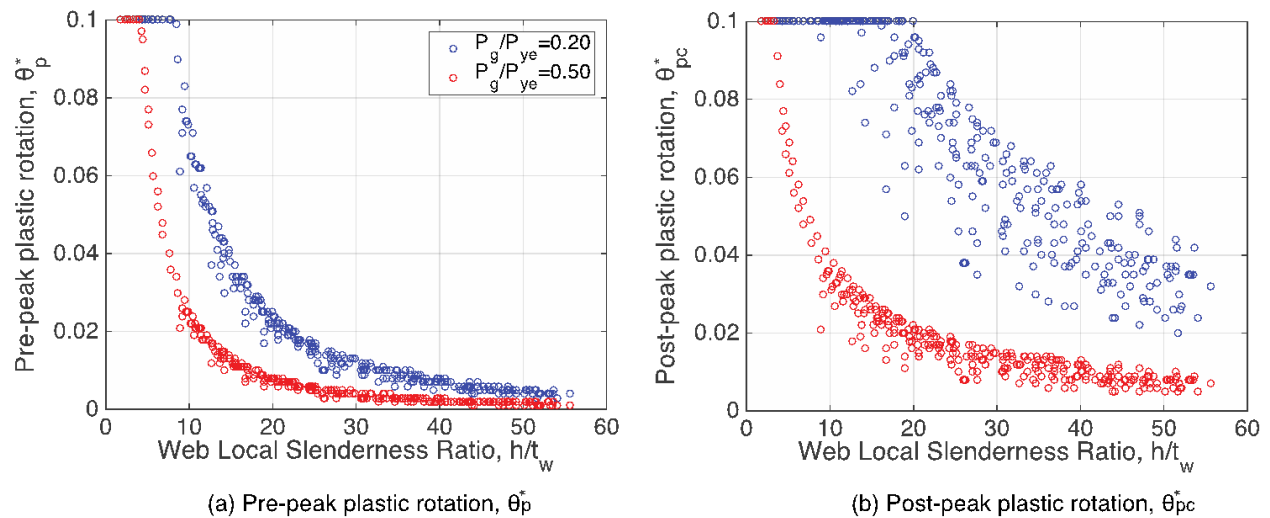


Figure 3.42: Trends of pre- and post-peak plastic deformations with respect to the cross-section web local slenderness ratio for modelling the first-cycle envelope curve of steel wide-flange columns, from ATC (2016).

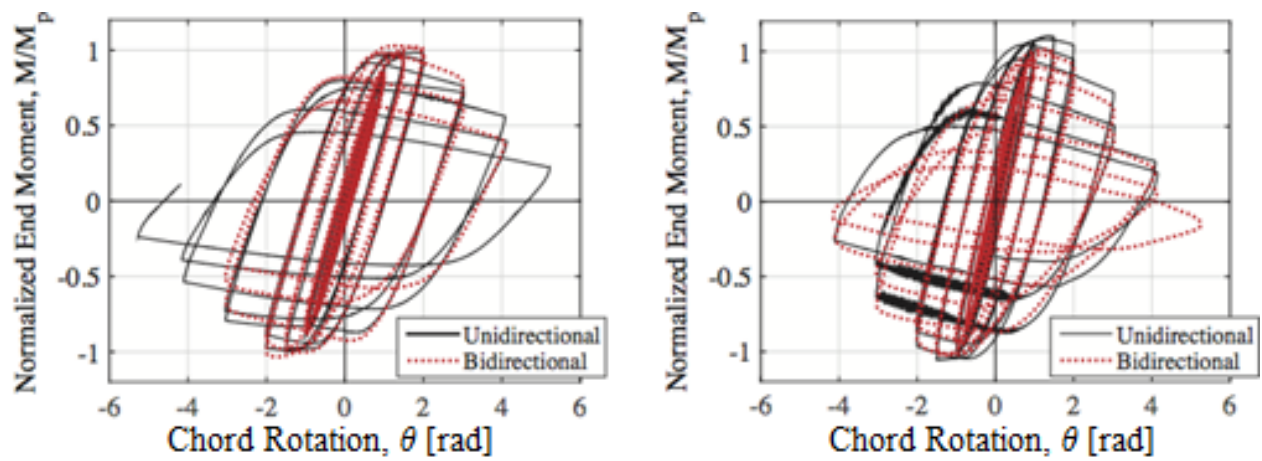
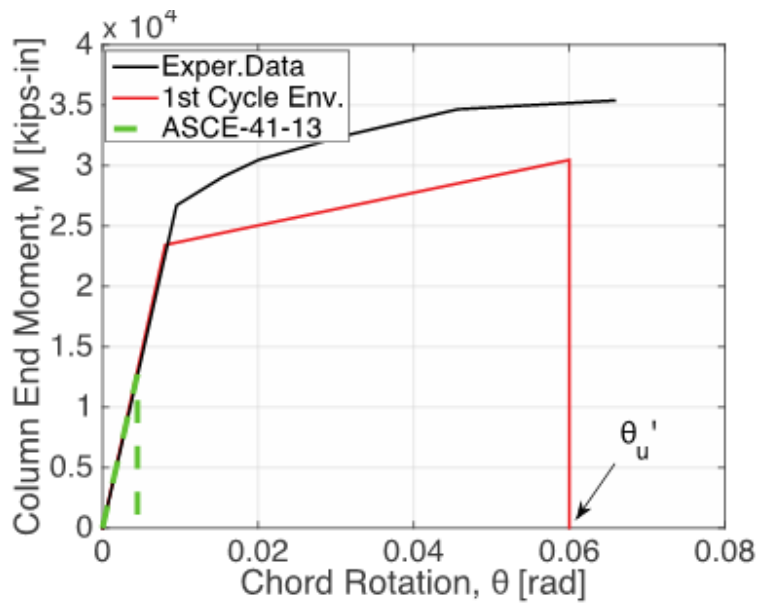
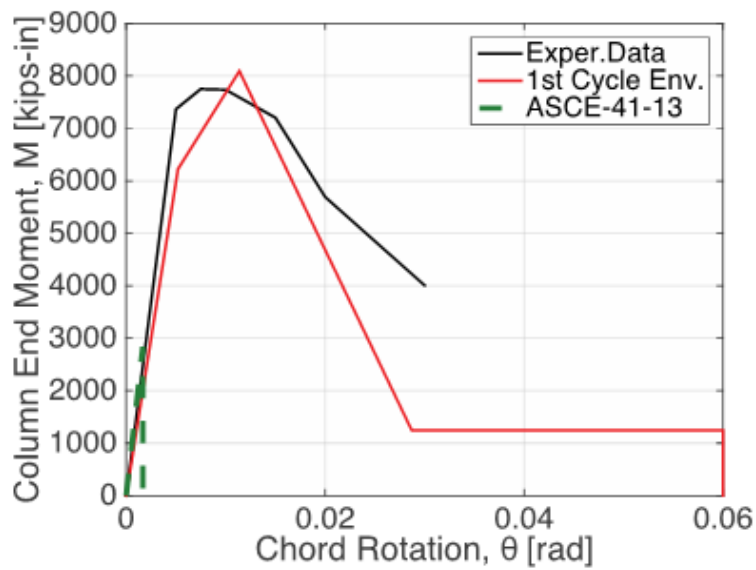


Figure 3.43: Comparison of unidirectional loading with bidirectional loading. Left: W24X146  $P_g/P_{ye} = 0.2$ ; right: W24X84  $P_g/P_{ye} = 0.2$ . From Elkady and Lignos (2016).



(a) W14X233-55,  $P_g/P_{ye} = 0.15$ ,  $P/P_{ye} = -0.15$  to  $0.75$



(b) W16X89,  $P_g/P_{ye} = 0.50$ ,  $P/P_{ye} = 0.25$  to  $0.75$

Figure 3.44: Comparisons of proposed modelling recommendations with ASCE 41-13 for end columns as part of steel MRF systems. Images from ATC (2016), data from Newell and Uang (2006) and Lignos et al. (2016).

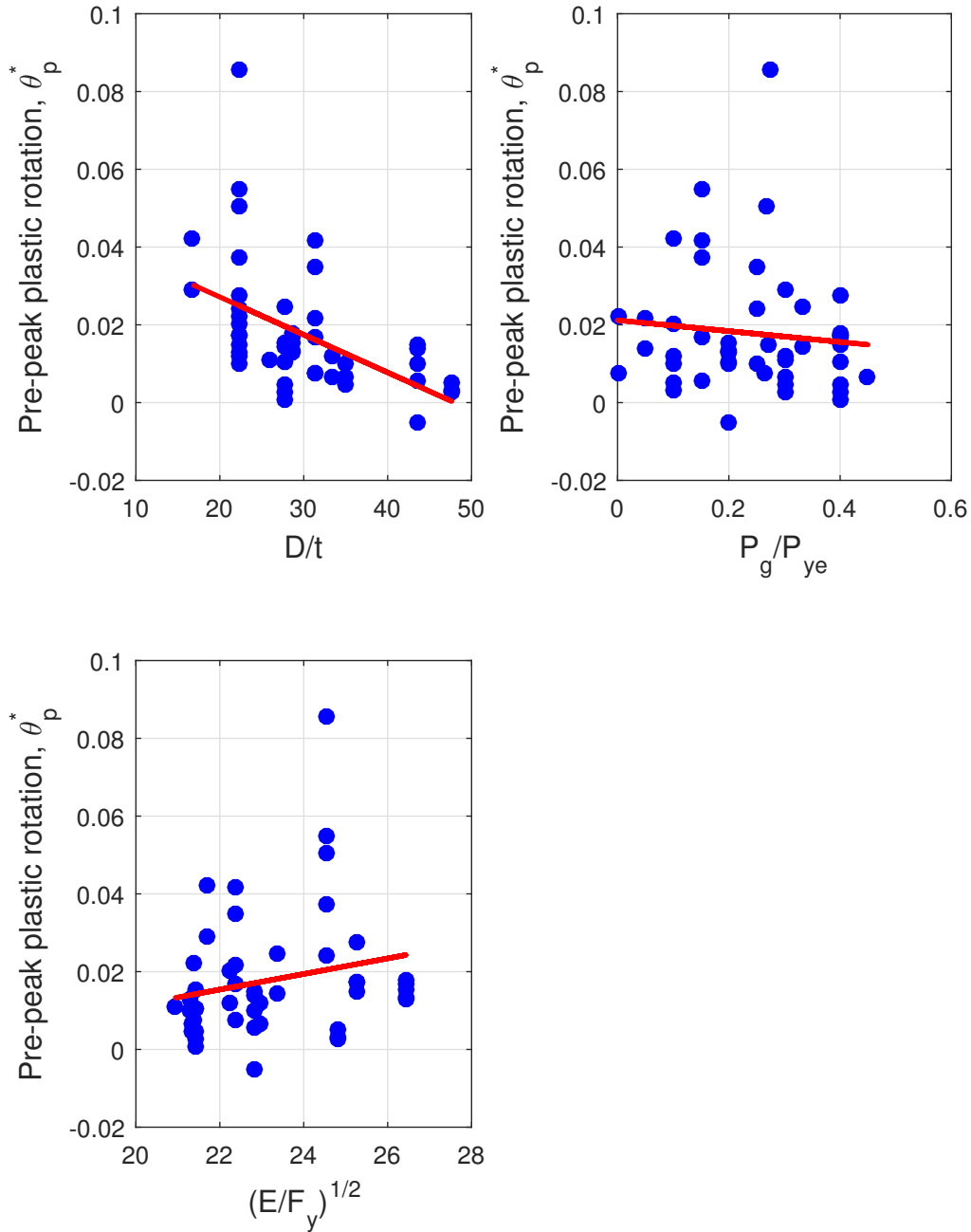


Figure 3.45: Trends on modelling parameters for steel HSS columns subjected to symmetric cyclic loading protocols.

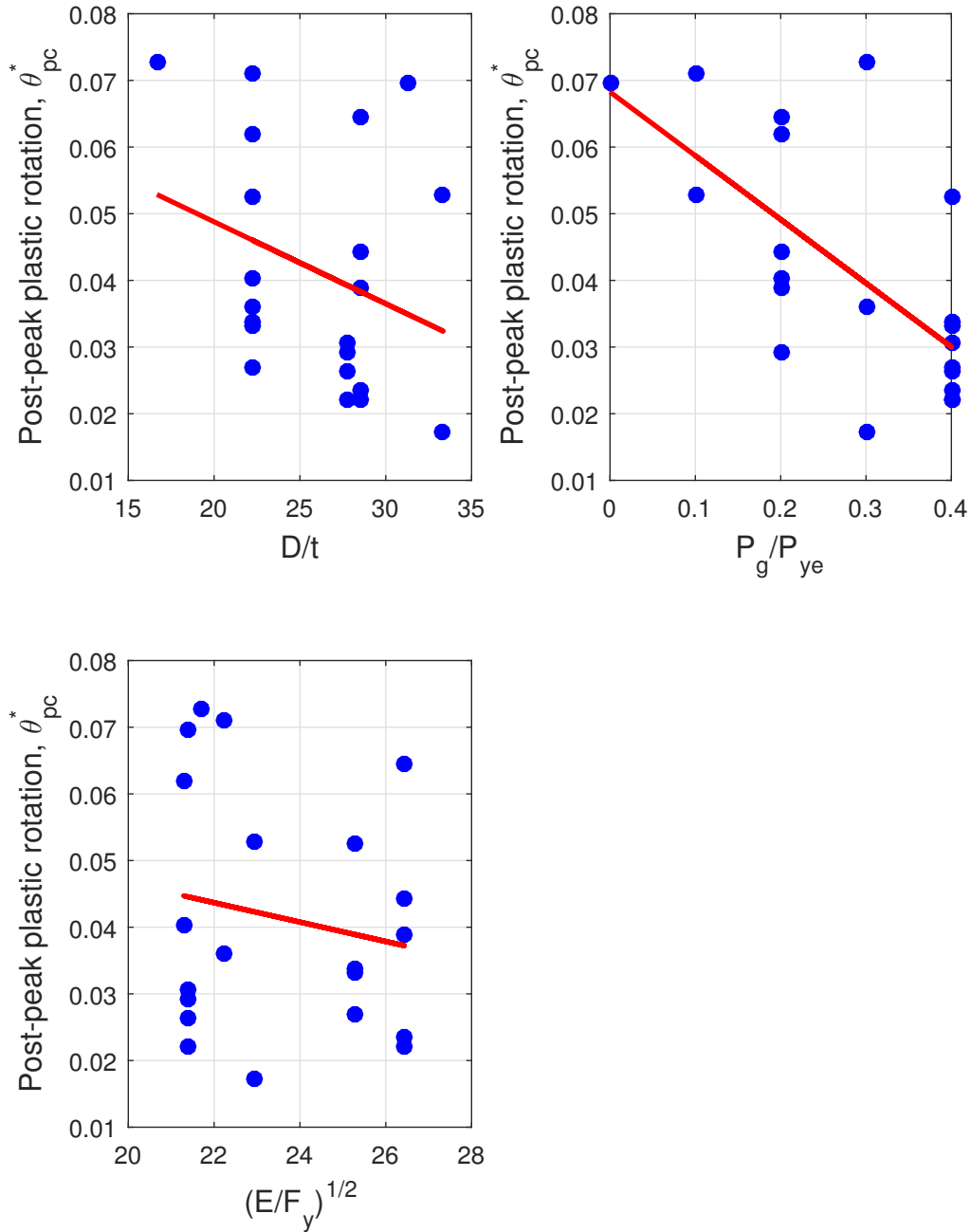


Figure 3.46: Trends on modelling parameters for steel HSS columns subjected to symmetric cyclic loading protocols.

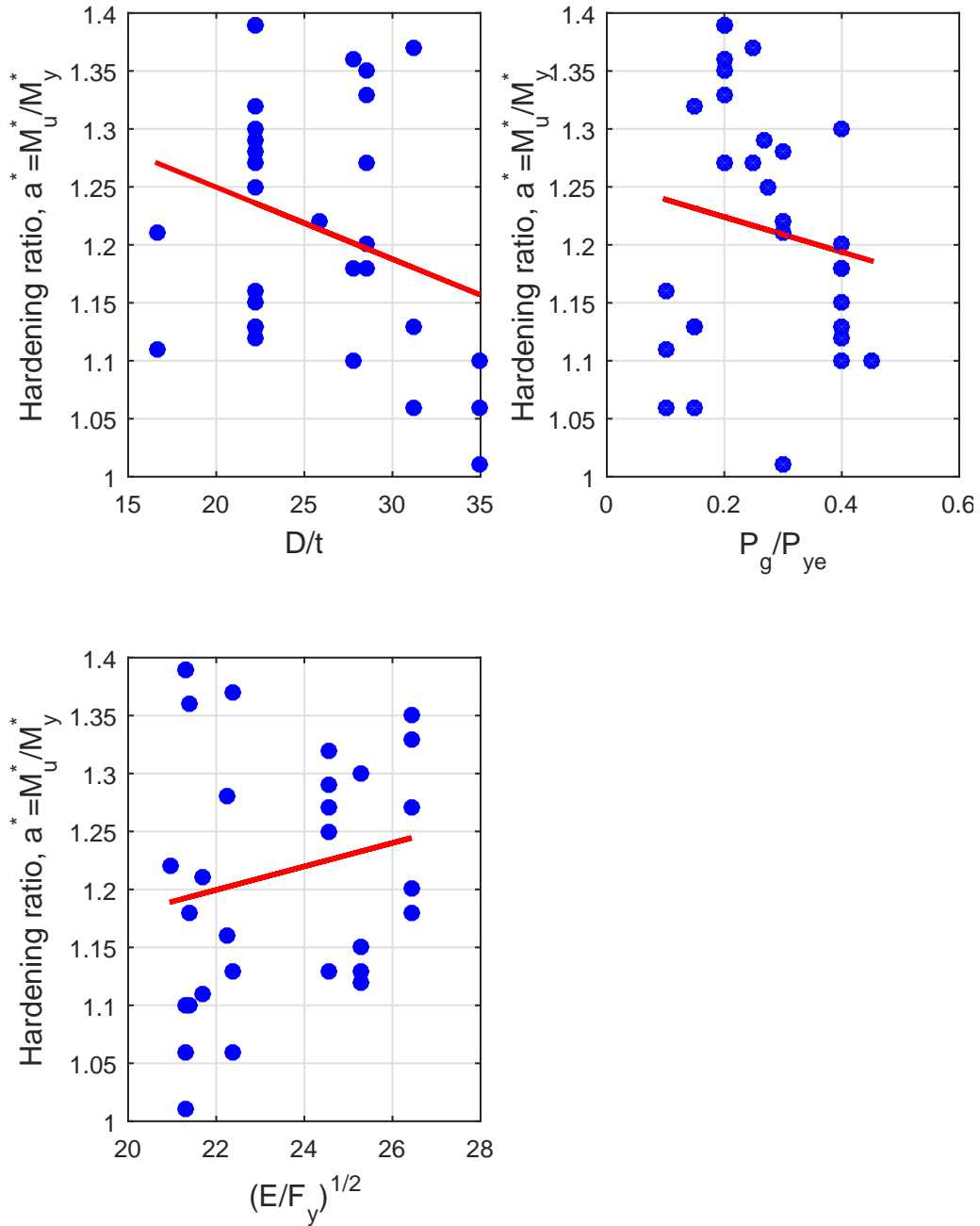


Figure 3.47: Trends on modelling parameters for steel HSS columns subjected to symmetric cyclic loading protocols.

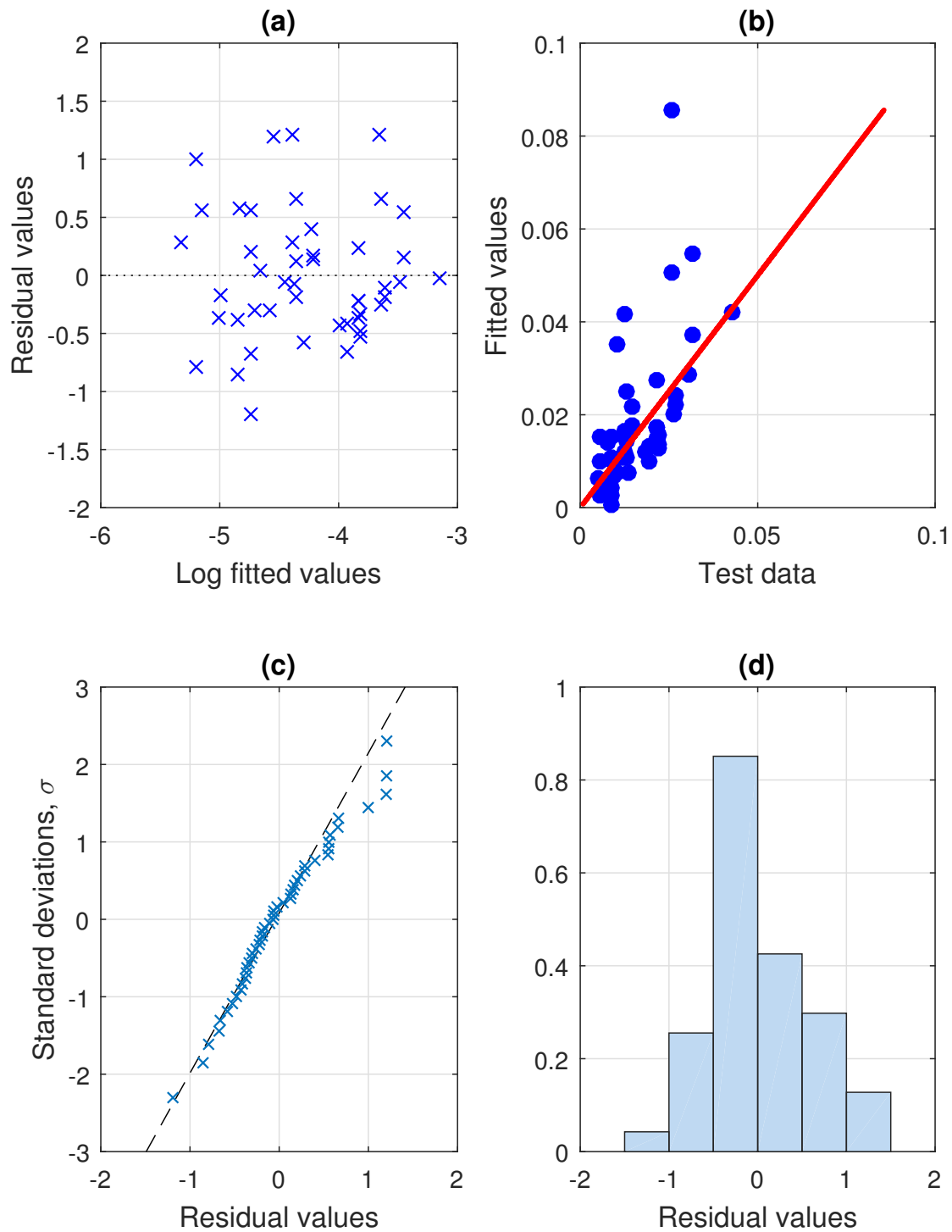


Figure 3.48: Diagnostics for the regression of  $\theta_p^*$  of the first-cycle envelope component model for HSS columns. (a) Residuals versus fitted values; (b) Fitted values versus test data; (c) QQ-plot; (d) Histogram of residuals.

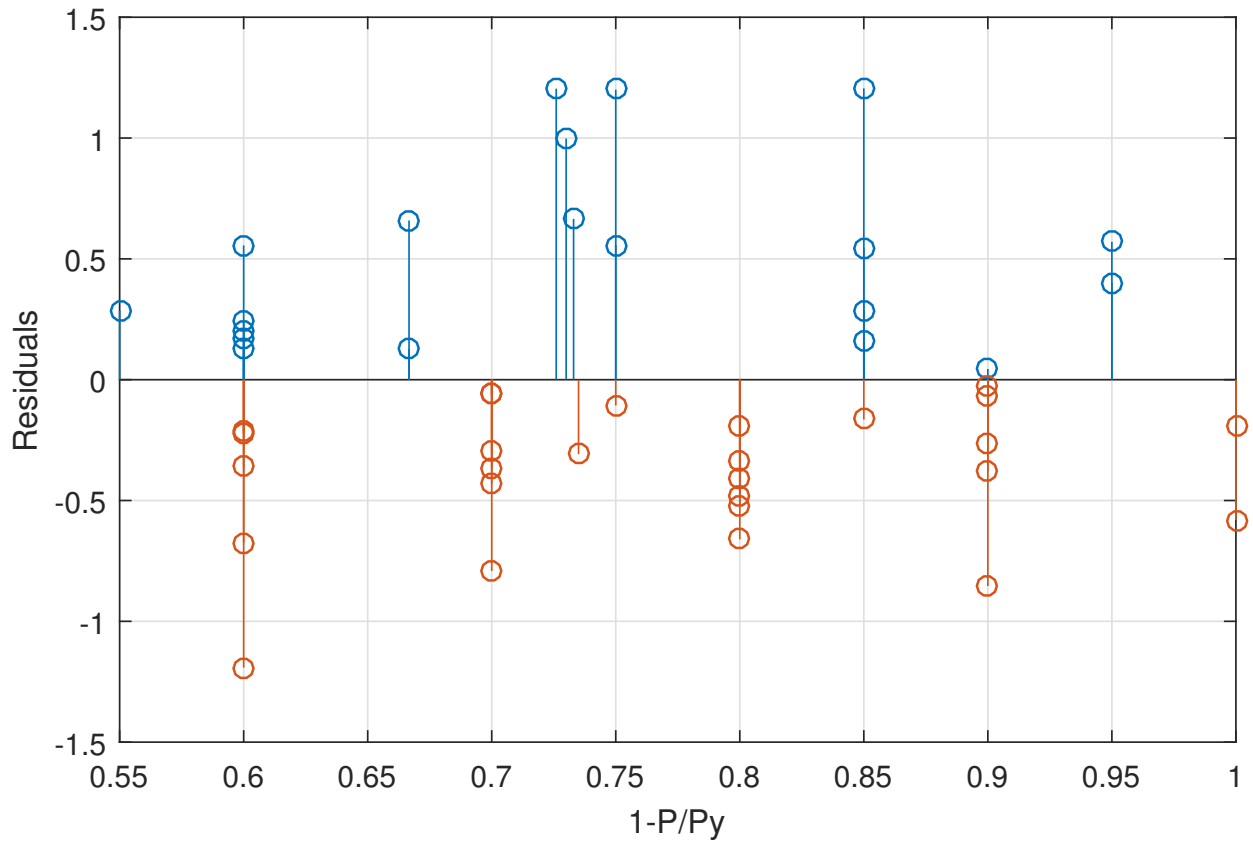


Figure 3.49: Plot of residuals of  $\theta_p^*$  versus  $P_g/P_{ye}$  for the first-cycle envelope component model for HSS columns.

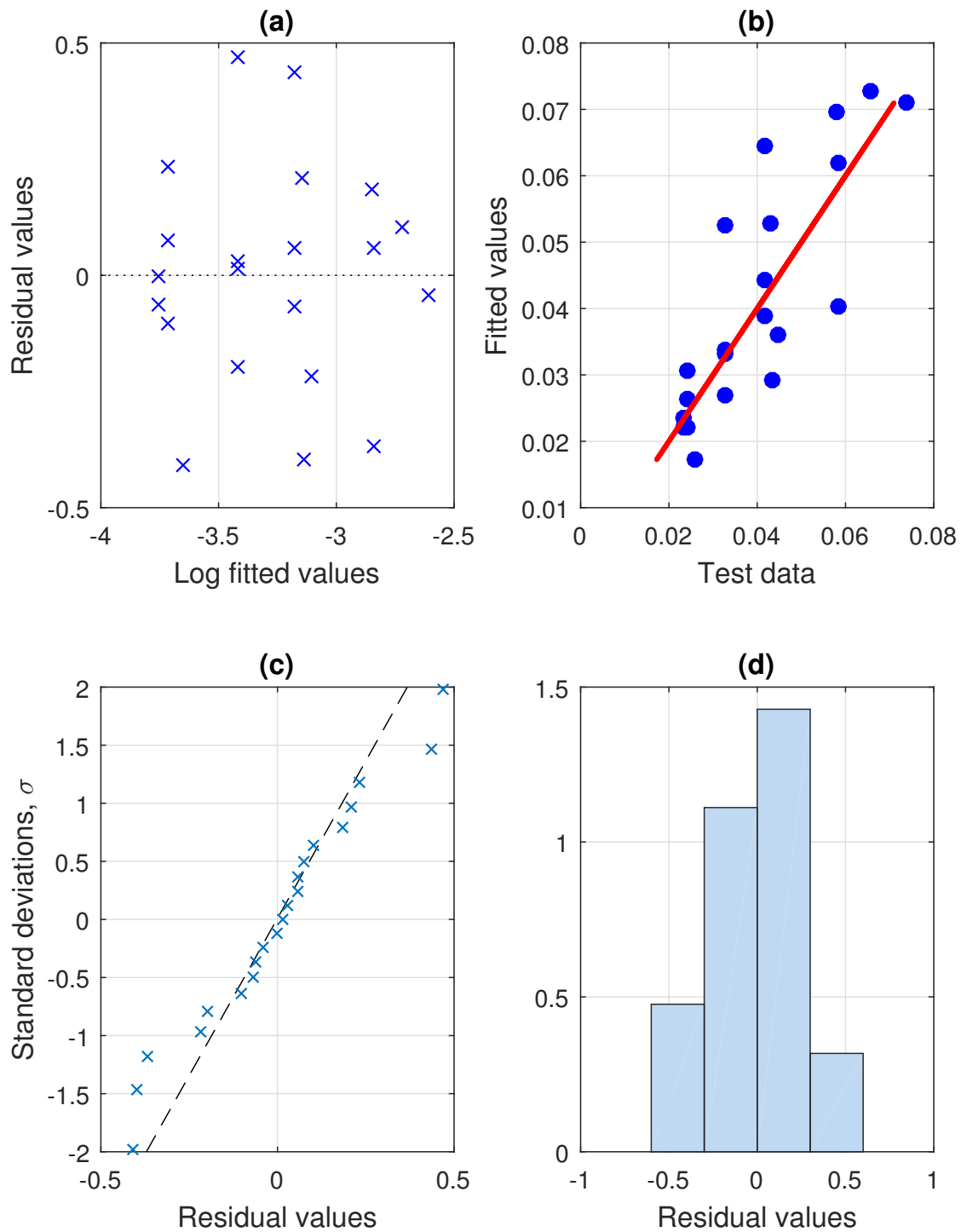


Figure 3.50: Diagnostics for the regression of  $\theta_{pc}^*$  of the first-cycle envelope component model for HSS columns. (a) Residuals versus fitted values; (b) Fitted values versus test data; (c) QQ-plot; (d) Histogram of residuals.

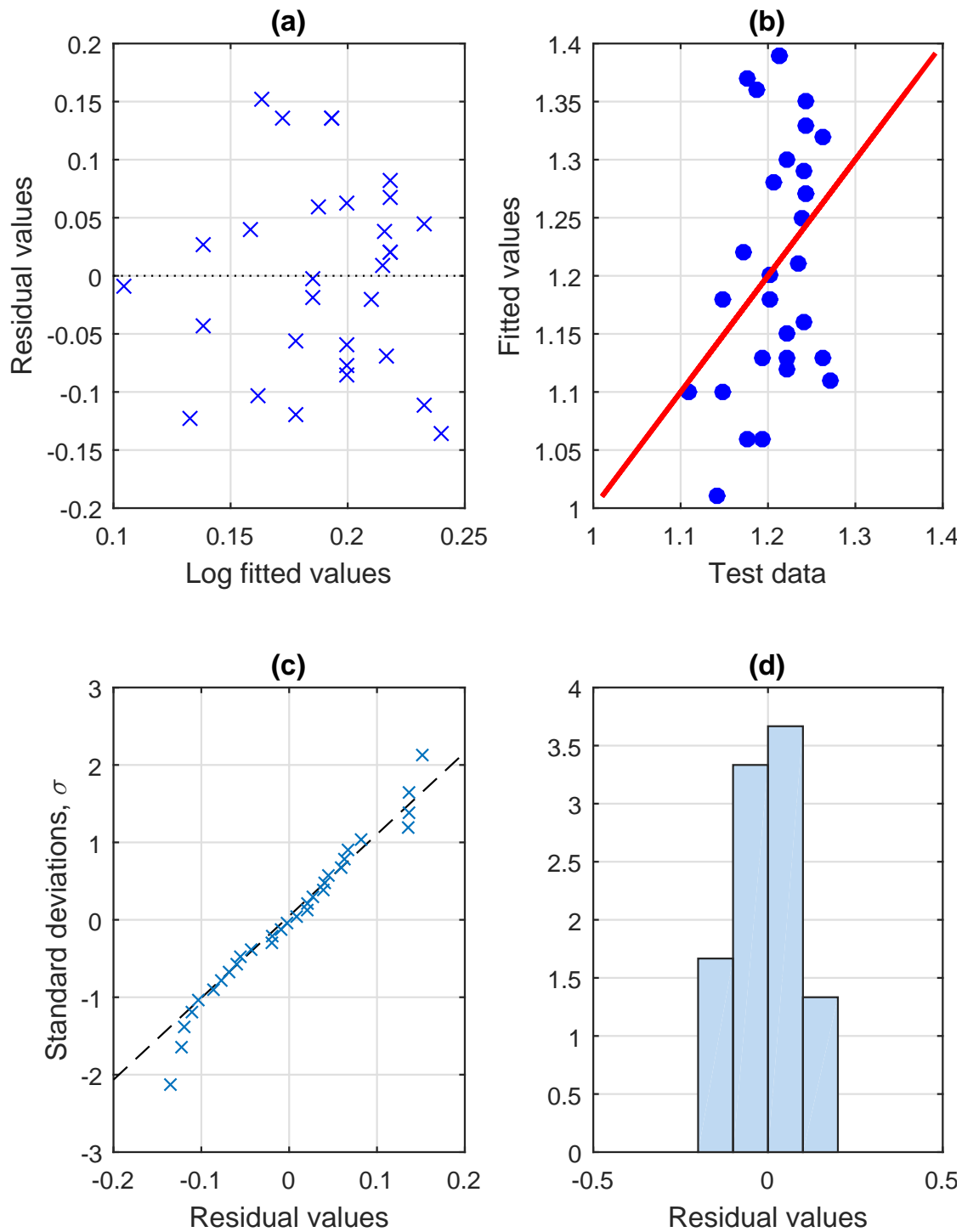
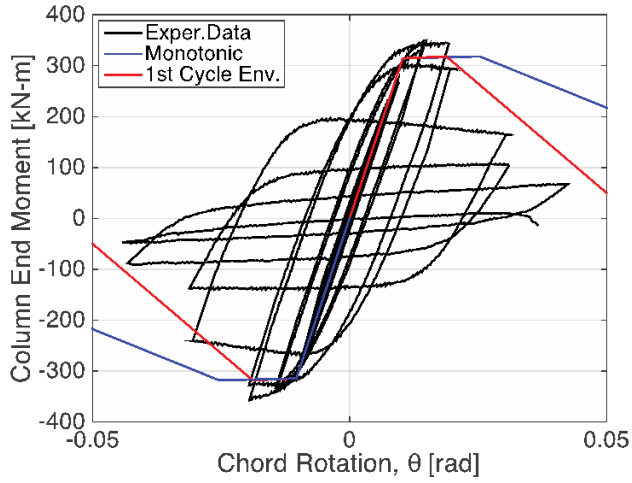
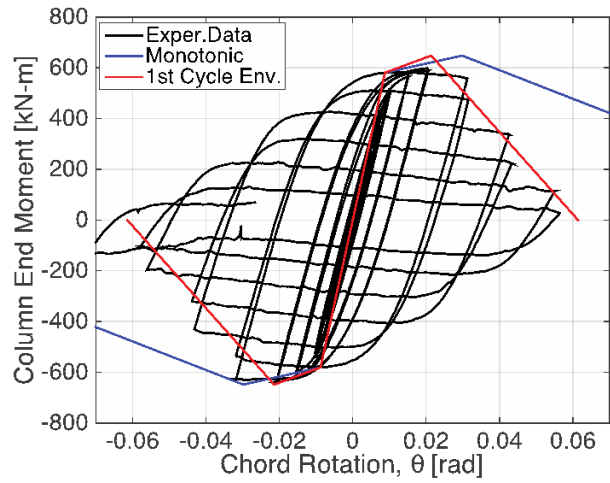


Figure 3.51: Diagnostics for the regression of  $a^* = M_{max}^*/M_y^*$  of the first-cycle envelope component model for HSS columns. (a) Residuals versus fitted values; (b) Fitted values versus test data; (c) QQ-plot; (d) Histogram of residuals.

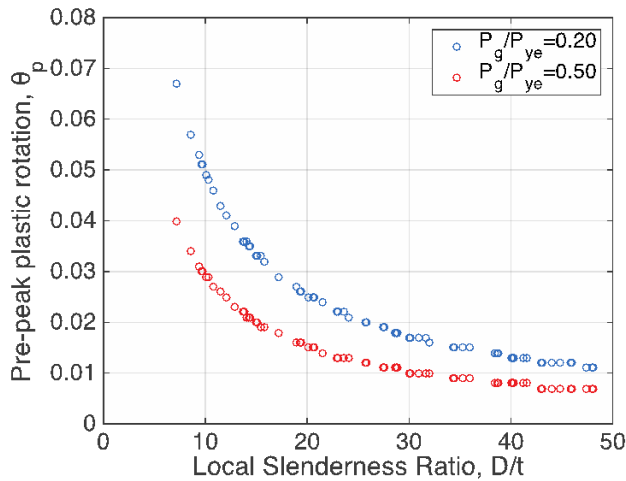


(a) HSS10x10x3/8,  $P_g/P_{ye} = 0.30$ , Reversed Cyclic

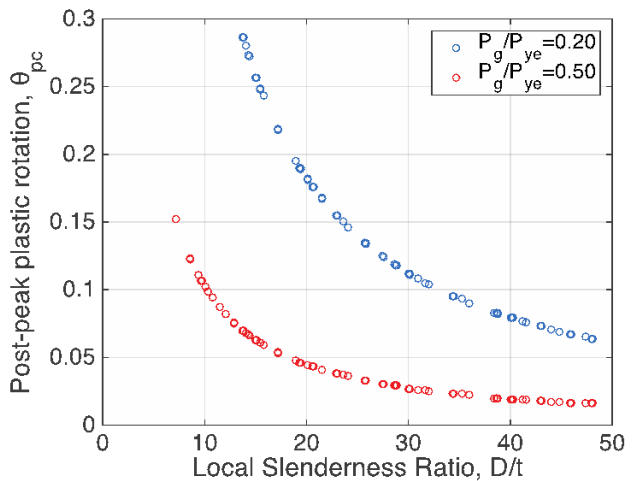


(b) HSS12x12x5/8,  $P_g/P_{ye} = 0.30$ , Reversed Cyclic

Figure 3.52: Comparison of experimental data with proposed component modelling options for HSS columns, data from Suzuki and Lignos (2015).



(a) Pre-peak plastic rotation,  $\theta_p$



(b) Post-peak plastic rotation,  $\theta_{pc}$

Figure 3.53: Trends of pre- and post-peak plastic deformations with respect to the cross-section web local slenderness ratio for modelling the monotonic backbone curve of HSS columns, from ATC (2016).

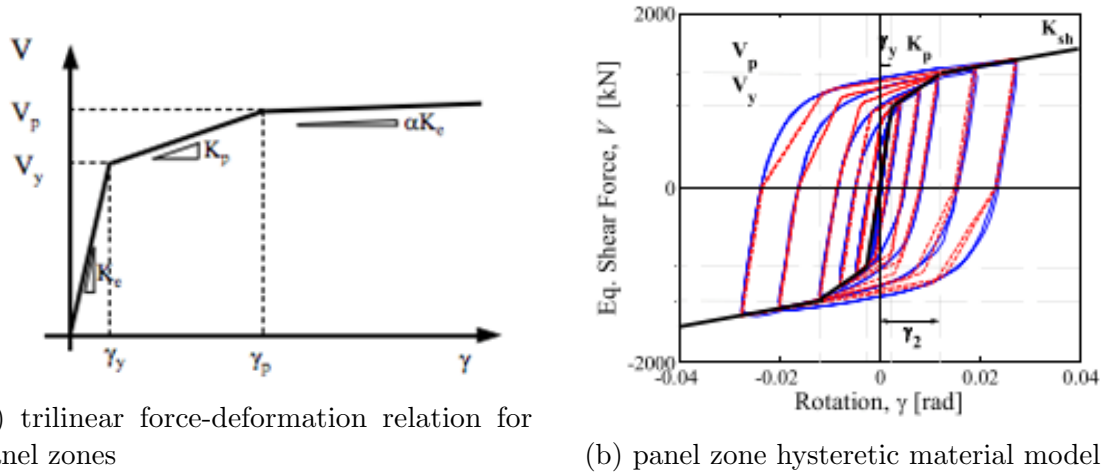


Figure 3.54: Image (a) from Gupta and Krawinkler (1999) and (b) from Elkady and Lignos (2014), with data from Engelhardt et al. (2000).

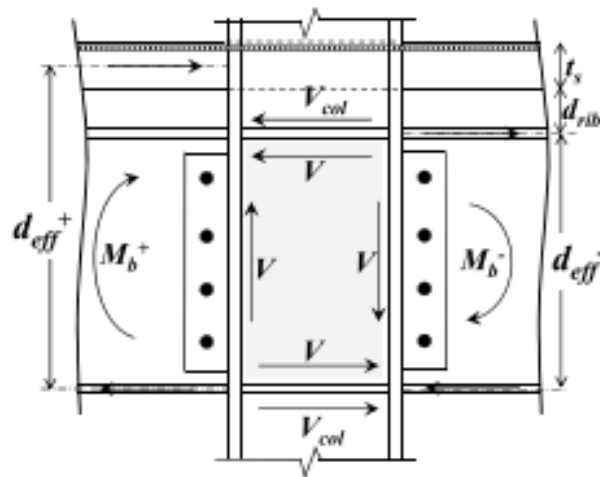


Figure 3.55: Boundary forces acting on interior composite panel zone, image from Elkady and Lignos (2015b).

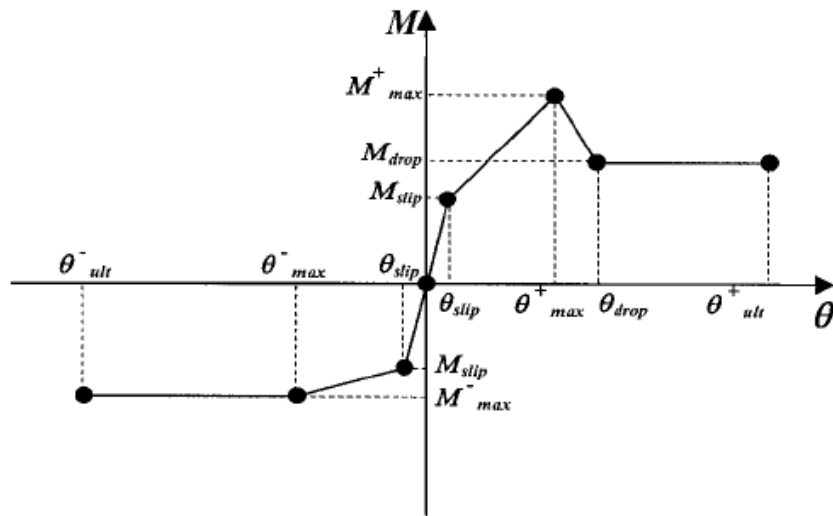


Figure 3.56: Idealized moment-rotation relation for hinge model for beams as part of partially-restrained connections with intermediate stiffness. Image from ATC (2016), adopted from Liu and Astaneh-Asl (2004).

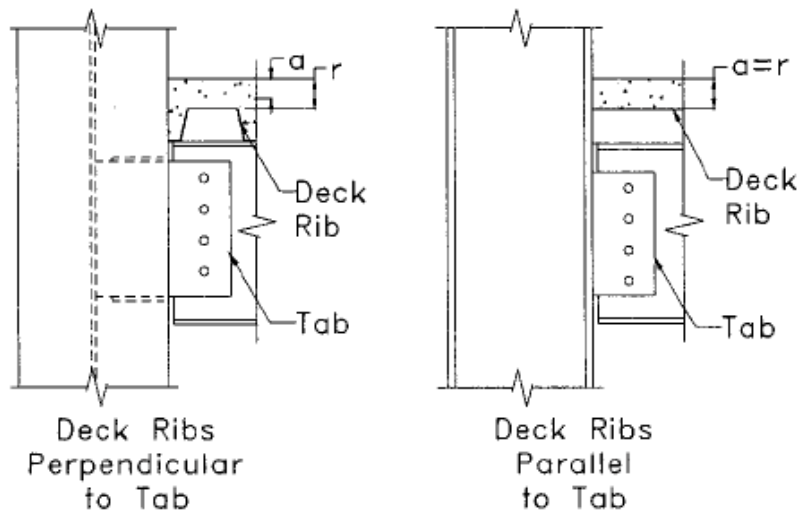


Figure 3.57: Effective depth for calculation of moment capacity. Image from ATC (2016), adopted from Liu and Astaneh-Asl (2004).

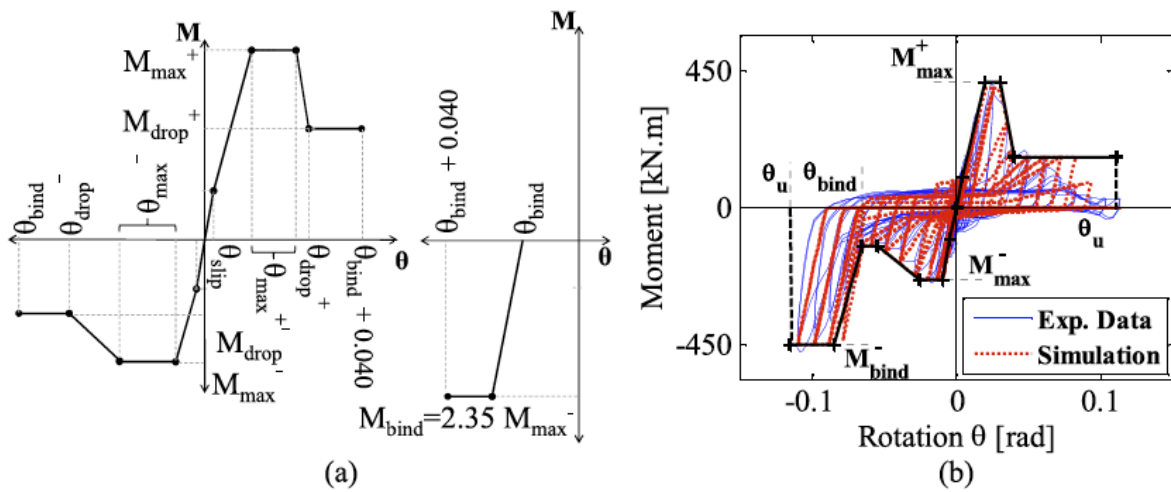


Figure 3.58: (a) Modified envelope curve for composite shear tab connections including flexural strength stiffening as a result of beam binding; (b) illustration with experimental data. Image from Elkady and Lignos (2015b), test data from Liu and Astaneh-Asl (2004).

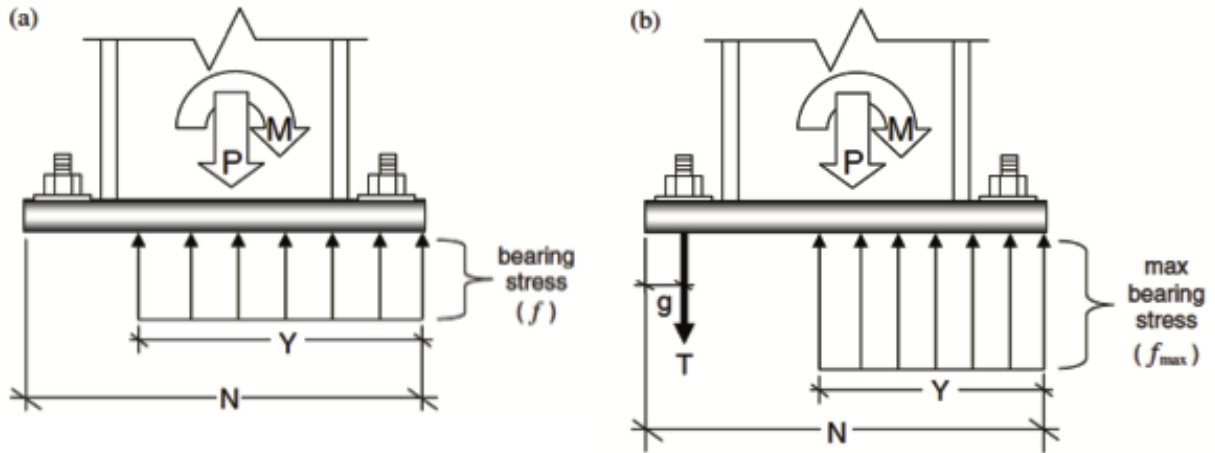


Figure 3.59: Stress distributions assumed in current U.S. design practice for (a) low; and (b) high-eccentricity conditions, from Kanvinde et al. (2012).

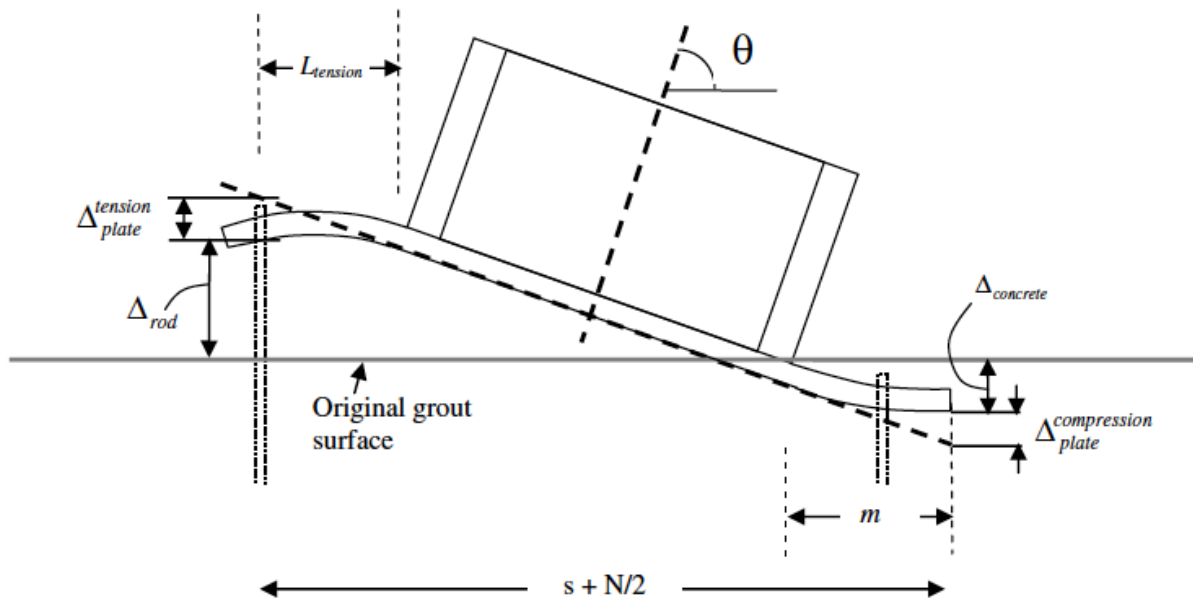


Figure 3.60: Assumed deformation mode and contribution of various components, from Kanvinde et al. (2012).

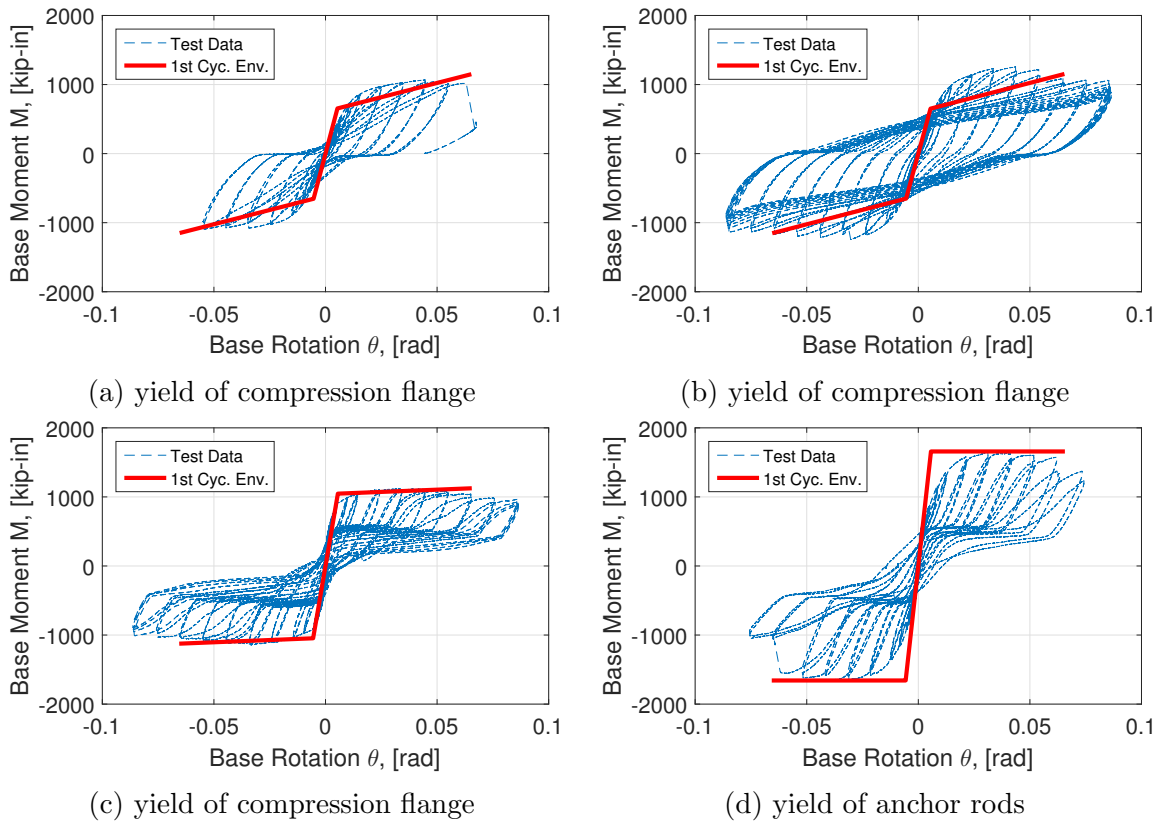
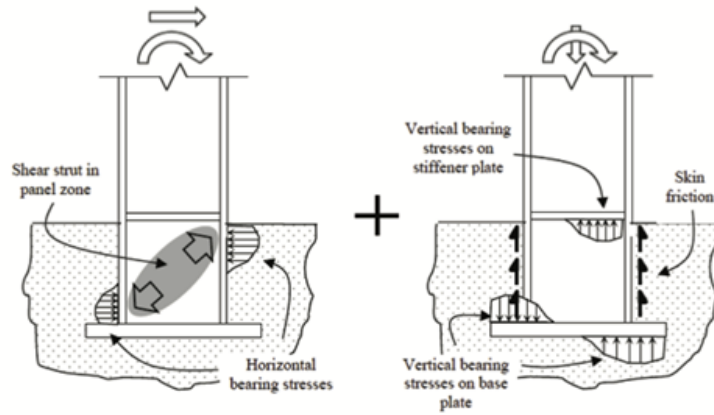
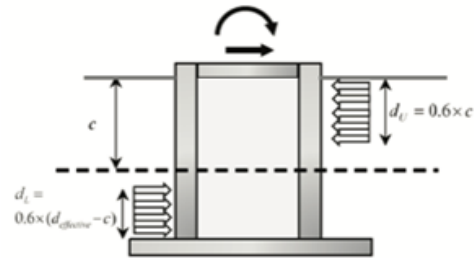


Figure 3.61: Comparison between test data and proposed ATC-114-1 first-cycle envelope component model for exposed column bases. Data taken from Gomez (2010).

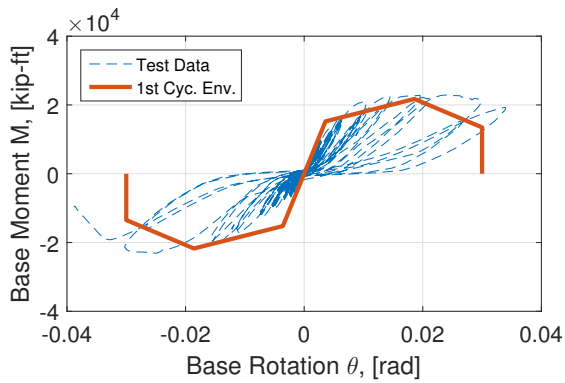


(a)

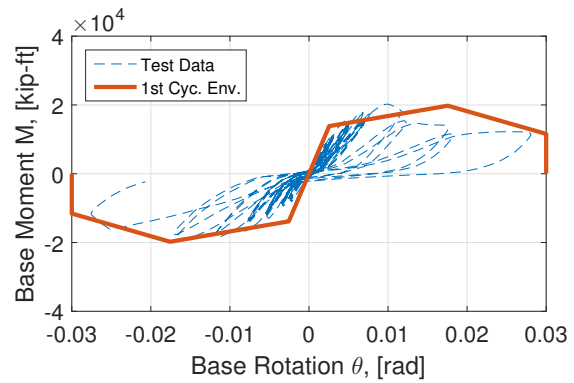


(b)

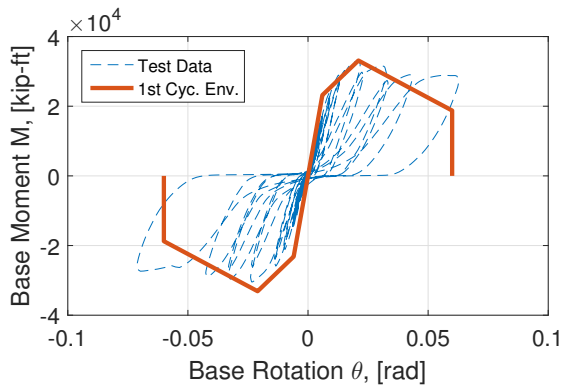
Figure 3.62: Load resisting mechanisms for embedded column bases (a) horizontal bearing and panel zone accompanied by vertical bearing and skin friction, (b) critical condition for horizontal bearing failure; in the case shown  $d_{effective} = d_{embed}$ . Images from Grilli (2015).



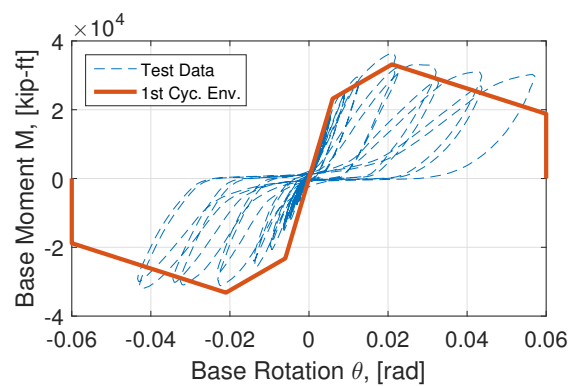
(a) Brittle failure



(b) Brittle failure



(c) Ductile failure



(d) Ductile failure

Figure 3.63: Comparison between test data and proposed ATC-114-1 first-cycle envelope component model for embedded column bases. Data taken from Grilli (2015).

# Chapter 4

## Case Studies

### 4.1 Introduction

In order to evaluate the performance of the proposed modelling recommendations provided in Chapter 3 for steel moment-resisting frames (MRFs), three archetype buildings with perimeter steel special moment frames (SMFs) as the lateral load resisting system are evaluated. 4-, 12-, and 20-story office buildings located in urban California were chosen as the archetype buildings. The evaluation of the component models was done through a series of nonlinear static analysis procedures (pushover analysis, or NSP) and nonlinear response history analysis procedures (NRHA).

The objectives of the case studies are to compare the implementation of the proposed ATC-114 provisions versus the ASCE-41-13 guidelines; assess the effects of modelling the composite beam action; and to investigate the effects of explicitly modelling the panel zone on the overall seismic performance of the archetype buildings.

To evaluate the objectives, three modelling options are considered: (1) component modelling based on the proposed ATC-114 monotonic backbone or proposed ATC-114 first-cycle envelope developed in Chapter 3, or the ASCE-41-13 (ASCE, 2014) guidelines; (2) either explicit modelling of the beam-to-column joint panel zone (PZ) or using a centreline modelling

approach (CL); and consideration of the effects of the composite beams and panel zones or modelling only the bare frame. Therefore, for the purposes of the case studies 10 separate models are developed for each of the 4-, 12-, and 20-story SMFs as follows: 2 models based on the ASCE-41-13 provisions, with and without explicit panel zone modelling; 4 based on the proposed ATC-114 first-cycle envelope for use in the nonlinear static analysis, with/without explicit panel zone modelling and with/without modelling the composite action; and 4 models based on the proposed ATC-114 monotonic backbone for use in NRHA, with/without explicit panel zone modelling and with/without modelling the composite action. The following section provides the details for the archetype buildings and their nonlinear building models.

## 4.2 Description of archetype buildings

The archetype buildings used in the case studies reflect typical office buildings designed for downtown Los Angeles, California, with 3-bay perimeter SMFs as the seismic force resisting system (NIST, 2010; Lignos et al., 2015). These SMFs were designed based on response spectrum analysis for seismic design category  $D_{\max}$  in California. The following provisions were used in the design of the archetype buildings: AISC 341-05 (AISC, 2005b), AISC 358-05 (AISC, 2005a), and ASCE/SEI 7-05 (ASCE, 2006).

The first story height of each of the structures is specified as 15 feet (4572 mm), the typical story height is 13 feet (3962 mm), and the column center-to-center bay width is 20 feet (6096 mm). The typical plan view of the buildings is shown in Figure 4.1. The steel of all structural components is ASTM A992 Gr. 50 steel with a nominal yield stress  $F_y = 50$  ksi (345 MPa). All fully-restrained beam-to-column connections are specified as reduced beam section (RBS) moment connections as per ANSI/AISC 358-05 (AISC, 2005a). Column splices are provided every two stories at mid-story height, with the first splice starting between stories two and three. A summary of all the member sizes for the 4-, 12-, and 20-story SMFs can be found in Table 4.1. A detailed description of the design assumptions for the archetype

buildings can be found in NIST (2011) and Lignos et al. (2015).

### **4.2.1 Ground motion selection**

For the NRHA, the set of 44 far-field ground motions from FEMA-P695 (FEMA, 2009) are selected to evaluate the building performance. The ground motions are scaled such that the mean of the absolute acceleration spectrum from the unscaled intensities of the 44 ground motions represents the absolute acceleration design spectrum in urban California for soil type D (Lignos et al., 2015). The building performance and comparisons between various component models are based on three different levels of ground motion intensity of interest to the engineering profession, these are: a service level earthquake (SLE), scaled such that there is 50% probability of exceedence over 50 years; a design basis earthquake (DBE), scaled such that there is a 10% probability of exceedence over 50 years; and a maximum considered earthquake (MCE), scaled such that there is a 2% probability of exceedence over 50 years. Each of the frames as a part of the NRHA are analysed with the full set of 44 ground motions scaled at all three of the intensity levels. A fourth intensity is also used to evaluate the building performance near collapse. In this case, the ground motions are scaled at 3 times the DBE intensity. The results from this analysis are not included herein due to brevity.

### **4.2.2 Numerical modelling of the steel special moment frames**

The numerical building models are developed based on the East-West 3-bay perimeter SMF from each of the archetype buildings using the software Open System for Earthquake Engineering Simulation (OpenSees) (McKenna, 1997) version 2.5.0. The nonlinear behaviour of the steel structural components is modelled using a concentrated plasticity approach. In the approach taken, the elastic behaviour of the components is governed through the use of elastic beam-column elements, while the inelastic behaviour is developed through the use of multi-linear spring elements. In this case, the modified Ibarra-Medina-Krawinkler (IMK) model is employed (Ibarra and Krawinkler, 2005; Lignos and Krawinkler, 2011).

The parameters of the multi-linear spring elements follow either the ASCE-41-13 deterioration model, or the ATC-114 deterioration model, the parameters of these two models are shown in Figure 4.2. For each of the structural components, the parameters of the ASCE-41-13 deterioration model are calibrated based on the guidelines provided in Chapter 9 of ASCE-41-13 (ASCE, 2014). The parameters of the ATC-114 deterioration model are calibrated based on the proposed recommendations provided in Chapter 3. The elastic stiffness of the nonlinear spring elements is modified to be rigid-plastic using a modification factor,  $n$ , chosen to be 10 as recommended in Ibarra and Krawinkler (2005). The stiffness of the beam-column elements were adjusted appropriately.

The following sections give a description of the specific modelling considerations for of each of the structural components considered in the SMFs.

### **Steel beams as a part of fully restrained beam-to-column connections**

The nonlinear spring properties are defined based on the predicted moment-rotation relation as specified from component models for beams with RBS as a part of fully-restrained beam-to-column connections. For the numerical building models developed based on the ASCE-41-13 provisions, reference is given to Chapter 9 of ASCE-41-13 (ASCE, 2014) for the component models. For the models based on the proposed ATC-114 monotonic backbone, the component models are given in Section 3.3.1, and in Section 3.3.2 for the models based on the ATC-114 first-cycle envelope. For the NRHA, the cyclic and in-cycle deterioration of the beam components are modelled explicitly using the modified IMK deterioration model through the use of the reference cumulative plastic rotation,  $\Lambda$  (Ibarra et al., 2005; Lignos and Krawinkler, 2009). The equations to predict  $\Lambda$  are provided in Section 3.3.1 for beams with RBS, based on those provided in Lignos and Krawinkler (2011).

The physical beam components are represented numerically through the use of three beam-column elements and two spring elements, with reference to the configuration shown in Figure 4.3. The nonlinear springs are placed at a distance  $a + 0.5b$  from the column face,

where  $a$  is the distance from the beam end to the RBS cut-out, and  $b$  is the length of the cut-out, such that the plastic hinge is assumed to be located at the center of the RBS cut-out.

### Steel wide-flange columns

The columns of the SMF are modelled using one beam-column element, and two spring elements, as shown in Figure 4.3. The spring elements are located at a distance  $d_b/2$  away from the intersection of the beam and column centerlines, where  $d_b$  is the depth of the beam, with reference to Figure 4.3 for the configuration. The component models for the numerical building models based on the ASCE-41-13 provisions are provided in Chapter 9 of ASCE-41-13 (ASCE, 2014). The models based on the proposed ATC-114 monotonic backbone the component models were given in Section 3.4.1, and in Section 3.4.1 for the models based on the proposed ATC-114 first-cycle envelope. For the NRHA, the cyclic and in-cycle deterioration of the column components were modelled explicitly using the modified IMK deterioration model through the use of the reference cumulative plastic rotation,  $\Lambda$ . Since specific recommendations have not yet been developed for columns, as recommended by the guidelines provided in ATC-72 (PEER/ATC, 2010) for the modelling of steel frame buildings, the equations to predict  $\Lambda$  for beams in non-RBS fully-restrained beam-to-column connections were utilized. The predictive equations are provided in Section 3.3.1 based on the work done by Lignos and Krawinkler (2011).

As explained in Section 3.4, the axial load on columns resulting from gravity was found to have dominant effect over the transient axial loading resulting from dynamic overturning effects. Therefore, the proposed ATC-114 component models can be developed considering the gravity loading on the column,  $P_g$ , these forces can be obtained directly based on the tributary area of each column in the SMF. However, for the ASCE-41-13 component models provide no such specifications, and the procedure to obtain the loading on the column is as follows: (1) assume  $P_g = 0$  on the columns, and run an initial pushover analysis for the analytical model; (2) obtain the maximum interior and exterior loads on the columns for

each story; (3) apply these loads to each of the interior and exterior columns, and re-run the pushover analysis. The axial loads from (2) are also used to calculate the strength parameters in the ASCE-41-13 component models.

### **Beam-to-column joint panel zones**

The beam-to-column joint panel zones are modelled using the Krawinkler parallelogram approach described in Section 3.5. Eight rigid elastic beam-column elements are used to create the rectangle, with a single spring element to provide the panel zone response in the top-right corner. Additionally, releases to the rotational degree of freedom are provided at the three corners that do not contain the spring in order to prevent transfer of moment between these elements. When the panel zones are not modelled explicitly, in the case of centerline models, the beam and column elements were extended to the mid point of the panel zone using the respective un-modified elements (i.e., not considering a rigid offset). The panel zone modelling options are shown in Figure 4.4, and an elevation view of the 4-story SMF model is shown in Figure 4.3.

### **Composite action**

In order to account for the effects of the composite slab, the beams and panel zones are modified according to the procedures provided in Sections 3.3.3 and 3.5.2, for the beams and panel zones respectively. For the composite panel zones, the following properties are assumed for all of the models:  $d_{rib} = 3.5$  inches (89 mm), where  $d_{rib}$  is the depth of the rib of the steel deck, and  $t_s = 5.0$  inches (127 mm), where  $t_s$  is the total depth of the concrete slab. Full composite action is assumed between the steel beams and the slab, and the specified compressive strength of the concrete was assumed to be  $f'_c = 5000$  psi (35 MPa). These properties are representative of a typical slab with fully-composite action.

## Calculations of gravity loading and nodal masses

As specified in NIST (2010), the gravity loading on the archetype buildings is specified as: a uniform deadload of 90 psf (4.3 kPa) with an additional 25 psf (1.2 kPa) cladding load applied to the perimeter of the building, and a uniform liveload of 50 psf (2.4 kPa) on the floors or 25 psf on the roof. A load combination of 1.05DL+0.25LL, is used in order to combine the contributions of the dead and live loading, where DL and LL are the dead and live loads, respectively. These gravity loads are applied directly to the columns based on the tributary area of each column. The loads not applied directly to the frame are applied to a leaning column in order to simulate the P-Delta effects. A damping ratio of 2.5% is applied to the first natural period and to 20% of the first period. A summary of gravity loads and masses applied to the models is given in Table 4.2. The first period of each of the models is given in Table 4.3.

### 4.2.3 Nonlinear static analysis

For the nonlinear static analysis, the representation of the seismic forces is done through a first-mode lateral load pattern that was applied to the structure according to ASCE-41-13 (ASCE, 2014). The reference load pattern is assigned as follows

$$F_i = \phi_1(i) * m(i), \quad (4.1)$$

where  $F_i$  is the force applied at floor level  $i$ ,  $\phi_1(i)$  is the eigenvector from the first mode at floor  $i$ , and  $m(i)$  is the sum of the nodal masses at floor  $i$ .

The results of the pushover analyses are assessed through the use of story-based engineering demand parameters (EDPs). The recorded EDPs for the nonlinear static analysis are: the base shear versus roof displacement, the peak story drift ratios (SDRs), the peak story shear forces, and the peak floor overturning moments (OTM). Furthermore, the force-deformation response of key nonlinear spring elements are recorded in order to track the force distribution

in the SMF.

### Target roof displacements

As a method to relate the nonlinear static and response history analyses, the target roof drifts according to each of the considered intensity levels (i.e., SLE, DBE, MCE) are calculated. The target roof displacements are calculated according to the ASCE-41-13 coefficient method from Section 7.4 of ASCE-41-13 (ASCE, 2014) for each of the ground motion intensity levels.

The equation to calculate the target roof displacement is summarized from ASCE-41-13 as follows:

$$\Delta_t = (SF)C_0C_1C_2S_a\frac{T_e^2}{4\pi^2}g, \quad (4.2)$$

where  $SF$  is the scale factor related to each intensity level,  $C_0$  is the relation between the MDOF system and an SDOF system,  $C_1$  is to account for the inelastic effects,  $C_2$  is to represent the cyclic effects,  $T_e$  is the effective period of the model, and  $g$  is the acceleration due to gravity.

$$C_0 = \phi_1(r)\Gamma_1 = \phi_1(r)\frac{\phi_1^T M \{1\}}{\phi_1^T M \phi_1}, \quad (4.3)$$

where  $\Gamma_1$  is the mass participation factor for the first mode, and  $\phi_1(r)$  is the correspondingly normalized value from the first mode eigenvector at the roof level, and  $M$  is the lumped mass matrix.

$$C_1 = 1 + \frac{\mu_{strength} - 1}{aT_e^2}, \quad (4.4)$$

where  $a$  is the site class factor taken as 60 for site class D.

$$\mu_{strength} = \frac{S_a}{V_y/W}C_m, \quad (4.5)$$

where  $S_a$  is the spectral acceleration,  $V_y$  is the yield base shear,  $W$  is the seismic weight of

the model, and  $C_m = 1$  since for all models  $T_i > 1.0$  sec.

$$C_2 = 1 + \frac{1}{800} \left( \frac{\mu_{strength} - 1}{T_e} \right)^2 \quad (4.6)$$

A summary of the calculated target roof displacements normalized by the height of the building,  $\Delta_r/H$ , can be found in Table 4.4.

#### 4.2.4 Nonlinear response history analysis

The nonlinear response history analyses are carried out using OpenSees. Each of the FEMA-P695 far-field ground motion records are scaled by the appropriate scale factors corresponding to each of the desired intensity levels. Each NRHA is run until either the end of the ground motion record is reached, or until collapse of the numerical model occurs. Collapse is defined as the point that a story or a number of stories displaces sufficiently, and the first order shear within the same story or stories becomes zero due to P-Delta accelerated by component deterioration. This definition is consistent with experimental studies from small and full-scale collapse experiments (Lignos et al., 2011a, 2013).

The results of the NRHA are assessed through the following EDPs: peak story drift ratios, peak story shear forces, and peak floor overturning moments. For each of the EDPs the median value of the 44 ground motions is calculated at each story level, as well as the value corresponding to the 14th and 86th percentiles. Finally, the EDPs of the NRHA are compared with those of the pushover analyses at each of the predicted roof drift levels according to the ASCE-41-13 coefficient method.

### 4.3 Results of the nonlinear static analysis

Nonlinear static analysis is conducted for all three archetype buildings discussed in Section 4.2 by using a first mode lateral load pattern. Due to brevity, the 12-story steel frame building is used for illustration but the findings are applicable to the other two archetypes that were

analysed. Figure 4.5 shows the global pushover curve based on the bare and composite model representations of the 12-story archetype building. In particular, the predicted response from five models is superimposed in this figure namely, a bare model with explicit consideration of the panel zone. Beams and columns are modelled with current ASCE-41-13 nonlinear modelling provisions (i.e., noted “PZ-ASCE-41-13”); a bare and composite model with explicit consideration of the panel zone. Beams and columns are modelled with the proposed 114 nonlinear modelling recommendations (i.e., noted “PZ-114-1st-Cycle Env.”, “Composite-PZ-114-1st-Cycle Env.”); and a bare and composite centerline model in which beams and columns are modelled with the proposed 114 nonlinear modelling recommendations (i.e., “CL-114-1st-Cycle Env.”, “Composite-CL-114-1st-Cycle Env.”). In Figure 4.5, the base shear force,  $V$ , is normalized with respect to the seismic weight,  $W$ , of the archetype in the EW loading direction. The roof displacement,  $\Delta_r$  is normalized with respect to the total height,  $H$ , of the archetype building. From Figure 4.5 the following observations hold true:

- When the predicted nonlinear static response of steel SMFs designed according to the current AISC seismic provisions (AISC, 2010a,b) is based on the bare properties of steel beams (i.e., no consideration of composite beam effects), there is practically no need to explicitly consider the parallelogram panel zone model (Gupta and Krawinkler, 2000c) in the numerical model representation of the steel SMF.
- The post-yield global stiffness of the archetype buildings based on the ASCE-41-13 model is significantly underestimated compared to the proposed ATC-114 model. This is primarily attributed to the assumed fixed 3% strain-hardening ratio of the ASCE-41-13 component model regardless of the compactness of the employed cross-section of the respective beam and/or column (see Section 2.3).
- The post-capping global stiffness of the archetype buildings based on the ASCE-41-13 model is very steep due to the characteristic vertical strength drop in the ASCE-41-13 component model. This issue is likely to cause convergence problems as discussed in prior studies (Lignos et al., 2015).

- Table 4.3 summarizes the overstrength factors for all three archetype buildings that were analysed based on various modelling approaches. Based on Table 4.3 and Figure 4.5, the predicted overstrength,  $\Omega_s$ , obtained from single-mode NSPs based on the composite nonlinear building model is on the order of 1.3x larger than the one predicted based on a bare nonlinear building model.  $\Omega_s = V_{max}/V$ , where  $V_{max}$  is the maximum base shear from a pushover analysis and  $V$  is the design base shear as per ASCE-7-06 (ASCE, 2006). It is also observed that the composite beam effects also increase the global elastic lateral stiffness of the respective numerical model by 1.4x, on average. These findings are consistent with recent studies by Elkady and Lignos (2014, 2015b).
- From Figure 4.5, when the composite effects are considered in the nonlinear building model, the predicted nonlinear static response of the archetypes is inherently more ductile than that predicted based on bare nonlinear building models. This is in part attributed to the delay of the local buckling formation at the top flange of the respective steel beams due to the slab restraint and the shift of the neutral axis towards the top flange prior to concrete slab cracking. It should be noted that the effective beam depth is larger than that of the bare beam when the slab is considered in the nonlinear building model; therefore, the panel zone shear demands are larger than those predicted by bare models. This results in panel zone shear yielding. This is shown in Figure 4.6 that illustrates the predicted panel zone behaviour in terms of panel zone moment demands versus panel zone shear distortion,  $\gamma$ , based on various nonlinear component-modelling options. From this figure, when the composite beam action is neglected, the predicted panel zone response is elastic, which could be misleading especially if the predicted response of a steel moment-resisting frame system is based on centerline models (see Figure 4.5). This illustrates the significance of the composite action in the predicted response of steel SMFs.
- Figure 4.7a shows the compressive axial load demands in the first story steel columns of the 12-story SMF based on single-mode NSPs at various seismic intensities of interest.

From this figure, due to dynamic overturning effects end columns experience much higher compressive axial load demands than those seen in interior columns with the same story. Based on current ASCE-41-13 modelling provisions such column would be treated as force-controlled elements regardless of the seismic intensity of interest. However, Figures 4.7b and 4.7c show that a similar steel column has an appreciable plastic deformation capacity when experiencing similar levels of compressive axial load ratio; therefore should not be treated as a force-controlled element. This is reflected in the proposed nonlinear modelling recommendations discussed in Section 3.4.1. From Figure 4.7d, when the same column experiences a collapse-consistent loading history (Suzuki and Lignos, 2014) its plastic deformation capacity is about 3 times more than that measured from a typical symmetric loading history.

The implication of various nonlinear modelling options is also illustrated based on the assessment of story-based EDPs of the respective archetypes based on nonlinear static analysis. Figure 4.8 shows the predicted peak SDRs along the height of the 12-story archetype building for two target roof drift ratios and based on various nonlinear modelling options. From Figure 4.8a, at 1% target roof drift ratio, the predicted peak SDRs of the 12-story archetype are practically not influenced from the employed component model. The reason is that most of the structural components are not far into their inelastic range. However, from Figure 4.8b (far into the inelastic range), the predicted peak SDRs of the 12-story archetype are very sensitive to the choice of the employed nonlinear component model. In particular, from Figure 4.8b, the consideration of composite beam effects in the nonlinear building model can shift the global collapse mechanism of the respective archetype. This is consistent with recent findings by Elkady and Lignos (2014) regarding the composite beam effects. From this figure, it should also be noted that a modeller should also tie the selected numerical model complexity with the performance objective of interest as discussed in Lignos et al. (2015).

## 4.4 Results of the nonlinear response history analysis

This section discusses the main findings of the present study based on story-based peak EDP comparisons between the predicted nonlinear static response of the building archetypes based on a single-mode NSP that were considered and that obtained based on rigorous NRHA. The building archetypes were subjected to the set of 44 far-field ground motions from FEMA P695 (FEMA, 2009) as discussed in Section 4.2.1. The counted median response of 44 nonlinear building simulations corresponding to each one of the employed ground motions is compared with the single-mode NSP predictions for three story-based EDPs of interest, including peak SDRs; peak story shear force ( $V_{I+P-\Delta}$ ); and peak overturning moment ( $OTM_{I+P-\Delta}$ ) demands including the effects of P-Delta. Due to brevity, the discussion is based on the comparisons shown for the 12-story archetype building. However, the findings are applicable in all cases that were considered in the context of the present study.

The NSP to NRHA comparisons for all three story-based EDPs of interest are shown in Figure 4.9 for two seismic intensities of primary interest to the engineering profession; a DBE that corresponds to a 10% probability of exceedance over 50 years; and a MCE that corresponds to a 2% probability of exceedance over 50 years. It should be noted that the NRHA predictions are based on the composite model representations of the archetype buildings that explicitly consider the possibility for panel zone yielding due to shear distortion (noted as “NRHA-Median”). The NSP predictions summarized in Figure 4.9 are based on three selected nonlinear building models that their structural components were modelled based on the proposed ATC-114 nonlinear modelling recommendations: (a) the bare model with explicit consideration of the panel zone (noted as “NSP-Bare-PZ”); (b) a bare centerline model (noted as “NSP-Bare-CL”); (c) a composite model that explicitly captures the panel zone (noted as “NSP-Composite-PZ”).

Figures 4.9a and 4.9b show the peak story drift ratios along the height of the 12-story archetype as predicted by NSP and NRHA for the DBE and MCE seismic intensities, respectively. For both seismic intensities, peak story drift ratios are underestimated in the

upper stories. This is attributed to the higher-mode effects that are not explicitly captured by single-mode NSPs (Chopra and Goel, 2004; Krawinkler and Seneviratna, 1998). From Figure 4.9b (far into the inelastic range), peak story drift ratios are over predicted by all single-mode NSP options in the lower stories. This is attributed to the fact that the first-mode lateral load pattern that is employed to conduct the NSPs remains constant through out the nonlinear static procedure (Krawinkler and Seneviratna, 1998). However, the composite model tends to predict the story drift distribution of the 12-story archetype much closer to NRHA than the other models.

Figures 4.9c and 4.9d show the normalized peak story shear predictions based on various NSP options for the 12-story archetype for DBE and MCE seismic intensities, respectively. From this figure, all NSP predictions underestimate the peak story shear demands in mid- and upper stories of the 12-story archetype. For seismic intensities associated with low-probability of occurrence earthquakes (i.e., MCE) the maximum base shear force from the NSP is approximately 20% less than that predicted based on the median response from the NRHA. When the composite beam effects are considered in the nonlinear building model the corresponding base shear force is under predicted by approximately 10% compared to the NRHA median base shear. These effects, which increase with the number of stories, are attributed to the dynamic redistribution of story shear forces during the nonlinear building response. This tends to amplify story shear forces compared to those obtained from a pre-determined in single-mode NSPs (Krawinkler et al., 2011).

Figures 4.9e and 4.9f show the NSP peak floor OTM predictions for the 12-story archetype building for DBE and MCE seismic intensities, respectively. From both figures, the distribution of the OTM is almost linear. This is to be expected from the peak story shear force distribution shown in Figures 4.9c and 4.9d. From Figures 4.9e and 4.9f, at the base, the difference between single-mode NSP predictions and those from NRHA are smaller compared to those from peak story shear forces shown in Figure 4.9c and 4.9f for the DBE and MCE seismic intensities, respectively. This is attributed to the fact that maximum shear forces in individual

stories along the height of the archetypes occur at different times.

## 4.5 Summary

Case studies on archetype buildings with perimeter steel SMFs were conducted in order to assess the proposed component modelling recommendations provided in Chapter 3. Each of the 4-, 12-, and 20-story archetype buildings were modelled according to both the ASCE-41-13 (ASCE, 2014) guidelines, as well as the proposed recommendations in Chapter 3. From this, 10 different nonlinear building models were developed for both nonlinear static and response history analysis procedures.

The conclusions based on the nonlinear static analysis are as follows:

- Based on the NSP, the additional model complexity of the parallelogram panel zone model does not appreciably effect the results of the bare frame archetype buildings designed according to the current AISC seismic provisions (AISC, 2010a,b) in the ranges analysed.
- The building models that include the composite frame effects could be inherently more ductile than those including only the bare frame. This is in part attributed to the delay of the local buckling formation at the top flange of the respective steel beams due to the slab restraint. Furthermore, it was observed that typically the panel zone shear demands when the composite action are considered are larger than those of the bare frame only. Increased panel zone shear demands were observed to lead to panel zone shear yielding. Although this is a stable failure mechanism, excessive panel zone yielding may contributed to beam-to-column connection fracture. However, when only the bare frame is modelled, in certain cases the panel zone may remain elastic. Therefore it is important to explicitly model the panel zones when considering the effects of the composite slab on the steel beams in order to correctly capture the model response.
- On average, the static overstrength when including the composite action is 1.3x larger

than when only the bare frame is considered. The global elastic lateral stiffness when the composite action is included is approximately 1.4x larger than the bare frame only.

- Building models developed base on the ASCE-41-13 provisions tend to underestimate the post-yield global stiffness, primarily due to the constant 3% strain hardening assumed for all structural components.
- Building models developed based on the ASCE-41-13 provisions lead to very steep post-peak global stiffness. Due to the typical vertical drop in the corresponding member flexural strength in the ASCE-41-13 component model, this is likely to cause convergence problems within the nonlinear static and response history analysis.
- For models analysed such that the components are in the elastic region, or not too far in the inelastic region, there is practically no difference between different component modelling options. However, significant differences arise between the model responses based on different modelling options when the components are far into the inelastic region. Furthermore, different modelling options may lead to different global collapse mechanisms, especially the modelling of the composite beam effects.
- Due to dynamic overturning effects, the end columns of the SMF in the lower stories experience axial loads greater than  $50\%P_{cr}$ , such that these elements would be considered as force-controlled as per ASCE-41-13 (ASCE, 2014). However, wide-flange columns with axial load ratios up to near  $75\%P_{ye}$  show appreciable plastic deformation capacity, and should be treated as deformation-controlled elements, as discussed in Section 3.4.1. Such differences become larger once a column experiences a loading history that is representative of the ratcheting behaviour that a steel frame building experiences prior to collapse.

Based on direct comparisons between the single-mode NSP approaches and the rigorous NRHA, the main findings are summarized as follows:

- In agreement with previous studies (e.g., Chopra and Goel, 2004; Krawinkler and Seneviratna, 1998), for a single-mode NSP, there is a tendency to under predict the

SDR in the upper stories. This is attributed to the higher mode effects that are not captured by the single-mode NSP.

- At high lateral drift demands, the single-mode NSP tends to over predict the SDR in the lower stories. As observed by Krawinkler and Seneviratna (1998) this is attributed to the fact that the load pattern remains constant throughout the analysis. Generally, it was found that the results of the NSP from the composite frame models more closely estimated the SDRs from the NRHA versus the bare frame models.
- The story shear forces from the NSP tend to under predict those from the NRHA in the mid- and upper-stories. This is due to the dynamic redistribution of forces during the building nonlinear response, and tend to amplify with increasing stories.

Story	Elevation [inches]	Beam Size	Column Size Exterior	Column Size Interior	Doubler Plate Exterior Col.	Doubler Plate Interior Col.
4-story frame						
1	166.55	W21X73	W24X103	W24X103	0	5/16
2	322.55	W21X73	W24X103	W24X103	0	5/16
3	478.55	W21X57	W24X62	W24X62	0	5/16
4	634.55	W21X57	W24X62	W24X62	0	5/16
12-story frame						
1	166.55	W30X124	W24X207	W24X207	0	1/2
2	322.55	W30X132	W24X207	W24X207	0	7/16
3	478.55	W30X132	W24X162	W24X207	1/16	5/8
4	634.55	W30X132	W24X162	W24X207	1/16	5/8
5	790.55	W30X116	W24X146	W24X176	0	5/8
6	946.55	W30X116	W24X146	W24X176	0	5/8
7	1102.55	W30X116	W24X131	W24X162	1/16	11/16
8	1258.55	W30X116	W24X131	W24X162	1/16	11/16
9	1414.55	W27X94	W24X131	W24X131	0	9/16
10	1570.55	W27X94	W24X131	W24X131	0	9/16
11	1726.55	W27X84	W24X84	W24X94	1/16	9/16
12	1882.55	W27X84	W24X84	W24X94	1/16	9/16
20-story frame						
1	166.55	W33X169	W14X426	W24X335	0	1/4
2	322.55	W33X169	W14X426	W24X335	0	1/4
3	478.55	W33X169	W14X426	W24X335	0	1/4
4	634.55	W33X169	W14X426	W24X335	0	1/4
5	790.55	W33X169	W14X398	W24X335	0	1/4
6	946.55	W33X169	W14X398	W24X335	0	1/4
7	1102.55	W33X169	W14X370	W24X335	0	1/4
8	1258.55	W33X169	W14X370	W24X335	0	1/4
9	1414.55	W33X169	W14X311	W24X279	0	5/16
10	1570.55	W33X141	W14X311	W24X279	0	5/16
11	1726.55	W33X141	W14X283	W24X250	0	1/2
12	1882.55	W33X141	W14X283	W24X250	0	1/2
13	2038.55	W33X141	W14X233	W24X250	1/16	1/2
14	2194.55	W33X141	W14X233	W24X250	1/16	1/2
15	2350.55	W30X108	W14X159	W24X162	1/4	9/16
16	2506.55	W30X108	W14X159	W24X162	1/4	9/16
17	2662.55	W30X108	W14X132	W24X162	3/8	9/16
18	2818.55	W30X108	W14X132	W24X162	3/8	9/16
19	2974.55	W24X62	W14X132	W24X103	0	3/16
20	3130.55	W24X62	W14X132	W24X103	0	3/16

Table 4.1: Member sizes and elevations for each of the archetype frames. From NIST (2010).

Floor	Column Loads [kip]	Leaning Col. Loads [kip]	Frame Nodal Mass [kip·s <sup>2</sup> /in]
Roof	34.97	621	0.43
Typical	42.34	690	0.46
First	42.78	692	0.46

Table 4.2: Story nodal loads and masses for the archetype buildings.

Stories	Period, $T$ [sec] $T = C_u T_a$	Computed Period, $T_1$ [sec]				Static Overstrength $\Omega_s, V_{max}/V$			
		Bare-PZ	Comp-PZ	Bare-CL	Comp-CL	Bare-PZ	Comp-PZ	Bare-CL	Comp-CL
4	0.95	1.46	1.19	1.55	1.24	2.09	2.43	2.19	2.85
12	2.25	2.76	2.26	2.97	2.41	2.81	3.43	2.76	4.11
20	3.37	3.95	3.16	4.26	3.42	2.27	2.95	2.24	3.43

Table 4.3: Model periods and static overstrength for nonlinear static analysis.

Intensity Level	Bare-PZ [ $\Delta_r/H$ ]	Comp-PZ [ $\Delta_r/H$ ]	Bare-CL [ $\Delta_r/H$ ]	Comp-CL [ $\Delta_r/H$ ]
4-Story Frames				
SLE	0.010	0.008	0.010	0.008
DLE	0.020	0.015	0.020	0.016
MCE	0.029	0.023	0.030	0.024
12-Story Frames				
SLE	0.005	0.005	0.005	0.006
DLE	0.009	0.009	0.009	0.011
MCE	0.014	0.013	0.013	0.017
20-Story Frames				
SLE	0.003	0.003	0.004	0.003
DLE	0.006	0.006	0.007	0.006
MCE	0.009	0.009	0.011	0.009

Table 4.4: Target roof displacement ratios per the ASCE-41-13 coefficient method.

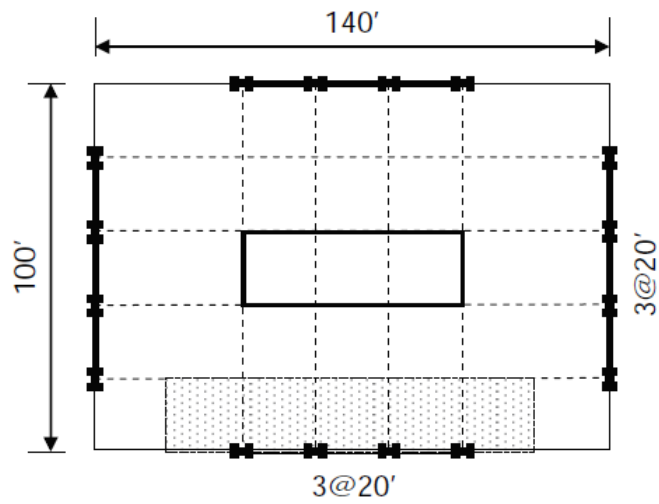
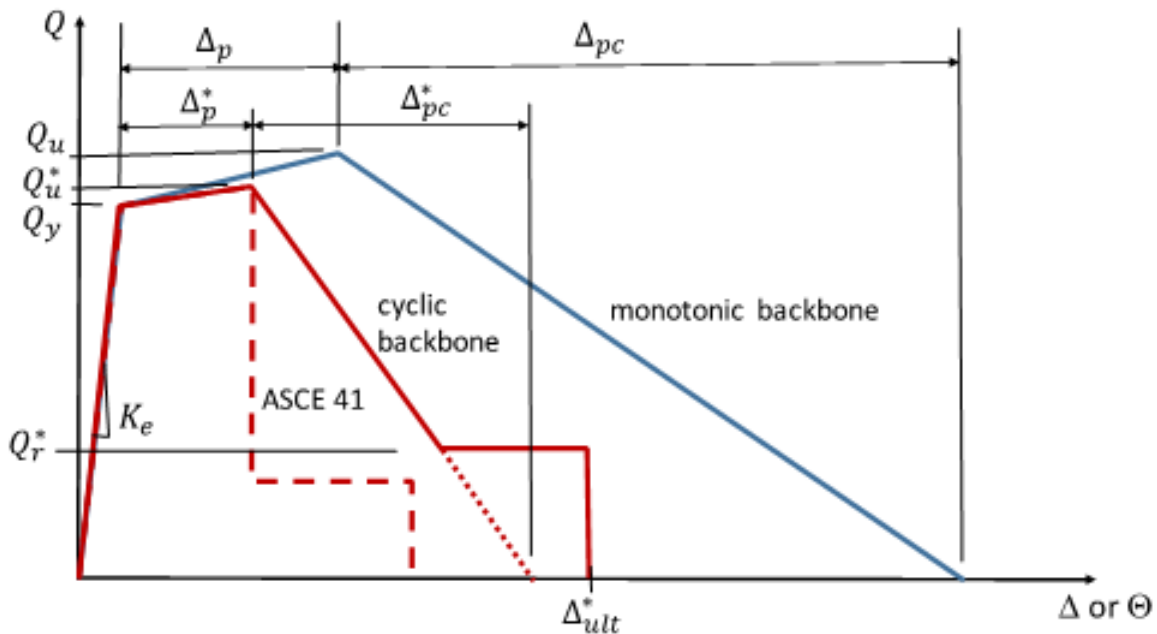


Figure 4.1: Plan view of archetype buildings, from NIST (2010).



**Definitions:**

- $Q$  - characteristic stress resultant (force or moment) in a structural component
- $Q_u$  - peak strength of the monotonic backbone
- $Q_u^*$  - peak strength of the cyclic backbone
- $Q_y$  - effective yield strength of the component
- $Q_r^*$  - residual strength of the cyclic backbone
- $\Delta$  or  $\Theta$  - characteristic deformation (displacement or rotation) in a structural component
- $\Delta_p$  - plastic deformation up to the peak strength of the monotonic backbone
- $\Delta_p^*$  - plastic deformation up to the peak strength of the cyclic backbone
- $\Delta_{pc}$  - plastic deformation of the descending portion of the monotonic backbone
- $\Delta_{pc}^*$  - plastic deformation of the descending portion of the cyclic backbone
- $\Delta_{ult}^*$  - ultimate deformation capacity at which point characteristic strength of the component is lost or where the component loses the resistance to resist vertical gravity loads
- cyclic backbone - idealized envelope of component response under cyclic loading
- monotonic backbone - idealized component response under monotonic loading
- ASCE 41 - Idealized component response under cyclic loading as specified in ASCE 41

Figure 4.2: General component model for the ATC-114 project, from ATC (2016).

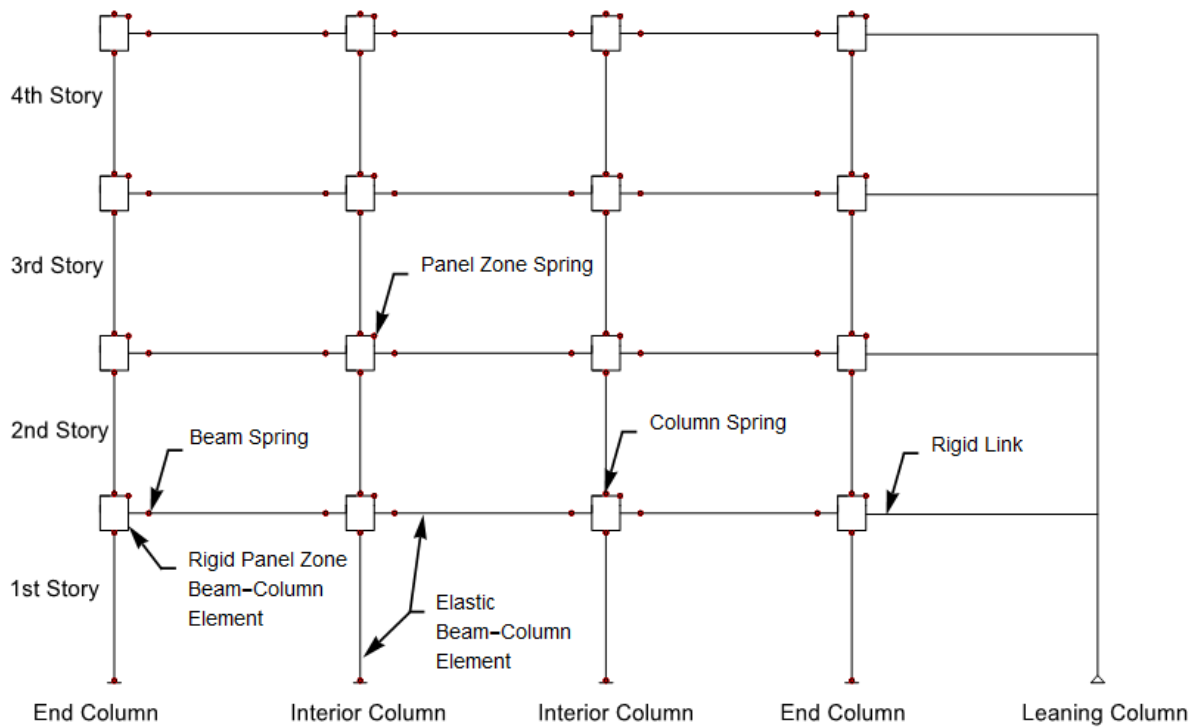
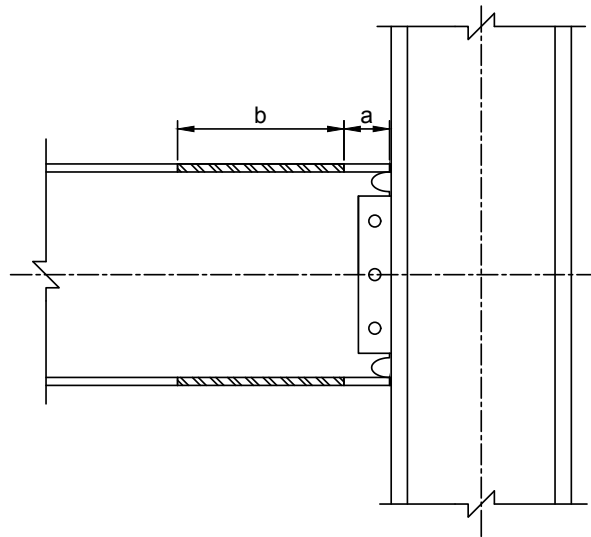
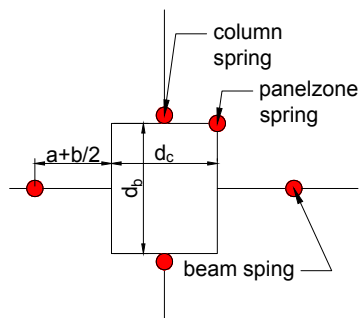


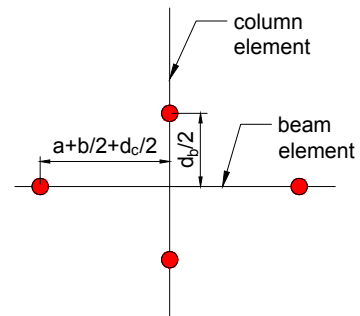
Figure 4.3: Visualization of the 4-story numerical model with explicit modelling of the beam-to-column joint panel zones.



(a) physical beam-to-column joint panel zone



(b) panel zone model



(c) centerline model

Figure 4.4: Physical details and model representations of beam-to-column joint panel zones for RBS connections.

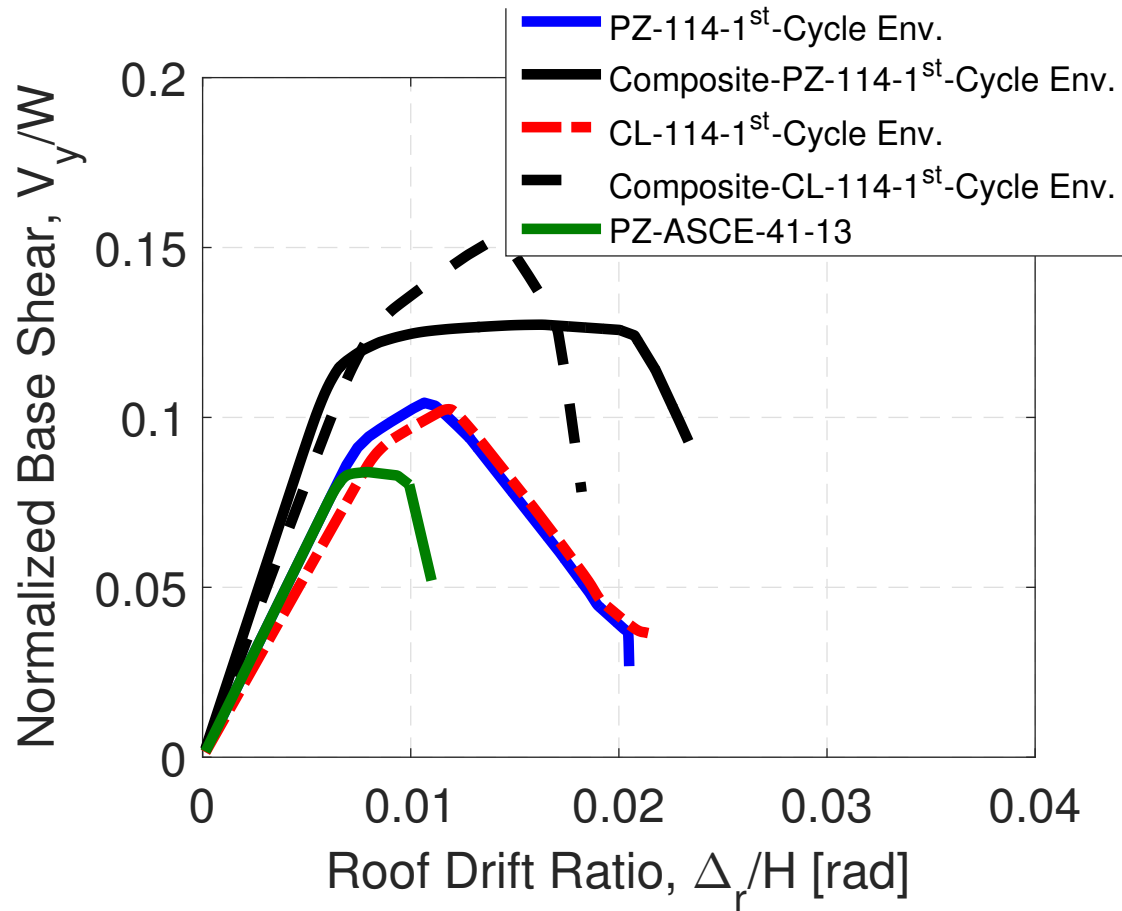


Figure 4.5: Global pushover curves based on single-mode nonlinear static procedure and various component-modelling options.

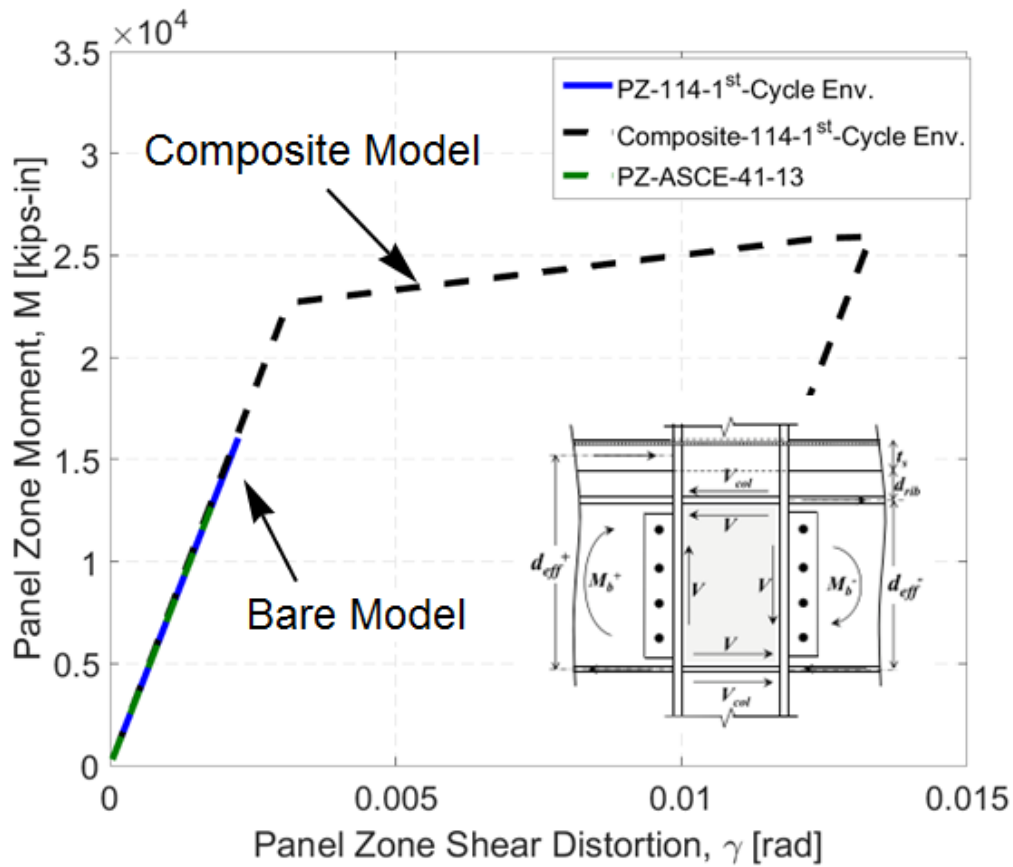
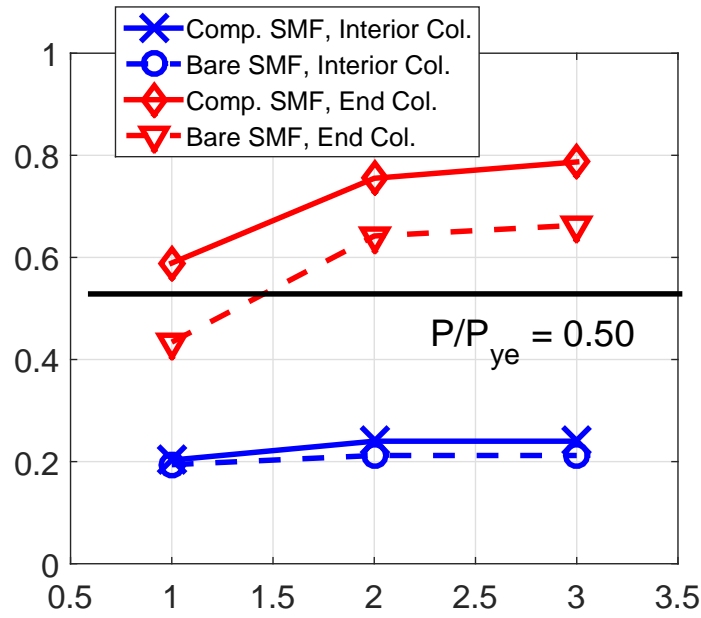
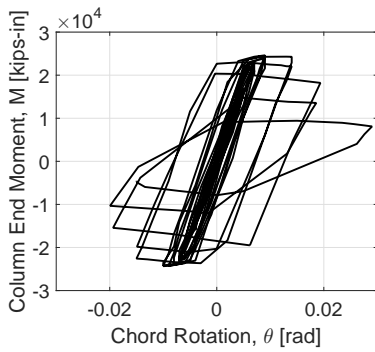


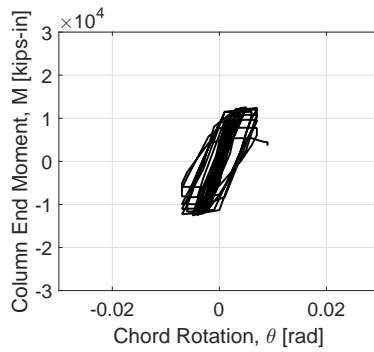
Figure 4.6: Prediction of the nonlinear static response of the first story interior beam-to-column panel zone joint of the 12-story steel SMF based on first-mode nonlinear static procedure.



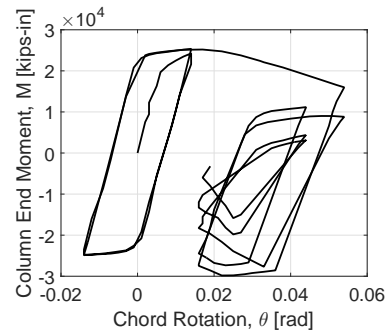
(a)



(b)

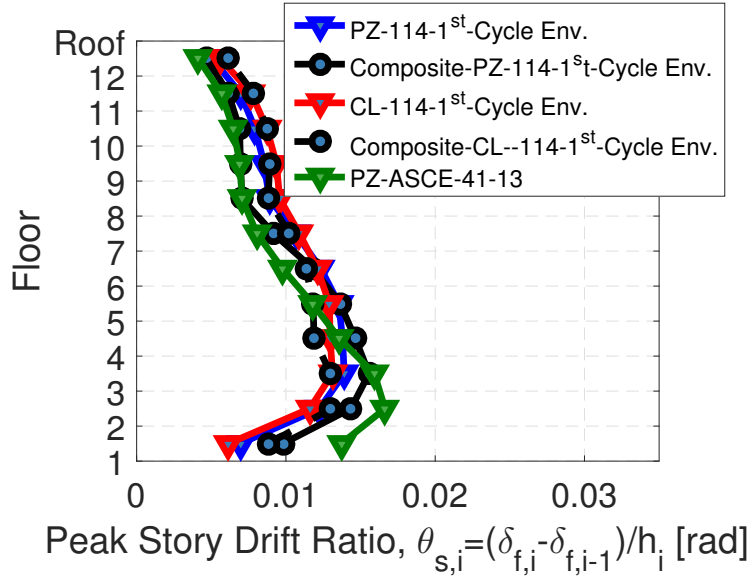


(c)

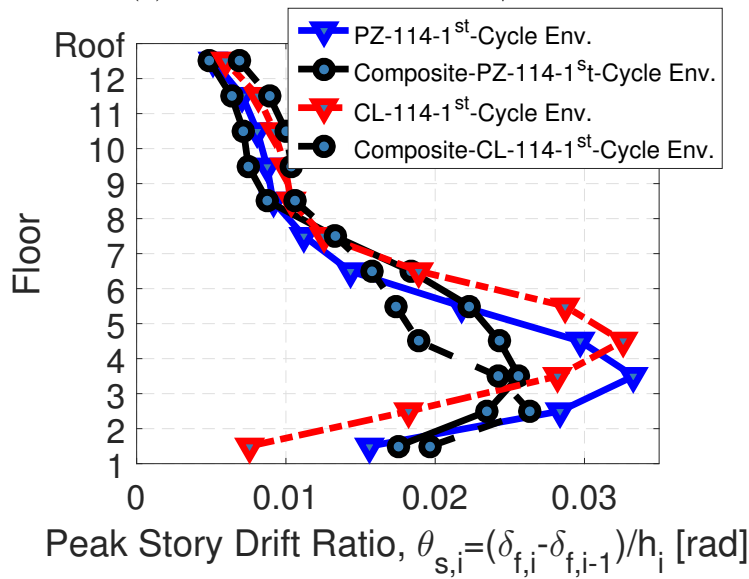


(d)

Figure 4.7: (a) Compressive axial force column demands for 12-story archetype based on nonlinear static procedure, first-mode lateral load pattern. Representative moment-rotation relation of a W24X192 steel column with varying axial load ratios,  $P_g/P_{ye}$ : (b) 50%, symmetric protocol (c) 75%, symmetric protocol and (d) 50%, collapse consistent protocol.



(a) target roof drift ratio,  $\Delta_r/H = 1\%$



(b) target roof drift ratio,  $\Delta_r/H = 1.5\%$

Figure 4.8: Predicted peak story drift ratios along the height of the 12-story archetype based on nonlinear static procedure, first-mode lateral load pattern.

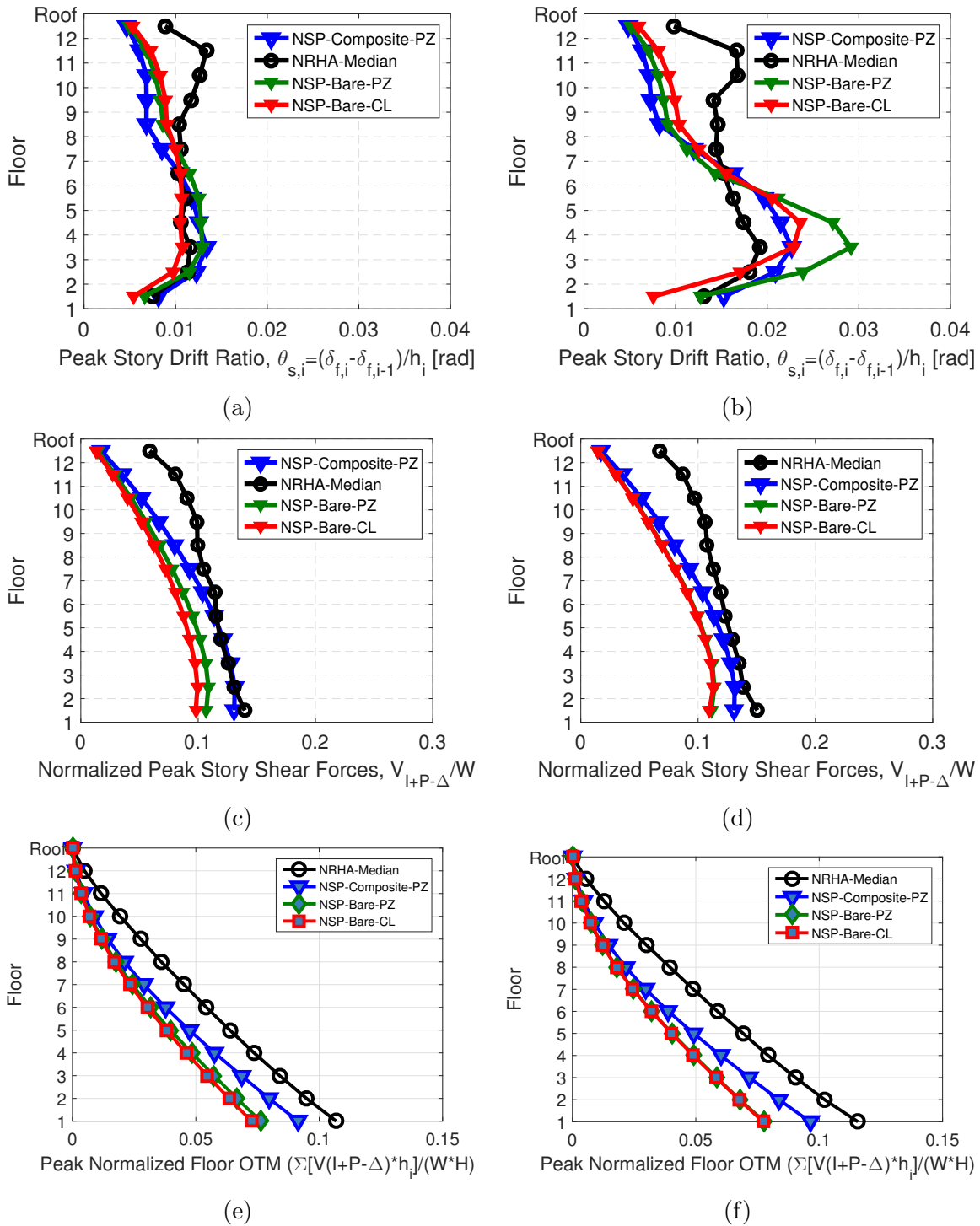


Figure 4.9: NSP to NRHA comparison of predicted story-based engineering demand parameters, 12-story archetype; left DBE seismic intensity; right MCE seismic intensity.

# Chapter 5

## Summary and Conclusions

### 5.1 Summary

The goal of this thesis is to advance the state of knowledge for the nonlinear modelling of steel components in support of performance-based seismic assessment of new and existing steel moment-resisting frame (MRF) systems. The completion of this goal was accomplished through the fulfilment of three main objectives: to assess the limitations in the current ASCE-41-13 (ASCE, 2014) nonlinear modelling provisions; to propose a set of recommendations for the nonlinear modelling of steel MRFs by updating component models when appropriate; and to evaluate the effects of implementing the proposed recommendations through a series of case studies on archetype buildings. Such recommendations were evaluated based on both nonlinear static and response history analyses.

The damage progression for each of the structural components considered in the nonlinear modelling of steel MRFs was provided in order to ensure that the component models developed are able to capture the relevant deterioration mechanisms observed in the structural components of interest. Current limitations in ASCE-41-13 (ASCE, 2014) guideline for the modelling of MRFs were assessed. The available component models for each of the structural components considered in steel MRFs that may address these limitations are provided in

Chapter 2 as a part of the literature review.

The component models developed as a part of this thesis are based on the multiple-regression analysis of available experimental data. Along with each of the predictive equations the full set of statistical results are provided. A measure of the variability in the response parameters that comprise the component models is provided in order to assess the uncertainty of the structural component's predicted force-deformation relation. Each of the component models are validated by comparing the predicted force-deformation relation with data from representative experiments.

The case studies on the 4-, 12-, and 20-story archetype buildings with perimeter steel special moment frames (SMFs) are outlined in Chapter 4. Such archetypes reflect the state of practice in terms of today's steel construction in regions of high seismicity in the West-Coast of the United States. Ten different nonlinear models were developed for each of the three archetype buildings in order to investigate the effects of: implementing the proposed modelling recommendations, versus the existing ASCE-41-13 provisions; modelling the composite slab steel beams and panel zones, versus the bare steel components; and explicitly modelling the beam-to-column joint panel zones, versus making a centerline approximation that is quite common in engineering practice.. Nonlinear static and response history analyses were carried out on the 10 nonlinear building models in order to assess the aforementioned objectives.

The proposed recommendations provided in this thesis will be used as a part of future updates to the ASCE-41 provisions. The major conclusions from each of aforementioned chapters are presented in the following section.

## 5.2 Conclusions and Recommendations

### 5.2.1 Limitations with the ASCE-41-13 nonlinear modelling provisions for steel moment-resisting frames

For the development of numerical buildings models for the performance-based seismic assessment of steel MRFs practising engineers typically use the guidelines provided in ASCE-41-13 (ASCE, 2014). However, as summarized below there are a number of limitations with the ASCE-41-13 guidelines, addressing these limitations was the primary motivation of this thesis. The major limitations found in the ASCE-41-13 guidelines are summarized below:

- There are no statistical parameters provided to assess the variability of the input parameters on the component model response. In this case, the robustness of a structural system cannot be assessed.
- The component models are generally based on limited test data that was from at least 20 years ago. In many cases (e.g., steel columns), the input parameters of those models were based off of empirical judgement due to lack of available data.
- There are no component models included in ASCE-41-13 suitable for nonlinear dynamic analysis procedures that can explicit model cyclic and in-cycle deterioration in strength and stiffness.
- Consideration for the effects of the composite slab on the response of both beams and panel zones of the steel frame has been overlooked.
- Recent research suggests that columns with an axial load ratio greater than  $50\%P_{cr}$  should be modelled as deformation-controlled.
- No guidelines are provided for the modelling of columns subjected to varying axial loads, or bi-directional loading.
- No guidelines are provided for the nonlinear modelling of steel column splices, as well as column base connections.

## 5.2.2 Proposed component modelling recommendations

In order to address the aforementioned limitations with the ASCE-41-13 provisions for the nonlinear modelling of steel MRFs, a number of state-of-the-art component models were developed for the performance-based seismic assessment of new and existing steel MRFs. Empirical equations relating the geometric and material properties to the response parameters of the respective structural component model were developed using multiple-regression analysis procedures carried out on test data. The component models that were developed as a part of this thesis are presented along side existing state-of-the-art component models to form a set of recommendations to address the limitations in the ASCE-41-13 provisions. The major conclusions with regards to the nonlinear modelling of steel MRF components developed in Chapter 3 are:

### **Steel beams as a part of fully-restrained beam-to-column connections**

- From the statistical evaluation of beams in fully-restrained beam-to-column connections, for all connection types, the web depth-to-thickness ratio,  $h/t_w$ , was found to be the most important parameter in predicting the plastic rotation capacity of a steel beam regardless of the beam-to-column connection type. Other important parameters were the flange depth-to-thickness ratio,  $b_f/2t_f$ , the shear span to depth ratio,  $L/d$ , and the ratio of the unbraced length to radius of gyration,  $L_b/r_y$ .
- The ratio of the effective flexural yield strength to plastic moment for beams in fully-restrained beam-to-column connections subjected to reversed-cyclic loading protocols was found to be  $M_y^*/M_{pe} = 1.15$ .
- The mean ratio of ultimate rotation based on the first-cycle envelope to monotonic backbone for bare steel beams in fully-restrained beam-to-column connections was found to be  $\theta_{ult}^*/\theta_{ult} = 0.65$ . This is comparable to the value of 0.70 assumed in ATC-72 (PEER/ATC, 2010).
- For steel beams in fully-restrained beam-to-column connections with a depth  $d \geq 21"$  the ASCE-41 component models were found to generally overestimate the pre-peak

plastic rotation of a steel beam regardless of the beam-to-column connection type. For beams with  $d < 21$ ", the plastic deformation parameters seem to be more reasonably predicted, indicating that there may be some bias in the ASCE-41-13 provisions towards beams with smaller depths. This could be due to the fact that the majority of the available experiments on steel beams that were used to develop the first generation of the ASCE-41 component models were conducted on small scale beams (e.g., W18). The proposed component models are found to provide a reasonable estimation of test data, and are able to capture the gradual decrease in flexural strength in the post-peak region.

#### **Steel beams as a part of pre-Northridge WUF-B connections**

- The component model for steel beams with  $d < 24$ " is practically similar to the one provided in ASCE-41-13 (ASCE, 2014). For beams with  $d > 24$ ", the recommendations are practically similar to those of FEMA-355D (FEMA, 2000).
- Generally, both ASCE-41-13 and the proposed recommendations will underestimate the pre-peak plastic rotation for beams in pre-Northridge WUF-B connections.
- For beams with  $d < 18$ ", an upper-bound flexural strength can be utilized in the modelling procedure, as typically such beams have an appreciable plastic deformation prior to the occurrence of fracture.

#### **Wide-flange steel columns**

- The axial force exerted on steel wide-flange columns due to gravity loading,  $P_g$ , has a greater influence on the column force-deformation response than the transient component resulting from the dynamic overturning effects on columns hysteretic behaviour. Therefore, the constant gravity load  $P_g$  can be used to predict the behaviour of steel columns in nonlinear modelling procedures.
- The parameter with a dominant affect on the force-deformation behaviour of steel wide-flange columns from a statistical evaluation is found to be the ratio of the applied compressive axial load to expected yield strength,  $P_g/P_{ye}$ . This is true for columns

subjected to both monotonic and reversed-cyclic loading histories. Both the web and flange slenderness ratios (i.e.,  $h/t_w$  and  $b_f/2t_f$ ) were found to be significant on the force-deformation relation of wide flange steel columns. However it was observed that the  $h/t_w$  had a dominant effect over  $b_f/2t_f$ . Due to the high correlation between the flange and web depth-to-thickness ratios for the sections considered in the database, only  $h/t_w$  is considered in each of the equations. As well, it was found that the global slenderness ratio,  $L_b/r_y$ , was significant in each of the response parameters.

- For steel wide-flange columns, in all cases it was found that ASCE-41-13 component models overestimate the pre-peak plastic rotation for the first-cycle envelope curve. The proposed component models are found to provide a reasonable estimation of test data, and are able to capture the gradual decrease in flexural strength in the post-peak region.
- Each of  $h/t_w$ ,  $L_b/r_y$ , and  $P_g/P_{ye}$  were found to have a significant relation with the post-yield hardening ratio of steel wide-flange columns. This observation is true for columns subjected to both monotonic and reversed-cyclic loading histories, and is converse to the constant 3% strain hardening assumed under ASCE-41-13 (ASCE, 2014).
- The plastic-deformation capacity of steel wide-flange columns under bi-directional lateral drift demands is practically similar to those under uni-directional loading, and can therefore be modelled according to provisions developed for uni-directional loading.
- Steel wide-flange columns exhibit appreciable plastic deformation even with axial loads greater than 50% of their axial yield strength. The limit for force-controlled elements per ASCE-41-13 (ASCE, 2014) should be revised to columns with  $P_g/P_{ye} \geq 0.60$  that have  $h/t_w > 43$  and  $kL_b/r_y > 120$ .
- End columns in steel MRFs typically experience increased axial load demands during seismic events due to the dynamic overturning effect. Full-scale testing has shown that the constant gravity load has a greater influence on the column force-deformation

history than the transient component of the axially compressive load. As such, from full-scale experimental observations, columns with varying axially compressive loads of up to  $75\%P_{ye}$  show appreciable plastic deformation capacity. Therefore, the constant gravity load,  $P_g$ , may be considered when modelling end columns in steel MRFs.

- The ratio between the mean value of the total plastic deformation of a monotonic curve with respect to that of a first-cycle envelope curve for the same cross-section is, on average, 2.8. This value is consistent with what is currently reported in Chapter 16 of ASCE 7-16 (ASCE, 2016) for deformation-controlled elements (i.e., recommended value is 3.0).

#### **Hollow structural steel columns**

- Based on the first-cycle envelope, the dominant parameter from the statistical evaluation of HSS columns in the pre-peak plastic region is found to be the HSS depth-to-thickness ratio,  $D/t$ . The ratio of the elastic modulus to effective yield stress,  $E/F_y$ , is found to be significant only in the pre-peak plastic deformation only of an HSS column. In the post-peak plastic region, the ratio of the axial gravity load to expected yield strength,  $P_g/P_{ye}$ , is found to be the dominant parameter.
- Relationships between the hardening ratio and each of the local slenderness, the expected yield stress, and the axial load ratio of HSS columns can be established. Therefore, the strain hardening is not a constant 3% as assumed in ASCE-41-13, and varies with each of these three parameters.
- HSS columns should be considered as force-controlled elements for  $P_g/P_{ye} > 0.60$ , and  $D/t > 33$  per ASCE-41-13 (ASCE, 2014).

#### **Column splice connections**

- Using a fracture mechanics based design formula, the strength capacity of pre-Northridge column splices can be verified based on the maximum tensile stresses due to axial tension and bi-axial bending at the splice location.

#### **Column base connections**

- In both exposed and column base connections, the flexural strength parameters of the first-cycle envelope can be estimated reasonably well based on principles of engineering mechanics.
- The average pre-peak plastic rotation capacity of exposed column base connections based on data deduced from tests under reversed-cyclic loading is approximately  $\theta_p^* = 0.065$  radians.
- The average pre-peak plastic rotation capacity of embedded column base connections based on data deduced from tests under reversed-cyclic loading is approximately  $\theta_p^* = 0.015$  radians. The average ultimate rotation was found to be approximately  $\theta_{pc}^* = 0.06$  radians for ductile failure modes, and  $\theta_{pc}^* = 0.03$  radians for brittle failure modes.

### 5.2.3 Findings from case studies

Case studies on archetype buildings with perimeter steel SMFs were conducted in order to assess the proposed component modelling recommendations provided in Chapter 3. The 4-, 12-, and 20-story perimeter SMFs designed according to current US practice for urban California were chosen as the archetype buildings for the case studies (NIST, 2010). Each of the 4-, 12-, and 20-story archetype buildings were modelled according to both the ASCE-41-13 (ASCE, 2014) guidelines, as well as the proposed recommendations in Chapter 3. Additionally, the effects of the composite action on the steel beams and panel zones was considered, as well as explicit modelling of the panel zone parallelogram. From this, 10 different nonlinear building models were developed. A rigorous nonlinear first-mode nonlinear static analysis (NSP) and nonlinear response history analysis (NRHA) was carried out for each of these building models. The NRHA was carried out using the FEMA P695 far-field ground motion set.

The conclusions based on the nonlinear static analysis are as follows:

- Based on the NSP, the additional model complexity of the parallelogram panel zone model does not affect the results of the bare frame archetype buildings designed according

to the current AISC seismic provisions (AISC, 2010a,b) in the ranges analysed.

- The building models that include the composite frame effects could be inherently more ductile than those including only the bare frame. This is in part attributed to the delay of the local buckling formation at the top flange of the respective steel beams due to the slab restraint. Furthermore, it was observed that typically the panel zone shear demands when the composite action are considered are larger than those of the bare frame only. Increased panel zone shear demands were observed to lead to panel zone shear yielding. Although this is a stable failure mechanism, excessive panel zone yielding may contributed to beam-to-column connection fracture. However, when only the bare frame is modelled, in most cases the panel zone remained elastic. Therefore it is important to explicitly model the panel zones when considering the effects of the composite slab on the steel beams in order to assess the seismic response of typical steel MRFs designed in seismic regions.
- On average, the static overstrength when including the composite action is 1.3x larger than when only the bare frame is considered. The global elastic lateral stiffness when the composite action is included is approximately 1.4x larger than the bare frame only. Note that these differences can be larger if the gravity framing system is considered as part of the analytical model representation of the archetype building (see Elkady and Lignos 2015).
- Building models developed based on the ASCE-41-13 provisions lead to very steep post-peak global stiffness. Due to the typical vertical drop in the corresponding member flexural strength in the ASCE-41-13 component model, this is likely to cause convergence problems within the nonlinear static analysis.
- For models analysed such that their components are in the elastic region, or not too far in the inelastic region, there is practically no difference between different component modelling options. However, significant differences arise between the model responses based on different modelling options when the components are far into the inelastic

region. Furthermore, different modelling options may lead to different global collapse mechanisms, especially the modelling of the composite beam effects.

- Due to dynamic overturning effects, the end columns of the SMF in the lower stories experience axial loads greater than  $50\%P_{cr}$ , such that these elements would be considered as force-controlled as per ASCE-41-13 (ASCE, 2014). However, wide-flange columns with axial load ratios up to near  $75\%P_{ye}$  show appreciable plastic deformation capacity. Due to the presence of geometric imperfections, columns loaded to  $75\%$  of  $P_{ye}$  may buckle. Therefore, columns should be treated as deformation-controlled elements, as discussed in Section 3.4.1 for loads  $P \leq 0.60P_{ye}$ . Such differences become larger once a column experiences a loading history that is representative of the ratcheting behaviour that a steel frame building experiences prior to collapse.

Based on direct comparisons between the single-mode NSP approaches and the rigorous NRHA, the main findings are summarized as follows:

- In agreement with previous studies (e.g., Chopra and Goel, 2004; Krawinkler and Seneviratna, 1998), for a single-mode NSP, there is a tendency to under predict the SDR in the upper stories. This is attributed to the higher mode effects that are not captured by the single-mode NSP.
- At high lateral drift demands, the single-mode NSP tends to over predict the SDR in the lower stories. As observed by Krawinkler and Seneviratna (1998) this is attributed to the fact that the load pattern remains constant throughout the analysis. Generally, it was found that the results of the NSP from the composite frame models more closely estimated the SDRs from the NRHA versus the bare frame models.
- The story shear forces from the NSP tend to under predict those from the NRHA in the mid- and upper-stories. This is due to the dynamic redistribution of forces during the building nonlinear response, and tend to amplify with increasing stories.

# References

- AISC (2005a). *Prequalified connections for special and intermediate steel moment frames for seismic applications*, ANSI/AISC 358-05. American Institute of Steel Construction, Chicago, Illinois, United States.
- AISC (2005b). *Seismic provisions for structural steel buildings*, ANSI/AISC 341-05. American Institute of Steel Construction, Chicago, Illinois, United States.
- AISC (2010a). *Seismic provisions for structural steel buildings*, ANSI/AISC 341-10. American Institute of Steel Construction, Chicago, Illinois, United States.
- AISC (2010b). *Specification for structural steel buildings*, ANSI/AISC 360-10. American Institute of Steel Construction, Chicago, Illinois, United States.
- ASCE (2006). *Minimum design loads for buildings and other structures*, ASCE/SEI 7-05. American Society of Civil Engineers, Reston, Virginia, United States.
- ASCE (2014). *Seismic Evaluation and Retrofit of Existing Buildings*, ASCE 41-13. American Society of Civil Engineers, Reston, Virginia, United States.
- ASCE (2016). *Minimum design loads for buildings and other structures*, ASCE/SEI 7-16. American Society of Civil Engineers, Reston, Virginia, United States.
- ATC (2016). “Guidelines for Nonlinear Structural Analysis for Design of Buildings: Part IIa—Steel Moment Frames.” *Report No. ATC-114 90% Draft*, Applied Technology Council.

- Bech, D., Tremayne, B., and Houston, J. (2015). "Proposed changes to steel column evaluation criteria for existing buildings." *Proc., ATC/SEI 2nd Conference on Improving the Seismic Performance of Existing Buildings and Other Structures*, San Francisco, California, United States, 255–272.
- Bruneau, M., Mahin, S., and Popov, E. (1987). "Ultimate behavior of butt welded splices in heavy rolled steel sections." *Report No. UBC/EERC-87/10*, University of California, Berkeley, Berkeley, California, United States.
- Bruneau, M. and Mahin, S. A. (1990). "Ultimate behavior of heavy steel section welded splices and design implications." *Journal of Structural Engineering*, 116(8), 2214–2235.
- Bruneau, M. and Mahin, S. A. (1991). "Full-scale tests of butt-welded splices in heavy-rolled steel sections subjected to primary tensile stresses." *Engineering Journal*, 28(1), 1–17.
- Charney, F. A. and Downs, W. M. (2004). "Modeling procedures for panel zone deformations in moment resisting frames." *Proc., Connections in Steel Structures V*, Amsterdam, Netherlands.
- Chatterjee, S. and Hadi, A. S. (2015). *Regression analysis by example*. John Wiley & Sons.
- Chi, B. and Uang, C.-M. (2002). "Cyclic response and design recommendations of reduced beam section moment connections with deep columns." *Journal of Structural Engineering*, 128(4), 464–473.
- Chopra, A. K. and Goel, R. K. (2004). "A modal pushover analysis procedure to estimate seismic demands for unsymmetric-plan buildings." *Earthquake Engineering & Structural Dynamics*, 33(8), 903–927.
- Cordoba, P. and Deierlein, G. (2005). "Validation of the seismic performance of composite rc frames: Full-scale testing, analytical modeling, and seismic design." *Report No. 155*, The

John A. Blume Earthquake Engineering Center, Stanford University, Stanford, California, United States.

Elkady, A. (2016). “Collapse risk assessment of steel moment resisting frames designed with deep wide-flange columns in seismic regions.” Ph.D. thesis, McGill University, Montreal, Quebec, Canada.

Elkady, A. and Lignos, D. G. (2013). “Effect of composite action on the dynamic stability of special steel moment resisting frames designed in seismic regions.” *Proc., ASCE Structures Congress 2013*, ASCE, Pittsburgh, Pennsylvania, United States, 2151–2160.

Elkady, A. and Lignos, D. G. (2014). “Modeling of the composite action in fully restrained beam-to-column connections: implications in the seismic design and collapse capacity of steel special moment frames.” *Earthquake Engineering & Structural Dynamics*, 43(13), 1935–1954.

Elkady, A. and Lignos, D. G. (2015a). “Analytical investigation of the cyclic behavior and plastic hinge formation in deep wide-flange steel beam-columns.” *Bulletin of Earthquake Engineering*, 13(4), 1097–1118.

Elkady, A. and Lignos, D. G. (2015b). “Effect of gravity framing on the overstrength and collapse capacity of steel frame buildings with perimeter special moment frames.” *Earthquake Engineering & Structural Dynamics*, 44(8), 1289–1307.

Elkady, A. and Lignos, D. G. (2016). “Dynamic stability of deep and slender wide-flange steel columns — full scale experiments.” *Proc., Annual Stability Conference*, Orlando, Florida, United States, Structural Stability Research Council (SSRC).

Engelhardt, M. and Sabol, T. (1994). *Testing of Welded Steel Moment Connections in Response to the Northridge Earthquake*. AISC Progress Report, Chicago, Illinois, United States.

Engelhardt, M. D., Fry, G., Jones, S., Venti, M., and Holliday, S. (2000). “Behavior and design of radius-cut, reduced beam section connections.” *Report No. SAC/BD-00/17*, SAC Joint Venture, a partnership of the Structural Engineers Association of California, Applied Technology Council, and California Universities for Research in Earthquake Engineering, Sacramento, California, United States.

FEMA (1997a). “Connection test summaries.” *Report No. FEMA-289*, prepared by the SAC Joint Venture, a partnership of the Structural Engineers Association of California (SEAOC), Applied Technology Council (ATC), and California Universities for Research in Earthquake Engineering (CUREE), for the Federal Emergency Management Agency, Washington, D.C., United States.

FEMA (1997b). “NEHRP guidelines for the seismic rehabilitation of buildings.” *Report No. FEMA-273*, Federal Emergency Management Agency, Washington, DC, United States.

FEMA (2000). “State of the Art Report on Connection Performance.” *Report No. FEMA 355-D*, prepared by the SAC Joint Venture, a partnership of the Structural Engineers Association of California (SEAOC), Applied Technology Council (ATC), and California Universities for Research in Earthquake Engineering (CUREE), for the Federal Emergency Management Agency, Washington, D.C., United States.

FEMA (2000). “State of the art report on systems performance of steel moment frames subject to earthquake ground shaking.” *Report No. FEMA-355C*, prepared by the SAC Joint Venture, a partnership of the Structural Engineers Association of California (SEAOC), Applied Technology Council (ATC), and California Universities for Research in Earthquake Engineering (CUREE), for the Federal Emergency Management Agency, Washington, DC, United States.

FEMA (2009). “Quantification of Building Seismic Performance Factors, FEMA P-695.”

*Report No. P-695*, Federal Emergency Management Agency, Washington, DC, United States.

Fisher, J. M. and Kloiber, L. A. (2006). *Base plate and anchor rod design*. American Institute of Steel Construction, Chicago, Illinois, United States.

Gomez, I. R. (2010). “Behavior and design of column base connections.” Ph.D. thesis, University of California, Davis, California, United States.

Grilli, D. (2015). “Seismic response of embedded column base connections and anchorages.” Ph.D. thesis, University of California, Davis, California, United States.

Gupta, A. and Krawinkler, H. (1999). “Seismic demands for the performance evaluation of steel moment resisting frame structures.” *Report No. 132*, The John A. Blume Earthquake Engineering Research Center, Stanford University, Stanford, California, United States.

Gupta, A. and Krawinkler, H. (2000a). “Behavior of ductile SMRFs at various seismic hazard levels.” *Journal of Structural Engineering*, 126(1), 98–107.

Gupta, A. and Krawinkler, H. (2000b). “Dynamic P-delta effects for flexible inelastic steel structures.” *Journal of Structural Engineering*, 126(1), 145–154.

Gupta, A. and Krawinkler, H. (2000c). “Estimation of seismic drift demands for frame structures.” *Earthquake Engineering & Structural Dynamics*, 29(9), 1287–1305.

Hertz, J., Lignos, D. G., and Rogers, C. (2015). “Full-scale experimental testing of extended beam-to-column and beam-to-girder shear tab connections subjected to shear.” *Proc., 8th International Conference on Behaviour of Steel Structures in Seismic Areas*, Vol. 4, Shanghai, China, 2015.

Ibarra, L. F. and Krawinkler, H. (2005). *Global collapse of frame structures under seismic excitations*. Pacific Earthquake Engineering Research Center.

- Ibarra, L. F., Medina, R. A., and Krawinkler, H. (2005). “Hysteretic models that incorporate strength and stiffness deterioration.” *Earthquake engineering & structural dynamics*, 34(12), 1489–1511.
- Kanvinde, A. M., Grilli, D. A., and Zareian, F. (2012). “Rotational Stiffness of Exposed Column Base Connections: Experiments and Analytical Models.” *Journal of Structural Engineering*, 138(5), 549–560.
- Kim, K. D. and Engelhardt, M. D. (2002). “Monotonic and cyclic loading models for panel zones in steel moment frames.” *Journal of Constructional Steel Research*, 58(5), 605–635.
- Krawinkler, H. (1978). “Shear in beam-column joints in seismic design of steel frames.” *Engineering Journal*, 15(3).
- Krawinkler, H., Bertero, V., and Popov, E. P. (1971). “Inelastic Behavior of Steel Beam-to-Column Subassemblages.” *Report No. EERC-71-7*, University of California, Berkeley, California, United States.
- Krawinkler, H., Lignos, D. G., and Putman, C. (2011). “Prediction of nonlinear response-pushover analysis versus simplified nonlinear response history analysis.” *Proc., Structures Congress*, Las Vegas, Nevada, United States.
- Krawinkler, H. and Seneviratna, G. (1998). “Pros and cons of a pushover analysis of seismic performance evaluation.” *Engineering structures*, 20(4), 452–464.
- Lignos, D., Krawinkler, H., and Whittaker, A. (2011a). “Prediction and validation of sidesway collapse of two scale models of a 4-story steel moment frame.” *Earthquake Engineering & Structural Dynamics*, 40(7), 807–825.
- Lignos, D. G., Cravero, J., and Elkady, A. (2016). “Experimental investigation of the hysteretic behavior of wide-flange steel columns under high axial load and lateral drift demands.” *Proc., 11th Pacific Structural Steel Conference*, Shanghai, China.

- Lignos, D. G., Eads, L., and Krawinkler, H. (2011b). “Effect of composite action on collapse capacity of steel moment frames under earthquake loading.” *Proc., EUROSTEEL*, Budapest, Hungary.
- Lignos, D. G., Hikino, T., Matsuoka, Y., and Nakashima, M. (2013). “Collapse assessment of steel moment frames based on e-defense full-scale shake table collapse tests.” *Journal of Structural Engineering*, 139(1), 120–132.
- Lignos, D. G. and Krawinkler, H. (2007). “Deterioration modeling of steel components in support of collapse prediction of steel moment frames under earthquake loading.” *Proc., ASCE Structures Congress*, Long Beach, California, United States, SEI Institute.
- Lignos, D. G. and Krawinkler, H. (2009). “Sidesway collapse of deteriorating structural systems under seismic excitations.” *Report No. 172*, The John A. Blume Earthquake Engineering Research Center, Stanford University, Stanford, California, United States.
- Lignos, D. G. and Krawinkler, H. (2010). “A steel database for component deterioration of tubular hollow square steel columns under varying axial load for collapse assessment of steel structures under earthquakes.” *Proc., 7th International Conference on Urban Earthquake Engineering (7CUEE) & 5th International Conference on Earthquake Engineering (5ICEE)*, Tokyo, Japan, Tokyo Institute of Technology.
- Lignos, D. G. and Krawinkler, H. (2011). “Deterioration Modeling of Steel Components in Support of Collapse Prediction of Steel Moment Frames under Earthquake Loading.” *Journal of Structural Engineering*, 137(11), 1291–1302.
- Lignos, D. G. and Krawinkler, H. (2012). “Development and utilization of structural component databases for performance-based earthquake engineering.” *Journal of Structural Engineering*, 139(8), 1382–1394.
- Lignos, D. G., Putman, C., and Krawinkler, H. (2015). “Application of simplified analysis

- procedures for performance-based earthquake evaluation of steel special moment frames.” *Earthquake Spectra*, 31(4), 1949–1968.
- Liu, J. (2000). “Experimental and analytical studies of the cyclic behavior of simple connections in steel frame buildings.” Ph.D. thesis, University of California, Berkeley, California, United States.
- Liu, J. and Astaneh-Asl, A. (2000). “Cyclic testing of simple connections including effects of slab.” *Journal of Structural Engineering*, 126(1), 32–39.
- Liu, J. and Astaneh-Asl, A. (2004). “Moment-rotation parameters for composite shear tab connections.” *Journal of Structural Engineering*, 130(9), 1371–1380.
- Lu, L.-W., Ricles, J. M., Mao, C., and Fisher, J. W. (2000). “Critical issues in achieving ductile behaviour of welded moment connections.” *Journal of Constructional Steel Research*, 55(1), 325–341.
- MacRae, G. A. (1989). “The Seismic Response of Steel Frames.” Ph.D. thesis, University of Canterbury, Christchurch, New Zealand.
- MacRae, G. A., Urmson, C. R., Walpole, W. R., Moss, P., Hyde, K., and Clifton, C. (2009). “Axial shortening of steel columns in buildings subjected to earthquakes.” *Bulletin of the New Zealand Society for Earthquake Engineering*, 42(4), 275.
- McKenna, F. T. (1997). “Object-oriented finite element programming: Frameworks for analysis, algorithms and parallel computing.” Ph.D. thesis, University of California, Berkeley, Berkeley, California, United States.
- Nakashima, M., Matsumiya, T., Suita, K., and Zhou, F. (2007). “Full-scale test of composite frame under large cyclic loading.” *Journal of Structural Engineering*, 133(2), 297–304.
- Nakashima, M., Takanashi, K., and Kato, H. (1990). “Test of steel beam-columns subject to sidesway.” *Journal of Structural Engineering*, 116(9), 2516–2531.

- Nam, T. T. and Kasai, K. (2012). “Study on shake-table experimental results regarding composite action of a full-scale steel building tested to collapse.” *Proc., International Conference on Urban Earthquake Engineering/4th Asia Conference on Earthquake Engineering, Tokyo Institute of Technology, Tokyo, Japan, 1111–1116.*
- Newell, J. D. and Uang, C.-M. (2006). *Cyclic behavior of steel columns with combined high axial load and drift demand.* University of California, San Diego, California, United States.
- NIST (2010). *Evaluation of the FEMA P-695 Methodology for Quantification of Building Seismic Performance Factors.* US Department of Commerce, Engineering Laboratory, National Institute of Standards and Technology, Gaithersburg, Maryland, United States.
- NIST (2011). “Nonlinear Structural Analysis For Seismic Design: A Guide for Practicing Engineers.” *Report No. NEHRP Seismic Design Technical Brief No. 4,* NEHRP Consultants Joint Venture, a partnership of the Applied Technology Council and the Consortium of Universities for Research in Earthquake Engineering for the National Institute of Standards and Technology, Gaithersburg, Maryland, United States.
- NZS (1997). *Steel Structures Standard, NZS 3404: Part 1.* New Zealand Standards, New Zealand.
- PEER/ATC (2010). “Modeling and acceptance criteria for seismic design and analysis of tall buildings.” *Report No. ATC-72-1,* prepared by the Applied Technology Council in cooperation with the Pacific Earthquake Engineering Research Center, Redwood City, California, United States.
- Picard, A. and Beaulieu, D. (1985). “Behaviour of a simple column base connection.” *Canadian Journal of Civil Engineering, 12(1), 126–136.*
- Popov, E. P., Bertero, V. V., and Chandramouli, S. (1975). “Hysteretic behavior of steel columns.” *Report No. UCB/EERC-75/11,* Earthquake Engineering Research Center, University of California, Berkeley, Berkeley, California, United States.

- Popov, E. P., Blondet, M., and Stepanov, L. (1997). “Cyclic testing of four full-scale steel beam-column connections with “dogbones”.” *Report No. UCB/EERC-96/05*, Department of Civil Engineering, University of California Berkely, Berkely, California, United States.
- Ricles, J., Fisher, J., Lu, L.-W., and Kaufmann, E. (2002). “Development of improved welded moment connections for earthquake-resistant design.” *Journal of Constructional Steel Research*, 58(5), 565–604.
- Ricles, J., Zhang, X., Lu, L., and Fisher, J. (2004). “Development of seismic guidelines for deep column steel moment connections.” *Report No. 04-13*, Advanced Technology for Large Structural Systems Engineering Research Center, Lehigh University, Bethlehem, Pennsylvania, United States.
- Rodas, P. T., Zareian, F., and Kanvinde, A. (2016). “Hysteretic model for exposed column–base connections.” *Journal of Structural Engineering*, 04016137.
- SAC/FEMA (1996). “Experimental Investigations of Beam-Column Subassemblages.” *Report No. SAC-96-01 Parts I and II*, SAC Joint Venture, a partnership of the Structural Engineers Association of California, Applied Technology Council, and California Universities for Research in Earthquake Engineering.
- Shaw, S. M. (2013). “Seismic performance of partial joint penetration welds in steel moment resisting frames.” Ph.D. thesis, University of California, Davis, California, United States.
- Shaw, S. M., Stillmaker, K., and Kanvinde, A. M. (2015). “Seismic response of partial-joint-penetration welded column splices in moment-resisting frames.” *Engineering Journal*, 52(2), 87–108.
- Shin, S. and Engelhardt, M. D. (2013). “Cyclic performance of deep column moment frames with weak panel zones.” *Proc., NEES Annual Meeting*.

- Stillmaker, K., Kanvinde, A., and Galasso, C. (2015). “Fracture mechanics-based design of column splices with partial joint penetration welds.” *Journal of Structural Engineering*, 142(2), 04015115.
- Suita, K., Yamada, S., Tada, M., Kasai, K., Matsuoka, Y., and Shimada, Y. (2008). “Collapse experiment on 4-story steel moment frame: Part 2 detail of collapse behavior.” *Proc., 14th world conference on earthquake engineering*, Vol. 1217, Beijing, China.
- Suzuki, Y. and Lignos, D. G. (2014). “Development of loading protocols for experimental testing of steel columns subjected to combined lateral drift and high axial load.” *Proc., 10th National Conference on Earthquake Engineering (10th NCEE)*, Anchorage, Alaska, United States.
- Suzuki, Y. and Lignos, D. G. (2015). “Large scale collapse experiments of wide flange steel beam-columns.” *Proc., 8th International Conference on Behaviour of Steel Structures in Seismic Areas*, Vol. 4.
- The MathWorks, Inc. (2015). *MATLAB and Statistics Toolbox Release 2015a*. Natick, Massachusetts, United States.
- Trautner, C. A., Hutchinson, T., Grosser, P. R., and Silva, J. F. (2015). “Effects of Detailing on the Cyclic Behavior of Steel Baseplate Connections Designed to Promote Anchor Yielding.” *Journal of Structural Engineering*, 142(2), 04015117.
- Tremblay, R., Tchegotarev, N., and Filiatrault, A. (1997). “Seismic performance of rbs connections for steel moment resisting frames: Influence of loading rate and floor slab.” *Proc., Second International Conference on the Behavior of Steel Structures in Seismic Areas, STESSA 97*, Kyoto, Japan.
- Tsai, K.-C. and Popov, E. (1988). “Steel beam-column joints in seismic moment resisting frames.” *Report No. UCB/EERC-88/19*, Earthquake Engineering Research Center, University of California, Berkeley, Berkeley, California, United States.

- Uang, C.-M. and Fan, C.-C. (2001). “Cyclic stability criteria for steel moment connections with reduced beam section.” *Journal of Structural Engineering*, 127(9), 1021–1027.
- Uang, C.-M., Ozkula, G., and Harris, J. (2015). “Observations from cyclic tests on deep, slender wide-flange structural steel beam-column members.” *Proc., The Annual Stability Conference, Structural Stability Research Council (SSRC)*, Nashville, Tennessee, United States.
- Uang, C.-M., Yu, Q.-S. ., Noel, S., and Gross, J. (2000). “Cyclic testing of steel moment connections rehabilitated with rbs or welded haunch.” *Journal of Structural Engineering*, 126(1), 57–68.
- Wang, S. (1988). “Seismic response of steel building frames with inelastic joint deformation.” Ph.D. thesis, Lehigh University, Bethlehem, Pennsylvania, United States.
- Wen, R., Akbas, B., and Shen, J. (2013). “Practical moment–rotation relations of steel shear tab connections.” *Journal of Constructional Steel Research*, 88, 296–308.
- Yu, Q. S., Gilton, C., and Uang, C.-M. (2000). “Cyclic response of rbs moment connections: Loading sequence and lateral bracing effects.” *Report No. SSRP 99-13*, Department of Structural Engineering, University of California, San Diego, La Jolla, California, United States.
- Zareian, F. and Kanvinde, A. (2013). “Effect of Column-Base Flexibility on the Seismic Response and Safety of Steel Moment-Resisting Frames.” *Earthquake Spectra*, 29(4), 1537–1559.
- Zhang, X. and Ricles, J. M. (2006). “Experimental evaluation of reduced beam section connections to deep columns.” *Journal of structural engineering*, 132(3), 346–357.